EFFECTS OF DYNAMICAL PROCESSES ON ATMOSPHERIC KELVIN WAVE VARIABILITY

Dissertation
with the aim of achieving a doctoral degree
at the Faculty of Mathematics, Informatics and Natural Sciences
Department of Earth System Sciences
at University of Hamburg

submitted by
Katharina Meike Holube

Hamburg, 2025

Department of Earth Sciences

Date of Oral Defense:	27.11.2025
Reviewers:	Prof. Dr. Nedjeljka Žagar Dr. Frank Lunkeit
Members of the examination commission:	Prof. Dr. Nedjeljka Žagar Prof. Dr. Carsten Eden Prof. Dr. Boualem Khouider Prof. Dr. Hermann Held Dr. Frank Lunkeit
Chair of the Subject Doctoral Committee Earth System Sciences:	Prof. Dr. Dirk Notz
Dean of Faculty MIN:	Prof. Dr.-Ing. Norbert Ritter

Eidesstattliche Versicherung | Declaration on Oath

Hiermit erkläre ich an Eides statt, dass ich die vorliegende Dissertationsschrift selbst verfasst und keine anderen als die angegebenen Quellen und Hilfsmittel benutzt habe.

Sofern im Zuge der Erstellung der vorliegenden Dissertationsschrift generative Künstliche Intelligenz (gKI) basierte elektronische Hilfsmittel verwendet wurden, versichere ich, dass meine eigene Leistung im Vordergrund stand und dass eine vollständige Dokumentation aller verwendeten Hilfsmittel gemäß der Guten wissenschaftlichen Praxis vorliegt. Ich trage die Verantwortung für eventuell durch die gKI generierte fehlerhafte oder verzerrte Inhalte, fehlerhafte Referenzen, Verstöße gegen das Datenschutz- und Urheberrecht oder Plagiate.

I hereby declare and affirm that this doctoral dissertation is my own work and that I have not used any aids and sources other than those indicated.

If electronic resources based on generative artificial intelligence (gAI) were used in the course of writing this dissertation, I confirm that my own work was the main and value-adding contribution and that complete documentation of all resources used is available in accordance with good scientific practice. I am responsible for any erroneous or distorted content, incorrect references, violations of data protection and copyright law or plagiarism that may have been generated by the gAI.

Hamburg, 19. September 2025

Katharina Meike Holube

This document was typeset using the `classicthesis` template developed by André Miede and Ivo Pletikosić available at https://bitbucket.org/amiede/classicthesis/.

ABSTRACT

Equatorial Kelvin waves (KWs) contribute significantly to the variability of the tropical atmospheric circulation; therefore, it is important to understand their excitation mechanisms, energetics and interactions with other waves and the mean flow. Kelvin waves are a part of the circulation response to latent heat release in the tropics. Additionally, several studies have shown that dynamical processes related to Rossby waves in the subtropics can act as KW sources. However, the dynamical mechanisms and their relative influences compared to diabatic processes are not conclusively understood. In this thesis, KW energy sources resulting from dynamical and diabatic processes are systematically compared using atmospheric data, with a focus on stationary KWs. The dynamical KW energy source mainly results from wave-mean flow interactions, both in the atmosphere and in idealized shallow-water model simulations.

The methodology is based on expanding the circulation in terms of normal-mode functions on the sphere to identify Kelvin waves, Rossby waves, inertia-gravity waves and mixed Rossby-gravity waves. Wave-mean flow interactions and wave-wave interactions of these modes are quantified to disentangle the mechanisms constituting the KW energy sources. This method allows for a consistent comparison of idealized shallow-water model simulations with reanalysis data. For the analysis of three-dimensional data, a numerical framework was developed that quantifies the dynamical processes, specifically the advection of momentum and temperature, based on the normal-mode expansion coefficients. For diabatic processes, the momentum and temperature tendencies due to parametrizations in ERA5 data are used.

The excitation of KWs by dynamical processes involving Rossby waves in the subtropics is demonstrated in shallow-water model simulations as a proof of concept. The model formulation based on normal modes allows to specify an external forcing that only acts on Rossby waves. Kelvin waves develop as a resonant response to interactions of forced Rossby waves with the zonal mean flow in geostrophic balance. This mechanism can also be interpreted as the growth of an eigenmode of the shallow-water equations, linearized with respect to the zonal mean flow. Such eigenmodes incorporate the wave-mean flow interactions in their spatial structures and eigenfrequencies.

In the atmosphere, a considerable portion of the KWs is stationary. Along with non-radiative diabatic heating, which includes latent heat release, the advection of warm air in the upper troposphere shapes the three-dimensional structure of the stationary KWs, while dissipation and momentum advection have secondary contributions.

Although temperature advection and non-radiative diabatic heating maintain the stationary KWs, these processes induce KW energy sinks, because the associated temperature tendencies are shifted relative to the KWs. The main KW energy source results from the meridional advection of zonal momentum in the winter hemisphere, which strengthens the KW easterlies over the Indian Ocean. Because this process is stronger than the KW energy sink due to temperature advection, dynamical processes overall induce a KW energy source. The temporal variability of the KW energy tendencies is governed by non-radiative diabatic heating.

A large part of the dynamical KW energy source results from wave-mean flow interactions, while wave-wave interactions have a smaller contribution. The interactions of equatorial $n = 1$ Rossby waves with the zonal mean flow in geostrophic balance have the strongest effect among the wave-mean flow interactions. These interactions induce a KW energy source, because the easterlies of the stationary $n = 1$ Rossby waves in the upper troposphere are located east of the KW easterlies.

For the first time, energy transfers between normal modes of the primitive equations are quantified in reanalysis data. Specifically, the energy that KWs gain through interactions of $n = 1$ Rossby waves with the zonal mean flow is supplied by both the $n = 1$ Rossby waves and the zonal mean flow. In these interactions, the $n = 1$ Rossby waves also receive energy from the zonal mean flow.

The numerical part of this thesis paves the way for quantifying the influences of dynamical and diabatic processes on other wave modes in the atmosphere, for example mixed Rossby-gravity waves and $n = 1$ Rossby waves. This would improve the understanding of wave dynamics in the tropical atmosphere and of tropical-extratropical interactions.

ZUSAMMENFASSUNG

Äquatoriale Kelvin-Wellen (KW) tragen erheblich zur Variabilität der tropischen Atmosphärenzirkulation bei; daher ist es wichtig, ihre Anregungsmechanismen, Energetik und Wechselwirkungen mit anderen Wellen und dem Grundstrom zu verstehen. Kelvin-Wellen sind Teil der Zirkulationsantwort auf die Freisetzung latenter Wärme in den Tropen. Darüber hinaus haben mehrere Studien gezeigt, dass dynamische Prozesse im Zusammenhang mit Rossby-Wellen in den Subtropen als KW-Quellen dienen können. Allerdings sind die dynamischen Mechanismen und ihre relativen Einflüsse im Vergleich zu diabatischen Prozessen nicht abschließend geklärt. In dieser Arbeit werden KW-Energiequellen, die aus dynamischen und diabatischen Prozessen resultieren, anhand von Atmosphärendaten systematisch verglichen, wobei der Schwerpunkt auf stationären KW liegt. Die dynamische KW-Energiequelle ergibt sich hauptsächlich aus Wellen-Grundstrom-Wechselwirkungen, sowohl in der Atmosphäre als auch in idealisierten Flachwasser-Modellsimulationen.

Die Methodik basiert auf der Entwicklung der Zirkulation nach einer Basis aus Eigenmoden auf der Kugel, um Kelvin-Wellen, Rossby-Wellen, Trägheits-Schwerewellen und gemischte Rossby-Schwerewellen zu identifizieren. Die Wellen-Grundstrom-Wechselwirkungen und Wellen-Wellen-Wechselwirkungen dieser Moden werden quantifiziert, um die Mechanismen zu entwirren, die die KW-Energiequellen erzeugen. Diese Methode ermöglicht einen konsistenten Vergleich von idealisierten Flachwassermodellsimulationen mit Reanalysedaten. Für die Analyse von dreidimensionalen Daten wurde ein numerisches Schema entwickelt, welches die dynamischen Prozesse, insbesondere die Advektion von Impuls und Temperatur, basierend auf den Eigenmoden-Entwicklungskoeffizienten quantifiziert. Für diabatische Prozesse werden die Impuls- und Temperaturtendenzen durch Parametrisierungen in ERA5-Daten verwendet.

Die Anregung von KW durch dynamische Prozesse unter Beteiligung von Rossby-Wellen in den Subtropen wird in Flachwasser-Modellsimulationen als Proof of Concept aufgezeigt. Die auf Eigenmoden basierende Modellformulierung ermöglicht es, einen externen Antrieb zu spezifizieren, der nur auf Rossby-Wellen wirkt. Kelvin-Wellen entwickeln sich als resonante Antwort auf Wechselwirkungen von angetriebenen Rossby-Wellen mit dem zonalen Grundstrom im geostrophischen Gleichgewicht. Dieser Mechanismus kann auch als Wachstum einer Eigenmode der um den Grundstrom linearisierten Flachwassergleichungen interpretiert werden. Solche Eigenmoden berücksichtigen die Wellen-Grundstrom-Wechselwirkungen in ihren räumlichen Strukturen und Eigenfrequenzen.

In der Atmosphäre ist ein beträchtlicher Teil der KW stationär. Zusammen mit der strahlungsfreien diabatischen Heizung, zu der auch die Freisetzung latenter Wärme gehört, bestimmt die Advektion warmer Luft in der oberen Troposphäre die dreidimensionale Struktur der stationären KW, während Dissipation und Impulsadvektion sekundäre Beiträge leisten.

Obwohl die Temperaturadvektion und die strahlungsfreie diabatische Heizung die stationären KW aufrechterhalten, rufen diese Prozesse KW-Energiesenken hervor, da die damit verbundenen Temperaturtendenzen relativ zu den KW verschoben sind. Die

Hauptenergiequelle der KW resultiert aus der meridionalen Advektion von zonalem Impuls in der Winterhalbkugel, welche die KW-Ostwinde über dem Indischen Ozean verstärkt. Da dieser Prozess stärker ist als die KW-Energiesenke aufgrund der Temperaturadvektion, rufen dynamische Prozesse insgesamt eine KW-Energiequelle hervor. Die zeitliche Variabilität der KW-Energietendenzen wird durch die strahlungsfreie diabatische Heizung bestimmt.

Die dynamische KW-Energiequelle resultiert hauptsächlich aus Wellen-Grundstrom-Wechselwirkungen, während Wellen-Wellen-Wechselwirkungen einen geringeren Beitrag leisten. Die Wechselwirkungen der äquatorialen $n = 1$ Rossby-Wellen mit dem zonalen Grundstrom im geostrophischen Gleichgewicht haben den stärksten Einfluss unter den Wellen-Grundstrom-Wechselwirkungen. Diese Wechselwirkungen rufen eine KW-Energiequelle hervor, da sich die Ostwinde der stationären $n = 1$ Rossby-Wellen in der oberen Troposphäre östlich der KW-Ostwinde befinden.

Erstmalig werden Energieübertragungen zwischen Eigenmoden der primitiven Gleichungen in Reanalysedaten quantifiziert. Insbesondere wird die Energie, die KW durch Wechselwirkungen von $n = 1$ Rossby-Wellen mit dem zonalen Grundstrom erhalten, sowohl von den $n = 1$ Rossby-Wellen als auch vom zonalen Grundstrom bereitgestellt. In diesen Wechselwirkungen erhalten die $n = 1$ Rossby-Wellen auch Energie vom zonalen Grundstrom.

Der numerische Teil dieser Arbeit ebnet den Weg für die Quantifizierung der Einflüsse dynamischer und diabatischer Prozesse auf andere Wellenmoden in der Atmosphäre, beispielsweise gemischte Rossby-Schwerewellen und $n = 1$ Rossby-Wellen. Dies würde das Verständnis der Wellendynamik in der tropischen Atmosphäre und der Wechselwirkungen zwischen den Tropen und Extratropen verbessern.

PUBLICATIONS

First Author

The following three publications and pre-publications are part of this dissertation and are included in the appendix:

Appendix A

Holube, K. M., Lunkeit, F., Vasylkevych, S., and Žagar, N. (2024). Resonant Excitation of Kelvin Waves by Interactions of Subtropical Rossby Waves and the Zonal Mean Flow. *Journal of the Atmospheric Sciences* 81.11, 1833-1848. https://doi.org/10.1175/JAS-D-24-0033.1

Appendix B

Holube, K. M., Lunkeit, F., Vasylkevych, S., and Žagar, N. Influences of dynamical and diabatic processes on stationary and transient equatorial Kelvin waves. Under minor revisions in the *Journal of Advances in Modeling Earth Systems (JAMES)*.

Appendix C

Holube, K. M., Lunkeit, F., Vasylkevych, S., and Žagar, N. Energy transfer from the zonal mean flow and $n = 1$ Rossby waves to Kelvin waves through normal-mode interactions. To be submitted to the *Journal of Geophysical Research: Atmospheres*.

Minor contributions

I contributed to the following publication through discussions, by supporting the formal analysis and editing the manuscript draft.

Chen, P., **Holube, K. M.**, Lunkeit, F., Žagar, N., Zhao, Y.-B. and Lu, R. Equatorial wave circulation associated with subseasonal convective variability over the subtropical western North Pacific in boreal summer. Submitted to *Weather and Climate Dynamics*. https://doi.org/10.5194/egusphere-2025-2485

ACKNOWLEDGMENTS

I am deeply grateful to everyone who has supported me throughout my PhD time. Firstly, I would like to thank my supervisor, Nedjeljka Žagar, for the great guidance, support and all the advice ever since I joined her group. Thank you for suggesting to pursue a PhD in your group, for teaching me about the beauty of atmospheric dynamics, and for also leaving me freedom to study what interests me. I am very grateful to my co-supervisor, Frank Lunkeit, for always having an open door and kind advice. Thank you for clearing up my confusion a number of times, and for showing me how to structure my thoughts and texts. I would also like to thank Sergiy Vasylkevych for teaching me about TIGAR, normal modes and everything that goes with it, and for long discussions. Thank you for being patient and for motivating me to take the analysis one step further when I needed it. I would like to thank my panel chair Stefan Bühler and my mentor Mira Shevchenko for the support and for monitoring my progress.

I am very grateful to all current and former members of the Grindelberg hallway for letting me be part of this great one-of-a-kind community. I would like to thank Sándor Mahó for great conversations and discussions. Thanks a lot, Chen Wang, for sharing office, breaks and advice. I would like to thank Peishan Chen for the great productive and relaxing times, in Hamburg and around the world. Thank you, Valentino, Iana, Heena, Alexia, Juntian, Ole, Theo, Amelie, Xintong, Kyriakos, Bernhard, Yuan-Bing, Robin, Richard and Frank for good times in lunch and coffee breaks and at conferences and retreats, and for your tips on occasional questions.

Specifically for reading the essay of my thesis, or parts of it, I would like to thank Sándor Mahó, Sergiy Vasylkevych, Juntian Chen and Janina Bömeke.

I would like to thank everyone in the graduate school of TRR 181, especially the organizers Lea Diederichsen, Jennifer Fandrich and Johanna Cordes. I am thankful to Saskia Pfeiffer, Lea Pöhls and Anna Leßmeister for organizing the Fast-Track PhD program at the Hamburg Research Academy.

Thank you, Janina, Niklas, Dominik, Mailin, Nele, Teika and Anja for spending good times while studying together and becoming friends. I would like to thank my friends outside of Hamburg, especially Sebastian, Clara, Hannah and Florian, for beautiful visits and for staying in touch. Finally, a big Thank you! goes to my family for the love and support at all times.

CONTENTS

Part I

UNIFYING ESSAY

1

INTRODUCTION

The large-scale atmospheric circulation can be described as a combination of waves and a background flow. For instance, high- and low-pressure systems in the mid-latitudes can be understood as Rossby waves, superimposed on the westerly jet stream. Special wave types occur in the tropics, where the horizontal component of the Coriolis force is weaker than in the mid-latitudes and it changes sign at the equator (Vallis, 2017). Moreover, defining a background flow is less straightforward in the tropics compared to higher latitudes, because the direction and strength of zonal wind vary along the equator. In fact, part of the time-averaged tropical circulation can be described as stationary equatorial waves (Wallace et al., 2023).

In the linear wave theory, which applies best when the wave amplitudes are small, the waves are independent of each other. However, waves of finite amplitude can interact with one another and with the background flow (Craik, 1985). Through such interactions, energy is transferred between different waves (e.g. Ripa, 1983c).

The Kelvin wave (KW), which is one of the equatorial wave types, is studied in this thesis. Kelvin waves contribute significantly to the variability of the tropical atmosphere, and their accurate representation in weather and climate models is of major importance (Stephan et al., 2021; Wallace et al., 2023). However, KWs are still subject to uncertainties in recent model simulations (Bartana et al., 2023; Dias et al., 2023; Žagar et al., 2025). Therefore, it is crucial to understand the excitation mechanisms of KWs, their interactions with other modes and the zonal mean flow, and the associated energy sources. Kelvin waves can develop due to diabatic heating and dynamical, i.e. adiabatic, processes. This thesis examines how KWs are influenced by dynamical processes, which consist of wave interactions, in comparison with diabatic processes.

In the following, the definition of KWs is given (section 1.1) and different methods for the identification of KWs in atmospheric data and model outputs are outlined (section 1.2). Subsequently, the role of KWs for various phenomena in the tropical atmosphere is described (section 1.3). Section 1.4 then gives an overview of KW generation mechanisms, with a focus on dynamical processes. Finally, the specific research questions addressed in this thesis are posed in section 1.5.

1.1 The Kelvin wave solution of the shallow-water equations

The rotating shallow-water equations, which can be used as a simplified model for atmospheric phenomena, describe the dynamics of a shallow, incompressible fluid layer in the presence of rotation. Equatorial waves are eigenmodes of these equations, linearized around the state of rest, and they are derived in spherical geometry or on the equatorial β-plane. The Kelvin wave is the slowest eastward-propagating equatorial wave, and the other eigensolutions are Rossby, inertia-gravity (IG) and mixed Rossby-gravity (MRG) waves (Matsuno, 1966; Longuet-Higgins, 1968).

The simplest mathematical expression for the Kelvin wave is obtained under the equatorial β-plane approximation, where the Coriolis parameter $f = \beta y$ is a linear

function of the meridional displacement y from the equator. On a zonally periodic domain, the zonal velocity u and depth perturbation h of the KW with zonal wavenumber k are

$$u = \hat{u} \exp\left(-\frac{y^2}{4a_e^2}\right) \exp\left(ik\lambda\right) \quad \text{and} \quad h = \frac{D}{\sqrt{gD}} u\,, \tag{1.1}$$

shown in Fig. 1.1, while the meridional velocity is zero (Vallis, 2017). The meridional extent, or trapping scale, of the KW depends on the mean depth D of the fluid via the equatorial radius of deformation $a_e = (\sqrt{gD}/(2\beta))^{1/2}$. Further variables are the zonal wind amplitude $\hat{u}$, gravity g, and longitude λ.

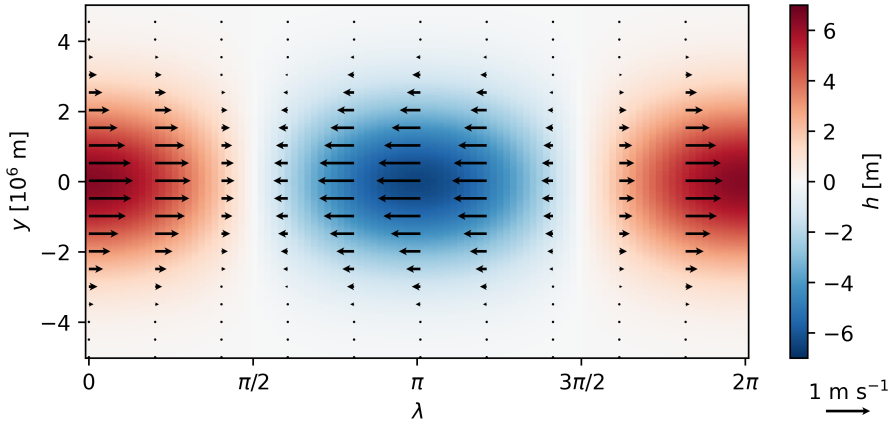

Figure 1.1: Kelvin wave with zonal wavenumber $k = 1$ on the equatorial β-plane. The mean depth is $D = 400$ m, and the zonal wind amplitude is set to $\hat{u} = 1$ m s^{-1}.

The zonal velocity of the KW is in geostrophic balance with the meridional geopotential gradient (Vallis, 2017). The velocity field of the KW has both a divergent and a rotational component (Hendon, 1986). On the equatorial β-plane, the dispersion relation of the KW, given by

$$\omega = k\sqrt{gD}\,, \tag{1.2}$$

indicates a non-dispersive eastward propagation (Vallis, 2017). On the sphere, the KW is slightly dispersive, and its spatial structure slightly deviates from Eq. 1.1, so that its trapping scale depends on the zonal wavenumber (Boyd and Zhou, 2008b). Furthermore, the KW on the sphere has non-zero but weak meridional velocities (Longuet-Higgins, 1968).

1.2 Identification of Kelvin waves

The theoretical properties of the KW solution given in section 1.1 serve as the basis for identifying KWs in atmospheric data and model outputs. Identification methods for KWs rely on their non-dispersive eastward propagation, their spatial structure, or a combination of both. However, these properties can be modified by processes not included in the linear KW solution, e.g., moist processes. Consequently, the different methods may yield varying results (Knippertz et al., 2022). In the following, three main categories of KW identification methods are outlined:

1. Projecting 3D atmospheric data onto the spatial structure of the KW for each wavenumber (e.g. Žagar et al., 2009).

2. Filtering KWs according to their wavenumbers and frequencies at a single level (e.g. Hayashi, 1982; Wheeler and Kiladis, 1999). The Kelvin waves identified using this method, called wavenumber-frequency decomposition (WFD), will be referred to as WFD-KWs below.

3. A combination of frequency filtering and projection onto the spatial structure at a single level (e.g. Yang et al., 2003).

In this thesis, the three-dimensional (3D) normal-mode decomposition is used, which belongs to the first category. Following Kasahara and Puri (1981) and Tanaka (1985), 3D fields of geopotential and wind are projected onto multivariate normal-mode functions, which are an orthogonal basis for the atmospheric circulation on the sphere. The vertical structures of these normal modes (Fig. C.16) are numerical solutions of a Sturm-Liouville problem that includes a given stratification profile. Each vertical structure function is associated with a parameter D_m, called the equivalent depth. The horizontal structures of the 3D normal modes are the eigenmodes of the shallow-water equations on the rotating sphere, whose mean depth is D_m. Thus, the set of normal modes includes KWs, whose trapping scale is determined by their vertical structures and zonal wavenumbers. The projection of atmospheric data onto the 3D normal modes yields the amplitudes and phases of the KWs at individual points in time. This method does not involve assumptions about the wave propagation. Therefore, the resulting KWs include phenomena with arbitrary phase velocities, including stationary waves (Žagar et al., 2022).

An alternative, widely used method for the KW identification is WFD (category 2 above), which relies on the wave propagation characteristics. This method involves the Fourier transform in zonal direction and time of atmospheric variables. From the resulting power spectrum as a function of zonal wavenumber and frequency, the occurrence of WFD-KWs is inferred by comparison with the theoretical dispersion relation (Eq. 1.2) (Hayashi, 1971, 1982; Wheeler and Kiladis, 1999). In contrast to the 3D normal-mode decomposition, WFD can be applied to individual atmospheric variables on a single level and latitude, e.g., outgoing longwave radiation (OLR). With this approach, atmospheric phenomena associated with the spatio-temporal variability of convection with specific wavenumbers and frequencies are identified as WFD-KWs (Takayabu, 1994), which are then frequently referred to as convectively coupled Kelvin waves (CCKWs) (Kiladis et al., 2009). Their spatial structures deviate from the KWs derived from dry linear equations (Khouider et al., 2012).

The third category is a hybrid method, combining the isolation of eastward-propagating phenomena using the Fourier transform with a projection of each variable onto the spatial structure of the KW on the equatorial β-plane (Eq. 1.1). This method is applied at individual vertical levels and requires selecting the meridional trapping scale of the waves (Yang et al., 2003).

With the described methods, KWs that vary on various time scales have been identified in atmospheric data. An overview of these waves and the associated atmospheric phenomena is given in the following section.

1.3 Kelvin waves in the tropical atmosphere

Shortly after KWs were theoretically derived, evidence for their occurrence in the stratosphere was provided by Wallace and Kousky (1968) using frequency-filtered radiosonde data. These waves can be generated by heat sources in the troposphere and propagate upward, depending on the background flow (Holton, 1972; Hayashi and Golder, 1978). In the stratosphere, WFD-KWs provide a momentum source for the westerly phase of the quasi-biennial oscillation (QBO), which is a periodic variation of the zonal mean zonal wind in the tropical stratosphere (Lindzen and Holton, 1968; Garcia and Richter, 2019). Around the tropopause, variations in the background flow on seasonal and interannual time scales also modulate the occurrence and propagation of WFD-KWs (Flannaghan and Fueglistaler, 2013; Suzuki et al., 2025).

In addition to the described stratospheric waves, a KW that takes 33 hours to circumnavigate the Earth was detected by Hamilton (1984). This period is consistent with the eigenfrequency of the KW with an equivalent depth of 10 km. The 33-hour KW is referred to as a free normal mode, because the influence of processes not considered in the linear wave theory appears to be weak. This wave has a barotropic vertical structure, and its horizontal structure extends into the extratropics (Matthews and Madden, 2000). Numerous free normal modes of different wave types have been detected in surface pressure data (Sakazaki and Hamilton, 2020; Sakazaki and Schindelegger, 2025).

The tropical atmosphere also contains stationary KWs. A well-known simplified model for the stationary, i.e. time-averaged, circulation in the tropics is the analytically derived circulation response to a localized heat source, representing latent heat release associated with convection (Gill, 1980). This circulation (Fig. 1.2a) consists of equatorial Rossby waves of the first meridional mode ($n = 1$) to the west of the heating, which are anticyclonic vortices, and KW westerlies to the east of the heating (Fig. 1.2b). The Rossby vortices resemble the observed circulation in the upper troposphere in the eastern hemisphere (Fig. 1.2c), and the KWs resemble the westerlies over the Pacific. This wave circulation is consistent with the enhanced convection over the Maritime Continent, which is indicated by upward motion (Wallace et al., 2023). Together with easterlies at lower levels (not shown), the KW westerlies in the upper troposphere are part of the Walker Circulation (Gill, 1980). This overturning circulation in the zonal-vertical plane is driven by diabatic heating, linked to sea surface temperature variations across the Pacific Ocean (Davey and Gill, 1987; Holton, 1992).

Another tropical phenomenon associated with KWs is the Madden-Julian Oscillation (MJO), which is a planetary-scale envelope of convective systems that propagates eastward from the Indian Ocean to the western Pacific, recurring every 30-90 days (Zhang et al., 2020). The spatial structure of the MJO is baroclinic, and it can be described as a combination of Kelvin and $n = 1$ Rossby waves (Adames and Wallace, 2014; Žagar and Franzke, 2015). Kelvin waves can emerge from the eastern side of this structure (Hendon and Salby, 1994). The phase velocity of the MJO is about 5 m s^{-1}, which is slower than that of KWs with a baroclinic vertical structure in the troposphere. Therefore, the MJO may be interpreted as a combination of equatorial wave modes, which interact with each other (Kitsios et al., 2019). Raphaldini et al. (2021) and Teruya et al. (2024) employed data-driven methods to describe such interactions, which appear to be associated with an energy transfer from KWs to $n = 1$ Rossby waves, facilitated by moist processes.

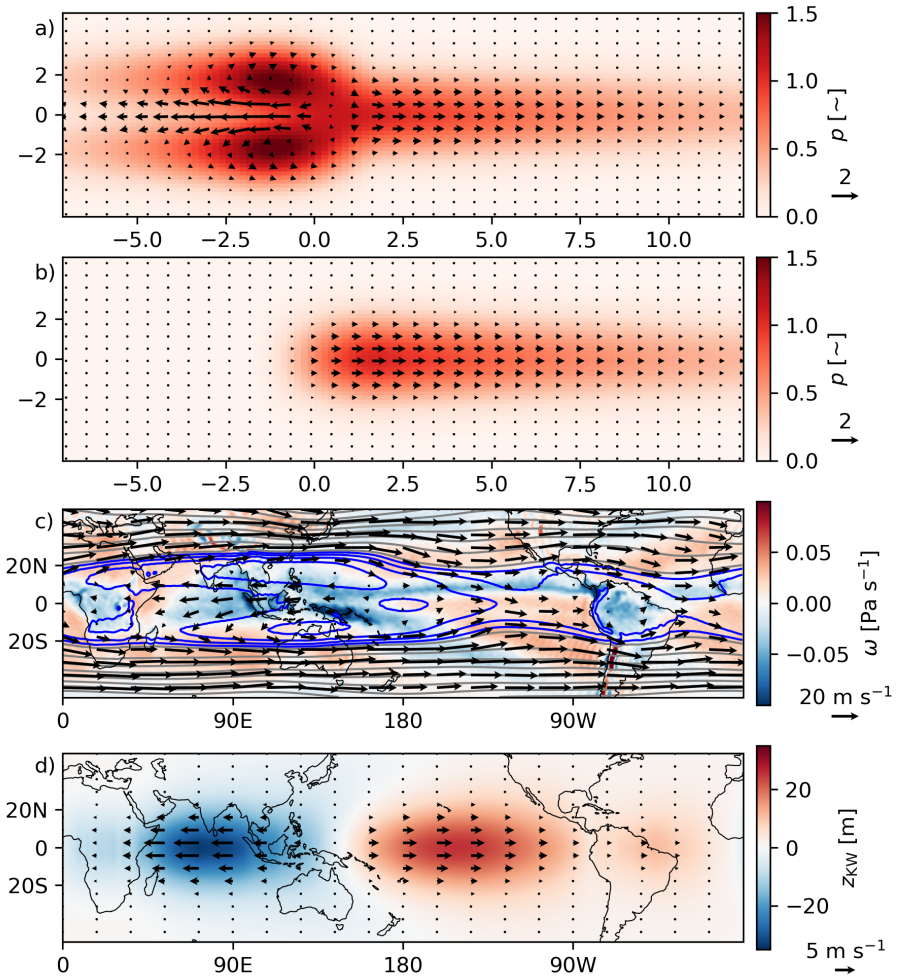

Figure 1.2: a) Circulation pattern derived by Gill (1980) as nondimensional pressure and horizontal velocity on a nondimensional grid, b) Kelvin wave part of a). c) Atmospheric circulation in the upper troposphere, consisting of horizontal velocity and geopotential (contours) at 150 hPa, shading: vertical velocity ω in pressure coordinates at 300 hPa, negative values indicate upward motion, similar to Fig. 14.4 in Wallace et al. (2023). d) Kelvin wave part of c), obtained using normal-mode decomposition, similar to Fig. 16 in Žagar et al. (2015). c) and d) show ERA5 reanalysis data (Hersbach et al., 2020), averaged over four years as described in Appendix C.

Many previous studies argue that the variability of tropical convection on a time scale of several days is associated with WFD-KWs (e.g., Kiladis et al., 2009). Connections between WFD-KWs and various tropical phenomena have also been suggested, such as the development of tropical cyclones (e.g., Ventrice et al., 2012; Lawton and Majumdar, 2023). WFD-KWs identified using OLR are associated with equivalent depths of about 12-50 m (Kiladis et al., 2009), whereas the vertical modes corresponding to these equivalent depths contain relatively low KW energy. This is one of the differences between WFD-KWs and KWs identified using 3D normal-mode decomposition (Žagar et al., 2022).

The reliable modeling of Kelvin waves is essential, not least because they are associated with organized convection and extreme rainfall in the tropics (Ferrett et al., 2020). However, forecast errors occur in KWs, in particular at the beginning of the forecast (Žagar

et al., 2013) and in connection to the vertical wind shear (Žagar et al., 2025). Additionally, the representation of the MJO in weather and climate models is subject to uncertainties (Jiang et al., 2020). Model biases in WFD-KWs can impact subseasonal predictions (Dias et al., 2023), and Dias et al. (2018) suggested that the accurate representation of WFD-KWs in forecast models is also associated with prediction skill in the extratropics. Furthermore, global climate models have biases in simulating WFD-KWs, and exhibit intensified WFD-KWs in a warmer climate, though results vary between different models (Bartana et al., 2023). In contrast, aqua-planet simulations suggest a decrease of WFD-KWs with global warming (Chien and Kim, 2024). The described discrepancies and model errors indicate that the roles of different processes that influence KWs have not yet been conclusively clarified.

In this thesis, KWs are identified using the 3D normal-mode decomposition, which, as mentioned in section 1.2, does not involve assumptions about the wave propagation. Therefore, phenomena with arbitrary time scales contribute to the analyzed KW signal, if their spatial structure (partly) aligns with that of the KW. This structure is defined in terms of wind and geopotential, and does not involve moisture. The energy of the KWs consists of kinetic and available potential energy (Tanaka, 1985). The stationary KWs, shown in Fig. 1.2d, contribute about 40% to the time-averaged KW energy. The remainder is due to KW variability on various time scales, as evident in the power spectrum in Fig. C.19a. For instance, the KW energy exhibits seasonal variations, and it is largest in boreal summer (Blaauw and Žagar, 2018; Žagar et al., 2022). The variability of KWs on subseasonal time scales (Fig. C.19a) is consistent with their contribution to the MJO (Žagar and Franzke, 2015). Eastward-propagating structures with shorter time scales are also included in the KWs (Žagar et al., 2022), and these structures can be associated with convection (Castanheira and Marques, 2015).

The stationary KWs contain easterly and westerly winds (Fig. 1.2d) over the Indian Ocean and Pacific Ocean, respectively. The winds and geopotential balance out to zero in the zonal average, because the KW is defined for $k \geq 1$, consistent with e.g. Kosovelj et al. (2019) and Žagar et al. (2022). Both easterlies and westerlies are also present in the KW response to a heat source with a single zonal wavenumber on the sphere (Matsuno, 1966). Only the westerlies over the Pacific Ocean (Fig. 1.2d) resemble the KW part of the circulation pattern discussed by Gill (1980) (Fig. 1.2b), which is however not directly comparable with the circulation on the spherical Earth because it is derived on a zonally infinite domain. Due to the strong convection over the Maritime continent, the Gill (1980)-pattern is nevertheless widely used to interpret the tropical atmospheric circulation (Wallace et al., 2023).

1.4 Kelvin wave generation mechanisms

Kelvin waves are a part of the circulation response to latent heat release associated with tropical convection, and such heat sources may vary on different spatial and temporal scales (Matsuno, 1966; Hayashi, 1970; Gill, 1980; Salby and Garcia, 1987; Mapes, 2000; Khouider and Majda, 2006). The stationary KW response to a tropical heat source was studied by Matsuno (1966) and Gill (1980), as described in section 1.3. However, their models use strong damping, for which the underlying processes are not clear, and the strength of the damping might not be realistic (e.g. Stechmann and Ogrosky, 2014, and

references therein). When the heat forcing is obtained from OLR observations, no dissipation is required to model the stationary KWs in the atmosphere (Stechmann and Ogrosky, 2014). The mentioned studies analyze the stationary solutions of linear equations, neglecting dynamical processes such as advection. When nonlinear effects are considered, the circulation does not change qualitatively, while the upper-level winds are enhanced and the lower-level winds are weakened (Gill and Phlips, 1986). When the long-wave approximation, which filters out gravity waves in Gill (1980)'s equations, is not made, wave interactions and gravity waves modify the circulation pattern, especially for weak dissipation (Kacimi and Khouider, 2018). Furthermore, the presence of a background flow can influence the wave response to heating (e.g., Monteiro et al., 2014). This thesis discusses the impacts of diabatic heating and temperature and momentum advection on stationary KWs in the atmosphere.

In addition to tropical heating, KWs can be affected by the extratropical circulation, and the underlying mechanisms depend on the background flow (e.g. Hoskins and Yang, 2000). Rossby waves can only cross the equator at longitudes with westerlies in the tropics, such as over the eastern Pacific (Webster and Holton, 1982). Otherwise, equatorward-propagating Rossby waves encounter a critical line and break (Charney, 1969). However, this does not imply that the tropics are shielded from mid-latitude influences. Even if the waves do not reach the tropics, nonlinear processes occurring around the critical line may provide a forcing for WFD-KWs (Murakami, 1974; Tulich and Kiladis, 2021).

The influence of dynamical processes originating outside of the tropics on equatorial waves has been studied in simplified models by applying a forcing in the subtropics. Such a forcing preferentially excites waves whose eigenfrequencies are close to the frequency of the forcing (Zhang and Webster, 1992; Zhang, 1993). Equatorial easterlies reduce the frequency of the KWs through the Doppler effect and thus amplify the KW response to low-frequency forcing (Zhang and Webster, 1992). When a subtropical forcing propagates eastward together with the KWs, the resulting KW growth can be understood as a resonance effect (Zhang, 1993). Such a forcing represents Rossby waves that are advected eastward by the subtropical jet. Similarly, KWs are part of the response to eastward-propagating vorticity forcing in the subtropics in primitive-equation model simulations (Hoskins and Yang, 2000). Consistent with the described mechanisms, the generation of WFD-KWs connected to Rossby waves that break at a critical line has been demonstrated in aqua-planet simulations. In this case, the forcing is constituted by eddy momentum flux convergence associated with the wave breaking, which projects onto the meridional structure of the KW (Tulich and Kiladis, 2021).

Zhang and Webster (1992), Zhang (1993) and Hoskins and Yang (2000) focused on the direct effects of external forcings in the subtropics on KWs. In their simulations, other waves develop as well, whose interactions could also influence the KW. Previous studies have examined such dynamical effects on KWs in idealized models, but not specifically for the resonant wave excitation. For instance, in the shallow-water model simulations conducted by Barpanda et al. (2023), meridional advection of vorticity has a greater impact on tropical divergence and the associated KWs than the stationary vorticity forcing in the subtropics. Furthermore, KWs develop in the absence of an external forcing due to interactions of baroclinic $n = 1$ Rossby waves with a barotropic shear flow (Namazi and Khouider, 2013). In this thesis, the resonant excitation of KWs involving Rossby waves

in the subtropics is simulated to examine the effects of the internal model dynamics separately from external forcings.

In the atmosphere, connections between WFD-KWs and subtropical Rossby waves have also been demonstrated (Straub and Kiladis, 2003; Cheng et al., 2022). In particular, the WFD-KW excitation mechanism through eddy momentum flux convergence in the subtropics, as simulated by Tulich and Kiladis (2021), was identified in reanalysis data (Cheng et al., 2022). Additionally, studies that did not specifically focus on the subtropics found that dynamical processes are vorticity sources for WFD-KWs in the lower and mid-troposphere (Matthews, 2021) and energy sources for KWs (Tanaka, 1985).

These findings raise the question of how the influences of dynamical and diabatic processes on KWs compare with each other. In aqua-planet simulations, eddy momentum flux convergence in the subtropics associated with breaking Rossby waves has a stronger influence on WFD-KWs than convective heating in the tropics (Tulich and Kiladis, 2021). This thesis employs the 3D normal-mode decomposition to compare the influences of dynamical and diabatic processes on KWs in the atmosphere, including stationary KWs.

In the 3D normal-mode framework, the energy sources and sinks of KWs can be quantified following Tanaka (1985), who identified dynamical processes as a source of KW energy. This result appears only as a small aspect within a broader analysis of various normal modes. In the winter climatology, Castanheira and Marques (2021) also found a dynamical KW energy source, and because the KW energy is approximately constant in the time-average, it follows that diabatic processes are a KW energy sink. Furthermore, Castanheira and Marques (2021) showed that the dynamical KW energy source is enhanced during the MJO. Beyond the mentioned results, the normal-mode energy budget of tropical waves has been less intensely studied, whereas this method has been applied to the general circulation (e.g. Tanaka and Kung, 1988; Marques et al., 2014) and extratropical phenomena (Tanaka and Terasaki, 2005; Marques and Castanheira, 2017; Castanheira and Marques, 2019).

The KW energy tendencies were evaluated by Tanaka (1985) and Castanheira and Marques (2021) as integrated quantities and spectra. This makes it difficult to infer details about the underlying dynamical mechanisms. Furthermore, the contributions of latent heat release and radiative heating to the diabatic KW energy tendencies are not known. This thesis provides additional insights into the KW energy tendencies by explicitly evaluating both dynamical and diabatic sources.

The dynamical KW energy tendencies are composed of the interactions of various modes. This becomes apparent when the circulation is regarded as a linear combination of normal modes, which are eigenmodes of the linearized equations with respect to the state of rest. The interactions of these modes are represented by the quadratic terms in the equations, such as advection. Applying the normal-mode decomposition to each factor of these quadratic terms allows to split them into wave-mean flow and wave-wave interactions. Wave-mean flow interactions include, for example, momentum tendencies that result from the wave being advected by the zonal mean flow. Wave-wave interactions refer to the products of wave-related quantities. Previous studies did not investigate the impact of these interactions on KWs in the normal-mode framework. However, shallow-water model simulations showed that wave-mean flow interactions can generate MRG waves, which also contribute to the tropical circulation variability (Mahó et al., 2024a,b).

Wave-wave interactions have also been suggested as a MRG wave source (Raupp and Silva Dias, 2005). In the atmosphere, the wave-mean flow and wave-wave interactions have been evaluated in the context of the Arctic Oscillation (Tanaka and Terasaki, 2005). The normal-mode decomposition has been used to quantify the kinetic energy transfers between different scales involving Rossby and inertia-gravity modes (Morfa and Stephan, 2025). Considering both kinetic and available potential energy, the impacts of wave-mean flow and wave-wave interactions on Kelvin waves are discussed in this thesis.

1.5 Research questions

This thesis investigates how dynamical processes influence equatorial Kelvin waves. In reanalysis data, the dynamical processes are also compared with diabatic processes.

First, a specific dynamical KW excitation mechanism is identified in idealized shallow-water model simulations to answer the question:

1. How can Kelvin waves be excited by dynamical processes associated with Rossby waves in the subtropics?

In the atmosphere, the stationary Kelvin waves and the Kelvin wave energy budget are studied to answer the following questions:

2. Which processes maintain the stationary Kelvin wave pattern along the equator?
3. How do Kelvin wave energy sources due to dynamical and diabatic processes compare, and where do these processes take place?

The dynamical KW energy sources are examined in more detail by answering the following research questions both for the idealized simulations and using 3D reanalysis data:

4. Which advection terms underlie the sources of Kelvin wave energy?
5. What are the contributions of wave-mean flow interactions and wave-wave interactions to the dynamical Kelvin wave energy sources?
6. Which modes transfer energy to Kelvin waves?

Question 1 is the research question of Appendix A, and questions 2 and 3 are the research questions of Appendix B. The decomposition of the dynamical processes into wave-mean flow and wave-wave interactions is discussed in Appendix A for the shallow-water model simulations, and in Appendix C for reanalysis data.

A very recent study by Chien et al. (2025) investigated question 3 for WFD-KWs using ERA5 reanalysis data. The KW identification method used in this thesis differs in several aspects, including the position of the rigid lid, which Chien et al. (2025) positioned at the tropopause, while it is located at 1 Pa in this thesis to impose fewer constraints on the vertical structure of the KWs. In addition, this thesis uses the temperature tendencies due to parametrizations of non-radiative and radiative processes from ERA5 data to quantify the effects of diabatic heating, which Chien et al. (2025) estimated as the residual of the temperature budget.

Discussing questions 4-6 in the context of both the idealized simulations and the atmosphere is insightful, because the simplifying assumptions are compared with real-world

conditions. This allows to assess the limitations of shallow-water model simulations in representing the atmospheric dynamics. Conversely, the use of a simplified model facilitates the understanding of the complex mechanisms involved. The idealized simulations and atmospheric data are analyzed with the same method to identify KWs and to evaluate their energy tendencies.

This essay has the following structure. Chapter 2 gives an overview of the normal-mode decomposition of the primitive equations and shallow-water equations. The wave-mean flow and wave-wave interactions, the normal-mode energetics method and the reanalysis data used are also summarized in chapter 2. Chapter 3 discusses questions 1-3. Question 4 is addressed in chapter 4. Questions 5 and 6 are covered in chapter 5, followed by the conclusions in chapter 6.

2

METHOD

This chapter describes the unified analysis framework for the primitive equations (section 2.1) and shallow-water equations (section 2.2), based on the expansion of the circulation in terms of the normal modes of these equations linearized with respect to the state of rest. This allows to evaluate wave-mean flow interactions and wave-wave interactions (section 2.3) and the normal-mode energy budget (section 2.4). The reanalysis data used in this thesis are specified in section 2.5.

2.1 Eigenmodes of the linearized primitive equations

The primitive equations describe the large-scale atmospheric dynamics (Haltiner and Williams, 1980). In the pressure coordinate system, this set of equations comprises prognostic equations for the components of horizontal velocity $\mathbf{V} = (u, v)^T$

$$\frac{\partial u}{\partial t} - 2\Omega v \sin\varphi + \frac{1}{a\cos\varphi}\frac{\partial \Phi}{\partial \lambda} = -\frac{1}{\cos\varphi}\mathbf{V}\cdot\nabla(u\cos\varphi) - \omega\frac{\partial u}{\partial p} + S_u\,, \tag{2.1}$$

$$\frac{\partial v}{\partial t} + 2\Omega u \sin\varphi + \frac{1}{a}\frac{\partial \Phi}{\partial \varphi} = -\frac{1}{\cos\varphi}\mathbf{V}\cdot\nabla(v\cos\varphi) - \omega\frac{\partial v}{\partial p} - \frac{(u^2+v^2)\tan\varphi}{a} + S_v\,, \tag{2.2}$$

the hydrostatic equation

$$\frac{\partial \Phi}{\partial p} = -\frac{RT}{p}\,, \tag{2.3}$$

the prognostic equation for temperature

$$\frac{\partial T}{\partial t} = -\mathbf{V}\cdot\nabla T - \omega\frac{\partial T}{\partial p} + \frac{RT}{c_p p}\omega + S_T\,, \tag{2.4}$$

and the continuity equation

$$\nabla\cdot\mathbf{V} + \frac{\partial \omega}{\partial p} = 0\,. \tag{2.5}$$

Geopotential is denoted Φ, and the pressure vertical velocity is denoted ω. The parameters are the Earth's radius a and angular velocity Ω, and the specific gas constant R and specific heat capacity c_p at constant pressure of dry air. The coordinates are $\lambda \in [0, 2\pi)$, $\varphi \in (-\frac{\pi}{2}, \frac{\pi}{2})$ and pressure p. Sources and sinks of momentum and temperature that are not explicitly included in the primitive equations, such as diabatic heating and frictional dissipation, are denoted $\mathbf{S} = (S_u, S_v, S_T)^T$; they are referred to as diabatic processes.

Following Tanaka (1985), the 3D normal modes are eigenmodes of Eqs. 2.1-2.5, linearized around the state of rest with reference temperature $T_0(p)$, from which the reference geopotential $\Phi_0(p)$ is obtained with the hydrostatic equation. Equations 2.3, 2.4 and 2.5 are combined to a single equation, which reads

$$-\frac{\partial}{\partial t}\frac{\partial}{\partial p}\left(\frac{p^2}{R\gamma_0}\frac{\partial \Phi'}{\partial p}\right) + \nabla\cdot\mathbf{V} = \frac{\partial}{\partial p}\left(\frac{p}{\gamma_0}\left(-\mathbf{V}\cdot\nabla T' - \omega\frac{\partial T'}{\partial p} + \frac{\omega R T'}{p c_p} + S_T\right)\right) \tag{2.6}$$

with static stability $\gamma_0 = \frac{RT_0}{c_p} - p\frac{dT_0}{dp}$. Perturbations of temperature and geopotential with respect to T_0 and Φ_0 are denoted with primes. The linearized primitive equations are Equations 2.1, 2.2 and 2.6 with their right-hand sides set to zero. The method of separation of variables is applied with the ansatz

$$(u, v, \Phi') = (\hat{u}, \hat{v}, g\hat{h})G(\sigma)\,, \tag{2.7}$$

where $\hat{u}$, $\hat{v}$ and $\hat{h}$ are functions of (λ, φ, t). This results in the vertical structure equation

$$\frac{d}{dp}\left(\frac{p^2 g}{R\gamma_0}\frac{dG}{dp}\right) + \frac{G}{D} = 0 \tag{2.8}$$

with boundary conditions

$$p\frac{dG}{dp} + \frac{\gamma_0}{T_0}G = 0 \quad \text{at} \quad p = p_s\,, \quad \text{and} \quad \frac{p}{\gamma_0}\frac{dG}{dp} \to 0 \quad \text{as} \quad p \to 0 \tag{2.9}$$

(Staniforth et al., 1985). The lower boundary condition applies at the reference pressure $p_s = 1013.25$ hPa. The vertical structure functions $G_m(p)$ are the eigensolutions of Eqs. 2.8 and 2.9 (Kasahara and Puri, 1981). The index m denotes the vertical mode, starting from the barotropic mode for $m = 1$, followed by baroclinic modes with an increasing number of zero-crossings. Examples for vertical structure functions are shown in Fig. C.16. Because Eqs. 2.8 and 2.9 constitute a Sturm-Liouville problem, the vertical structure functions are mutually orthogonal with respect to the inner product in Eq. B.23, and their eigenvalues, which are the inverses of the equivalent depths D_m, are positive (Staniforth et al., 1985).

The separation of variables also yields equations describing the horizontal dynamics. These are the linear shallow-water equations on the rotating sphere, also called Laplace's tidal equations, which read in nondimensional form

$$\frac{\partial \mathbf{X}_m}{\partial \tilde{t}} + \mathbf{L}_m \mathbf{X}_m = 0\,. \tag{2.10}$$

Each vertical mode is associated with a set of shallow-water equations with mean depth D_m. The nondimensional prognostic variables

$$\mathbf{X}_m = \begin{pmatrix} \tilde{u}_m \\ \tilde{v}_m \\ \tilde{h}_m \end{pmatrix} = \begin{pmatrix} u_m \sqrt{gD_m}^{-1} \\ v_m \sqrt{gD_m}^{-1} \\ h_m D_m^{-1} \end{pmatrix} \tag{2.11}$$

are obtained from u, v and $\Phi' = gh$ through projection onto the vertical mode m under consideration. The nondimensional time is $\tilde{t} = 2\Omega t$. The linear operator

$$\mathbf{L}_m = \begin{pmatrix} 0 & -\sin\varphi & \frac{\gamma_m}{\cos\varphi}\frac{\partial}{\partial\lambda} \\ \sin\varphi & 0 & \gamma_m\frac{\partial}{\partial\varphi} \\ \frac{\gamma_m}{\cos\varphi}\frac{\partial}{\partial\lambda} & \frac{\gamma_m}{\cos\varphi}\frac{\partial}{\partial\varphi}(\cos\varphi(\cdot)) & 0 \end{pmatrix} \tag{2.12}$$

contains the nondimensional parameter $\gamma_m = \frac{\sqrt{gD_m}}{2a\Omega}$ (Kasahara, 2020).

The eigenmodes of Eq. 2.10 with nondimensional eigenfrequencies $\nu_{k,n,m}$ are the Hough harmonics $\mathbf{H}_{k,n,m}(\lambda, \varphi) = \mathbf{\Theta}_{k,n,m}(\varphi)e^{ik\lambda}$, which represent Rossby, IG, Kelvin and

MRG modes (Longuet-Higgins, 1968). Their numerical computation is described by Swarztrauber and Kasahara (1985). In the following, the multi-index r combines m, the zonal wavenumber k and the meridional mode n. The meridional structure of $\mathbf{H}_r$ is given by the Hough functions $\mathbf{\Theta}_r = (U_r, -iV_r, Z_r)^T$. These vector functions combine three variables, which are zonal and meridional velocity and fluid depth (or geopotential height). The Hough harmonics are mutually orthogonal with respect to the inner product in Eq. A.24 (Longuet-Higgins, 1968).

The 3D normal modes consist of the horizontal structure functions $\mathbf{H}_r$ and vertical structure functions G_m. Projecting the horizontal velocity and geopotential fields on a 3D normal mode yields the complex expansion coefficient

$$W_r = \frac{1}{2\pi p_s} \int_0^{2\pi} \int_{-\frac{\pi}{2}}^{\frac{\pi}{2}} \int_0^{p_s} \begin{pmatrix} u\sqrt{gD_m}^{-1} \\ v\sqrt{gD_m}^{-1} \\ \Phi'(gD_m)^{-1} \end{pmatrix} \cdot \mathbf{\Theta}_r^* \, e^{-ik\lambda} G_m \, \cos\varphi \, dp \, d\varphi \, d\lambda \,, \tag{2.13}$$

which specifies the amplitude and phase of the mode r (Tanaka, 1985). The complex conjugate is denoted with $*$. Because the 3D normal modes are an orthogonal basis, the velocity and geopotential fields have a unique representation as a linear combination of normal modes using these expansion coefficients (Kasahara and Puri, 1981). Since u, v and Φ' are real, the expansion coefficients for negative k are the complex conjugates of those for positive k. Therefore, k is considered to be non-negative by combining the waves with $\pm k$.

Applying the projection on normal modes as in Eq. 2.13 to the nonlinear equations 2.1, 2.2 and 2.6 yields the prognostic equation

$$\frac{dW_r}{dt} = -2\Omega \, i\nu_r W_r + f_r \,, \tag{2.14}$$

with

$$f_r = \frac{2g}{p_s} \int_V \begin{pmatrix} (N_u + S_u)\sqrt{gD_m}^{-1} \\ (N_v + S_v)\sqrt{gD_m}^{-1} \\ \frac{\partial}{\partial p}\left(\frac{p}{\gamma_0}(N_T + S_T)\right) \end{pmatrix} \cdot \mathbf{H}_r^* G_m \, dV \,, \tag{2.15}$$

which is the projection of the momentum and temperature tendencies due to dynamical processes

$$\mathbf{N} = \begin{pmatrix} N_u \\ N_v \\ N_T \end{pmatrix} = \begin{pmatrix} -\frac{1}{\cos\varphi}\mathbf{V}\cdot\nabla(u\cos\varphi) - \omega\frac{\partial u}{\partial p} \\ -\frac{1}{\cos\varphi}\mathbf{V}\cdot\nabla(v\cos\varphi) - \omega\frac{\partial v}{\partial p} - \frac{\left(u^2+v^2\right)\tan\varphi}{a} \\ -\mathbf{V}\cdot\nabla T - \omega\frac{\partial T}{\partial p} + \frac{\omega R T'}{p c_p} \end{pmatrix} \tag{2.16}$$

and the diabatic sources on the mode r, where the 3D integral over the atmosphere is denoted

$$\int_V dV = \frac{1}{4\pi g} \int_0^{2\pi} \int_{-\frac{\pi}{2}}^{\frac{\pi}{2}} \int_0^{p_s} dp \, \cos\varphi \, d\varphi \, d\lambda \,. \tag{2.17}$$

The first term on the right-hand side of Equation 2.14 describes the linear wave propagation of the mode r with constant amplitude and phase speed. The second term modifies

the amplitude and phase speed of this mode through mode interactions and diabatic processes (Tanaka, 1985). Equation 2.14 is the starting point for deriving the normal-mode energy budget (section 2.4).

The time series of $W_r(t)$ contains variability on multiple time scales. The average of $W_r(t)$ over the time series under consideration is in the following referred to as the stationary wave $\overline{W}_r$. Assuming that the trend of W_r is small, the stationary wave is obtained from the time average of Eq. 2.14 as

$$\overline{W}_r = \frac{\overline{f}_r}{2\Omega i \nu_r} = -\frac{i\overline{f}_r}{2\Omega\nu_r} \,. \tag{2.18}$$

The stationary wave is therefore phase-shifted by 90° relative to the tendencies $\overline{f}_r$ that maintain it, further details are given in section B.2.1.

2.2 Nonlinear spectral shallow-water model

The idealized simulations in this thesis are conducted with the TIGAR model (Vasylkevych and Žagar, 2021), which solves the nonlinear shallow-water equations on the sphere using Hough harmonics as basis functions. Following Vasylkevych and Žagar (2021), the model equations read

$$\frac{\partial \mathbf{X}}{\partial \tilde{t}} + \mathbf{L}\mathbf{X} = \mathbf{N}_{\mathrm{SW}} + \mathbf{F} + \mathbf{Q} \,. \tag{2.19}$$

The nonlinear dynamical terms

$$\mathbf{N}_{\mathrm{SW}} = -\gamma \begin{pmatrix} \frac{1}{\cos\varphi}\tilde{\mathbf{V}}\cdot\tilde{\nabla}(\tilde{u}\cos\varphi) \\ \frac{1}{\cos\varphi}\tilde{\mathbf{V}}\cdot\tilde{\nabla}(\tilde{v}\cos\varphi) + \left(\tilde{u}^2+\tilde{v}^2\right)\tan\varphi \\ \tilde{\mathbf{V}}\cdot\tilde{\nabla}\tilde{h} + \tilde{h}\tilde{\nabla}\cdot\tilde{\mathbf{V}} \end{pmatrix} \tag{2.20}$$

are quadratic, as in the primitive equations, and include horizontal advection, but no vertical advection. The nondimensional viscosity and external forcing are denoted $\mathbf{F} = (F_u, F_v, F_h)^T$ and $\mathbf{Q} = (Q_u, Q_v, Q_h)^T$, respectively. The nondimensional fluid depth is $\tilde{h} = h/D - 1$, where h is the total fluid depth, i.e. including D, and the nondimensional gradient operator is $\tilde{\nabla} = a\nabla$. Because the shallow-water equations represent a single vertical mode, $\mathbf{X}$, $\mathbf{L}$ and γ do not have the index m. Topography is neglected throughout this thesis.

Expanding Eq. 2.19 in terms of Hough harmonics yields the prognostic equation for the expansion coefficient

$$\frac{dW_r}{d\tilde{t}} + (i\nu_r + d_r)W_r = f_r + q_r \,. \tag{2.21}$$

In this case, the multi-index r combines k and n. The spectral viscosity d_r acts only on the smallest resolved scales (Gelb and Gleeson, 2001). The projection of the nonlinear terms on the mode r is

$$f_r = \frac{1}{2\pi}\int_0^{2\pi}\int_{-\frac{\pi}{2}}^{\frac{\pi}{2}} \mathbf{N}_{\mathrm{SW}}\cdot\boldsymbol{\Theta}_r^* \, e^{-ik\lambda}\,\cos\varphi\, d\varphi\, d\lambda \,, \tag{2.22}$$

and similarly, q_r is the projection of $\mathbf{Q}$ on the mode r, so that $f_r + q_r$ are the two-dimensional (2D) equivalent of Eq. 2.15. The TIGAR model solves Equation 2.21 with a

pseudospectral method, i.e., $\mathbf{N}_{\mathrm{SW}}$ is evaluated on the 2D grid (Vasylkevych and Žagar, 2021). The model formulation in terms of Hough harmonics allows to specify a forcing that acts only on Rossby modes (section A.2.4).

2.3 Wave-mean flow and wave-wave interactions

Both the shallow-water equations and the primitive equations include quadratic nonlinear terms ($\mathbf{N}$ and $\mathbf{N}_{\mathrm{SW}}$, respectively), representing interactions between the normal modes. In the following, these interactions are described for the shallow-water equations with a notation that differs slightly from section A.2.2, while the corresponding theory for the primitive equations is given in Appendix C.

The nonlinear terms are the sum over the interactions of all combinations of modes a and b, excluding permutations:

$$\mathbf{N}_{\mathrm{SW}} = \sum_{a,b} \mathbf{N}_{\mathrm{SW}}(a,b)\,. \tag{2.23}$$

Interactions of two modes a and b involve the advection of momentum or fluid depth of the mode a by the velocity of the mode b and vice versa. The specific expression for the (a,b) interactions is

$$\mathbf{N}_{\mathrm{SW}}(a,b) = -\gamma \begin{pmatrix} \frac{1}{\cos\varphi}\left(\tilde{\mathbf{V}}_a \cdot \tilde{\nabla}\left(\tilde{u}_b \cos\varphi\right) + \tilde{\mathbf{V}}_b \cdot \tilde{\nabla}\left(\tilde{u}_a \cos\varphi\right)\right) \\ \frac{1}{\cos\varphi}\left(\tilde{\mathbf{V}}_a \cdot \tilde{\nabla}\left(\tilde{v}_b \cos\varphi\right) + \tilde{\mathbf{V}}_b \cdot \tilde{\nabla}\left(\tilde{v}_a \cos\varphi\right)\right) + 2\left(\tilde{u}_a\tilde{u}_b + \tilde{v}_a\tilde{v}_b\right)\tan\varphi \\ \tilde{\mathbf{V}}_a \cdot \tilde{\nabla}\tilde{h}_b + \tilde{\mathbf{V}}_b \cdot \tilde{\nabla}\tilde{h}_a + \tilde{h}_a\tilde{\nabla}\cdot\tilde{\mathbf{V}}_b + \tilde{h}_b\tilde{\nabla}\cdot\tilde{\mathbf{V}}_a \end{pmatrix}, \tag{2.24}$$

and the self-interactions of the mode a are

$$\mathbf{N}_{\mathrm{SW}}(a,a) = -\gamma \begin{pmatrix} \frac{1}{\cos\varphi}\tilde{\mathbf{V}}_a \cdot \tilde{\nabla}\left(\tilde{u}_a \cos\varphi\right) \\ \frac{1}{\cos\varphi}\tilde{\mathbf{V}}_a \cdot \tilde{\nabla}\left(\tilde{v}_a \cos\varphi\right) + \left(\tilde{u}_a^2 + \tilde{v}_a^2\right)\tan\varphi \\ \tilde{\mathbf{V}}_a \cdot \tilde{\nabla}\tilde{h}_a + \tilde{h}_a\tilde{\nabla}\cdot\tilde{\mathbf{V}}_a \end{pmatrix}. \tag{2.25}$$

If one of the interacting modes belongs to the zonal mean flow ($k = 0$), the interactions are referred to as wave-mean flow interactions, and else as wave-wave interactions.

Evaluating Eq. 2.22 for the mode interactions yields their influence on a third mode r, and the three modes a, b and r are referred to as a triad. The mode r is only influenced by the (a, b) interactions if its zonal wavenumber satisfies $k_r = k_a \pm k_b$. The influence of the interacting modes on the mode r can also be computed from the complex amplitudes and interaction coefficient of the modes a, b and r, as described by Ripa (1983b). The same applies to self-interactions, i.e. $a = b$. In general, the modes in a triad can have different types, e.g., Rossby waves can interact with gravity waves (Ripa, 1983b; Eden et al., 2019).

A special type of triad is the resonant triad, in which the eigenfrequencies of the constituent modes add up to zero (Ripa, 1983b). Theoretical studies analyzed resonant triads of equatorial waves for the shallow-water equations (Ripa, 1982, 1983b,c) and for the primitive equations on the equatorial β-plane (Raupp et al., 2008). One of their findings is that the geostrophically balanced zonal mean flow does not exchange energy

with wave modes in resonant triads, instead, it facilitates the energy exchange as a "catalyst mode".

This thesis does not discuss interactions of individual modes, only their combined effects. The circulation is split into several non-intersecting groups of orthogonal modes, e.g. one group contains Kelvin waves with all zonal wavenumbers, while another group is the zonal mean flow in geostrophic balance involving all meridional Rossby modes (see section A.2.2). The interactions of groups of modes are also computed with Equations 2.24 and 2.25, except that each variable represents the sum of all modes in one group. This is how Mahó et al. (2024a) attributed the generation of MRG waves to wave-mean flow interactions.

The interactions of two modes can in principle influence any other mode whose zonal wavenumber satisfies the mentioned condition. This differs from the widespread use of the term 'wave-mean flow interaction', referring to waves and the mean flow influencing each other. For example, the forcing mechanism of the quasi-biennial oscillation by the absorption of gravity waves at the critical level is frequently called wave-mean flow interactions (e.g. Lindzen and Holton, 1968; Holt et al., 2022). In the terminology used in this thesis, the forcing of the zonal mean flow by this mechanism would be referred to as wave-wave interactions, because zonally averaged momentum tendencies result from the mutual advection of waves.

2.4 Normal-mode energetics

In the following, the expressions for the energy of normal modes are given for the shallow-water model and for the 3D normal modes. Subsequently, the energy budget equation is discussed.

In the shallow-water system, the energy of one mode consists of its squared velocities and depth perturbations, integrated over the sphere:

$$I_{\mathrm{SW},k,n} = (2-\delta_{0k})\frac{gD}{2}|W_{k,n}|^2 = \frac{1}{2}\int_0^{2\pi}\int_{-\frac{\pi}{2}}^{\frac{\pi}{2}}\left(u_{k,n}^2 + v_{k,n}^2 + \frac{g}{D}h_{k,n}^2\right)\cos\varphi\, d\varphi\, d\lambda\,, \tag{2.26}$$

where $\delta_{0k} = 1$ for $k = 0$ and 0 otherwise. The depth perturbation of the mode with indices (k,n) is $h_{k,n} = \tilde{h}_{k,n}D$. For the sum over all modes, the depth perturbation is $\sum_{k,n}\tilde{h}_{k,n}D = \tilde{h}D = h - D$, and therefore, the energy is

$$I_{\mathrm{SW}} = (2-\delta_{0k})\frac{gD}{2}\sum_k\sum_n|W_{k,n}|^2 = \frac{1}{2}\int_0^{2\pi}\int_{-\frac{\pi}{2}}^{\frac{\pi}{2}}\left(u^2 + v^2 + \frac{g}{D}(h-D)^2\right)\cos\varphi\, d\varphi\, d\lambda\,, \tag{2.27}$$

consisting of kinetic and available potential energy (Kasahara, 1976).

In the primitive equations, the energy of the mode r

$$\begin{aligned} I_r &= \frac{(2-\delta_{0k})}{4}p_s D_m|W_r|^2 = \frac{1}{2}\int_V\left(u_r^2 + v_r^2 + \frac{\Phi_r^2}{gD_m}\right)dV \\ &= \int_V\frac{1}{2}\left(u_r^2 + v_r^2 + \frac{R}{\gamma_0}T_r^2\right)dV + \frac{1}{8\pi g}\int_0^{2\pi}\int_{-\frac{\pi}{2}}^{\frac{\pi}{2}}\frac{p_s\Phi_r^2(p_s)}{RT_0(p_s)}\cos\varphi\, d\varphi\, d\lambda \end{aligned} \tag{2.28}$$

consists of kinetic energy, available potential energy and an additional term arising from the lower boundary condition (Eq. 2.9) (Tanaka and Kung, 1988). Note that the energy in

Eq. 2.28 has the unit J m^{-2}, which differs from the unit of the energy of normal modes in the shallow-water model (Eqs. 2.26 and 2.27), which is J kg^{-1}.

The energy in Eq. 2.27 and the sum over all modes of Eq. 2.28 are conserved in the respective equations linearized around the state of rest. Furthermore, the energy in Eq. 2.27 is conserved in resonant triad interactions (Ripa, 1983b). Tanaka and Kung (1988) make assumptions under which the energy in Eq. 2.28 is conserved in the nonlinear primitive equations.

The prognostic equation for the energy of the 3D normal modes is

$$\begin{aligned} \frac{dI_r}{dt} &= \frac{2-\delta_{0k}}{2} p_s D_m \mathrm{Re}\left(\frac{dW_r}{dt} W_r^*\right) \\ &= \int_V \left[(N_u + S_u)u_r + (N_v + S_v)v_r + \frac{R}{\gamma_0}\left(N_T + S_T\right)T_r\right] dV\,. \end{aligned} \tag{2.29}$$

Equation 2.29 is derived from Equations 2.14 and 2.28, applying integration by parts and neglecting the boundary terms as described in Appendix B. A similar energy tendency equation applies to the rotating shallow-water equations, which is given in Eq. A.8 in terms of spectral variables.

The net energy tendency of a normal mode is related to various sources and sinks, which are given by the individual summands in Eq. 2.29. The energy tendencies resulting from dynamical processes are further broken down into the contributions of momentum and temperature advection in different spatial directions. The energy of the mode r increases if the velocity (temperature) source due to mode interactions or diabatic sources is in phase with the velocity (temperature) of this mode. Additionally, the energy tendencies resulting from diabatic temperature tendencies are separated into the effects of short-wave radiation, long-wave radiation and non-radiative processes like latent heat release (see section 2.5). The spatial origin of energy sources and sinks is determined by evaluating the integral in Eq. 2.29 over selected spatial directions only.

The dynamical energy tendencies are further decomposed into the contributions of mode interactions by evaluating Eq. 2.29 for $\mathbf{N}(a,b)$. The resulting energy tendency of the mode r is associated with energy tendencies of the mode a due to (b,r) interactions and energy tendencies of the mode b due to (a,r) interactions, as well as further terms usually assumed to be small (see Appendix C). When the residual of the energy tendencies of the modes a, b and r is indeed small, conclusions about energy exchanges between these three modes may be drawn. However, quantifying the energy transfer from one mode to another is in general not possible when three modes are involved (e.g. Marques and Castanheira, 2012). Special cases for the energy transfer between two modes are discussed in Appendix C. The statements in this paragraph also apply when a, b and r represent non-intersecting groups of modes.

The described methods for normal-mode decomposition and energetics diagnostics are applied at individual points in time. Averaging the resulting time series allows to assess which terms predominantly act as sources or sinks. For example, the time-averaged energy tendency of mode r due to meridional advection of zonal momentum is

$$\overline{-\int_V v\frac{\partial u}{\partial \varphi} u_r\, dV} = -\int_V \overline{\left(v\frac{\partial u}{\partial \varphi}\right)}\,\overline{u}_r\, dV - \int_V \left(v\frac{\partial u}{\partial \varphi}\right)' u_r'\, dV\,. \tag{2.30}$$

The first term on the right-hand side is the energy tendency of the stationary part of the mode r, and the second term results from co-variability of the momentum tendencies and zonal momentum of the mode r.

2.5 Reanalysis data

This thesis relies on analysis and forecast data from the ERA5 reanalysis (Hersbach et al., 2020). The forecast data contain momentum and temperature tendencies due to parametrizations in the IFS model, which is used to produce the ERA5 reanalysis. These correspond to the diabatic tendencies S_u, S_v and S_T, from which the KW energy tendencies are evaluated with Eq. 2.29. This is a novel aspect compared to previous studies, in which the diabatic energy sources were evaluated as the residual. A small residual still remains in the KW energy budget due to the discretization and truncation, but this is small enough to regard the computational scheme as valid (section B.2.5).

In addition to the temperature tendencies due to the combined effect of all parametrizations, the temperature tendencies due to short-wave and long-wave radiation parametrizations are available, allowing to separate radiative and non-radiative processes. A substantial part of the latter is latent heat release, as detailed in section B.2.1.

The KW energy tendencies and the stationary KWs are analyzed in hourly forecast data for January and July 2018. The KW energy budget is also evaluated for one year (1st December 2017 to 30th November 2018), for which the momentum and temperature tendencies due to parametrizations are averaged over each forecast with a lead time of 12 hours. In addition, 6-hourly analysis data are used to decompose the dynamical KW energy tendencies into mode interactions for a time series spanning 2016-2019.

All data are interpolated to 137 pressure-levels that are close to the model-levels as described in sections B.2.4 and B.11. The horizontal grid has a resolution of $\approx 0.45°$. For the normal-mode expansion, a triangular truncation with $k + n < 120$ is employed, and 94 vertical modes are used. Although the applied vertical truncation results in errors in the lower troposphere, the energy budget of KWs is well closed (section B.2.5).

3 INFLUENCE OF DYNAMICAL PROCESSES ON KELVIN WAVES

This chapter examines how dynamical processes affect Kelvin waves from three perspectives. Section 3.1 describes a specific KW excitation mechanism using idealized simulations. Subsequently, dynamical and diabatic processes are compared in reanalysis data. The processes that maintain the stationary KW pattern are identified (section 3.2), and the KW energy budget is evaluated (section 3.3).

3.1 Resonant Kelvin wave excitation

In the following, the resonant KW excitation associated with eastward-moving Rossby waves in the subtropics is explained. Shallow-water model simulations are conducted, which contain Rossby waves and a zonal background flow. The dynamical mechanisms acting on KWs are isolated, as the external forcing does not influence the KWs.

The initial condition of the simulations contains only the zonal background flow in geostrophic balance, featuring westerlies in the subtropics and weak easterlies at the equator (Fig. A.1), similar to but weaker than the zonal mean flow in the upper troposphere. This idealized zonal mean flow is not strong enough to advect Rossby waves eastward. Therefore, an eastward-moving forcing with a specified frequency ω_0 that only acts on Rossby waves with $k = 1$ is applied in the subtropics (Fig. A.3). Part of the Rossby wave response to this forcing also moves eastward with this frequency (Fig. A.4a), and the amplitude of these Rossby waves is modulated periodically (Fig. A.6a). The eastward-moving forced Rossby waves mimic Rossby waves in the upper troposphere, superimposed on the subtropical jet.

Simulations with two different forcing frequencies were conducted, and KWs developed in both. In the reference simulation, the forcing frequency is equal to the KW eigenfrequency ν'_K, modified by the background flow (see section A.6). In this case, the KW energy increases during the entire simulation (Fig. A.6a) and beyond. To illustrate the sensitivity to the forcing frequency, a second simulation was carried out, in which the forcing frequency is 20% lower than the KW eigenfrequency. In this simulation, KWs also develop, and their energy oscillates over time (Fig. A.6b).

To better understand the influence of the forcing frequency on the KW energy growth, the nondimensional prognostic equation for the expansion coefficient W_K of the KW with $k = 1$ is approximated as follows:

$$\frac{dW_K}{d\tilde{t}} + i\nu'_K W_K = \hat{f} e^{-i\omega_0 \tilde{t}} . \tag{3.1}$$

The left-hand side describes the wave propagation, which is determined by ν'_K. The right-hand side approximates the influence of the Rossby wave-mean flow interactions on KWs, which will be identified as the main effect (section 5.1). The forced Rossby wave-mean flow interactions moves eastward with the external forcing, this is represented as $e^{-i\omega_0 \tilde{t}}$ in Eq. 3.1, where $\hat{f}$ represents the amplitude of these interactions, see section A.4.3.

Because no KWs are present at the beginning of the simulation ($W_K(0) = 0$), the solution of Eq. 3.1 is

$$W_K = -i\hat{f}e^{-i\nu'_K\tilde{t}}\,\frac{e^{i(\nu'_K-\omega_0)\tilde{t}}-1}{\nu'_K-\omega_0}\,. \tag{3.2}$$

From Eq. 3.2, the time-series of non-dimensional KW energy $\tilde{I}_K$ is evaluated, similar to Eq. 2.26. If the forcing frequency deviates from the KW eigenfrequency, this energy is

$$\tilde{I}_K(\tilde{t}) = \frac{4\hat{f}^2}{(\nu'_K-\omega_0)^2}\sin^2\left(\frac{\nu'_K-\omega_0}{2}\tilde{t}\right)\,, \tag{3.3}$$

and this is in qualitative agreement with the simulation with the lower forcing frequency (Fig. A.8). The amplitude and period of the energy variation depend on the deviation of ω_0 from the KW eigenfrequency.

In the limit of ω_0 approaching ν'_K, the KW energy grows resonantly as

$$\tilde{I}_K(t) = \hat{f}^2t^2\,. \tag{3.4}$$

This approximates the KW energy growth in the reference simulation (Fig. A.8).

The described simulations demonstrate that KWs can develop through dynamical processes involving subtropical Rossby waves, which have an eastward-moving component with appropriate frequency. The specific processes and mode interactions are examined in sections 4.1 and 5.1. The persistent growth of KW energy in the resonance case is unique compared to previous studies demonstrating the KW generation by dynamical processes (Namazi and Khouider, 2013; Barpanda et al., 2023). This growth would be damped if the planetary-scale waves were influenced by dissipation.

3.2 Stationary Kelvin waves

In the stationary KW pattern, shown in Fig. 3.1a for January 2018, the winds are strongest in the upper troposphere, and the temperature has different signs above and below. Easterly winds are found in the eastern hemisphere, while westerlies are located over the Pacific Ocean. The stationary KWs are the response to the time-averaged dynamical and diabatic tendencies (Eq. 2.18). In the following, the contributions of different processes to the stationary KWs are discussed, for details see section B.3.

The stationary KW response to non-radiative diabatic heating contains westerlies over the Pacific and easterlies over the Indian Ocean around 300 hPa (Fig. 3.1b). These winds are located east and west of the strong latent heat release over the Maritime Continent. The KWs discussed in this thesis, which are defined for $k \geq 1$, are influenced by anomalies of the heating relative to the zonal average. The KW westerlies are located to the east of the positive heating anomalies, and the KW easterlies are located east of the negative heating anomalies, similar to the idealized stationary waves presented by Matsuno (1966).

While the wind direction in the stationary KW response to diabatic heating is the same as in the observed stationary KWs, the maximum winds in the latter are located at higher levels. There, the stationary KW winds result from advection of temperature; the contribution of vertical advection is shown in Fig. 3.1c. Upward vertical motion induces positive temperature tendencies by advecting warm air from below at the same

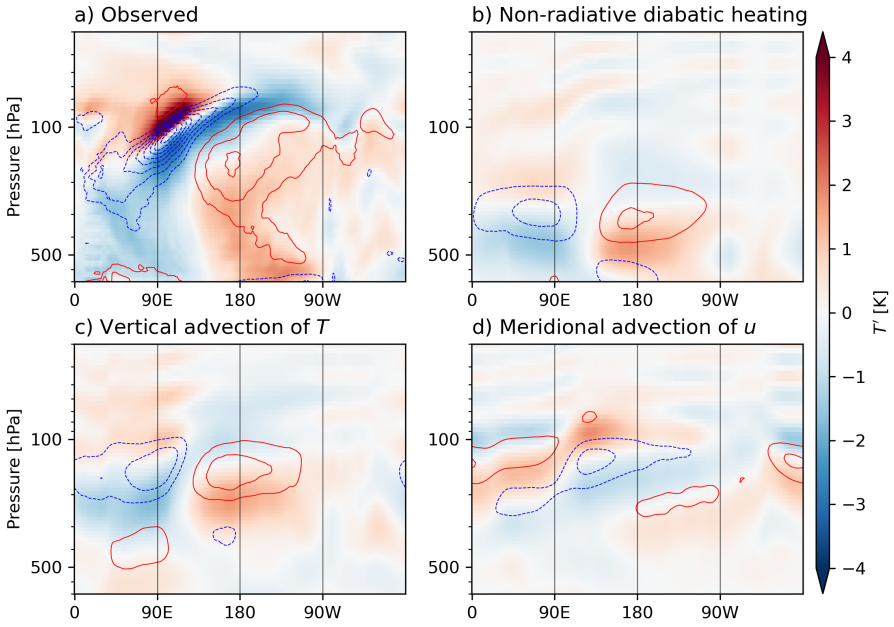

Figure 3.1: Zonal wind (contours with a spacing of 2 m s^{-1}) and temperature (shading) of stationary Kelvin waves in January 2018. b)-d) show the contributions of different processes, computed with Eq. 2.18, to the total stationary Kelvin wave in a). A truncation of the vertical modes is applied at $m = 40$.

longitudes as the non-radiative diabatic heating. The KW response to these temperature tendencies contains easterlies and westerlies around 150 hPa. The described process does not include the cooling of ascending air due to adiabatic expansion, whose influence on the KWs is weak. Furthermore, the horizontal advection of temperature partly shapes the narrow region of KW easterlies around 100° E (Fig. B.2d).

Another process contributing to the the KW easterlies in the eastern hemisphere is the meridional advection of zonal momentum (Fig. 3.1d). This advection is located over the Indian Ocean, where it produces easterly wind tendencies, which result in an energy source for KWs, as will be described in section 3.3. Finally, dissipative and radiative processes have a minor contribution to the stationary KWs (section B.3).

While non-radiative diabatic heating and temperature advection take place in various tropical regions, the enhanced heating over the Maritime Continent appears to strongly influence the stationary KWs, which have an energy maximum for $k = 1$ (Fig. B.3). Stationary KWs have a preference for low zonal wavenumbers because in Eq. 2.18 the eigenfrequency of the KW, which increases with zonal wavenumber, is in the denominator.

In summary, the major part of the stationary KW pattern is the response to positive temperature tendencies over the Maritime Continent (Fig. 3.1b, c). This is similar to the findings of Stechmann and Ogrosky (2014), who derived the stationary KW pattern from OLR, neglecting dissipation and momentum tendencies. Figure 3.1 complements their results by distinguishing diabatic heating and vertical temperature advection, which take place at different altitudes, and by evaluating the influence of momentum advection. Accordingly, the stationary KWs are maintained by both dynamical and diabatic processes.

3.3 Kelvin wave energy budget

Now, the energy budget of Kelvin waves, evaluated using reanalysis data, is discussed. The processes that have a large contribution to the stationary KWs (section 3.2) do not necessarily act as energy sources. In fact, if the stationary KW would be maintained only by a single process, the energy tendency due to this process would be zero, because according to Eq. 2.18, the stationary wave response is phase-shifted by 90° relative to the tendencies. In this case, the contributions of different longitudes to the energy tendencies balance out to zero. However, because several processes determine the stationary KW pattern, the phase shift between the KW and any individual tendency is not exactly 90°. Therefore, different processes induce non-zero energy tendencies of stationary KWs, which balance out each other.

The time-averaged KW energy tendencies for the sum over all zonal wavenumbers and vertical modes are shown in Fig. 3.2. For most terms, the energy tendencies of the stationary KWs have a smaller magnitude than the total KW energy tendencies, but the same sign. The largest KW energy source results from a dynamical process, namely advection of zonal momentum, which enhances the KW wind in the eastern hemisphere (Fig. B.10). The largest sink is associated with momentum dissipation (Fig. 3.2), including drag from turbulent fluxes, particularly in strong shear zones (see section B.4). The KW energy tendencies related to v tendencies are negligible.

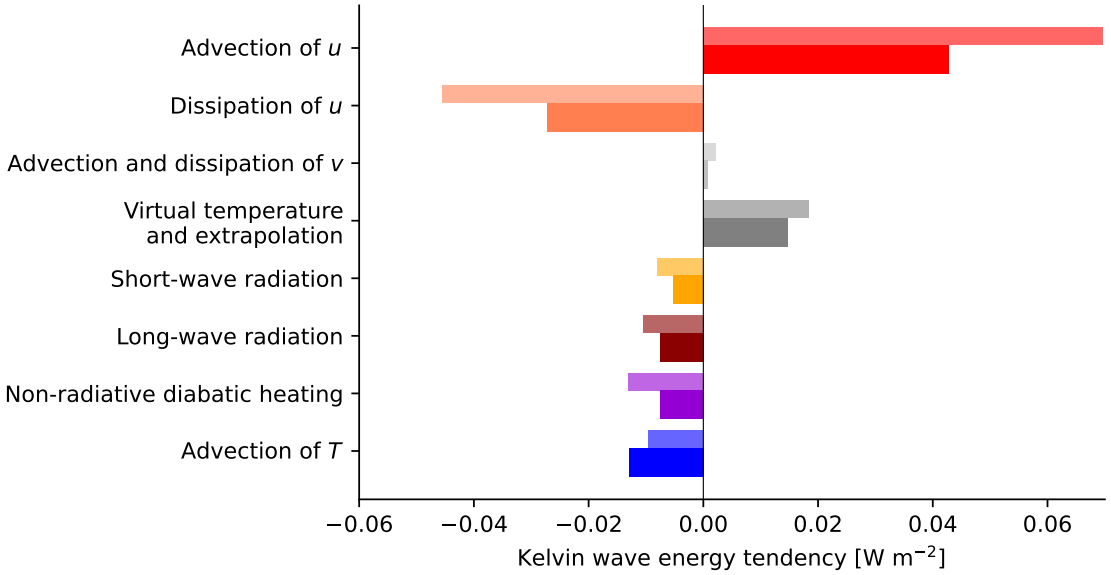

Figure 3.2: Kelvin wave energy tendencies due to dynamical and diabatic processes, for January 2018. Thick bars show tendencies for stationary Kelvin waves (e.g., the first term in Eq. 2.30), thin bars show the time-averaged energy tendencies of all Kelvin waves.

Additional KW energy sources arise from differences between the dry primitive equations in pressure coordinates and the IFS model, which has a hybrid vertical coordinate. In the IFS model, geopotential gradients are connected to the virtual temperature, and thus incorporate effects of moisture on the air density (section B.10). Another energy source arises from extrapolating between the surface pressure and the reference pressure (section B.11). While these terms are not negligible, they amount to less than half of the Kelvin wave energy tendency due to advection of zonal momentum (Fig. 3.2). Further-

more, long-wave and short-wave radiation induce sinks of KW energy, for details see sections B.4 and B.5.

Non-radiative diabatic heating results in a KW energy sink (Fig. 3.2), although it has a strong influence on the stationary KWs (Fig. 3.1). The cold KW temperature over the Indian Ocean is collocated with positive temperature tendencies due to latent heat release. The resulting KW energy sink outweighs the strengthening of positive KW temperature over the Pacific Ocean (Fig. B.5d). Similarly, dynamical temperature tendencies produce a sink of KW energy because warm air is advected into regions of cold KW temperature over the Indian Ocean (Fig. B.5c). Section 4.2 will show that this warm air is mainly advected from below.

In total, dynamical processes are a source of KW energy, while diabatic processes act as a sink in the time average. Using a different KW identification method, Tulich and Kiladis (2021) concluded as well that the dynamical energy source for WFD-KWs, which in their simulations results from eddy momentum flux convergence in the subtropics, exceeds the effect of heating in the tropics. The vertical profiles of the energy tendencies in their study are similar to those obtained with the normal-mode method (Fig. 3.3), with dynamical processes located in the upper troposphere and the KW energy sink due to tropical heating in the mid-troposphere. However, the major part of the KW energy tendencies evaluated in this thesis is associated with the stationary KWs (Fig. 3.3b), while the WFD-KWs studied by Tulich and Kiladis (2021) do not include stationary waves.

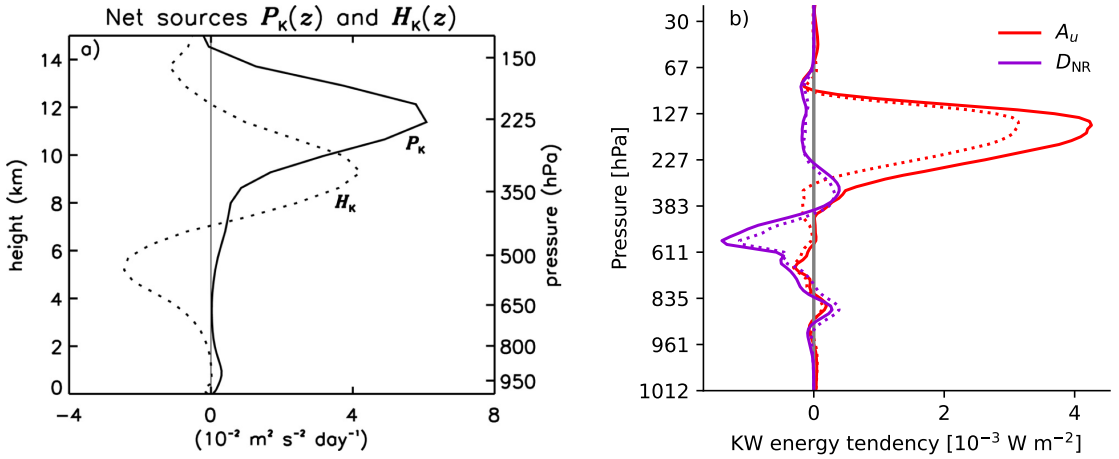

Figure 3.3: a) Vertical structures of the net remote eddy source $\boldsymbol{P}_K$ (solid) and tropical heating source $\boldsymbol{H}_K$ (dotted) for WFD-KWs in the study of Tulich and Kiladis (2021) (their Fig. 7a). b) Vertical structures of Kelvin wave energy tendencies, solid line: time average, dashed line: energy tendency of stationary Kelvin wave. To display the quantities in W m^{-2}, they are multiplied with $\Delta p/g$, where Δp is the pressure difference between two levels.

The WFD-KWs studied by Tulich and Kiladis (2021) and Cheng et al. (2022) propagate eastward, and thus their energy sources require eastward-propagating momentum or temperature tendencies. Such tendencies are associated with Rossby waves, which are advected by the subtropical jet. Due to the matching frequencies, Cheng et al. (2022) explain the resulting WFD-KW energy source as a resonance effect. The total KW energy tendencies obtained with the normal-mode energy budget comprise covariability between

the momentum or temperature tendencies and the KWs on all resolved time scales, and the analysis of individual frequencies is beyond the scope of this thesis.

The temporal variability of the KW energy tendencies is associated with the KW energy tendency due to non-radiative diabatic heating (Fig. B.7); the correlation coefficient between these two time series is 0.61. The KW energy tendencies due to advection of zonal momentum also exhibit temporal variations between the seasons and on a time scale of several days. However, this KW energy source is only weakly correlated with the total KW energy tendencies. The temporal variations of this source are partly balanced out by those of the KW energy sinks, e.g. dissipation of zonal momentum (Fig. B.17).

The main result that, in the time average, the largest KW energy source results from dynamical processes, is consistent with the studies of Tanaka (1985), Castanheira and Marques (2021) and Tulich and Kiladis (2021). Furthermore, a case study of WFD-KW variability over the western and central Pacific conducted by Straub and Kiladis (2003) illustrates that dynamical processes can have a stronger impact on the Kelvin wave variability than tropical SSTs. While Chien et al. (2025) argued that diabatic heating results in a greater energy source for WFD-KWs, their discussion focuses on the second baroclinic mode. An alternative method to investigate dynamical sources of KWs is the vorticity budget. Matthews (2021) evaluated the impact of vorticity sources on WFD-KWs and finds that dynamical processes act as a source in the lower and mid-troposphere, but as a sink in the upper troposphere. However, the findings of Matthews (2021) and Chien et al. (2025), who identified WFD-KWs as composites associated with convective variability, are not easily comparable to the results in this thesis, which were obtained with normal-mode decomposition.

4 CONTRIBUTIONS OF ADVECTION TERMS TO THE KELVIN WAVE ENERGY TENDENCIES

Both in reanalysis data and the shallow-water model simulations, a KW energy source results from dynamical processes (chapter 3), including advection of momentum and temperature or fluid depth. In the following, the KW energy tendencies resulting from advection in different spatial directions are discussed in the shallow-water model simulations (section 4.1) and in reanalysis data (section 4.2).

4.1 Shallow-water model simulations

In the reference simulation, where the KW energy increases throughout, the KW energy tendency is positive and oscillates (black line in Fig. 4.1). This oscillation corresponds to periodic variations in the Rossby wave amplitude (Figs. A.4 and A.6). The KW energy tendency results from momentum and depth tendencies (Eq. 2.20), which act as a KW energy source if they are in phase with the momentum or depth perturbations of the Kelvin wave. Figure 4.1 illustrates the processes that contribute to the KW energy tendency in the reference simulation, which are advection of momentum and fluid depth, as well as the nonlinear part of the depth tendencies due to divergence. These processes will be discussed in the following.

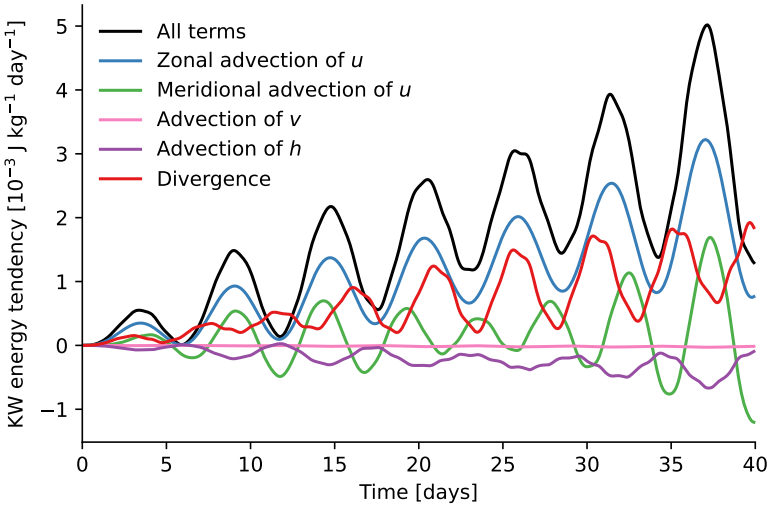

Figure 4.1: Kelvin wave energy tendency in the numerical simulation (All terms), decomposed into contributions of momentum and fluid depth advection, and of depth tendencies due to divergence ($\tilde{h}\tilde{\nabla} \cdot \tilde{\mathbf{V}}$ in Eq. 2.20).

The largest contributor to the KW energy tendencies is the zonal advection of zonal momentum (Fig. 4.1). This process is primarily associated with the advection of Rossby waves, which develop in response to the external forcing, by the background flow. Due to the shear in the background flow, the waves are not only displaced but also

deformed. This leads to momentum tendencies that can, in general, influence all wave modes, including KWs. In addition, meridional advection of zonal momentum results in KW energy tendencies that oscillate around zero (Fig. 4.1). Advection of meridional momentum has a minor impact on the KW energy tendencies, because the meridional velocity of KWs is small.

A small KW energy sink results from advection of fluid depth (Fig. 4.1). This term is small because a considerable fraction of the flow is in linear geostrophic balance, in which the velocity is perpendicular to the depth gradient, so that no fluid depth is advected. Another process resulting in depth tendencies is divergence, which changes the height of the fluid column. For a given divergence, the height of the fluid column decreases more if the initial fluid column is taller. Therefore, the depth tendencies due to divergence have a nonlinear component, which induces energy tendencies. In the reference simulation, this process has a strong impact (Fig. 4.1) because the zonal mean flow, which is in geostrophic balance, has large depth perturbations in the equatorial region (Fig. A.1). The energy tendencies due to divergence are particular to this formulation of the balanced zonal mean flow in the shallow-water model, and their analog in the atmosphere is less clear.

Now, the spatial distribution of momentum tendencies and the sensitivity to the latitude of the forcing are discussed for the interactions of the zonal mean flow with the forced part of the Rossby wave response to the external forcing, as in section A.4.4. These interactions comprise the major part of the KW energy tendencies (see section A.4.3). The forced Rossby waves propagate eastward with the same phase velocity as the Kelvin waves, and their amplitude is constant (Fig. A.4a). Since the zonal mean flow changes relatively little over time, the magnitude of the momentum and depth tendencies due to the forced Rossby wave-mean flow interactions, as well as their phase shift relative to the Kelvin waves, are approximately constant. Therefore, the tendencies at the first time step are discussed (Figs. A.9 and A.10), which are representative for the entire simulation.

The zonal momentum tendencies due to zonal advection are located in the subtropics (Fig. A.9a), where the zonal velocities of the Rossby vortices are advected eastward by the zonal mean flow. In particular, this leads to momentum tendencies around 15°-30° N, which align with the flank of the meridional KW structure. Therefore, the KWs are influenced by this process, which is evident in their positive energy tendencies (Fig. 4.1). In contrast, advection of zonal mean zonal momentum by meridional winds of the forced Rossby waves results in smaller and opposite momentum tendencies (Fig. A.9a). These tendencies are small because the meridional Rossby wave velocities are located at latitudes of weak shear near the maximum of the zonal background flow.

Changing the location of the Rossby wave forcing, while retaining the same background flow, modifies the influence of individual processes on the KWs (Fig. A.10). When the forcing is shifted closer to the equator, the meridional advection of zonal momentum results in larger tendencies, as the meridional velocities are collocated with stronger shear and higher KW velocities. The impact of zonal advection of zonal momentum on the Kelvin waves increases when the forcing is located 5° further south than in the reference simulation, because the momentum tendencies are collocated with stronger KW velocities. However, the strength of the background westerlies decreases towards the equator, reducing the zonal advection of zonal momentum and its effects on the KWs for a forcing location 10° further south than in the reference simulation. Moreover, the contribution of the depth tendencies due to divergence increases when the forcing is

shifted towards the equator, where the fluid depth perturbations are larger. The total Kelvin wave tendencies result from a combination of all these processes, which partly balance each other out (Fig. A.10).

In summary, while zonal advection of zonal momentum was identified as the process contributing most to the KW energy tendencies in the reference simulation, meridional advection of zonal momentum has a greater effect when the Rossby vortices are centered in the shear flow. Meridional advection of zonal momentum was also identified as the main contributor to the generation of MRG waves in idealized simulations (Mahó, 2024). Barpanda et al. (2023) obtained the structure and latitude of the subtropical Rossby vortices, which amplify KWs in their simulations, from the response to tropical heating. These Rossby vortices are indeed located in the shear flow south of the maximum background winds. However, in the vorticity budget analyzed by Barpanda et al. (2023), the meridional vorticity gradient, rather than the meridional shear of the zonal flow, determines the strength of the vorticity advection.

4.2 Reanalysis data

In the following, the processes underlying the dynamical KW energy tendencies are discussed using reanalysis data. Figure B.4 shows that the meridional advection of zonal momentum results in the largest energy source in the time average. This is partly counteracted by an energy sink due to vertical advection of temperature. The following discussion focuses on these two processes.

The zonal wind in the upper troposphere is sheared between stronger westerlies in the subtropics and weaker westerlies or easterlies near the equator. Advection of zonal momentum by an equatorward meridional flow thus results in westerly velocity tendencies, while a poleward flow enhances easterlies. Figure B.10 illustrates the KW energy tendencies due to meridional advection of zonal momentum in January 2018. Easterly Kelvin wave wind is found in the upper troposphere west of about 130° East, while westerly KW wind is found over the Pacific (Fig. B.10a). The KW energy tendencies due to meridional advection of zonal momentum are mainly located around 100° East (Fig. B.10b). There, KW easterlies are strengthened through advection of zonal momentum by southerly meridional wind in the northern-hemisphere subtropics (Fig. B.10c). The temporal variability of the KW energy source is related to the variability of the meridional velocity and of the KW zonal velocity.

The KW energy source due to meridional advection of zonal momentum is mainly located in the winter hemisphere (Figure B.6), where the westerly jet and the associated wind shear are stronger than in the summer hemisphere. In the discussed example for January, the KW energy tendencies are therefore associated with meridional velocities in the northern hemisphere. Conversely, in July, this KW energy source originates in the southern hemisphere.

The meridional winds required for the meridional advection of zonal momentum can result from deep convection, which induces divergent outflow in the upper troposphere. Conversely, equatorward-propagating Rossby wave trains contain divergence in the upper troposphere, which may also enhance the convection (Straub and Kiladis, 2003). This divergence, driven by dynamical processes, involves meridional winds, but differentiating these from the thermodynamically driven outflow is beyond the scope of this thesis. Furthermore, the Rossby vortices studied by Straub and Kiladis (2003) are

tilted in such a way that they transport westerly momentum poleward, and this could also strengthen the KW easterlies. Tulich and Kiladis (2021) also found a relation between the upper-troposphere dynamical WFD-KW energy source and tropical convection. They performed sensitivity simulations, in which the extratropical eddies were damped and nevertheless an eddy momentum flux forcing was found due to the circulation associated with tropical convection.

Now, the KW energy sink resulting from temperature advection is studied in more detail. Over the Indian Ocean, where the KW temperature is negative, advection of warm air in the mid- and upper troposphere induces the KW energy sink. This advection is related to ascending motion associated with deep convection. Energy tendencies only result from the nonlinear contribution, which is $\omega \partial T'/\partial p$, containing the vertical variation of temperature perturbations relative to the reference temperature profile. For the latter, a mid-latitude profile is chosen to represent the global stratification. Specifically, the analytical temperature profile from Jablonowski and Williamson (2006) is used, where the tropopause is located at 200 hPa. In the tropics, however, temperature continues to decrease around $150 - 250$ hPa because the tropopause is located at higher levels. As a result, perturbations relative to the reference temperature decrease with height at these levels, which is why upward vertical motion advects warm air from below, resulting in positive temperature tendencies. This process reduces the magnitude of the negative KW temperature over the Indian Ocean and enhances positive KW temperature over the western Pacific (Fig. B.5c), leading to a net KW energy sink.

The vertical advection of temperature does not only involve the described differences between the tropical and higher-latitude profiles. Around 120°-200° E, positive temperature anomalies relative to the zonal average are found in the equatorial region, which decrease with height, especially during boreal winter (Bao et al., 2022). Temperature advection by upward motion in the region of these anomalies results in positive temperature tendencies, which can induce KW energy tendencies.

The KW energy sink due to vertical advection of temperature could be connected to positive KW energy tendencies due to meridional advection of zonal momentum. This is the case when, in a region of deep convection, upward vertical motion occurs together with a divergent outflow in the upper troposphere, so that the KW easterlies are strengthened and the negative KW temperature is weakened. In the Rossby vortices studied by Straub and Kiladis (2003), divergence in the upper troposphere also occurs together with vertical motion.

In summary, meridional advection of zonal momentum induces the primary source of KW energy. This process strengthens the KW easterlies over the Indian Ocean. The importance of meridional advection suggests that the shallow-water model simulations in which the forcing is shifted equatorward compared to the reference simulation may provide a better representation of atmospheric processes. In the atmosphere, the KW energy source due to momentum advection is partly counterbalanced by a sink of KW energy resulting from vertical advection of temperature, which reduces the negative KW temperature in the upper troposphere. This process does not have a direct counterpart in the shallow-water model.

5 WAVE-MEAN FLOW AND WAVE-WAVE INTERACTIONS

In the following, the dynamical KW energy source is separated into wave-mean flow and wave-wave interactions. The shallow-water model simulations are discussed first (section 5.1), followed by the reanalysis data (section 5.2). Finally, the question of which modes transfer energy to Kelvin waves is addressed (section 5.3).

5.1 Shallow-water model simulations

To determine the KW energy tendencies arising from wave-mean flow and wave-wave interactions, the Hough harmonics are categorized into four groups: Rossby waves with $k > 0$, Kelvin waves, Rossby modes with $k = 0$, and gravity modes with all k, which include the MRG wave. The total KW energy tendency results from the interactions of these modes (see section 2.3). Kelvin waves are primarily excited by interactions of Rossby waves with the mean flow (Fig. A.7), although gravity wave-mean flow interactions also have a small contribution to the KW energy source. Wave-wave interactions of Rossby waves induce less than 1% of the KW energy growth because their velocity and depth perturbations have a smaller magnitude than those of the zonal mean flow.

Since the external forcing has a zonal wavenumber of $k = 1$, most Rossby waves in the reference simulation have this zonal wavenumber. Their interactions with the zonal mean flow influence modes with $k = 1$, which is the sum of the zonal wavenumbers of the interacting modes. In addition, wave-wave interactions of Rossby waves with $k = 1$ excite modes with $k = 2$, while modes with higher k are generated through higher-order interactions. Due to the predominance of Rossby wave-mean flow interactions, the KWs that develop in the simulation mainly have a zonal wavenumber of $k = 1$ (Fig. A.5).

The KW energy tendencies due to Rossby wave-mean flow interactions are qualitatively approximated using the interactions of the zonal mean flow with the forced part of the Rossby wave response to the external forcing (Fig. A.4a). These interactions maintain a constant phase shift relative to the growing KWs because they move eastward with the same phase velocity. As a result, the forced Rossby wave-mean flow interactions exert a steady influence on the KWs, whose energy growth can be interpreted as a resonance effect (section 3.1).

An alternative interpretation for the KW excitation is that the zonal mean flow modifies the structure of the KW in such a way that it is directly affected by the Rossby wave forcing. Such modified structures can be identified by computing eigenmodes of the shallow-water equations, linearized with respect to the zonal mean flow, as described in section A.6 following Kasahara (1980). The wave-mean flow interactions are included in these linearized equations, so that their impact is reflected in the spatial structures and eigenfrequencies of the eigenmodes (Kasahara, 1980, 1981; Mitchell, 2013). One of the eigenmodes resembles the Kelvin wave solution of the linearized equations around the state of rest, because it consists of 99% Kelvin waves (Fig. A.11). This eigenmode also contains small proportions of $n = 1$ and $n = 3$ Rossby waves, which is why it is influenced by the external forcing. The frequency ν'_K of this eigenmode is used as

the forcing frequency in the reference simulation, because it accounts for the influence of the background flow on the wave propagation. However, the eigenmodes of the linearized equations with respect to the zonal mean flow are not easily applicable for flow decomposition and energy diagnostics because they are not mutually orthogonal (section A.6). Additional complications could arise from representing the circulation in terms of time-dependent or unstable modes. In contrast, the normal mode functions of the linearized equations with respect to the state of rest are clearly defined and orthogonal, which makes them a suitable expansion basis for the atmospheric circulation.

In the reference simulation, the dynamics are characterized by stable modes, whereas, in general, the eigensolutions of the linearized equations around a background flow can be unstable. Above certain thresholds in the Rossby and Froude numbers, unstable eigenmodes occur, which couple Rossby and Kelvin modes (Wang and Mitchell, 2014). If stronger zonal velocities would be chosen instead of the background flow in Fig. A.1, similar instabilities might arise.

5.2 Reanalysis data

The KW energy tendencies due to wave-mean flow and wave-wave interactions in reanalysis data are computed using the pseudospectral method described in Appendix B. For this, the atmosphere is split into seven parts: Kelvin waves (KW), $n = 1$ Rossby waves (R1), $n > 1$ Rossby waves (R), mixed Rossby-gravity waves (MRG), inertia-gravity waves (G), the part of the zonal mean flow that is in geostrophic balance (R0), i.e. K-modes (Kasahara, 1978) and the part of the zonal mean flow that is not in geostrophic balance (G0). Note that 0 in R0 and G0 denotes $k = 0$, while 1 in R1 abbreviates $n = 1$.

The (R1, R0) interactions contribute most to the dynamical KW energy source (Fig. C.2a), while the (G, R0) interactions act as a KW energy sink with smaller magnitude. These two energy tendencies are further broken down into advection of momentum and temperature (Fig. C.5a and d). The following discussion will address the advection terms that induce the largest KW energy tendencies, with a focus on the (R1, R0) interactions. As described in section C.3.2, the underlying processes can be conceptually understood using wind and temperature fields of stationary waves.

The largest contribution to the (R1, R0) interactions is the meridional advection of zonal momentum. The balanced zonal mean zonal winds feature westerlies in the subtropics and weak easterlies around the equator (Fig. C.9a). In the upper troposphere, the time-averaged R1 winds advect zonal momentum away from the equator in the eastern hemisphere and toward the equator over the Pacific (Fig. C.8). Similar to the meridional advection by the total winds described in section 4.2, these momentum tendencies result in a KW energy source, because they enhance the KW winds both over the eastern hemisphere and over the Pacific. Conversely, meridional winds in the opposite direction would result in a KW energy sink. Therefore, a suitable phase shift between the KW and R1 is required for meridional advection of zonal momentum to function as a KW energy source. For $k = 1$, for which the KW energy tendencies due to (R1, R0) interactions are largest (Fig. C.3), the zonal winds of KW and R1 in the upper troposphere are shifted by 43°. Accordingly, equatorward R1 wind is collocated with westerly KW wind, and vice versa, so that meridional advection of R0 momentum strengthens the KW winds.

The phase shift between Rossby and Kelvin waves is also important for the KW energy source that results from zonal advection of zonal momentum. The advection of the

R1 winds by the easterly zonal mean flow at the equator results in easterly (westerly) momentum tendencies west (east) of the maximum R1 easterlies around 100° E. There, easterly (westerly) KW winds are present, and they are intensified by the momentum tendencies. Similarly, the phase shift between KW and R1 is responsible for the KW energy source arising from the zonal advection of temperature.

A further contribution to the (R1, R0) interactions is the vertical advection of temperature, which results in positive KW energy tendencies (Fig. C.5a). Similar to the total temperature perturbations relative to the reference temperature discussed in section 4.2, the temperature associated with R0 decreases with height in the tropics (Fig. C.7a). The advection of R0 temperature by the upward vertical velocity of R1 over the Pacific (Fig. C.7d) therefore strengthens the positive KW temperature (Fig. C.1b). Over the Indian Ocean, the negative KW temperature is enhanced as the R1 vertical wind advects low R0 temperature downward. In contrast, advection by upward vertical velocity of gravity waves over the Indian Ocean and Maritime Continent (Fig. C.7f) induces positive temperature tendencies. Consequently, the negative KW temperature in this region is reduced, so that the vertical advection of temperature functions as a KW energy sink in the gravity wave-mean flow interactions. This sink outweighs the KW energy source resulting from advection of R0 by the meridional velocity of gravity waves (Fig. C.5d).

Both in the shallow-water model simulations and in the atmosphere, wave-mean flow interactions are an energy source for KWs. However, in the simulations, propagating waves are resonantly excited, while the major part of the Rossby wave-mean flow interactions in the atmosphere is associated with stationary waves and seasonal variability (section C.3.1). Nevertheless, the co-spectrum of Kelvin waves and (R1, R0) interactions (Fig. C.4) indicates that these interactions also result in a small energy source for propagating waves with higher frequencies. A similar co-spectrum is presented by Cheng et al. (2022), illustrating the resonant WFD-KW generation through eddy momentum flux convergence associated with extratropical Rossby waves. However, this mechanism is not directly comparable with wave-mean flow or wave-wave interactions because Cheng et al. (2022) identify eddies as perturbations in time, and not deviations from the zonal mean, among other methodological differences. Furthermore, the contribution of waves that originate in the extratropics to the (R1, R0) interactions remains unclear. Therefore, no final conclusions are drawn in this thesis about the role of the simulated resonant KW excitation mechanism in the atmosphere.

5.3 Energy transfers

In the atmosphere, KWs gain energy due to (R1, R0) and (R1, R1) interactions; the origin of this energy is discussed in the following. The KW energy source due to (R1, R0) interactions is associated with R1 energy tendencies due to (KW, R0) interactions and R0 energy tendencies due to (KW, R1) interactions. Through these interactions, R1 receives energy, while R0 loses energy (Fig. C.2b), and the largest energy tendencies are found in the lowest zonal wavenumbers (Fig. C.3). Because the sum of the KW, R1 and R0 energy tendencies is small, which can not be a priori assumed (see section C.2.2), energy is approximately conserved in these interactions. From this, it can be concluded that R0 transfers energy to both KWs and R1. Similarly, KWs receive energy from R1 through (R1, R1) interactions, as the energy loss of R1 through (KW, R1) interactions is approximately

equal and opposite.

Before further discussing the energy transfers in the atmosphere, the shallow-water model simulations are examined to determine whether a similar energy transfer can be found there. For the reference simulation, the KW energy tendencies due to Rossby wave-mean flow interactions and the associated energy tendencies of Rossby waves and the mean flow are shown in Fig. 5.1. The energy tendency of Rossby waves due to Kelvin wave-mean flow interactions oscillates around zero, while the energy tendency of the mean flow due to Kelvin wave-Rossby wave interactions is small and positive. The sum of these three energy tendencies is positive and has a similar magnitude as the KW energy tendencies. Here, the conclusion that KWs receive energy from Rossby waves or the zonal mean flow can not be drawn, because no energy sink is found in these modes that would correspond to the KW energy source.

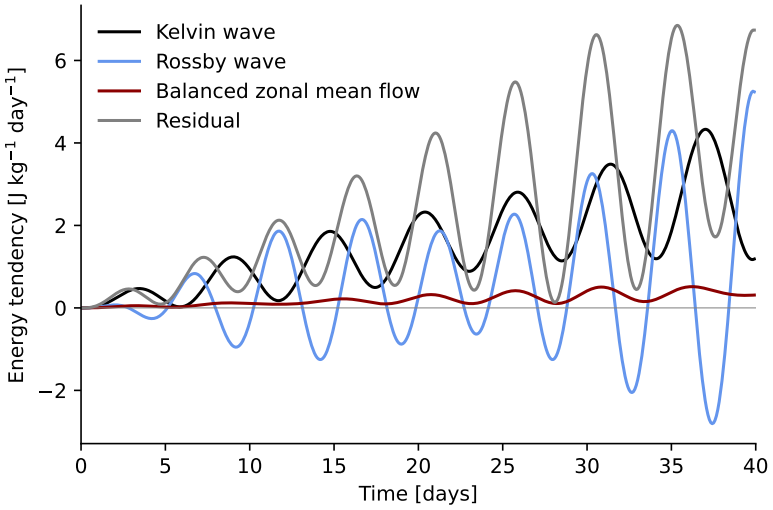

Figure 5.1: Kelvin wave energy tendencies due to Rossby wave-mean flow interactions, Rossby wave energy tendencies due to Kelvin wave-mean flow interactions, and energy tendencies of the zonal mean flow due to Rossby wave-Kelvin wave interactions in the reference simulation. The "Residual" is the sum of these three energy tendencies.

The large residual (Fig. 5.1) arises from the energy of the sum of all normal modes, I_{SW} (Eq. 2.27), not being conserved in the nonlinear shallow-water equations (Ripa, 1983b). These equations conserve the sum of kinetic and potential energy

$$E_{\mathrm{SW}} = \frac{1}{4\pi} \int_0^{2\pi} \int_{-\pi/2}^{\pi/2} \frac{1}{2} \left(h \left(u^2 + v^2 \right) + g h^2 \right) \cos\varphi \, d\varphi \, d\lambda \,, \tag{5.1}$$

(Vallis, 2017), where $h = D(\tilde{h} + 1)$ is the dimensional fluid depth. Because E_{SW} contains cubic terms and I_{SW} contains only quadratic terms, part of E_{SW} cannot be represented as the energy of normal modes. Therefore, an energy exchange can occur between $I_{\mathrm{SW}} D$ and $E_{\mathrm{SW}} - I_{\mathrm{SW}} D$, even in the absence of external sources and sinks. In the reference simulation, this energy exchange results in an increase of I_{SW}, evident as the residual in Fig. 5.1. However, such a residual does not always appear. For example, for resonant triad interactions, the energy of normal modes of the shallow-water equations on the equatorial β-plane is conserved (Ripa, 1983b). In contrast, the resonant Kelvin wave

excitation described in this thesis does not result from resonant triad interactions. Instead, the simulated KW growth is the resonant response to the interactions of the eastward-moving forced Rossby waves and the zonal mean flow.

Returning to the reanalysis data, the energy transfers between the R0, R1 and KW take place through both momentum and temperature advection (Fig. C.15), for details see section C.3.2. In particular, momentum and temperature advection result in energy sinks of R0. In a theoretical study of the primitive equations on the equatorial β-plane, Raupp et al. (2008) found that the mean flow does not gain or lose energy in resonant triad interactions. Instead, it facilitates the energy exchange between the two other modes in the resonant triad. The eigenfrequencies from linear theory of KW and R1 do not fulfill the resonance condition together with R0, which has an eigenfrequency of zero, meaning that the energy loss of R0 due to (KW, R1) interactions does not result from resonant triads. While the energy exchange in resonant triads involving KWs remains to be quantified in atmospheric data, the presented results indicate that resonant triad interactions have a minor contribution to the dynamical KW energy source.

KWs receive energy from R1 through advection of momentum and temperature by the zonal mean flow. In addition, KWs receive energy from R1 through (R1, R1) interactions, as previously mentioned. These two processes have an opposite effect to the energy transfer from KW to R1, which was determined by Raphaldini et al. (2021) and Teruya et al. (2024) with data-driven methods. While Teruya et al. (2024) argue that part of the energy transfer between KW and R1 is connected with moisture, diabatic effects are not included in the energy transfers described in this thesis, which result from dynamical processes only. The results of Raphaldini et al. (2021) and Teruya et al. (2024) might contain biases because they were obtained from the time series of R1 and KW energy or amplitudes, which do not contain information about the wave phases.

6 CONCLUSIONS AND OUTLOOK

This thesis explains how dynamical processes, consisting of momentum and temperature advection, influence equatorial KWs. For comparison, diabatic processes are also considered. The dynamical mechanisms are studied in shallow-water model simulations and reanalysis data using the same method based on normal-mode decomposition. This allows for a consistent analysis of the idealized simulations and atmospheric data. A novel numerical framework was developed for the pseudo-spectral computation of the 3D dynamical momentum and temperature tendencies using the normal-mode expansion coefficients. This allows to decompose the tendencies into wave-mean flow and wave-wave interactions. The influence of diabatic processes on KWs is determined using the tendencies due to parametrizations in ERA5 data, which is a novel aspect compared to previous studies, in which these processes were evaluated as a residual (e.g. Marques et al., 2020).

In contrast to previous studies comparing the influences of dynamical and diabatic processes on WFD-KWs, which, by definition, propagate eastward (Tulich and Kiladis, 2021; Chien et al., 2025), a substantial part of the KWs discussed in this thesis is stationary. These stationary KWs are primarily the response to non-radiative diabatic heating and advection of warm air in the upper troposphere, while momentum advection has a secondary contribution.

The energy tendencies of the stationary KWs are determined from the time-averaged momentum and temperature tendencies, relative to which the stationary wave response is phase-shifted. However, KW energy sources result from the part of the tendencies that is in phase with the KWs. Non-radiative diabatic heating and temperature advection induce KW energy sinks in the time average, because the temperature tendencies are partly collocated with KW temperatures of opposite sign. The vertical advection of temperature contributes most to the KW energy sink, while horizontal advection of temperature results in a small KW energy source. Non-radiative diabatic heating governs the temporal variability of the KW energy tendencies. The largest KW energy source results from advection of zonal momentum. Especially the meridional advection of zonal momentum in the winter hemisphere induces a KW energy source by strengthening the KW easterlies in the upper troposphere over the Indian Ocean. This KW energy source is stronger than the KW energy sink due to temperature advection, so that, in total, dynamical processes result in a KW energy source.

A novel aspect of this thesis is the decomposition of the dynamical KW energy source into wave-mean flow and wave-wave interactions. Wave-mean flow interactions have a stronger effect; especially the interactions of $n = 1$ Rossby waves with the balanced zonal mean flow are a major contributor to the KW energy source. These interactions do not contain resonant triads.

Through interactions of $n = 1$ Rossby waves with the mean flow, Kelvin waves gain energy from both of the interacting modes. The wave-wave interactions of $n = 1$ Rossby waves also transfer energy from $n = 1$ Rossby waves to Kelvin waves. These energy transfers are the result of dynamical processes only. In contrast, previous studies

identified an energy transfer from Kelvin to $n = 1$ Rossby waves using data-driven methods, which involve diabatic effects (Raphaldini et al., 2021; Teruya et al., 2024).

To identify a specific dynamical KW excitation mechanism, shallow-water model simulations were conducted, which demonstrate how Rossby wave-mean flow interactions can increase the KW energy. In these simulations, KWs are excited in connection with eastward-moving Rossby waves in the subtropics as a resonance effect. The growth of the KWs, which propagate eastward in the simulations, thus depends on the frequency of the subtropical Rossby waves. The KW energy source in the simulations partly results from the advection of zonal momentum. Zonal and meridional advection of zonal momentum have different contributions depending on the latitudinal configuration of the Rossby waves and the sheared background flow.

While the major part of the KW energy source due to interactions of $n = 1$ Rossby waves with the mean flow is associated with stationary waves, the idealized simulations contain propagating waves. An indication for the occurrence of the simulated mechanism in atmospheric data is thus provided in a co-spectral analysis, which shows that $n = 1$ Rossby wave-mean flow interactions act as an energy source for propagating Kelvin waves. However, the connection of this KW energy source with subtropical Rossby waves is not known, so that the occurrence of the simulated mechanism in the atmosphere remains to be investigated.

The described results highlight the importance of the mean flow for the energy tendencies of equatorial waves. The zonal mean flow is neglected in the derivation of the normal modes, but its influence is taken into account via the wave-mean flow interactions. The resulting energy tendencies suggest that errors in the background flow could impact numerical simulations of equatorial waves. In addition, the inaccurate representation of latent heat release on large scales, e.g., errors in the variability of the ITCZ, would considerably affect stationary KWs and the KW variability in weather and climate models.

Momentum dissipation, which is known to be too strong, leads to errors in numerical simulations of Kelvin waves (Žagar et al., 2025). This thesis complements previous studies by identifying dissipative processes as a large KW energy sink. Evaluating model errors from the energetics perspective could extend previous studies that diagnosed model errors using normal-mode decomposition (e.g. Žagar et al., 2005, 2020).

The result that the normal-mode energy budget is approximately closed for the KW, calls for applying this method to other modes, for example MRG waves or $n = 1$ Rossby waves. Tropical convection varies on various time scales (e.g. Kiladis et al., 2009), on which the coupling of convection and equatorial waves could differ. Investigating the connection between diabatic processes and equatorial waves and the associated energy tendencies may improve the understanding of tropical circulation variability, for example the onset and dynamics of the MJO. Another phenomenon for which the energy budget could be investigated is the 33-hour Kelvin wave, whose excitation is not conclusively clarified (e.g. Sakazaki and Hamilton, 2020).

This thesis considered Kelvin waves with zonal wavenumbers $k \geq 1$, which by definition contain both easterly and westerly winds. In contrast, the Kelvin waves in the well-known circulation response to tropical heating discussed by Gill (1980) have only one wind direction, but it should be noted that the circulation pattern derived by Gill (1980) on the infinite plane is not directly comparable to the spherical Earth. The requirement that KW easterlies and westerlies balance out in the zonal average disappears when the

set of Kelvin waves is complemented by one of the modes derived by Shigehisa (1983) for the zonal mean flow in geostrophic balance (S-modes). The influences of dynamical and diabatic processes on the S-mode whose meridional structure resembles the Kelvin wave are subject of future studies. In this thesis, the part of the atmospheric circulation associated with this S-mode is included as a combination of the geostrophically balanced modes with $k = 0$, which were derived by Kasahara (1978).

While the WFD-KW energy source due to eddy momentum flux convergence discussed in previous studies is associated with breaking equatorward-propagating Rossby waves (Tulich and Kiladis, 2021; Cheng et al., 2022), this thesis does not separate the KW energy sources into tropical and extratropical effects. This distinction should be investigated in follow-on work, because dynamical mechanisms could facilitate tropical-extratropical interactions.

The energy transfer from the zonal mean flow and the $n = 1$ Rossby waves to Kelvin waves relies on the phase shift between the two wave modes, while the reasons for this shift in the atmosphere remain to be investigated. Similar to the stationary KWs, the location of the stationary $n = 1$ Rossby waves might be determined by the non-radiative diabatic heating and advection of temperature. The zonal mean flow could also influence the shift between a stationary heating and its Rossby wave response, as simulated by Monteiro et al. (2014) in the shallow-water framework. However, the background flow in their simulations involves a strong orographic forcing. Further investigations could be conducted with the TIGAR model to understand the configuration of stationary KWs and $n = 1$ Rossby waves in the normal-mode framework. Limitations of the shallow-water model, such as the absence of vertical advection, might be overcome with 3D primitive-equation model simulations.

Energy transfers between modes with different wavenumbers can determine the slope of the energy spectrum (Augier and Lindborg, 2013, and references therein). Evaluating such scale interactions can shed light on the influence of parametrizations on energy transfers in models of different complexity (Malardel and Wedi, 2016). The mentioned studies rely on spherical harmonics, and this approach has been extended by separating rotational and divergent components using Helmholtz decomposition (Li et al., 2023). The normal-mode decomposition can lead to further insights because it involves the multivariate spatial structures of different wave types. Interactions of balanced and IG waves and the resulting tendencies of kinetic and available potential energy can be quantified with the method used in this thesis. Such an investigation would complement the works of Kitamura and Matsuda (2010), who analyzed interactions of geostrophic and IG modes in regional simulations of stratified turbulence, and of Morfa and Stephan (2025), who focused on transfers of kinetic energy by interactions of balanced or IG modes in a global high-resolution model.

The Kelvin wave excitation in the shallow-water model simulations described in this thesis can be interpreted as the growth of an eigenmode of the shallow-water equations, linearized around the zonal mean flow. This mode is directly influenced by the external Rossby wave forcing. The importance of the wave-mean flow interactions motivates an analysis of eigenmodes of the primitive equations, linearized around a background flow, which can be computed using Hough harmonics as described by Tanaka and Kung (1989). The role of these eigenmodes, which might be unstable, for the tropical circulation remains to be clarified. In addition, the primitive equations, linearized with respect to the background flow, can be used to further investigate the stationary tropical circulation.

One possible approach is to determine the circulation response to diabatic heating as well as other forcings, similar to the work of Valdes and Hoskins (1989), who focused on the mid-latitude response. Applying the normal-mode decomposition on this stationary circulation allows to compare its Rossby and IG wave components with observations.

The weak temperature gradient (WTG) approximation is widely used for the tropical dynamics (e.g. Majda and Klein, 2003). However, in the upper troposphere, longitudinal temperature variations of several Kelvin are found (Fig. C.1a), which are strongest in boreal winter (Bao et al., 2022). Together with the $n = 1$ Rossby wave, the Kelvin wave temperature contributes to these temperature variations (Fig. C.7e). Bao et al. (2022) argued that the pressure gradients associated with these temperature gradients are balanced out by the advection of zonal momentum. Decomposing the associated tendencies into mode interactions in follow-on studies might reveal a contribution of dynamical processes involving Kelvin waves to the maintenance of the tropical background circulation.

Part II

APPENDIX

A

RESONANT EXCITATION OF KELVIN WAVES BY INTERACTIONS OF SUBTROPICAL ROSSBY WAVES AND THE ZONAL MEAN FLOW

The work in this appendix is a research paper which has been published in the *Journal of the Atmospheric Sciences* as:

Holube, K. M., Lunkeit, F., Vasylkevych, S., and Žagar, N. (2024). Resonant Excitation of Kelvin Waves by Interactions of Subtropical Rossby Waves and the Zonal Mean Flow. *Journal of the Atmospheric Sciences* 81.11, 1833-1848. https://doi.org/10.1175/JAS-D-24-0033.1

Authors' Contributions[1]

- Holube, K. M.: Conceptualization, Formal analysis, Investigation, Methodology, Software, Visualization, Writing - Original Draft, Writing - Review and Editing.
- Lunkeit, F.: Conceptualization, Investigation, Supervision, Writing - Review and Editing.
- Vasylkevych, S.: Conceptualization, Formal analysis, Investigation, Methodology, Software, Writing - Review and Editing.
- Žagar, N.: Conceptualization, Funding Acquisition, Project administration, Supervision, Writing - Review and Editing.

Simulations in which Kelvin waves were excited by Rossby wave-mean flow interactions are the subject of K. M. Holube's Master's thesis, supervised by FL and NŽ. The published paper contains a more in-depth analysis with a modified simulation setup. Section A.4.4 is not included in the Master's thesis. Section A.6 is mainly the work of SV. Section A.7 applies the method described in Section A.6, and is also not included in the Master's thesis.

1 using the Contributor Role Taxonomy (CRediT) https://credit.niso.org/

Resonant Excitation of Kelvin Waves by Interactions of Subtropical Rossby Waves and the Zonal Mean Flow

Katharina M. Holube,[1] Frank Lunkeit,[1] Sergiy Vasylkevych,[1] and Nedjeljka Žagar[1]

[1] Meteorological Institute, Center for Earth System Research and Sustainability, Universität Hamburg, Hamburg, Germany

Abstract

Equatorial Kelvin waves can be affected by subtropical Rossby wave dynamics. Previous research has demonstrated the Kelvin wave growth in response to subtropical forcing and the resonant growth due to eddy momentum flux convergence. However, the relative importance of the wave-mean flow and wave-wave interactions for the Kelvin wave growth compared to the direct wave excitation by the external forcing has not been made clear. This study demonstrates the resonant Kelvin wave excitation by interactions of subtropical Rossby waves and the mean flow using a spherical shallow-water model. The use of Hough harmonics as basis functions makes Rossby and Kelvin waves prognostic variables of the model and allows the quantification of terms contributing to their tendencies in physical and wave space. The simulations show that Kelvin waves are resonantly excited by interactions of Rossby waves and the balanced zonal mean flow in the subtropics, provided the Rossby and Kelvin wave frequencies, which are modified by the mean flow, match. The resonance mechanism is substantiated by analytical expressions. The Kelvin wave tendencies are caused by velocity and depth tendencies: The velocity tendencies due to the meridional advection of zonal mean velocity can be outweighed by the zonal advection of Rossby wave velocity or by the depth tendencies due to Rossby wave divergence. Identifying the resonant excitation mechanism in data should contribute to the quantification of Kelvin wave variability originating in the subtropics.

Significance Statement

This study seeks to understand how Kelvin waves, which are eastward-propagating disturbances in the tropical atmosphere, are connected to Rossby wave dynamics in the subtropics. Using idealized simulations, the Kelvin wave excitation is explained as a resonance effect due to interactions of Rossby waves and the zonal mean flow. The mechanism contributes to the understanding of atmospheric wave interactions and extratropical effects on the tropics. Further work searching for evidence of the new mechanism in atmospheric data may shed a new light on subseasonal variability in the tropics, such as the Madden-Julian Oscillation.

A.1 Introduction

Many aspects of the large-scale atmospheric circulation are explained by reduced models which target particular regimes and scales of interest. These reduced models are usually derived separately for the extratropics, i.e. the quasi-geostrophic regime (e.g. Dolaptchiev and Klein, 2013), and the tropics (e.g. Majda and Klein, 2003). A reduced model suitable

for studying subtropical processes, which involve both Rossby waves and equatorial waves, is a model based on the nonlinear shallow-water equations on the sphere (e.g. Cho and Polvani, 1996; Kitamura and Ishioka, 2007; Kraucunas and Hartmann, 2007; Barpanda et al., 2023). Such a model offers insights into wave-wave and wave-mean flow interactions that are more challenging to obtain from tropical or mid-latitude β-plane models. In the present study, a spherical shallow-water model is used to investigate the excitation of the equatorial Kelvin wave (KW) by subtropical Rossby wave dynamics.

The extratropical influence on tropical processes has been addressed in a number of studies since Webster and Holton (1982) established that the influence can take place through equatorward-propagating Rossby waves in the region of westerlies at the equator (i.e. the westerly duct). Early studies found that the amplitude and structure of laterally forced equatorial waves strongly depend upon the tropical mean zonal wind (Zhang and Webster, 1992; Zhang, 1993). In the studies by Zhang and Webster (1992) and Zhang (1993), KWs could have been be excited by wave-mean flow interactions as well as by direct forcing because the truncated version of their linearized shallow-water model did not permit meridional geopotential advection and wave-wave interactions. They also found that the extratropical influence on the KWs was stronger in equatorial easterlies than in westerlies. Barpanda et al. (2023) employed a spherical shallow-water model with topography along the equator to study the influence of the subtropical jet on the coupling between KWs and subtropical Rossby waves. By diagnosing terms of the linearized vorticity equation in the steady state, these authors showed that KWs are affected by the advection of background absolute vorticity by the Rossby wave meridional velocity. In primitive-equation model simulations conducted by Hoskins and Yang (2000), KWs were excited by eastward-propagating subtropical heating or vorticity forcing. The Kelvin wave response was strongest when the forcing frequency was close to the frequency of the KWs, i.e. when the KW was nearly in resonance with the forcing. However, the wave could have been excited by wave-mean flow interactions, by wave-wave interactions, and directly by the external forcing.

The present study elucidates the role of subtropical wave-mean flow and wave-wave interactions on the KW excitation by idealized numerical simulations without direct effects of the external forcing on the Kelvin wave. We show that the Kelvin wave is excited by interactions of Rossby waves and the zonal mean flow in the subtropics when the phase speed of the eastward-shifted Rossby waves matches the KW phase speed.

Our analysis of the KW growth due to resonance is facilitated by a novel numerical model that solves the spherical shallow-water equations using the Hough harmonics as basis functions (Vasylkevych and Žagar, 2021). The Hough harmonics are eigensolutions of the spherical shallow-water equations linearized around the state of rest. In this formulation, the KW is defined as the part of the simulated circulation that projects on the slowest eastward-propagating component of the basis function set. For small mean fluid depths, the spherical eigensolution for the KW is almost identical to the Kelvin wave solution on the equatorial β plane, i.e. Matsuno (1966)'s Kelvin wave (e.g. Boyd, 2018; Žagar et al., 2022). On the sphere, KWs have a small meridional velocity component, are weakly dispersive and their trapping is defined by both the mean (or equivalent) depth and the zonal wavenumber (Boyd and Zhou, 2008a).

The nearly nondispersive nature of the large-scale Kelvin waves facilitates their identification in observations and weather and climate models, especially in relation to deep tropical convection (e.g. Kiladis et al., 2009; Knippertz et al., 2022). Filtering Kelvin waves

associated with subtropical processes is more complex in part because the amplitude of quasi-geostrophic wave dynamics well exceeds that of equatorial wave perturbations. Nevertheless, a significant enhancement of KW activity in parts of the tropics was found to be coupled with stronger eastward-propagating Rossby wave activity in the subtropics (Straub and Kiladis, 2003; Tulich and Kiladis, 2021; Cheng et al., 2022). When subtropical Rossby waves break at their critical line, they can affect KWs through the convergence of eddy momentum fluxes (Tulich and Kiladis, 2021). The subtropical jet advects the Rossby waves eastward, aligning their phase speed with that of the KWs. The phase of the eddy momentum flux convergence thus varies little relative to the propagating KWs, so that they grow through a resonance effect (Cheng et al., 2022). During austral winter, the extratropical effects can exceed the influence of local moist thermodynamics on KWs over the tropical Pacific (Straub and Kiladis, 2003).

The eddy momentum flux analyzed in reanalysis data in the above mentioned studies belongs to the wave-wave interaction process. As a first step towards quantifying the role of this process compared to wave-mean flow interactions and direct forcing on the KW variability, we perform idealized experiments which do not contain KWs in the initial state and which allow the quantification of terms contributing to the KW growth. In what follows, we first present the Transient Inertia-Gravity And Rossby wave model (TIGAR; Vasylkevych and Žagar, 2021) and the simulation setup (section A.2). The linear Rossby wave response to the forcing is described in section A.3. The excitation of KWs as a resonance effect is explained in section A.4. The conclusions and outlook are given in section A.5.

A.2 Modeling setup

In the following, the key features of TIGAR and the analysis method of the wave-wave and wave-mean flow interactions are outlined. Subsequently, the zonal mean flow, the external forcing and the parameters of our simulation setup are described.

A.2.1 Model formulation and energy equation

TIGAR solves the rotating shallow-water (RSW) equations in spherical coordinates $(\lambda, \varphi) \in [0, 2\pi) \times (-\pi/2, \pi/2)$, which in nondimensional form read as

$$\frac{\partial u}{\partial t} + \gamma \mathbf{V} \cdot \nabla u - \gamma u v \tan\varphi - v \sin\varphi + \frac{\gamma}{\cos\varphi} \frac{\partial h}{\partial \lambda} = F_u + Q_u \,, \tag{A.1a}$$

$$\frac{\partial v}{\partial t} + \gamma \mathbf{V} \cdot \nabla v + \gamma u^2 \tan\varphi + u \sin\varphi + \gamma \frac{\partial h}{\partial \varphi} = F_v + Q_v \,, \tag{A.1b}$$

$$\frac{\partial h}{\partial t} + \gamma \mathbf{V} \cdot \nabla h + \gamma (h+1) \nabla \cdot \mathbf{V} = F_h + Q_h \,. \tag{A.1c}$$

The horizontal velocity components $\mathbf{V} = (u, v)^T$ and the fluid depth h can be expressed as the state vector $\mathbf{X} = (u, v, h)^T$. The nondimensional variables are obtained as in Vasylkevych and Žagar (2021) by normalizing the depth deviation from the mean depth D with D, whereas the velocities are normalized with $\sqrt{gD}$. The parameter $\gamma = \sqrt{gD}/(2a\Omega)$ contains the free parameters of the system: the Earth's radius a, gravity g and rotation rate Ω, and D, representing the equivalent depth of one vertical mode in the troposphere and stratosphere. The spectral viscosity $\mathbf{F} = (F_u, F_v, F_h)^T$ damps the

smallest resolved scales for all three variables, and it is defined following Gelb and Gleeson (2001). The external forcing is denoted $\mathbf{Q} = (Q_u, Q_v, Q_h)^T$.

TIGAR is a pseudospectral model that uses the Hough harmonics $\mathbf{H}^k_{n,l}(\lambda, \varphi)$ as basis functions, which are eigensolutions of Eq. (A.1), linearized around a state of rest with depth D (Longuet-Higgins, 1968). This linearization reduces Eq. (A.1) to

$$\frac{\partial}{\partial t}\mathbf{X} + \mathbf{L}\mathbf{X} = 0, \tag{A.2}$$

with

$$\mathbf{L} = \begin{pmatrix} 0 & -\sin\varphi & \frac{\gamma}{\cos\varphi}\frac{\partial}{\partial\lambda} \\ \sin\varphi & 0 & \gamma\frac{\partial}{\partial\varphi} \\ \frac{\gamma}{\cos\varphi}\frac{\partial}{\partial\lambda} & \frac{\gamma}{\cos\varphi}\frac{\partial}{\partial\varphi}(\cos\varphi(\cdot)) & 0 \end{pmatrix}. \tag{A.3}$$

The Hough harmonics fulfill $\mathbf{L}\mathbf{H}^k_{n,l} = i\nu^k_{n,l}\mathbf{H}^k_{n,l}$ with eigenfrequency $\nu^k_{n,l}$. For each zonal wavenumber k, there is a range of meridional modes n for three types of wave solutions: the eastward-propagating inertia-gravity (IG) modes ($l = 1$), westward-propagating IG modes ($l = 2$) and Rossby modes ($l = 3$). The meridional structure of $\mathbf{H}^k_{n,l}(\lambda, \varphi) = \mathbf{\Theta}^k_{n,l}(\varphi)e^{ik\lambda}$ is defined by the Hough functions $\mathbf{\Theta}^k_{n,l}(\varphi) = \left(U^k_{n,l}(\varphi), iV^k_{n,l}(\varphi), Z^k_{n,l}(\varphi)\right)^T$. The Kelvin mode $\mathbf{H}^k_{0,1}$ is the lowest meridional mode ($n = 0$) of the eastward-propagating inertia-gravity modes. See Swarztrauber and Kasahara (1985) and Kasahara (2020) for details.

Expressing Eq. (A.1) in vector notation yields

$$\frac{\partial}{\partial t}\mathbf{X} + \mathbf{L}\mathbf{X} = \mathbf{N} + \mathbf{Q} + \mathbf{F}. \tag{A.4}$$

The term $\mathbf{N} = (N_u, N_v, N_h)^T$ contains the interactions of different modes, as discussed in section A.2.2.

The expansion of Eq. (A.4) in the basis of Hough harmonics yields prognostic equations for the complex Hough coefficients $\chi^k_{n,l}(t)$, which describe the evolution of amplitude and phase of each mode as

$$\frac{d\chi^k_{n,l}(t)}{dt} + \left(i\nu^k_{n,l} + d^k_{n,l}\right)\chi^k_{n,l}(t) = f^k_{n,l}(t) + q^k_{n,l}(t). \tag{A.5}$$

Linear tendencies of $\chi^k_{n,l}$ are caused by the linear propagation, which depends on the eigenfrequency $\nu^k_{n,l}$ of the mode and the scale-selective viscosity $d^k_{n,l}$, which damps modes with large k and n. The right-hand side of Eq. (A.5) contains the Hough transform of the interaction terms $\mathbf{N}(\lambda, \varphi, t)$, which is

$$f^k_{n,l}(t) = \frac{1}{2\pi}\int_0^{2\pi}\int_{-\pi/2}^{\pi/2}\mathbf{N}(\lambda, \varphi, t)\cdot\left(\mathbf{H}^k_{n,l}(\lambda, \varphi)\right)^*\cos\varphi\, d\varphi\, d\lambda, \tag{A.6}$$

where the complex conjugate is denoted *. Similarly, $q^k_{n,l}$ is the forcing in spectral space. Further details on the model numerics and time stepping are described in Vasylkevych and Žagar (2021).

The nondimensional energy of each mode is

$$I^k_{n,l} = \frac{1}{2}(2 - \delta_{0k})\left|\chi^k_{n,l}\right|^2, \tag{A.7}$$

where δ is the Kronecker delta. The energy of all modes $I = \sum_{n,l,k} I^k_{n,l}$ is conserved in the linearized system without sources and sinks. The dimensional energy is obtained by multiplying I with gD, and it is equal to the sum in the domain of the kinetic energy and available potential energy of dimensional variables in physical space (Kasahara and Puri, 1981).

The prognostic energy equation reads

$$\frac{dI^k_{n,l}}{dt} = -2d^k_{n,l} I^k_{n,l} + (2 - \delta_{0k}) \operatorname{Re}\left[f^k_{n,l} \left(\chi^k_{n,l}\right)^* + q^k_{n,l} \left(\chi^k_{n,l}\right)^* \right], \tag{A.8}$$

and it follows by differentiating Eq. (A.7) in time and using Eq. (A.5). The first term on the right-hand side of Eq. (A.8) is the energy sink due to spectral viscosity. The other terms describe energy fluxes in modal space and due to the forcing as in Mahó et al. (2024a).

A.2.2 Wave-mean flow and wave-wave interactions

In TIGAR, the backward transform of $\chi^k_{n,l}$ allows mode-selective filtering of the velocity components and depths associated with the modes and scales of interest. For filtering and diagnostics of our simulations, we split the modes into the following four groups: Rossby waves (denoted by R), inertia-gravity waves and mixed Rossby-gravity waves, denoted by G, Kelvin waves denoted by K and the zonal mean flow, which is denoted by 0. Note that our combination of IG and MRG waves into a single group (G) reflects their role in the present study, not their properties. The state vector thus consists of four parts, $\mathbf{X} = \sum \mathbf{X}_i$ for $i \in \{R, K, G, 0\}$.

The interaction terms $\mathbf{N}$ consist of the quadratic terms in Eq. (A.1), which are advection, the metric terms, and the part of the divergence term which is not included in $\mathbf{L}$, as it contains fluid depth deviations from D. The total interactions are split into the interactions of different modes according to $\mathbf{N} = \sum \mathbf{N}_{i,j}$ for $(i, j) \in \{R, K, G, 0\} \times \{R, K, G, 0\}$, where

$$\mathbf{N}_{i,j} = \frac{-\gamma}{\cos\varphi} \begin{pmatrix} u_i \frac{\partial u_j}{\partial \lambda} + v_i \frac{\partial (u_j \cos\varphi)}{\partial \varphi} \\ u_i \frac{\partial v_j}{\partial \lambda} + v_i \frac{\partial (v_j \cos\varphi)}{\partial \varphi} + (u_i u_j + v_i v_j) \sin\varphi \\ u_i \frac{\partial h_j}{\partial \lambda} + v_i \cos\varphi \frac{\partial h_j}{\partial \varphi} + h_i \left(\frac{\partial u_j}{\partial \lambda} + \frac{\partial (v_j \cos\varphi)}{\partial \varphi} \right) \end{pmatrix}. \tag{A.9}$$

The interactions of i and j with $i \neq j$ are $\mathbf{N}(i \leftrightarrow j) = \mathbf{N}_{i,j} + \mathbf{N}_{j,i}$. The self-interactions of i are $\mathbf{N}(i \leftrightarrow i) = \mathbf{N}_{i,i}$. Consequently, the terms involving waves and the mean flow are referred to as wave-mean flow interactions, and the products of wave terms are denoted wave-wave interactions. The energy flux due to the interactions is obtained using $f^k_{n,l}(i \leftrightarrow j)$ in Eq. (A.8). As triad interactions require that the sum of the zonal wavenumbers of the two interacting waves and the influenced mode must be zero (e.g. Ripa, 1982), the interactions of waves ($k > 0$) with the mean flow ($k = 0$) do not affect the mean flow.

A.2.3 Formulation of the background zonal mean state

There are a few ways to configure a steady-state zonal mean flow in a barotropic fluid. Kraucunas and Hartmann (2007) introduced a gradually-raising zonally symmetric

topography centered at the equator, which leads to the development of symmetric zonal jets in the extratropics. A side product of the so produced steady state is the presence of meridional velocities (Barpanda et al., 2023). An alternative approach applied here and by Mahó et al. (2024a) is based on taking the steady state of the equation set Eq. (A.1) with $v_0 = 0$. In this case the meridional momentum equation becomes

$$u_0 + \frac{\gamma u_0^2}{\cos\varphi} + \frac{\gamma}{\sin\varphi}\frac{\partial h_0}{\partial \varphi} = 0\,. \tag{A.10}$$

Equation (A.10) defines the nonlinear balance, whereas the removal of the second term leaves the equation of the zonal geostrophic flow on the sphere (linear balance). The Rossby modes with $k = 0$ (Kasahara, 1978) fulfill the linear balance and are a part of the Hough harmonic computation in TIGAR. These modes have zero frequency and are used to compute a geostrophic zonal flow from a specified velocity profile $u_0(\varphi)$: The projection of $u_0 + \gamma u_0^2/\cos\varphi$ on the zonal velocity components of Rossby modes with $k = 0$ gives a set of coefficients. The linear combination of modes with these coefficients yields the non-linearly balanced depth field $h_0(\varphi)$.

Our balanced background state is shown in Fig. A.1. The fluid has a mean depth of $D = 400$ m, which corresponds to a vertical mode with baroclinic structure in the troposphere (a single zero crossing below the tropopause) and with the largest KW variance in the troposphere-stratosphere KW climatology in the ERA5 reanalysis (Žagar et al., 2022). The imposed zonal velocity profile resembles the upper-tropospheric climatology (e.g. Simmons, 2022), albeit with smaller amplitudes, which are a compromise between high velocities and moderate deviations from the mean depth. The profile is a symmetrical tenth degree polynomial, which is fitted to weak easterlies in the equatorial region and westerlies which assume their maximum at 30° off the equator. The zonal velocity profile is continuously differentiable and the velocity is zero poleward of 60°. If the jet were narrower, as in Mahó et al. (2024a), or closer to the equator, the balanced flow would have greater velocities for similar depth perturbations. However, the sensitivity to variations of the idealized background flow is beyond the scope of our study.

According to the stability criterion based on the potential vorticity (Ripa, 1983a), the zonal flow in Fig. A.1 is stable since

$$\frac{\partial PV}{\partial \varphi} \geq 0 \quad \text{for all} \quad \varphi \quad \text{and} \quad \max\left(\frac{u_0}{\cos\varphi}\right) \leq \min\left(\frac{u_0 + \sqrt{h_0}}{\cos\varphi}\right)\,, \tag{A.11}$$

where the potential vorticity of the mean flow is $\mathrm{PV} = \frac{1}{h_0}\left(\sin\varphi - \frac{\gamma}{\cos\varphi}\frac{\partial(u_0\cos\varphi)}{\partial\varphi}\right)$.

The eigensolutions of Eq. (A.1), linearized around a non-resting balanced background state, have different eigenfrequencies and horizontal structures compared to the Hough harmonics, and we expect these differences to increase for stronger background flows. The numerical computation of these modified eigenmodes and their frequencies ${\nu'}^k_{n,l}$ is described in section A.6. For the background flow in Fig. A.1, the modified Rossby and Kelvin modes with $k = 1$ are discussed in section A.7. The modified Kelvin mode and the modified Rossby modes with low n are similar to the eigenmodes for the state of rest, in agreement with previous studies (Boyd, 1978; Kasahara, 1981; Zhang and Webster, 1989; Wang and Xie, 1996; Mitchell, 2013). This supports our definition of the Rossby and Kelvin waves as the part of the circulation projecting on the Hough harmonics. The modified eigenmodes are not suitable to be used as basis functions of a model, as they are

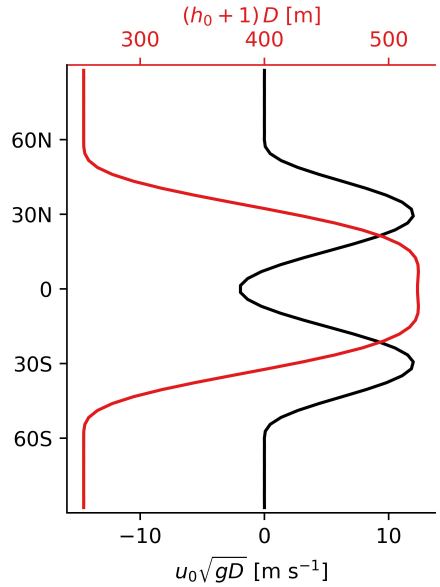

Figure A.1: Zonal mean flow u_0 and fluid depth perturbation h_0 of the background zonal mean state.

not an orthogonal basis (section A.6) and they vary in time for a changing background flow.

The modified frequencies include the Doppler shift by u_0, as well as effects of h_0. The comparison of the Kelvin and Rossby wave frequencies for the state of rest and the chosen background is presented in Fig. A.2. The weak equatorial easterlies decrease the KW frequency. However, the effect of the increased h_0 at the equator acts in the opposite sense so that the total effect is a somewhat greater KW frequency at each k. For example, the modified frequency of the KW with $k = 1$ is $\nu'^1_K = 1.01$ day$^{-1}(2\Omega)^{-1}$, which is higher than the unmodified frequency $\nu^1_K = 0.86$ day$^{-1}(2\Omega)^{-1}$. The Rossby wave frequencies for small k change relatively little.

The modified frequencies $\nu'^k_{n,l}$ are used to approximate the wave propagation in the presence of the background flow with analytical expressions. In the following, $\nu'^k_{n,l}$ denotes the modified frequencies if $n \leq 10$, and the frequencies of the Hough harmonics for $n > 10$. This choice has no qualitative effect on the results because the modes with $n > 10$ have small amplitudes in our simulations. In contrast, the frequencies of the Hough harmonics are used in numerical simulations solving Eq. (A.5), where the effects of the background flow are included in the interaction terms.

A.2.4 Subtropical Rossby wave forcing

We formulate a forcing that mimics Rossby waves advected by the subtropical jet in the upper troposphere. The speed of the westerly jet tends to be higher than the intrinsic westward Rossby wave phase speed, so that the Rossby waves are advected eastward (Tulich and Kiladis, 2021, and references therein). To simulate eastward-moving waves, the phase speed of the eastward-propagating forcing applied here is higher than u_0 of the relatively weak background flow in Fig. A.1. The eastward advection of Rossby waves is thus conceptually represented by the external forcing.

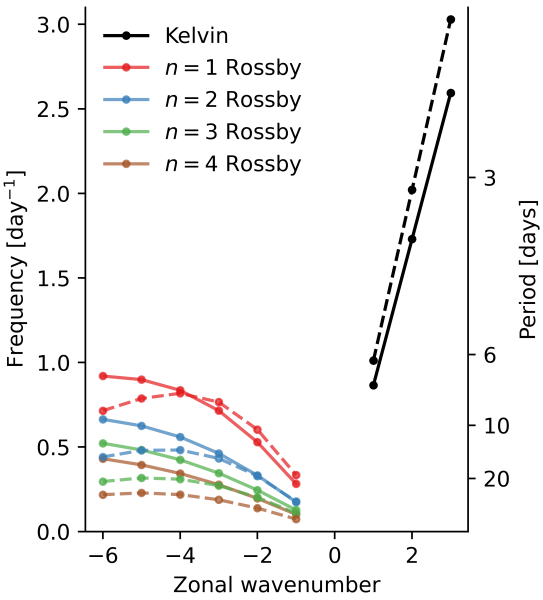

Figure A.2: Dimensional frequencies of the Kelvin and Rossby waves on the sphere as a function of the zonal wavenumber. Solid lines: frequencies for the state of rest. Dashed lines: modified frequencies for the balanced background state shown in Fig. A.1. The Rossby wave frequencies, which are negative, are shown as absolute values for negative k. The Rossby modes with $k = 0$ have zero frequencies and there is no Kelvin $k = 0$ mode.

While the eastward-propagating forcings employed by Zhang (1993) and Hoskins and Yang (2000) act on all modes of the system, the forcing in this study only affects Rossby waves. Such a forcing has a direct effect on the spectrum of the modified eigenmodes due to the non-resting background flow, including the modified Kelvin mode. However, the forcing only projects on the part of this modified mode that differs from the Kelvin wave. This difference accounts for the wave-mean flow interactions, which are included in the structure of the modified mode, because it is an eigensolution of the linearized equation (Eq. A.32) containing these interactions. As the Rossby wave forcing does not affect the KW, Kelvin waves can only be excited by wave-mean flow and wave-wave interactions in our simulations.

The forcing is restricted to $k = 1$ and is defined as

$$\mathbf{Q} = \sum_n \alpha_n \mathbf{\Theta}^1_{n,R} e^{i(\lambda - \omega_0 t)} \,. \tag{A.12}$$

It propagates eastward if the forcing frequency ω_0 is positive. The depth and velocity tendencies are located at the latitudes of subtropical westerlies (Fig. A.3). The idealized meridional structure of the forcing is chosen to simulate eastward-moving Rossby waves as a general proof of concept.

In the following, we describe how the coefficients α_n are determined, so that the linear combination of global Rossby modes becomes a localized structure: an idealized depth perturbation profile

$$h(\varphi) = \cos^2(6(\varphi - \varphi_0)) \quad \text{for} \quad \varphi \in (\varphi_0 - 15^\circ, \varphi_0 + 15^\circ) \tag{A.13}$$

is expressed as a linear combination of Rossby wave depth perturbations: $h(\varphi) = 2\sum_n \alpha'_n Z^1_{n,R}(\varphi)$ using a least squares fit. From the coefficients α'_n, the zonal Rossby wave

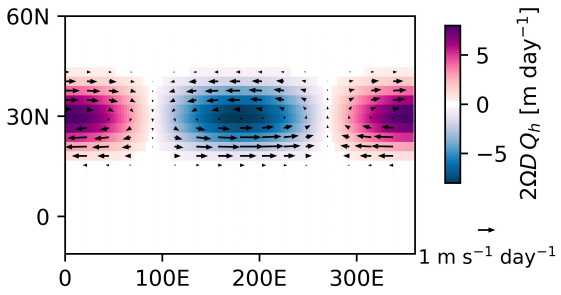

Figure A.3: Horizontal structure of the Rossby wave forcing for $\varphi_0 = 30°$ at the initial time. Shading denotes the forcing rate of the depth ($2\Omega D\,Q_h$); arrows stand for the momentum forcing rates ($2\Omega\sqrt{gD}\,(Q_u, Q_v)^T$).

velocities $u'(\varphi) = 2\sum_n \alpha'_n\, U^1_{n,R}(\varphi)$ are obtained. For the chosen φ_0 (section A.2.5), $u'(\varphi)$ contains zonal velocities at the equator, where the geostrophic balance does not apply, so that these velocities are not constrained by the prescribed depth perturbations. To localize the structure in the subtropics, we set $u'(\varphi)$ to zero for $\varphi \notin (\varphi_0 - 15°, \varphi_0 + 15°)$, which yields $u(\varphi)$. Finally, the coefficients α_n that fulfill $u(\varphi) = 2\sum_n \alpha_n U_{n,R}(\varphi)$ are computed with another least-squares fit and scaled with $0.005\pi^{-1}$ so that the Rossby waves produced by the forcing are about one order of magnitude weaker than the mean state. For the chosen φ_0, the amplitudes of α_n are large for low meridional modes except for $n = 1$ and close to zero for large n (not shown).

A.2.5 Simulation setup

The numerical simulations use a triangular truncation of 42 modes (T_{42}) in spectral space and a Gaussian grid with 128×64 grid points in the longitudinal and latitudinal directions, respectively. The simulations are run for 40 days and the time step is 12 min. The exponential time differencing fourth-order Runge-Kutta method is chosen for the time stepping, see Vasylkevych and Žagar (2021) for further details.

The initial condition is described in section A.2.3, and the forcing according to section A.2.4 is applied from the start of the simulations. In the reference (REF) simulation, $\varphi_0 = 30°$, and the forcing frequency matches the frequency of the modified $k = 1$ KW: $\omega_0 = \nu'^1_K = 1.01$ day^{-1} $(2\Omega)^{-1}$. The sensitivity to the forcing frequency is investigated by the simulation with a 20% lower frequency (LowF). Additional sensitivity experiments are conducted in which the forcing frequency is the same as in REF and the central latitude of the forcing varies: Three simulations are performed with $\varphi_0 = 20°$ (Q20), $\varphi_0 = 25°$ (Q25), and $\varphi_0 = 35°$ (Q35).

A.3 Linear Rossby wave response to periodic forcing

In the following, we describe the linear Rossby wave response to the forcing used in REF to facilitate the understanding of the nonlinear simulations described in section A.4. The linear response to the forcing (Eq. A.12) is the solution of

$$\frac{d\chi_n}{dt} + (i\nu'_n + d_n)\chi_n = \alpha_n\, e^{-i\omega_0 t}\,, \tag{A.14}$$

where χ_n is the Hough expansion coefficient for the nth meridional Rossby mode with $k = 1$. To approximate the effects of the mean flow on the wave propagation, Eq. (A.14) involves the modified frequency as discussed in section A.2.3. As the spectral viscosity only affects the waves with large wavenumbers, we can assume that $d_n = 0$ in the following analytical calculations. The solution of Eq. (A.14) is well known (e.g. Kasahara, 1984; Zhang, 1993):

$$\begin{aligned} \text{For } \chi_n(0) = 0: \ \chi_n(t) &= \alpha_n e^{-i\nu'_n t} \int_0^t e^{i(\nu'_n - \omega_0)t'} dt' \\ &= \frac{i\alpha_n}{\nu'_n - \omega_0} \left(e^{-i\nu'_n t} - e^{-i\omega_0 t} \right) , \end{aligned} \tag{A.15}$$

and it consists of two summands: the free solution of the homogeneous equation and the forced solution of the inhomogeneous part of Eq. (A.14).

Transforming each summand in Eq. (A.15) to physical space yields the velocities and depth perturbations of the free and forced Rossby waves. The evolution of the zonal velocity for the two components is shown in Fig. A.4 at 20°N, which is close to the latitude of the maximum velocity forcing (Fig. A.3).

The forced Rossby waves (inhomogeneous part of the solution) propagate eastward (Fig. A.4a), with their phase velocity determined by the choice of ω_0. The free Rossby wave solution (Fig. A.4b) is a superposition of waves with several n with different frequencies ν'_n. These frequencies are negative for the meridional modes with the largest amplitudes, for which n is small. As the phases of the Rossby waves with different n vary during the simulation, the magnitude of the zonal velocities of the free Rossby waves decrease with time. After about 30 days, the zonal velocities increase again as the phases of different modes align again (Fig. A.4b).

In the superposition of the free and forced Rossby waves (Fig. A.4c), the eastward propagation is clearly recognizable, and superposed on it are variations with a period of about 6 days. The variations also appear in the energy of the $k = 1$ Rossby waves calculated using Eq. (A.7) and Eq. (A.15):

$$I_n(t) = \frac{4\alpha_n^2}{(\nu'_n - \omega_0)^2} \sin^2 \left(\frac{\nu'_n - \omega_0}{2} t \right) . \tag{A.16}$$

The maxima of the $\sin^2$ function in Eq. (A.16) are about 5-6 days apart for small n (not shown).

In summary, the external forcing generates Rossby waves in the subtropics, which move eastward and vary periodically. Differences between the linear response and the nonlinear simulations will be described in the next section.

A.4 Kelvin wave excitation

Now we describe the excitation of KWs in the nonlinear simulations. The KW energy tendencies are then attributed to wave-wave and wave-mean flow interactions. Subsequently, we explain the major part of the KW excitation as a resonance mechanism with interactions between the mean flow and the forced Rossby waves.

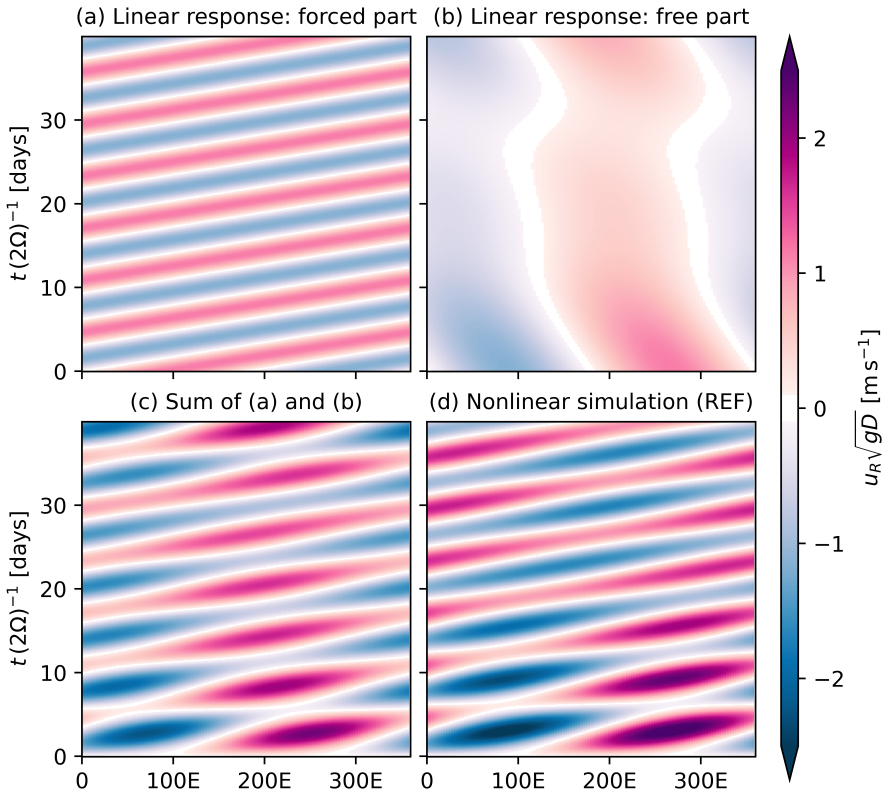

Figure A.4: Rossby wave zonal velocity anomalies at 20°N, excited in response to the forcing of Fig. A.3. (a) Forced and (b) free part of the linear response (Eq. A.15), and (c) their sum, (d) nonlinear REF simulation.

A.4.1 Nonlinear simulations

In REF, the Rossby waves generated by the external forcing are initially in phase with the forcing. As their amplitudes grow, their phases gradually shift eastward (Fig. A.5a). The initial growth of the Rossby waves is part of their periodic variation, which is similar to the linear response (Fig. A.4c and d). Rossby waves also appear as velocity and depth perturbations in the southern-hemispheric subtropics and north of the forcing, because several global modes, which have different phase velocities, are affected by the forcing (section A.2.4). After 15 days, the KW with $k = 1$ is evident in the equatorial region (Fig. A.5b), and it continues to grow throughout the simulation (Fig. A.5c,d). The depth perturbations at the equator are almost entirely composed of the $k = 1$ KW. The Kelvin waves have a fixed phase lag relative to the Rossby waves around 30° North. We refer to the KW growth as "excitation" because no KWs are present at the beginning of the simulation.

The KW energy evolution is shown in Fig. A.6, along with the energy variations in other components of the flow. In REF (Fig. A.6a), the KW energy grows with time and after one month it reaches about 20% of the Rossby wave energy. The energy of the mean flow slowly increases with time, while the Rossby wave energy oscillates due to the external forcing. This variation is similar to the linear response, but the period and amplitude of the energy variation differ (dotted versus full black lines in Fig. A.6a). One reason for this mismatch is the meridional variation of the mean flow: the strong

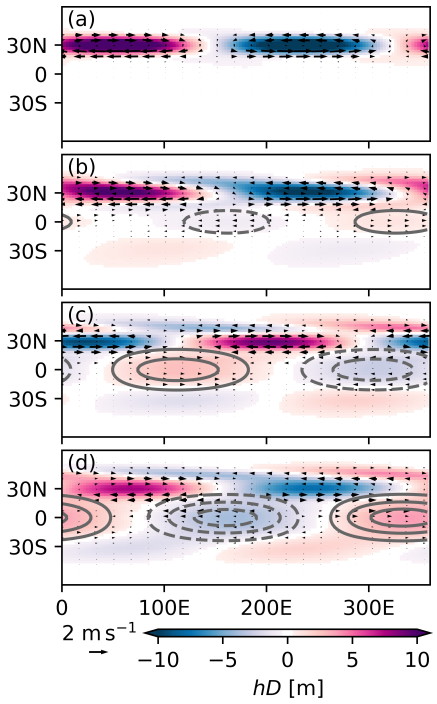

Figure A.5: Fluid depth perturbations $h\,D$ (shading) and velocity perturbations $(u, v)^T \sqrt{gD}$ (arrows) in the REF simulation after (a) 2 days, (b) 15 days, (c) 30 days and (d) 40 days. The KW depth perturbation $h_K\,D$ is shown by gray contours with line spacing of ± 1 m. Solid and dashed lines denote positive and negative depth perturbations, respectively.

westerlies slow down the westward Rossby wave propagation in the subtropics, so that the spatial structure of the Rossby waves is modified. Such modifications of waves by wave-mean flow interactions, which also appear in the modified structure of the modes in the presence of the background flow, are not considered in the linear response to the forcing. Due to the resting background state, such interactions are precluded there by design, and only the frequencies of the modes are changed. Additionally, the linear response does not include wave-wave interactions and temporal variations of the mean flow. In total, these processes slow the growth of the phase difference between the Rossby waves and the forcing. As a result, the period of the Rossby wave energy oscillation in REF is longer than in the linear response, and the mismatch increases over time (Fig. A.6a). The energy of the IG and MRG waves is close to zero.

In LowF, the KW energy is considerably lower than in REF, and it oscillates with a period of about 30 days (Fig. A.6b). For longer simulation times, the periodic behaviour in LowF continues, while the KW energy growth in REF stagnates much later (after about 120 days, not shown). This difference implies that the forcing frequency determines whether the KW energy grows continuously or oscillates with time. The energies of G and the mean flow in LowF are similar to REF. The Rossby wave energy in LowF oscillates with a longer period and greater amplitude than in REF (Fig. A.6b), which is in line with Eq. (A.16) where the absolute value of $\nu_n' - \omega_0$ is smaller when ω_0 is decreased by 20%.

The relatively small KW energy level in REF differs from the simulations by Hoskins and Yang (2000), where the Kelvin wave amplitudes were similar to the Rossby wave

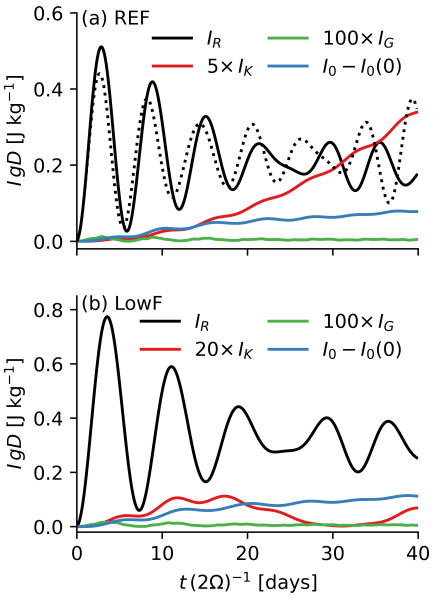

Figure A.6: Evolution of energy in nonlinear simulations. (a) REF and (b) LowF simulations. The energy is split among Rossby waves I_R, Kelvin waves I_K, inertia-gravity waves I_G and the zonal mean flow I_0. For waves, the energy is summed over all k. The dotted line in (a) is the solution for the linear case (Eq. A.16). Note that energies are multiplied by a factor of 5 and 100 in (a) and 20 and 100 in (b) for I_K and I_G, respectively.

amplitudes. This difference might be due to the direct effect of their heating or vorticity forcing on the Kelvin waves, among further differences in the model and setup.

In conclusion, the energy growth of the KWs depends on the frequency of the Rossby wave forcing. In the following subsections, we explain details of the KW excitation process. To better understand the initial excitation, we combine numerical simulations with the analytical solution, for which the Rossby waves are approximated with the linear response.

A.4.2 Wave-mean flow and wave-wave interactions

The KW energy tendency is caused by the quadratic terms, because the linear response to the external forcing only includes Rossby waves, and the spectral viscosity does not influence waves with small k. Using the notation introduced in Eq. (A.9) for interaction terms and neglecting the dissipation due to spectral viscosity, the energy tendency equation (Eq. A.8) for the KWs becomes

$$\begin{aligned}\frac{dI_K}{dt} &= 2(\mathrm{Re}[f_K(R \leftrightarrow 0)\chi_K^*] + \mathrm{Re}[f_K(G \leftrightarrow 0)\chi_K^*] + \mathrm{Re}[f_K(R \leftrightarrow R)\chi_K^*] \\ &+ \mathrm{Re}[f_K(R \leftrightarrow G)\chi_K^*] + \mathrm{Re}[f_K(K \leftrightarrow K)\chi_K^*] + \mathrm{Re}[f_K(K \leftrightarrow G)\chi_K^*] \\ &+ \mathrm{Re}[f_K(K \leftrightarrow 0)\chi_K^*] + \mathrm{Re}[f_K(G \leftrightarrow G)\chi_K^*] + \mathrm{Re}[f_K(R \leftrightarrow K)\chi_K^*])\,. \end{aligned} \tag{A.17}$$

Equation (A.17) involves all $k > 0$ as there is no KW with $k = 0$, and $f_K(0 \leftrightarrow 0)$ is thus omitted.

The various contributing terms are presented for the REF simulation in Fig. A.7. It shows that the total KW energy tendency due to all interactions, dI_K/dt, is positive,

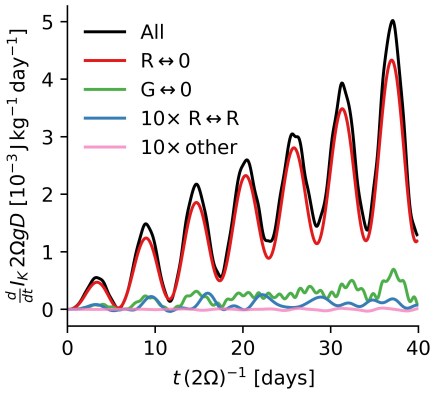

Figure A.7: KW energy tendencies (All) split into contributions due to Rossby wave-mean flow interactions ($R \leftrightarrow 0$), gravity wave-mean flow interactions ($G \leftrightarrow 0$), Rossby wave-wave interactions ($R \leftrightarrow R$) and all other wave-wave and wave-mean flow interactions (Eq. A.17). The sum over all zonal wavenumbers is shown.

which indicates that the interactions are roughly in phase with the Kelvin wave. The KW energy tendency oscillates with time due to the periodicity of the Rossby wave amplitude discussed in section A.3. About 90% of the KW energy tendency is caused by the Rossby wave-mean flow interactions ($R \leftrightarrow 0$). The second-largest tendency contribution is due to the gravity wave-mean flow interactions ($G \leftrightarrow 0$), which contribute about 10%. The Rossby wave-wave interactions ($R \leftrightarrow R$) are smaller than $R \leftrightarrow 0$ and cause less than 1% of the KW energy growth. The amplitude of the interactions depends on the magnitude of the depth perturbations and velocities of the interacting modes, which are smaller for the Rossby waves than for the mean flow. The other interactions (the last six terms in Eq. A.17) cause negligibly small KW energy tendencies (Fig. A.7), because they contain waves with small amplitudes.

The dominant zonal wavenumber of the Rossby wave-mean flow interactions is $k = 1$, which is the sum of the zonal wavenumbers of the Rossby waves and the mean flow. The zonal wavenumber of the KW excited by $R \leftrightarrow 0$ is thus $k = 1$ (Fig. A.5). Accordingly, the Rossby wave-wave interactions generate KWs with $k = 2$, whose energy is two orders of magnitude smaller than the $k = 1$ KW energy. KWs with higher k have even lower amplitudes because they are only excited by higher-order interactions, which are small.

The described results differ from Cheng et al. (2022), who explained the KW excitation with eddy momentum fluxes, i.e. wave-wave interactions, while the wave-mean flow interactions damped the KWs. However, our experiments do not necessarily contradict Cheng et al. (2022) who identified synoptic-scale Rossby waves in the subtropics as relevant for the KW growth and accordingly found $k = 5$ KWs excited by subtropical dynamics.

The dominant contribution of the Rossby wave-mean flow interactions to the KW excitation with peak signal at $k = 1$ is found in all sensitivity simulations with varying forcing latitudes (not shown). In LowF, the KW energy decreases after its initial growth because the phase of the Rossby wave-mean flow interactions shifts relative to the KWs. After about 30 days, the phases are aligned and the KW energy grows again. In REF, Q20, Q25 and Q35, however, the Rossby wave-mean flow interactions are always in phase with the KWs so that their energy grows continuously. In a longer run, the mismatch between the forcing frequency and the frequency of the modified Kelvin mode increases, because

the modified eigenmodes gradually change along with the mean flow. This leads to a stagnation of the KW growth. In the following, we focus on the dominant process, the Rossby wave-mean flow interactions.

A.4.3 Resonant Kelvin wave excitation

The Rossby wave-mean flow interactions contain interactions of both the forced and the free Rossby waves with the mean flow. Since the KW excitation is sensitive to the forcing frequency (section A.4.1), the interactions of the forced Rossby waves with the mean flow presumably cause a greater proportion of the energy growth than the free Rossby wave-mean flow interactions. Now we explain how the resonant KW excitation by these interactions takes place.

The forced Rossby wave-mean flow interactions excite KWs with $k = 1$, whose expansion coefficient evolves according to

$$\frac{d\chi_K}{dt} + i\nu'_K\chi_K = \hat{f}e^{-i\omega_0 t}. \tag{A.18}$$

The forced Rossby wave-mean flow interactions propagate eastward as determined by ω_0. The KW component of their Hough transform, evaluated at the initial time, is denoted $\hat{f}$. Equation (A.18) neglects the interactions of the free Rossby waves with the mean flow, the interactions of the IG, MRG and Kelvin waves with the mean flow, wave-wave interactions, as well as magnitude changes of the forced Rossby wave-mean flow interactions due to the temporally varying mean flow.

The solution of Eq. (A.18) is

$$\chi_K = -i\hat{f}e^{-i\nu'_K t}\,\frac{e^{i(\nu'_K-\omega_0)t}-1}{\nu'_K-\omega_0}. \tag{A.19}$$

In the limit of ω_0 approaching ν'_K, the L'Hôpital rule applies and the KW amplitude $|\chi_K|$ increases linearly. In this resonance case, the KW energy grows perpetually (Fig. A.8):

$$I_K(t) = \hat{f}^2t^2. \tag{A.20}$$

If the forcing frequency deviates from the KW eigenfrequency, the KW energy oscillates periodically according to

$$I_K(t) = \frac{4\hat{f}^2}{(\nu'_K-\omega_0)^2}\sin^2\left(\frac{\nu'_K-\omega_0}{2}t\right). \tag{A.21}$$

The period of this oscillation increases as ω_0 approaches ν'_K. In LowF, the period is 31 days.

The evolution of the KW energy in REF and LowF and the analytical approximation is shown in Fig. A.8. It confirms that the major part of the KW energy growth in REF is due to resonance with the forced Rossby wave-mean flow interactions (solid lines in Fig. A.8). The same applies to LowF, but the KW energy level is much smaller. In addition, the KW energy in the nonlinear simulations varies with a period of about 6 days (Fig. A.8). This is the period of the Rossby wave energy oscillation in Fig. A.6, which includes the free waves. Moreover, the simulated KW energy is greater than the analytical approximation because interactions of IG waves with the mean flow and wave-wave

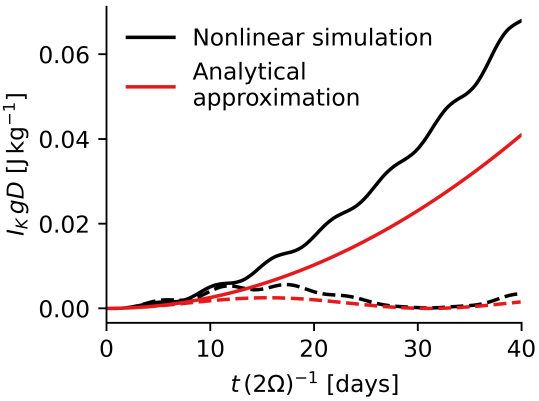

Figure A.8: Evolution of the $k = 1$ KW energy in the nonlinear simulations REF (solid black) and LowF (dashed black), and according to the analytical approximations (red lines) where the energy is changed only by the forced Rossby wave-mean flow interactions (Eqs. A.20-A.21).

interactions (Fig. A.7) also contribute to the KW growth. Nevertheless, the analytical approximation explains the qualitative behaviour seen in Fig. A.8 well, especially during initial stages of the simulations.

In addition to Kelvin waves, other modes can also be resonantly excited if ω_0 is close to their frequencies, and if other factors such as the meridional shear of the zonal flow result in a nonzero Hough transform of the wave-mean flow or wave-wave interactions for these modes. For instance, the meridional shear is essential for the energy exchange between extratropical barotropic and tropical baroclinic Rossby waves studied by Majda and Biello (2003). Furthermore, interactions of a barotropic flow with meridional shear and baroclinic Kelvin waves can excite other equatorial waves (Ferguson et al., 2009).

The modification of the eigenmodes by the non-resting background flow (see sections A.6 and A.7) offers a complementary interpretation of the KW excitation by Rossby wave-mean flow interactions. The forcing directly excites the modified Kelvin mode, and it is in phase with this mode because of the chosen forcing frequency (sections A.2.4 and A.2.5). Therefore, the amplitude of the modified Kelvin mode increases, which is diagnosed as Kelvin wave energy growth.

A.4.4 Tendencies due to forced Rossby wave-mean flow interactions in physical space

Now we analyze tendencies due to forced Rossby wave-mean flow interactions in physical space to separate the effects on the velocity and depth variables. We first discuss the tendencies for REF, and then explore their sensitivity to the location of the forcing for Q20, Q25 and Q35. The latitudinal variation of the mean flow influences the meridional structure of the forced Rossby wave-mean flow interactions, so that they impact various modes, including the KW. The analysis is shown for a single time step and longitude. The forced Rossby waves have a constant amplitude and they maintain a fixed phase shift relative to the KWs if their frequencies match. The impact on the KWs thus changes little over time, as the mean flow is approximately constant.

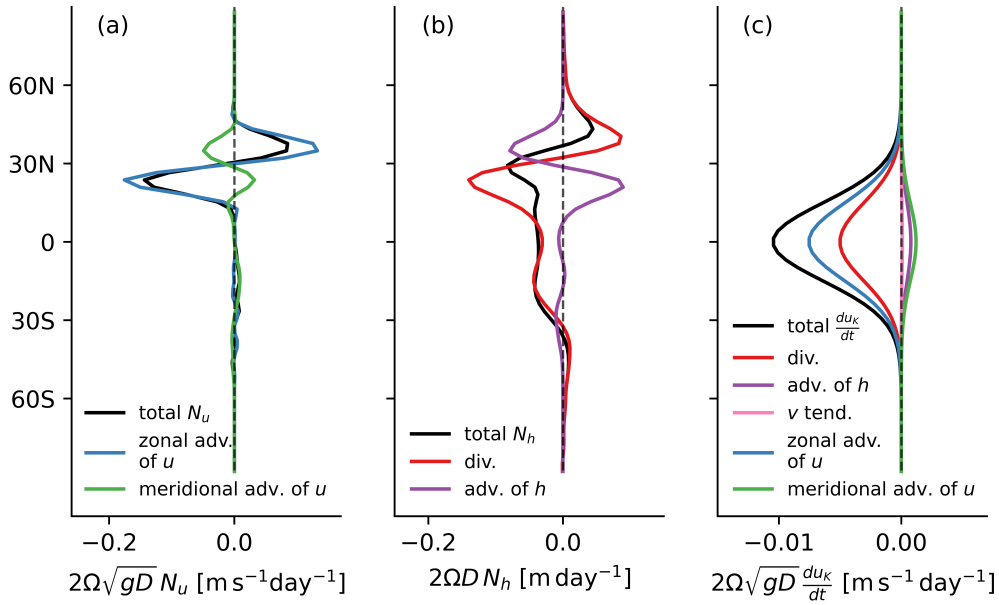

Figure A.9: (a)-(b) Interactions of forced Rossby waves and the mean flow in REF at $t = 0$ and 0°. Tendency of the (a) zonal velocity (N_u, Eq. A.22), and (b) fluid depth (N_h, Eq. A.23). (c) $k = 1$ KW zonal velocity tendency du_K/dt due to each term in (a) and (b) and the meridional velocity tendencies.

In the following, R denotes the forced Rossby waves, which have $k = 1$. The contribution of the forced Rossby wave-mean flow interactions to the zonal velocity tendency

$$N_u = \underbrace{\frac{-\gamma}{\cos\varphi} u_0 \frac{\partial u_R}{\partial \lambda}}_{\text{zonal advection}} \underbrace{-\gamma v_R \frac{\partial (u_0 \cos\varphi)}{\partial \varphi}}_{\text{meridional advection}} \tag{A.22}$$

consists of two advection terms: the zonal advection of u_R by the mean flow, and the meridional advection of the mean flow by v_R. Both terms have maxima in the subtropics as shown in Fig. A.9a for the initial time step. They have opposite signs, but the zonal advection term is more than twice as large and dominates the total effect.

The contribution of the forced Rossby wave-mean flow interactions to the depth tendency

$$N_h = \underbrace{-\frac{\gamma}{\cos\varphi} u_0 \frac{\partial h_R}{\partial \lambda} - \gamma v_R \frac{\partial h_0}{\partial \varphi}}_{\text{advection}} \underbrace{-\gamma h_0 \nabla \cdot \mathbf{V}_R}_{\text{divergence}} \tag{A.23}$$

is caused by advection of depth, and the Rossby wave divergence on the sphere, multiplied by the zonal mean depth perturbation. The two terms have opposite signs, but the amplitude of the divergence term is somewhat greater, making the total tendency N_h negative throughout the tropics to 30°N (Fig. A.9b). The advection term, which is small, would be zero if u_0 and v_R obeyed the linear geostrophic balance. The magnitude of the divergence term is determined by the relatively large h_0 of the balanced background flow.

The Kelvin wave tendencies due to N_u, N_v and N_h are evaluated using the Hough transform, and the sum of these tendencies is $\hat{f}$ in Eq. (A.18). The largest contribution to

the u_K tendency in REF is caused by the zonal advection of u_R (Fig. A.9c). This is due to the large magnitude of u_R around 20°N (Fig. A.9a), where the KW is still distinctly larger than zero. The meridional advection of zonal velocity has a weaker and opposite effect on the KWs, and the effect of the depth advection is even weaker (Fig. A.9c). The depth tendency due to the Rossby wave divergence is the second largest contributor to the KW tendencies. In agreement with the small meridional velocity of the KW, which is zero on the equatorial β-plane, the influence of the v tendency on the KW is negligible.

In the following, we investigate the relative importance of different terms contributing to the KW tendency in simulations with a poleward or equatorward-shifted forcing with respect to REF. The amplitudes of different terms in Q20, Q25 and Q35 are presented in Fig. A.10 along with REF. The comparison shows that the meridional advection term increases when the forcing is closer to the equator. This is caused by the stronger shear of the zonal background flow in that region, as well as the greater overlap of the Rossby wave-mean flow interactions with the meridional Kelvin wave structure. However, the Kelvin wave tendencies due to the meridional advection term are outweighed by the large KW tendencies due to the divergence term, which have opposite sign. The latter are stronger when the forcing is shifted equatorward, so that the Rossby waves are located in regions of larger h_0. Therefore, the KW tendencies due to the divergence term in Q20 and Q25 exceed the KW tendencies due to the zonal advection of u_R (Fig. A.10).

For Q25, the zonal advection term has a larger magnitude than in REF (Fig. A.10), because of the greater overlap of the Rossby wave-mean flow interactions with the meridional structure of the Kelvin waves. When the Rossby waves are located even closer to the equator (Q20), their zonal velocities are collocated with weaker u_0, which reduces the zonal advection term. Conversely, the Rossby waves are located in regions of stronger u_0 in Q35, but the resulting tendencies are further away from the equator so that their influence on the Kelvin waves is weaker than in REF. The KW tendencies due to the depth advection and due to the meridional velocity tendencies have in all simulations a similar magnitude as in REF (Fig. A.10). The total Kelvin wave tendencies are largest for Q25.

The presented sensitivity experiments demonstrate that the KW tendencies depend on the latitude of the forcing. Similarly, it can be expected to find sensitivity to the background flow and the prescribed mean depth which defines the meridional scale of the KW. Quantifying these sensitivities is beyond the scope of our study. Taking a different approach, Barpanda et al. (2023) found that the meridional advection of the background vorticity (Sverdrup effect) caused eddy divergence. In the equatorial region, this eddy divergence mainly belonged to the Kelvin modes. The Sverdrup effect is not easily compared with the momentum advection in our study, as Barpanda et al. (2023) analyzed different terms of the linearized vorticity equation for a steady state including meridional velocity, while we study the transient KW growth in a background with zero meridional velocity. However, the background meridional velocity in the setup of Barpanda et al. (2023) might have had a negligible effect, because the dominant Sverdrup effect only contains the Rossby wave meridional velocity, not that of the mean flow.

A.5 Conclusions and Outlook

We have investigated the KW excitation by interactions of the subtropical Rossby waves and the zonal mean flow on the sphere. Special aspects of the applied modeling frame-

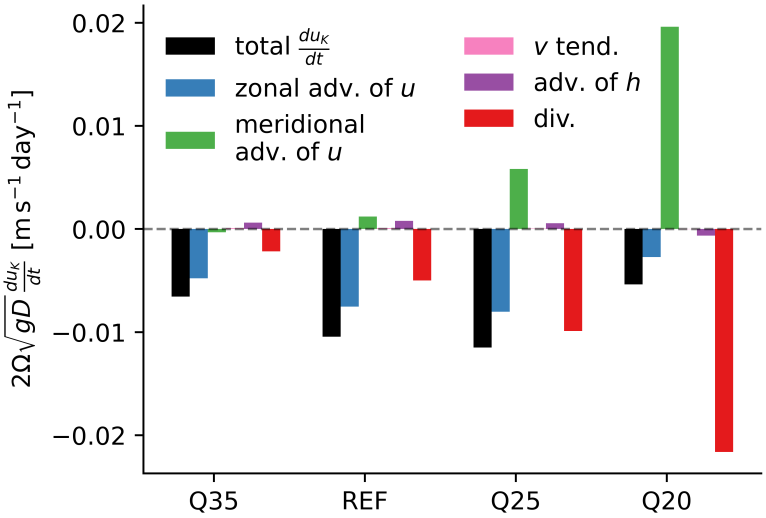

Figure A.10: Zonal velocity tendencies of the $k = 1$ KW due to different terms of the forced Rossby wave-mean flow interactions at 0°, 1.4°N for simulations in which the Rossby wave forcing is centered at different latitudes.

work are the balanced background jet and the external Rossby wave forcing. Such a forcing also affects the Kelvin mode modified with respect to the solution for the resting background state so that it contains a small contribution from the Rossby modes (section A.7). The modification arises from the effects of Rossby wave-mean flow interactions. However, we can not use the modified eigenmode to define the Kelvin wave, because it is ambiguous when the background flow varies, and because the modified eigenmodes do not form an orthogonal basis (section A.6). The KW definition as an eigenmode of the background state of rest is a meaningful way to analyze the real atmosphere with constantly varying background flows and instabilities.

As the KW is a prognostic variable of our model, the individual terms contributing to the KW energy growth in both physical and spectral space can be separated into wave-mean flow and wave-wave interactions. In spectral space, we have found that the wave-wave interactions are weak compared to the wave-mean flow interactions, because the mean flow is stronger than the waves. In physical space, the advection of the zonal Rossby wave velocity by the background flow causes part of the KW energy growth. The influence of the meridional advection of background zonal velocity by Rossby waves increases when the Rossby waves are collocated with stronger shear. The resulting KW tendencies are outweighed by the tendencies due to Rossby wave divergence in regions of large deviations from the mean depth. However, such a strong influence of the divergence term is associated with the formulation of the balanced background flow in the simplified model. The relative importance of the terms in the real atmosphere or three-dimensional (3D) models may be different.

Assuming stationary mean flow, the KW energy growth due to forcing with a prescribed frequency can be computed analytically. We showed a qualitative agreement between the temporal evolution of the KW energy in the resonance and non-resonance cases and the nonlinear simulations, especially for low-frequency forcing.

Our simulations are characterized by Rossby and Froude numbers smaller than one, and stable modes. For larger Rossby and Froude numbers and for stronger flows,

instabilities might appear. For example, Wang and Mitchell (2014) discussed unstable Rossby-Kelvin modes for Rossby numbers around one and Froude numbers of about 1-3, in the context of equatorial superrotation found on other planets. Furthermore, Kelvin waves can be excited by barotropic instability for weak surface-to-pole temperature gradients and can contribute to the superrotation (Polichtchouk and Cho, 2016).

While the KW excitation by convection is a well-studied process theoretically (e.g. Salby and Garcia, 1987) and in data (e.g. Bergman and Salby, 1994; Kiladis et al., 2009), nonlinear aspects of KW dynamics have yet to be fully understood. The near nondispersiveness and semi-geostrophy of the KW make the understanding of its variability and predictability only seemingly simpler compared to other large-scale equatorial modes. The impacts of wave-mean flow interactions and resonance effects on Kelvin waves in the atmosphere are subject of further work including the relative roles of the wave-mean flow interactions in comparison with wave-wave interactions and convective forcing in reanalysis data and climate models. Idealized simulations with a 3D version of the TIGAR model, currently under development, might also provide an opportunity to research the coupling of the Madden-Julian Oscillation with subtropical Rossby wave dynamics (Wedi and Smolarkiewicz, 2010; Yano and Tribbia, 2017).

Acknowledgments

This study is funded by the German Science Foundation DFG, Grant No. 461186383, and by the Federal Ministry of Education and Research (BMBF) and the Free and Hanseatic City of Hamburg under the Excellence Strategy of the Federal Government and the Länder. We are very grateful to Rupert Klein and two anonymous reviewers for their insightful comments, and to our colleague Sándor István Mahó for TIGAR-related discussions and for reading the manuscript.

Data availability statement

The output of the model simulations is available at https://doi.org/10.5281/zenodo.10673967.

A.6 Appendix A: Eigenmodes of the Linearized Equations around a Nonresting Background State

Hough harmonics, which provide the basis of spectral expansion in the TIGAR model, are defined as eigensolutions of Laplace tidal equations, i.e. Equation (A.1) linearized around the state of no motion. Since the linear operator $\mathbf{L}$ in Laplace tidal Eq. (A.2) is L^2 skew-adjoint, its nonzero eigenvalues are purely imaginary and the corresponding eigenfunctions (Hough harmonics) are mutually L^2-orthogonal. The L^2 inner product is

$$\langle \mathbf{X}_1 , \mathbf{X}_2 \rangle = \frac{1}{2\pi} \int_0^{2\pi} \int_{-\pi/2}^{\pi/2} \mathbf{X}_1 \cdot \mathbf{X}_2^* \cos\varphi \, d\varphi \, d\lambda \,, \tag{A.24}$$

where $\mathbf{X_i} = (u_i, v_i, h_i)^T$ for $i = 1, 2$. Furthermore, Longuet-Higgins (1968) demonstrated that $\mathbf{L}$ possesses a purely point spectrum and thus, the set of Hough harmonics is L^2 complete.

This remarkable analytical structure is destroyed when the nondimensional RSW equations (Eq. (A.1)) are linearized around a nontrivial zonal steady state $(u_0(\varphi), 0, h_0(\varphi))^T$. In that case the linearized equations read

$$\frac{\partial}{\partial t}\mathbf{X} + \mathbf{L}_b\mathbf{X} = 0, \tag{A.25}$$

with the modified linear operator

$$\mathbf{L}_b = \mathbf{L} + \mathbf{B}\,, \tag{A.26}$$

where $\mathbf{B}$ contains the background flow terms,

$$\mathbf{B} = \begin{pmatrix} \bar{\omega}\frac{\partial}{\partial\lambda} & \left(\cos\varphi\frac{d\bar{\omega}}{d\varphi} - 2\bar{\omega}\sin\varphi\right) & 0 \\ 2\bar{\omega}\sin\varphi & \bar{\omega}\frac{\partial}{\partial\lambda} & 0 \\ \frac{\gamma h_0}{\cos\varphi}\frac{\partial}{\partial\lambda} & \frac{\gamma}{\cos\varphi}\frac{\partial}{\partial\varphi}[h_0\cos\varphi\,(\cdot)] & \bar{\omega}\frac{\partial}{\partial\lambda} \end{pmatrix} \tag{A.27}$$

and $\bar{\omega}(\varphi) = \gamma u_0/\cos(\varphi)$.

Let $i\sigma$ be an eigenvalue of $\mathbf{L}_b$. We refer to $\mathrm{Re}(\sigma)$ as *modified frequency* and call the corresponding eigenfunction of $\mathbf{L}_b$ a *modified eigenmode*. It must be noted that the spectrum of $\mathbf{L}_b$ is not necessarily purely point. For instance, for certain background flows the continuous spectrum is not empty (Kasahara, 1980; Mitchell, 2013).

Moreover, for an arbitrary nontrivial steady state background, the modified eigenmodes do not form an orthogonal L^2 basis. This has been mentioned by Dickinson and Williamson (1972) (for $h_0 = 0$) and other authors (e.g. Teruya et al., 2024), however, the proof of this statement seems to be missing in the literature.

Proposition 1. The set of modified eigenmodes $\{\mathbf{e}_j\}$ is not an orthogonal basis in L^2, unless $\bar{\omega}$ is constant and $h_0 = 0$. Furthermore, under the same assumptions, the set of $\{\mathbf{P}_k\mathbf{e}_j\}$, where $\mathbf{P}_k$ is the projector onto the fields with zonal wave number k is not an orthogonal basis in $L^2([-\pi/2, \pi/2])$ with the scalar product

$$\langle \mathbf{X_1}\,, \mathbf{X_2}\rangle_\varphi = \int_{-\pi/2}^{\pi/2} \mathbf{X_1}\cdot\mathbf{X_2^*}\cos\varphi\; d\varphi\;. \tag{A.28}$$

Proof. From the assumption that the modified eigenmodes are an orthogonal basis, it follows that on any finite-dimensional span of modified eigenmodes $\mathbf{L}_b$ can be expressed as $\mathbf{L}_b = \mathbf{U}\mathbf{T}\mathbf{U}^*$ with unitary operator $\mathbf{U}$ and diagonal operator $\mathbf{T}$. By completeness of the basis, this generalizes to the whole domain of $\mathbf{L}_b$. The adjoint of $\mathbf{L}_b$ is $\mathbf{U}\mathbf{T}^*\mathbf{U}^*$. Since

$$\mathbf{L}_b\mathbf{L}_b^* = \mathbf{U}\mathbf{T}\mathbf{T}^*\mathbf{U}^* = \mathbf{U}\mathbf{T}^*\mathbf{T}\mathbf{U}^* = \mathbf{L}_b^*\mathbf{L}_b\,, \tag{A.29}$$

it follows that $\mathbf{L}_b$ is normal. However,

$$\mathbf{L}_b^*\mathbf{L}_b - \mathbf{L}_b\mathbf{L}_b^* = \begin{pmatrix} \alpha + \frac{(1-h_1^2)\gamma^2}{\cos^2\varphi}\frac{\partial^2}{\partial\lambda^2} & x_{12} & \gamma\beta h_0\frac{\partial}{\partial\varphi} + \cos\varphi\frac{d\bar{\omega}}{d\varphi}\gamma\frac{\partial}{\partial\varphi} \\ x_{21} & x_{22} & x_{23} \\ x_{31} & x_{32} & x_{33} \end{pmatrix}, \tag{A.30}$$

where $\alpha = (2\bar{\omega}+1)\sin 2\varphi\frac{\partial\bar{\omega}}{\partial\varphi} - (\cos\varphi\frac{\partial\bar{\omega}}{\partial\varphi})^2$, $\beta = \cos\varphi\frac{\partial\bar{\omega}}{\partial\varphi} - (2\bar{\omega}+1)\sin\varphi$, $h_1 = h_0 + 1$, and x_{ij} denotes matrix elements which are not required for our conclusion. Each of the summands of x_{11} in $\mathbf{L}_b^*\mathbf{L}_b - \mathbf{L}_b\mathbf{L}_b^*$ must be zero separately for $\mathbf{L}_b$ to be normal. From the

second summand being zero, it follows that h_0 must be zero. With $h_0 = 0$, x_{13} can only be zero if $\frac{d\bar{\omega}}{d\varphi}$ is zero. Thus, $\mathbf{L}_b$ is normal if and only if the background flow is absent, i.e. $\mathbf{L}_b = \mathbf{L}$, or if $\bar{\omega}$ is constant and $\frac{d\bar{\omega}}{d\varphi} = h_0 = 0$, while the latter case of solid-body rotation without variations in the fluid depth is not a steady state. The statement that the projections $\{\mathbf{P}_k \mathbf{e}_j\}$ do not form an orthogonal basis follows by applying the same argument to the operator $\mathbf{L}_b \mathbf{P}_k$.

Thus, for a nontrivial background flow, the modified eigenmodes are not mutually orthogonal, or they do not span the whole space, or both. For this reason, the modified eigenmodes, while dynamically important, are unsuitable as a basis of a forecast model or spectral expansion of atmospheric data.

The orthogonality of modes in shear flows discussed by Held (1985) using the conservation of pseudomomentum relies on a different inner product. Furthermore, generalized Hough modes which take into account horizontal and vertical shear might not form a complete system, and they are for the lowest order orthogonal to their adjoints (Ortland, 2005).

To compute the modified normal modes and corresponding eigenvalues, we use the FORTRAN program BGHough, which is part of TIGAR. This program implements the algorithm proposed in Kasahara (1980), which we describe below.

Substituting the ansatz

$$\mathbf{W} = (u, v, h)^T = \widehat{\mathbf{W}}(\varphi) e^{i(k\lambda - \sigma t)} \tag{A.31}$$

into the linarized RSW equation (A.25) yields

$$(\mathbf{L} - i\sigma \mathbf{I})\widehat{\mathbf{W}} + i\widehat{\mathbf{B}}\,\widehat{\mathbf{W}} = 0, \tag{A.32}$$

where $\mathbf{I}$ is the identity matrix, and

$$\widehat{\mathbf{B}} = \begin{pmatrix} \bar{\omega}k & i\left(2\bar{\omega}\sin\varphi - \cos\varphi \frac{d\bar{\omega}}{d\varphi}\right) & 0 \\ -2i\bar{\omega}\sin\varphi & \bar{\omega}k & 0 \\ \frac{k\gamma h_0}{\cos\varphi} & -\frac{i\gamma}{\cos\varphi}\frac{\partial}{\partial\varphi}[h_0 \cos\varphi\,(\cdot)] & \bar{\omega}k \end{pmatrix}. \tag{A.33}$$

To solve Eq. (A.32), $\widehat{\mathbf{W}}$ is expanded in terms of Hough functions, so that

$$\widehat{\mathbf{W}} = \sum_r C_r \mathbf{\Theta}_r^k \tag{A.34}$$

where the sum is taken over all Hough modes with the zonal wavenumber k available at the selected resolution.

Substituting Eq. (A.34) into Eq. (A.32) yields an eigenvalue problem

$$(\mathbf{M} - \sigma \mathbf{I})\mathbf{C} = 0 \tag{A.35}$$

where $\mathbf{C} = (C_1 \ldots C_R)^T$ and the matrix $\mathbf{M}$ is given by

$$\mathbf{M} = \begin{pmatrix} \nu_1^k + b_{11}^k & b_{12}^k & \ldots & b_{1R}^k \\ b_{21}^k & \nu_2^k + b_{22}^k & \ldots & b_{2R}^k \\ \vdots & \vdots & & \vdots \\ b_{R1}^k & b_{R2}^k & \ldots & \nu_R^k + b_{RR}^k \end{pmatrix} \tag{A.36}$$

with

$$b^k_{r'r} = \int_{-1}^{1} \widehat{\mathbf{B}}\boldsymbol{\Theta}^k_r \cdot \left(\boldsymbol{\Theta}^k_{r'}\right)^* . \tag{A.37}$$

The eigenvalue problem (Eq. A.35) is solved using DGEEV routine from LAPACK package and the resulting coefficients are normalized so that $\sum_r |C_r|^2 = 1$.

We remark that if σ_r is an eigenvalue of problem (A.35), then $i\sigma_r$ is the eigenvalue of the linearized RSW equation (A.25). Eigenvalues $i\sigma_r$, are not necessarily imaginary. The modified normal modes corresponding to $\mathrm{Im}(\sigma_r) > 0$ are linearly unstable, while the ones corresponding to $\mathrm{Im}(\sigma_r) < 0$ are exponentially stable, with growth and decay exponents, respectively, given by $\mathrm{Im}(\sigma_r)$. In all cases, the frequency of the modified mode is $\mathrm{Re}(\sigma_r)$.

Classifying the modified modes is a nontrivial task since a modified mode can, in principle, project on all Hough harmonics with the same zonal wave number. Boyd (1978) used the perturbation theory to define a modified Kelvin mode on the equatorial β-plane. Zhang and Webster (1989) classify the modified modes on the β-plane using an approximate dispersion relationship. This strategy is not currently feasible in spherical geometry as no such explicit approximate dispersion relationship is known.

For the sphere, there are at least two sensible classification strategies that are easy to implement. The first one is based on matching the spatial structures of modified modes and Hough harmonics. This defines the modified Kelvin mode as the one with the largest projection onto the "true" Kelvin wave (i.e. Kelvin mode for the state of no motion). The disadvantage of this approach is that for any fixed n, l, k, the modified frequencies of the modes with the largest projection on $\mathbf{H}^k_{n,l}$, $\mathbf{H}^{k\pm1}_{n,l}$, and $\mathbf{H}^k_{n\pm1,l}$ may significantly differ, resulting in non-smooth and non-monotone dispersion curves.

We solve this problem by adopting a hybrid approach based on both the spatial structures and the modified frequencies. First, a third of the modified modes with the largest "true" Rossby contribution, i.e. $\sum'_r |C_{r'}|^2$ with r' running over all Rossby and MRG Hough modes, is classified as Rossby/MRG. The remaining modes are considered IG. Within the Rossby and IG categories, the classification is based on the modified frequency $\nu_{r,\mathrm{mod}} = \mathrm{Re}(\sigma_r)$. The modified Rossby modes for a given k are sorted according to $\nu_{r,\mathrm{mod}}$ and the one with the lowest frequency is classified as modified MRG ($n = 0$ modified mode); the mode with the second lowest frequency is classified as $n = 1$ and so on. Similarly, the modified IG modes are also sorted according to $\nu_{r,\mathrm{mod}}$, and split into two bins at the median frequency. The bin containing the lowest frequencies corresponds to WIGs, while the other bin corresponds to EIGs. The modified Kelvin mode is then defined as the mode with the lowest frequency in the second bin ($n = 0$ modified EIG). We note that throughout the procedure the frequency is treated as a signed quantity and "lowest" and "highest" should be interpreted accordingly.

A.7 Appendix B: Modified Eigenmodes for the Background Flow in this Study

In the following, the eigenmodes with $k = 1$ of the linearized equations with respect to the background flow in the present study (Fig. A.1) are discussed. We identify the modified Kelvin mode as explained in section A.6. In this case, it is not important which of the alternative strategies is used for the task, as they both yield the same result. All of the modified Kelvin modes are stable and not decaying.

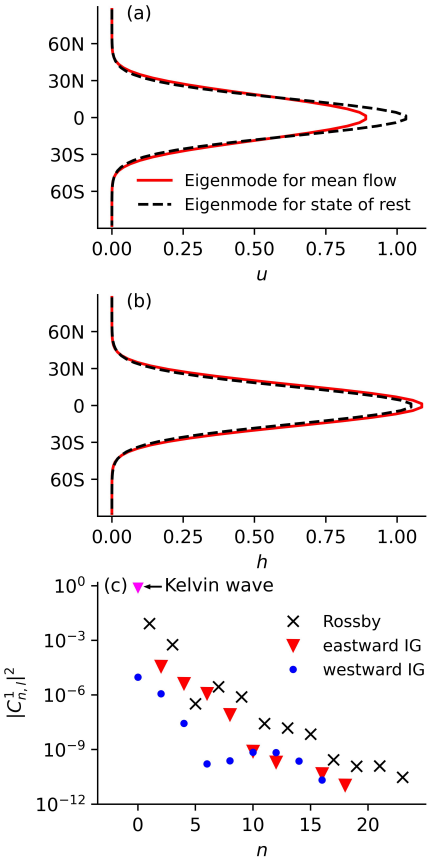

Figure A.11: Meridional structure of (a) zonal velocity and (b) fluid depth of the modified eigenmode corresponding to the $k = 1$ Kelvin mode for the background flow in Fig. A.1. (c) The Hough harmonic spectrum contains only symmetric modes, which have even n for IG modes and uneven n for Rossby modes.

The modified Kelvin modes also have a similar spatial structure as Kelvin Hough modes for the corresponding zonal wave number (Fig. A.11a,b). The differences in the meridional structure of the fluid depth are smaller than the differences in zonal velocity. Quantitatively, 99% of the energy of the modified $k = 1$ Kelvin mode is carried by the Hough Kelvin wave ($|C^1_{0,1}|^2 = 0.99$). The remaining 1% is the contribution of $n = 1$ and $n = 3$ Rossby modes (Fig. A.11c).

The modified Rossby modes with $k = 1$ and low n also match well with the respective Hough harmonics (Fig. A.12a). This is in line with Kasahara (1981), and small changes of the lowest Rossby modes through shear flows have also been found by Boyd (1978) and Mitchell (2013). For higher n, several Rossby modes contribute to the modified structure, but the IG wave contribution is small for all shown modes (Fig. A.12a).

The frequencies of the lowest ten modified Rossby modes are shown in Fig. A.12b. For small n, the frequencies with respect to the balanced background state in Fig. A.1 are higher than the frequencies for the state of rest because the increase of the absolute frequency induced by h_0 outweighs the decrease by the Doppler shift. The frequencies decrease with n, and the differences are mostly small.

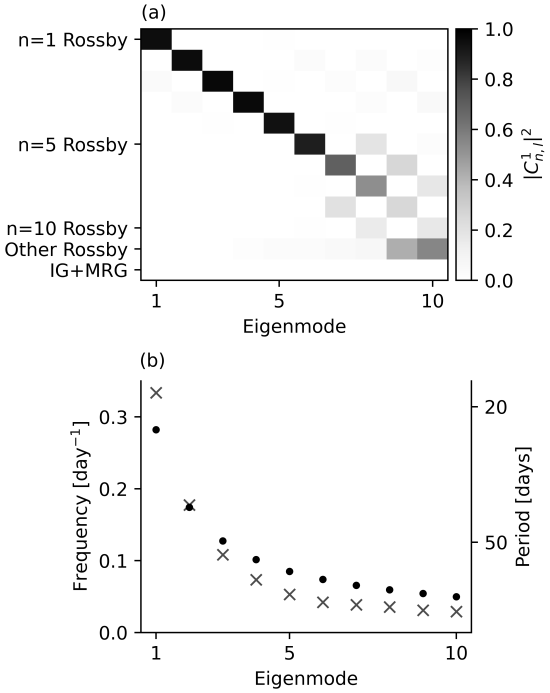

Figure A.12: (a) Hough harmonic spectrum of the $k = 1$ eigensolutions of the RSW equations, linearized around the background flow in Fig. A.1, which correspond to the $n = 1 \ldots 10$ Rossby modes. (b) Crosses represent the absolute frequencies of these modes as a function of n. Dots represent the frequencies for the state of rest.

B

INFLUENCES OF DYNAMICAL AND DIABATIC PROCESSES ON STATIONARY AND TRANSIENT EQUATORIAL KELVIN WAVES

The work in this appendix is a paper which is under minor revisions in the *Journal of Advances in Modeling Earth Systems*.

An earlier version is available as a preprint:

Holube, K. M., Lunkeit, F., Vasylkevych, S., and Žagar, N. (2025). Energy budget of the equatorial Kelvin wave: Comparing dynamical and diabatic sources. *ESS Open Archive*, May 20, 2025. https://doi.org/10.22541/essoar.174776017.78570412/v1

Authors' Contributions[1]

- Holube, K. M.: Conceptualization, Data curation, Formal analysis, Investigation, Methodology, Software, Visualization, Writing the original draft, Writing - Review and Editing.
- Lunkeit, F.: Conceptualization, Supervision, Writing - Review and Editing.
- Vasylkevych, S.: Conceptualization, Formal analysis, Investigation, Methodology, Validation, Writing - Review and Editing.
- Žagar, N.: Conceptualization, Data curation, Funding Acquisition, Project Administration, Supervision, Writing - Review and Editing.

1 using the Contributor Role Taxonomy (CRediT) https://credit.niso.org/

Influences of dynamical and diabatic processes on stationary and transient equatorial Kelvin waves

Katharina M. Holube,[1] Frank Lunkeit,[1] Sergiy Vasylkevych,[1] and Nedjeljka Žagar[1]

[1] Meteorological Institute, Center for Earth System Research and Sustainability, University of Hamburg, Hamburg, Germany

Key Points:

- The main source of Kelvin wave energy arises from meridional advection of zonal momentum of the subtropical jet in the eastern hemisphere.
- Temporal variability of Kelvin wave energy tendencies on time scales longer than one day is connected to non-radiative diabatic heating.
- Stationary Kelvin waves in the atmosphere result from non-radiative diabatic heating and vertical advection of warm air.

Abstract

Kelvin waves (KWs) in the atmosphere can generally be forced by both tropical convective heating and dry dynamical processes, including interactions with the extratropics. However, the relative influences of dynamical and diabatic processes on KWs have not been conclusively clarified. This study identifies stationary and transient KWs in ERA5 data using a three-dimensional normal-mode decomposition. Dynamical and diabatic processes act as energy sources and sinks for KWs and maintain the stationary KWs. The nonlinear dynamical momentum and temperature tendencies, i.e., those resulting from advection, are computed from the normal-mode expansion coefficients. For diabatic processes, tendencies due to parametrizations in short-term ERA5 forecasts are used. A large part of the KWs is stationary; these waves are maintained by non-radiative diabatic heating and upward advection of positive temperature anomalies over the Maritime Continent. These processes act as KW energy sinks because the temperature tendencies are phase-shifted relative to the stationary KWs. The largest KW energy source is meridional advection of zonal momentum, which induces easterly momentum tendencies in the upper-troposphere eastern hemisphere and thus strengthens the KW easterlies. The main KW energy sink results from momentum dissipation. The KW energy time series has a diurnal cycle, which is connected to short-wave radiation. On time scales of several days, the variability of the KW energy tendencies is governed by non-radiative diabatic heating including latent heat release. These results pave the way for investigating the energetics and interactions of other waves in the tropics and extratropics.

Plain Language Summary

Kelvin waves contribute to variability in space and time in the tropical atmosphere. While the Kelvin wave development associated with the release of latent heat in the tropics is well known, recent studies have shown that momentum transports can induce sources of Kelvin wave energy. This study quantifies how momentum transports by the

circulation and heat sources influence Kelvin waves. The time-averaged Kelvin waves mainly result from heating of the air and upward transport of warm air over the Indian Ocean and western Pacific Ocean. This process appears as an energy sink for Kelvin waves because, although it amplifies the waves at certain longitudes, it damps them at others. Further energy sinks result from frictional processes. Energy is transferred to Kelvin waves when their velocity is strengthened by transport of momentum, which has the strongest influence over the Indian Ocean. The temporal variability of the Kelvin wave energy is attributed to the release of latent heat and solar radiation. The applied method allows to further study the energetics of wave interactions in the tropics and at higher latitudes.

B.1 Introduction

Equatorial Kelvin waves (KWs) play an important role in the variability of the tropical atmosphere (Wallace et al., 2023). While it is widely known that KWs develop in response to tropical convective heating (Hayashi and Golder, 1978; Salby and Garcia, 1987; Mapes, 2000; Khouider and Majda, 2006; Nakamura and Takayabu, 2022; Chien and Kim, 2023), dry dynamical processes can also act as energy and vorticity sources for KWs (Tanaka, 1985; Castanheira and Marques, 2021; Matthews, 2021; Tulich and Kiladis, 2021; Cheng et al., 2022). Dynamical KW sources have been identified in association with eastward-moving extratropical wave trains, which are advected by the background flow and break at a critical line (Murakami, 1974; Straub and Kiladis, 2003; Yang et al., 2007; Cheng et al., 2022). Cheng et al. (2022) found evidence for the resonant KW forcing by eddy momentum flux convergence in reanalysis data. In idealized model simulations, dynamical mechanisms influencing KWs have been identified, such as the KW response to an eastward-moving forcing in the presence of equatorial easterlies (Zhang, 1993; Hoskins and Yang, 2000; Holube et al., 2024). In addition, subtropical Rossby gyres can force KWs via meridional advection of vorticity (Barpanda et al., 2023). The KW development due to wave-wave interactions has also been demonstrated (Garfinkel et al., 2021). These findings raise the question of how the influences of dynamical and diabatic processes on KWs compare with each other.

Comparisons of dynamical and diabatic KW sources have been conducted using numerical simulations (Hayashi and Golder, 1978). In aqua-planet simulations, Tulich and Kiladis (2021) analyzed the impacts of extratropical eddy momentum flux forcing and tropical heating on KWs, which were identified using wavenumber-frequency decomposition (WFD). The KWs obtained with this method, which involves a Fourier transform in zonal direction and time, are in the following referred to as WFD-KWs. Tulich and Kiladis (2021) quantified sources of kinetic and available potential energy (APE) of WFD-KWs using co-spectral analysis of zonal velocity or temperature with the momentum or heat sources, projected on the analytical meridional structure of the KW solution of the shallow-water equation system, linearized around the state of rest (Matsuno, 1966). In their level-by-level analysis, a mean depth was prescribed, which is connected to the meridional scale of the KW. Tulich and Kiladis (2021) found that the extratropical dynamical forcing, which is consistent with the concept of wave resonance (Hoskins and Yang, 2000), is a stronger energy source for WFD-KWs than diabatic heating in the tropics.

The present study compares the influences of dynamical and diabatic processes on KWs in reanalysis data. In a very recent study with a similar objective, the required diabatic temperature tendencies were estimated as the residual of the thermodynamic equation (Chien et al., 2025). A novel aspect of the present study is to use the temperature tendencies due to parametrizations from the ERA5 reanalysis (Hersbach et al., 2020), which allow to separate the contributions of radiative and non-radiative processes. While Chien et al. (2025) analyzed the energy sources of WFD-KWs, the present study identifies KWs using three-dimensional (3D) normal-mode decomposition. This method makes no assumptions about the wave propagation, which can be influenced by various processes. Instead, KWs are identified based on their spatial structure (Žagar et al., 2015). The resulting KWs contain a stationary component, which is the averaged KW signal over the considered time series, while stationary KWs are not included in the WFD-KWs. Further differences between WFD-KWs and the KWs obtained using normal-mode decomposition were discussed by Žagar et al. (2022).

The climatology and temporal variability of KWs identified with 3D normal-mode decomposition have been described by Blaauw and Žagar (2018) and Žagar et al. (2022). Consistent with several previous studies (e.g., Stechmann and Ogrosky, 2014; Kosovelj et al., 2019; Žagar et al., 2022), the KWs analyzed in our study do not contain a zonal mean component. Kelvin waves obtained with 3D normal-mode decomposition capture the signatures of various phenomena with different propagation characteristics. The stationary KWs make up 66% of the KW energy in the month on which our study focuses. We also analyze a time series of one year, in which the proportion of stationary KWs is 42%, while it is 41% for four years. The transient KWs contain seasonal and subseasonal variability, such as the Madden-Julian Oscillation (MJO), as well as KWs that propagate with different phase velocities (Žagar and Franzke, 2015; Castanheira and Marques, 2015, 2021; Žagar et al., 2022).

Stationary KWs can be considered as part of the Walker Circulation (Gill, 1980; Stechmann and Ogrosky, 2014). Stechmann and Ogrosky (2014) modeled the stationary KW response to diabatic heating for the first baroclinic mode. Their model closely represents the observed stationary KWs, although it neither includes dissipation nor momentum forcing. In this study, we confirm that these processes indeed play a secondary role for maintaining the stationary KWs by quantifying the contributions of different dynamical and diabatic processes.

The 3D normal-mode functions are multivariate functions comprising horizontal velocity and geopotential. The energy of a normal mode is thus the mechanical energy, which is the sum of kinetic energy and APE (Kasahara and Puri, 1981). Energy sources and sinks of 3D normal modes were first determined by Tanaka (1985), who found that KWs gain energy due to dynamical processes, specifically the advection of momentum and temperature. Castanheira and Marques (2021) confirmed this result for a longer time series and showed that the dynamical KW energy sources are enhanced during the active phase of the MJO. However, it remains unclear where the dynamical processes that the KW energy sources result from are located and which components of the 3D advection impact KWs the most.

In this study, we localize the KW energy sources as a function of latitude, longitude and pressure level. Furthermore, we calculate the nonlinear dynamical momentum and temperature tendencies from the normal-mode expansion coefficients in order to decompose these terms into wave-wave and wave-mean flow interactions. For comparison,

we quantify the KW energy tendencies due to diabatic processes, including dissipation, using the momentum and temperature tendencies due to parametrizations in ERA5 data, whereas previous studies evaluated the diabatic energy tendencies as the residual of the energy budget (Tanaka and Kung, 1988; Marques et al., 2020).

In section B.2, we describe the prognostic equations for KWs and their energy tendencies, the numerical discretization and the data used for this study. The contributions of dynamical and diabatic processes to the stationary KWs are shown in section B.3. The energy budget of the stationary KWs is presented in section B.4, before the temporal variability of the KW energy tendencies due to different processes is analyzed in section B.5. We discuss our results in section B.6 before drawing conclusions in section B.7.

B.2 Method

In the following, we explain the prognostic equation for the 3D normal modes, and how the contributions of different processes to the stationary waves are determined (subsection B.2.1). The normal-mode energy budget is described in subsection B.2.2. Details of the numerical framework and the data used in this study are given in subsections B.2.3 and B.2.4, respectively. The validity of the normal-mode energetics method is illustrated using a short time series (subsection B.2.5).

B.2.1 Prognostic equation for normal modes

The normal-mode decomposition can be applied to 3D atmospheric data, obtained using numerical models, in which diabatic and subgrid-scale processes are parametrized. The IFS model, which was used to produce the reanalysis data analyzed in this study, is based on the hydrostatic primitive equations (ECMWF, 2016a). In pressure coordinates, these equations read

$$\frac{\partial u}{\partial t} = \underbrace{2\Omega v \sin\varphi - \frac{1}{a\cos\varphi}\frac{\partial \Phi'}{\partial \lambda}}_{\text{Linear dynamical terms}} \underbrace{- \frac{1}{\cos\varphi}\mathbf{V}\cdot\nabla(u\cos\varphi) - \omega\frac{\partial u}{\partial p}}_{\text{Nonlinear dynamical terms } N_u} + \underbrace{S_u}_{\substack{\text{Parametrized}\\ \text{processes}}}, \tag{B.1a}$$

$$\frac{\partial v}{\partial t} = \underbrace{-2\Omega u \sin\varphi - \frac{1}{a}\frac{\partial \Phi'}{\partial \varphi}}_{\text{Linear dynamical terms}} \underbrace{- \frac{1}{\cos\varphi}\mathbf{V}\cdot\nabla(v\cos\varphi) - \omega\frac{\partial v}{\partial p} - \frac{\tan\varphi}{a}\left(u^2+v^2\right)}_{\text{Nonlinear dynamical terms } N_v} + \underbrace{S_v}_{\substack{\text{Parametrized}\\ \text{processes}}}, \tag{B.1b}$$

$$\frac{\partial T'}{\partial t} = \underbrace{\frac{RT_0}{c_p p}\omega - \omega\frac{dT_0}{dp}}_{\text{Linear dynamical terms}} \underbrace{- \mathbf{V}\cdot\nabla T' - \omega\frac{\partial T'}{\partial p} + \frac{RT'\omega}{c_p p}}_{\text{Nonlinear dynamical terms } N_T} + \underbrace{S_T}_{\substack{\text{Parametrized}\\ \text{processes}}}. \tag{B.1c}$$

These are prognostic equations for horizontal velocity $\mathbf{V} = (u, v)$ and temperature perturbations T' with respect to the horizontally homogeneous reference temperature $T_0(p)$. The pressure vertical velocity is denoted ω, and the geopotential perturbations are denoted Φ'. The constants are Earth's radius a, angular velocity Ω and gravity g, the specific gas constant R and the specific heat capacity c_p at constant pressure for dry air.

The coordinates are longitude $\lambda \in [0, 2\pi)$, latitude $\varphi \in (-\pi/2, \pi/2)$ and pressure p, and ∇ represents the horizontal gradient operator.

We distinguish between linear and nonlinear dynamical momentum and temperature tendencies in the sense of linearization around the state of rest. In Equation (B.1), the linear velocity tendencies are the Coriolis force and the pressure gradient force, while the nonlinear dynamical terms consist of momentum advection and metric terms. The linear temperature tendencies are the portions of vertical advection and adiabatic expansion that involve the reference temperature. They can be summarized as $\omega\gamma_0/p$ using the static stability of the reference state $\gamma_0 = \frac{RT_0}{c_p} - p\frac{dT_0}{dp}$. The nonlinear dynamical temperature tendencies contain the advection of temperature perturbations and the nonlinear part of the temperature tendency due to adiabatic expansion, representing the conversion between kinetic and potential energy. The latter nonlinear term is usually neglected (e.g., Tanaka, 1985; Marques and Castanheira, 2012) under the assumption $T' \ll T_0$. As we do not make this assumption, the term is retained in our analysis, and referred to as the conversion term.

The diabatic temperature tendencies S_T (Eq. B.1c) are analogous to the apparent heat source Q_1 defined by Yanai et al. (1973). This source includes release of latent heat, eddy fluxes of sensible heat, and radiative processes comprising short-wave radiation Q_{SW} and long-wave radiation Q_{LW}. Haertel and Kiladis (2004) and Kiladis et al. (2009) associate the effect of Q_1 with the convective cycle, which would imply that latent heat release is a substantial part of the non-radiative diabatic processes $S_T - Q_{\mathrm{SW}} - Q_{\mathrm{LW}}$.

Following Tanaka (1985), Eq. (B.1c) is combined with the hydrostatic equation and the continuity equation as

$$-\frac{\partial}{\partial t}\frac{\partial}{\partial p}\left(\frac{p^2}{R\gamma_0}\frac{\partial \Phi'}{\partial p}\right) + \nabla \cdot \mathbf{v} = \frac{\partial}{\partial p}\left(\frac{p}{\gamma_0}(N_T + S_T)\right) . \tag{B.2}$$

The 3D normal modes are eigenfunctions of Equations (B.1a), (B.1b) and (B.2), linearized around the state of rest, i.e., neglecting $\mathbf{N} = (N_u, N_v, N_T)^T$ and $\mathbf{S} = (S_u, S_v, S_T)^T$. These modes are an orthonormal basis for the velocity and geopotential fields, and they consist of Hough harmonics $\mathbf{H}_r(\lambda, \varphi) = (U_r, -iV_r, Z_r)^T e^{ik\lambda}$ and vertical structure functions $G_m(p)$ as described in section B.8. The Hough harmonics represent Rossby, inertia-gravity, mixed Rossby-gravity and Kelvin modes. The multi-index r denotes a combination of meridional mode n, vertical mode m and zonal wavenumber k. The complex expansion coefficient $W_r(t)$ specifies the amplitude and phase of the mode r. The prognostic equation for W_r results from the expansion of Eqs. (B.1a), (B.1b) and (B.2) in terms of vertical structure functions and Hough harmonics:

$$\frac{dW_r}{dt} = -2\Omega\, i\nu_r W_r + f_r\,, \tag{B.3}$$

where

$$f_r = \frac{1}{2\pi p_s}\int_0^{2\pi}\int_{-\frac{\pi}{2}}^{\frac{\pi}{2}}\int_0^{p_s}\begin{pmatrix}(N_u + S_u)\sqrt{gD_m}^{-1}\\ (N_v + S_v)\sqrt{gD_m}^{-1}\\ \frac{\partial}{\partial p}\left(\frac{p}{\gamma_0}(N_T + S_T)\right)\end{pmatrix} G_m\, dp \cdot \mathbf{H}_r^* \cos\varphi\, d\varphi\, d\lambda \tag{B.4}$$

is the projection of the nonlinear terms and parametrized processes onto the mode r. The reference pressure $p_s = 1013.25$ hPa is the lower boundary of the pressure coordinate

system, and D_m is the equivalent depth of the mode r. The first summand on the right-hand side of Eq. (B.3) represents the linear terms, according to which the free mode propagates zonally with phase velocity $2\Omega a \nu_r / k$, where ν_r is the nondimensional eigenfrequency. The second summand is the projection of the nonlinear dynamical terms and parametrized sources onto the mode r. These terms affect not only the phase but also the amplitude of the mode.

The time series of $W_r(t)$ contains variability on all time scales because the normal-mode decomposition does not involve filtering in time, in contrast to many other wave identification methods (Knippertz et al., 2022). The time average of $W_r(t)$ is in the following referred to as the stationary wave $\overline{W}_r$. We assume that the trend of W_r in the time series under consideration is small. Hence, we obtain the stationary wave from the time average of Eq. (B.3) as

$$\overline{W}_r = \frac{\overline{f}_r}{2\Omega i \nu_r} \,. \tag{B.5}$$

Therefore, the stationary wave is phase-shifted eastward (westward) by 90° relative to $\overline{f}_r$ if the wave is of eastward-propagating (westward-propagating) wave type according to linear theory. The contributions of individual processes constituting $\overline{f}_r$ to the stationary wave are also quantified with Eq. (B.5). The KW tendencies required for this are determined from the momentum tendencies as in Eq. (B.4) and from the temperature tendencies as follows, here for example for the diabatic temperature tendencies:

$$\overline{f}_r(\overline{S}_T) = -\frac{1}{2\pi p_s} \int_0^{2\pi} \int_{-\frac{\pi}{2}}^{\frac{\pi}{2}} \int_0^{p_s} \frac{\overline{S}_T}{\gamma_0} p \frac{dG_m}{dp} \, dp \, Z_r^* e^{-ik\lambda} \cos\varphi \, d\varphi \, d\lambda \,. \tag{B.6}$$

This neglects the boundary terms resulting from the integration by parts of Eq. (B.4), consistent with the evaluation of the KW energy tendencies described below.

B.2.2 Normal-mode energetics

The energy of the mode r is

$$I_r \;=\; (2-\delta_{0k}) \frac{p_s}{4} D_m W_r W_r^* = \frac{1}{2} \int_V \left(u_r^2 + v_r^2 + \frac{\Phi_r^2}{g D_m} \right) dV, \tag{B.7}$$

where δ_{0k} is the Kronecker delta, and the 3D integral over the atmosphere is

$$\int_V dV = \frac{1}{4\pi g} \int_0^{2\pi} \int_{-\pi/2}^{\pi/2} \int_0^{p_s} dp \, \cos\varphi \, d\varphi \, d\lambda \,. \tag{B.8}$$

Note that dV has the unit kg m^{-2}, therefore I_r is the energy per area in J m^{-2}. Using the vertical structure equation (Eq. B.21) and lower boundary condition (Eq. B.22), Eq. (B.7) becomes

$$\begin{aligned} I_r = K_r - \frac{1}{2} \int_V \Phi_r \frac{\partial}{\partial p} \left(\frac{p^2}{R\gamma_0} \frac{\partial \Phi_r}{\partial p} \right) dV = K_r + P_r \\ + \frac{1}{8\pi g} \int_0^{2\pi} \int_{-\pi/2}^{\pi/2} \Phi_r(p_s)^2 \frac{p_s}{R T_0(p_s)} \cos\varphi \, d\varphi \, d\lambda \end{aligned} \tag{B.9}$$

(Tanaka and Kung, 1988). The kinetic energy of the horizontal motion associated with the mode r is

$$K_r = \int_V \frac{1}{2}\left(u_r^2 + v_r^2\right)\, dV\,, \tag{B.10}$$

whereas the APE is

$$P_r = \int_V \frac{R}{2\gamma_0} T_r^2\, dV\,. \tag{B.11}$$

For each vertical mode and zonal wavenumber $k > 0$, the Kelvin wave is the slowest eastward-propagating inertia-gravity mode in the linear equation system. The expansion coefficients specifying the amplitude and phase of the circulation component with the spatial structure of the KW are denoted $W_{k,\mathrm{K},m}$. In the following, "Kelvin wave" refers to the sum over all $k > 0$ and m. The KW energy tendency is

$$\frac{dI_\mathrm{K}}{dt} = \sum_k \sum_m p_s D_m \mathrm{Re}\left(\frac{dW_{k,\mathrm{K},m}}{dt} W^*_{k,\mathrm{K},m}\right) = \int_V (\mathbf{N} + \mathbf{S}) \cdot \begin{pmatrix} u_\mathrm{K} \\ v_\mathrm{K} \\ \frac{R}{\gamma_0} T_\mathrm{K} \end{pmatrix} dV\,, \tag{B.12}$$

as follows from Eqs. (B.3) and (B.7), neglecting boundary terms resulting from integration by parts (see section B.9.2 for details of the derivation). If the velocity (temperature) tendency is in phase with the KW velocity (temperature), I_K increases.

The prognostic equation for KW energy can be symbolically written as

$$\frac{dI_\mathrm{K}}{dt} = A_u + A_v + A_T + A_\mathrm{co} + D_u + D_v + D_\mathrm{SW} + D_\mathrm{LW} + D_\mathrm{NR} + D_p\,, \tag{B.13}$$

with all terms defined in Table B.1. In addition to the KW energy tendencies due to dynamical and parametrized processes, the term D_p appears when virtual temperature T_v is considered (section B.10), and when hybrid-level data are interpolated to pressure levels (section B.11).

The KW energy tendencies affect both kinetic and potential energy of KWs. For a single mode, a momentum or heat source can not modify kinetic and available potential energy independently of each other, as explained in section B.12. If the meridional projection on Hough functions is not applied, the tendencies of kinetic energy and APE as well as energy conversion can be studied for each zonal wavenumber and vertical mode (Marques and Castanheira, 2012). However, this does not allow to analyze Kelvin waves separately from other meridional modes.

In the time average, the energy tendency due to a specific process, here momentum advection, is

$$\overline{A}_u = \overline{A}_{\overline{u}} + \overline{A}_{u'} = \int_V \overline{N}_u \overline{u}_\mathrm{K}\, dV + \overline{\int_V N'_u u'_\mathrm{K}\, dV}. \tag{B.14}$$

Here, the momentum tendency and zonal velocity are split into the time average and perturbations $N_u = \overline{N}_u + N'_u$ and $u_\mathrm{K} = \overline{u}_\mathrm{K} + u'_\mathrm{K}$ with $\overline{u'_\mathrm{K}} = \overline{N'_u} = 0$. The first summand in Eq. (B.14) is the energy tendency of the stationary wave due to momentum advection, and the second summand is the time-averaged energy tendency due to covarying momentum tendency fluctuations and velocity fluctuations.

Table B.1: Processes contributing to the Kelvin wave energy tendencies.

Dynamical KW energy tendencies due to	
total advection of u	$A_u = A_{u,\lambda} + A_{u,\varphi} + A_{u,p} = \int_V N_u u_K \, dV$
zonal advection of u	$A_{u,\lambda} = -\int_V \frac{u}{a\cos\varphi}\frac{\partial u}{\partial \lambda} u_K \, dV$
meridional advection of u	$A_{u,\varphi} = -\int_V \frac{v}{a\cos\varphi}\frac{\partial (u\cos\varphi)}{\partial \varphi} u_K \, dV$
vertical advection of u	$A_{u,p} = -\int_V \omega\frac{\partial u}{\partial p} u_K \, dV$
advection of v	$A_v = \int_V N_v v_K \, dV$
total advection of T'	$A_T = A_{T,\lambda} + A_{T,\varphi} + A_{T,p}$
zonal advection of T'	$A_{T,\lambda} = -\int_V \frac{R}{\gamma_0}\frac{u}{a\cos\varphi}\frac{\partial T}{\partial \lambda} T_K \, dV$
meridional advection of T'	$A_{T,\varphi} = -\int_V \frac{R}{\gamma_0}\frac{v}{a}\frac{\partial T}{\partial \varphi} T_K \, dV$
vertical advection of T'	$A_{T,p} = -\int_V \frac{R}{\gamma_0}\omega\frac{\partial T}{\partial p} T_K \, dV$
conversion term	$A_{co} = \int_V \frac{\omega R T'}{\gamma_0 c_p} T_K \, dV$
Diabatic KW energy tendencies involving parametrizations of	
zonal momentum dissipation	$D_u = \int_V S_u u_K \, dV$
meridional momentum dissipation	$D_v = \int_V S_v v_K \, dV$
short-wave radiation	$D_{SW} = \int_V \frac{R}{\gamma_0} Q_{SW} T_K \, dV$
long-wave radiation	$D_{LW} = \int_V \frac{R}{\gamma_0} Q_{LW} T_K \, dV$
non-radiative diabatic heating	$D_{NR} = \int_V \frac{R}{\gamma_0}(S_T - Q_{LW} - Q_{SW}) T_K \, dV$
Differences between Eq. (B.1) and ERA5 result in KW energy tendencies $D_p = D_{Tv} + D_E$ involving	
gradients of difference Φ_v between Φ and geopotential in ERA5 (section B.10)	$D_{Tv} = -\int_V \left(\frac{1}{a\cos\varphi}\frac{\partial \Phi_v}{\partial \lambda} u_K + \frac{1}{a}\frac{\partial \Phi_v}{\partial \varphi} v_K \right) dV$
geopotential gradients below the surface	D_E (Eq. B.38)

The energy sources of stationary KWs do not necessarily result from the processes for which the stationary KW response is large. According to Eq. (B.5), the stationary waves are shifted by 90° relative to the time-averaged tendencies $\overline{f}_r$. If the stationary KWs would result from only one process, their energy tendency due to this process would thus be zero, as the positive and negative contributions to the energy tendency at different longitudes balance out each other. However, the stationary KWs are determined by several processes, so that the phase shift between the KW and any individual tendency is not exactly 90°. This phase shift determines whether the dynamical and diabatic processes act as energy sources or sinks for the stationary KWs.

B.2.3 Numerical aspects

B.2.3.1 Spatial discretization

The tendencies of KW energy (Table B.1) are computed by multiplying the momentum (temperature) tendencies with the KW velocity (temperature) on the 3D grid and integrating over λ, φ and p. Omitting the integration over certain dimensions yields the contributions of individual latitudes, longitudes or pressure levels to the energy tendencies. For example, the contribution of each pressure level to the KW energy tendencies is obtained by integrating the product of the tendency and the KW variable over λ and φ. This localization is not straightforward when tendencies of normal modes are computed in spectral space from the expansion coefficients and interaction coefficients representing nonlinear interactions between triads of modes as, e.g., in Tanaka (1991) and Tanaka and Terasaki (2005).

To compute the nonlinear dynamical momentum and temperature tendencies, the 3D fields of u, v, T', their horizontal derivatives and Φ' are reconstructed as the sum of all modes r from the expansion coefficients W_r. The computation of zonal derivatives is straightforward since the zonal structure of the normal modes is given by Fourier modes. The meridional derivatives are reconstructed using precomputed meridional derivatives of Hough functions (Vasylkevych and Žagar, 2021). The pressure vertical velocity ω_r is obtained by integrating the divergence from the top of the atmosphere downward, assuming $\omega_r = 0$ at $p = 0$ (Žagar et al., 2023).

The temperature of the mode r is obtained from the hydrostatic equation:

$$T_r = -\frac{p}{R}\frac{\partial \Phi_r}{\partial p} = -\frac{gD_m}{R} p \frac{dG_m}{dp} Z_r \left(W_r e^{ik\lambda} + W_r^* e^{-ik\lambda} \right) . \tag{B.15}$$

Equation (B.15) includes the derivatives of vertical structure functions, defined at pressure levels $i \in \{1, \ldots, N\}$ as

$$\left(p \frac{dG_m}{dp} \right)_i = \frac{F_{i+1} - F_i}{p_{i+1} - p_{i-1}} \frac{p_{i+1} + p_i}{2} + \frac{F_i - F_{i-1}}{p_{i+1} - p_{i-1}} \frac{p_i + p_{i-1}}{2} , \tag{B.16a}$$

$$\left(p \frac{dG_m}{dp} \right)_1 = \frac{1}{2} \left(F_2 - F_1 \right) , \tag{B.16b}$$

$$\left(p \frac{dG_m}{dp} \right)_N = -F_{N-1} \frac{p_N + p_{N-1}}{4p_s - 2p_N - 2p_{N-1}} - F_N \frac{4p_s - p_N - p_{N-1}}{4p_s - 2p_N - 2p_{N-1}} , \tag{B.16c}$$

where $F_i = G_m(p_i) - G_m(p_s)$. The temperature computed using Eqs. (B.15) and (B.16) fulfills

$$\int_0^{p_s} T_r \, dp = \frac{1}{R} \int_0^{p_s} \left(\Phi_r - \Phi_r(p_s)\right) \, dp \,. \tag{B.17}$$

At p_s, the so obtained temperature perturbations are small (section B.9.1).

Once the 3D fields of the required variables have been calculated, the horizontal advection and metric terms are evaluated by multiplying the variables at each gridpoint. For vertical advection and the conversion term, which can be rewritten as vertical advection of geopotential perturbations

$$\frac{\omega R T'}{p c_p} = -\frac{1}{c_p} \omega \frac{\partial \Phi'}{\partial p} \,, \tag{B.18}$$

we use the energy-conserving vertical advection scheme of Simmons and Burridge (1981). The described computation of the nonlinear dynamical tendencies allows to decompose them into the interactions of various modes, which are the subject of future studies.

B.2.3.2 Temporal discretization

The 3D normal-mode decomposition is applied to instantaneous fields at discrete times t_i. The total KW energy tendency, averaged in the time interval $[t_i, t_{i+1}]$ with $t_{i+1} = t_i + \Delta t$, is obtained from the difference in KW energy:

$$\frac{\Delta I_\mathrm{K}}{\Delta t} = \frac{1}{\Delta t} \left(I_\mathrm{K}(t_i + \Delta t) - I_\mathrm{K}(t_i)\right) . \tag{B.19}$$

Equation (B.19) is used for comparison with the sum of all energy sources and sinks in Eq. (B.13), which are also analyzed as averages in the time interval. This average is, e.g., for A_u:

$$\int_V \frac{1}{4} \left(N_u(t_i) + N_u(t_i + \Delta t)\right) \left(u(t_i) + u(t_i + \Delta t)\right) \, dV. \tag{B.20}$$

B.2.4 Data

We study KWs in analysis and forecast data of the ERA5 reanalysis (Hersbach et al., 2020). Two datasets with different temporal resolutions are employed: An hourly dataset is applied to validate the method, analyze the stationary waves and to localize the origin of the energy tendencies. For evaluating variations over the course of one year, a 12-hourly dataset is used due to storage constraints. In addition, we use outgoing longwave radiation (OLR) data from NOAA PSL (2025b) to illustrate the variability of convection.

The hourly dataset consists of instantaneous values of u, v and T, and hourly mean values of tendencies due to parametrizations (ECMWF, 2016b), which are used as S_u, S_v, S_T, Q_SW and Q_LW. These data are taken from IFS model forecasts, which are part of the ERA5 reanalysis, for the two months of January and July 2018. The forecasts are initialized twice daily at 6 UTC and 18 UTC and have a lead time of up to 12 hours.

The 12-hourly dataset is studied for the period spanning 1st December 2017 to 30th November 2018. It contains the 12-hour average of the tendencies due to parametrizations, computed for each forecast. For the instantaneous variables, 6-hourly analyses are used.

All data are interpolated to a regular Gaussian grid with 400x800 points ($\approx 0.45°$ resolution) using the ECMWF interpolation libraries. The data are available on 137 hybrid model levels, and interpolated to 137 pressure levels as described in section B.11. For the normal-mode decomposition, we compute vertical structure functions on 137 pressure levels. We use 94 vertical structure functions, which have equivalent depths ≥ 0.71 m. Using a lower number of vertical structure functions than vertical grid points introduces truncation errors, which are largest in the lower troposphere. The Hough expansion coefficients are calculated for 120 meridional modes of each type, and 120 zonal wavenumbers, and a triangular truncation is employed ($k + n < 120$).

B.2.5 Validation of the Kelvin wave energy budget

The KW energy budget over a five-day period is shown in Fig. B.1 to illustrate the validity of the method. The KW energy varies with a diurnal period, along with day-to-day variability (Fig. B.1a), these variations are also evident in the KW energy tendency (Fig. B.1b).

The diurnal cycle of KW energy is predominantly caused by short-wave radiation (Fig. B.1b). The primary source of KW energy A_u arises from momentum advection, while $D_u + D_v$, A_T, and D_{LW} function as KW energy sinks. On most of the five days examined, non-radiative heating induces a KW energy sink, which varies on a shorter time scale than the other processes. The conversion term and the boundary term, which have been neglected in previous studies, are indeed small. The KW energy source D_{Tv} is positive and varies little. The KW energy tendency D_{E} arising from the extrapolation below the surface is mostly negative. Overall, Fig. B.1b shows that energy tendencies computed from Eq. (B.13) using the normal-mode framework represent well the ERA5 forecast data. In particular, there is a good agreement between the total energy tendencies computed with finite differences ($\Delta I_K / \Delta t$ line in Fig. B.1b) and the sum of the tendencies in Table B.1 ("All terms" line in Fig. B.1b).

The KW energy tendencies computed from the 12-hourly dataset differ slightly from the hourly data; Fig. B.1c compares the daily averages. Deviations result from the coarser discretization of Eq. (B.20). Furthermore, the KW energy tendencies in the 12-hourly dataset are influenced by the data assimilation, because they are computed using analyses resulting from several forecasts. In contrast, all quantities involved in the computation of energy tendencies in the hourly dataset are taken from the same forecast, in which the tendencies only result from dynamical and parametrized processes. Despite these differences, there is qualitative agreement between the hourly and 12-hourly datasets (Fig. B.1c).

B.3 Stationary Kelvin waves

In the following, we study which processes maintain the stationary KWs. We conduct this analysis for January 2018, during which stationary KWs contain 66% of the time-averaged KW energy. The upper-tropospheric winds of the stationary KWs are easterlies in the eastern hemisphere and westerlies over the Pacific (Fig. B.2a), while in July, the easterlies are located further west (Fig. B.12). When the stationary KWs are determined as in Eq. (B.5) from $\overline{f}_r$, which includes dynamical and diabatic processes, the qualitative structure matches the observed stationary KWs (Fig. B.2b). Deviations result from ten-

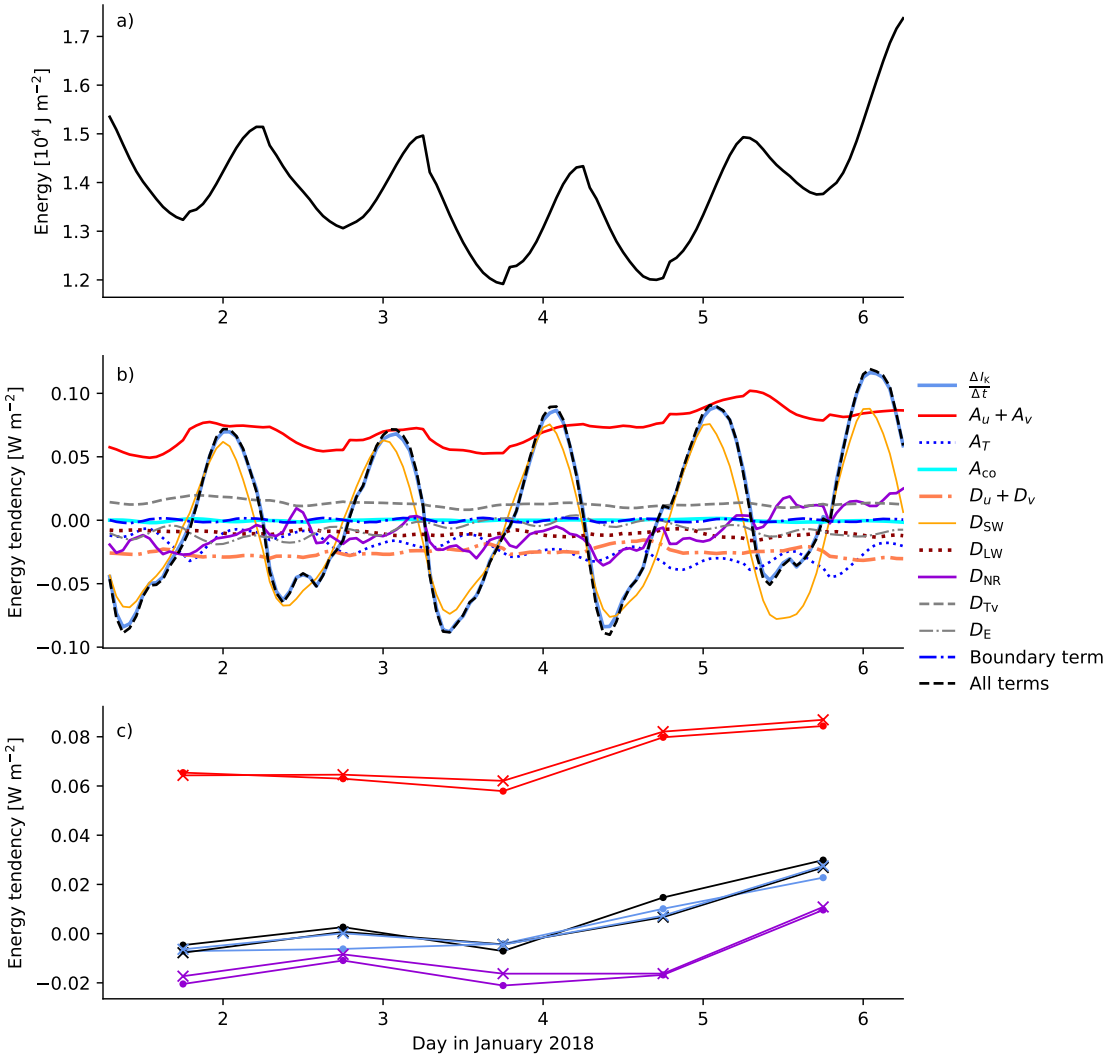

Figure B.1: a) Evolution of KW energy in ERA5 on 1-6 January 2018. b) Tendencies of Kelvin wave energy due to the various processes in Table B.1. The sum of all terms (Eq. B.13) is dashed, for $\Delta I_K/\Delta t$ see Eq. (B.19). c) Daily averages of selected Kelvin wave energy tendencies computed with hourly (x) and 12-hourly (dots) data.

dencies due to data assimilation, the trend over the month, and numerical inaccuracies. Because the KWs are multivariate, all contributions to the stationary KWs consist of both momentum and temperature (Fig. B.2), although they result from tendencies of a single variable.

As expected from the linear KW response to heating in idealized models, a non-negligible part of the stationary KWs results from non-radiative diabatic heating (Fig. B.2c). The stationary response contains easterlies over the Indian Ocean and westerlies over the Pacific around 300 hPa. This is in line with strong diabatic heating over the Maritime Continent. The circulation pattern derived by Gill (1980) on the infinite plane only contains the westerlies east of the heating, however, the KWs on the sphere in our definition have $k \geq 1$; they are only affected by heating anomalies relative to the zonal average. These anomalies contain negative temperature tendencies, which give rise to the easterly KW wind and the negative KW temperature below them.

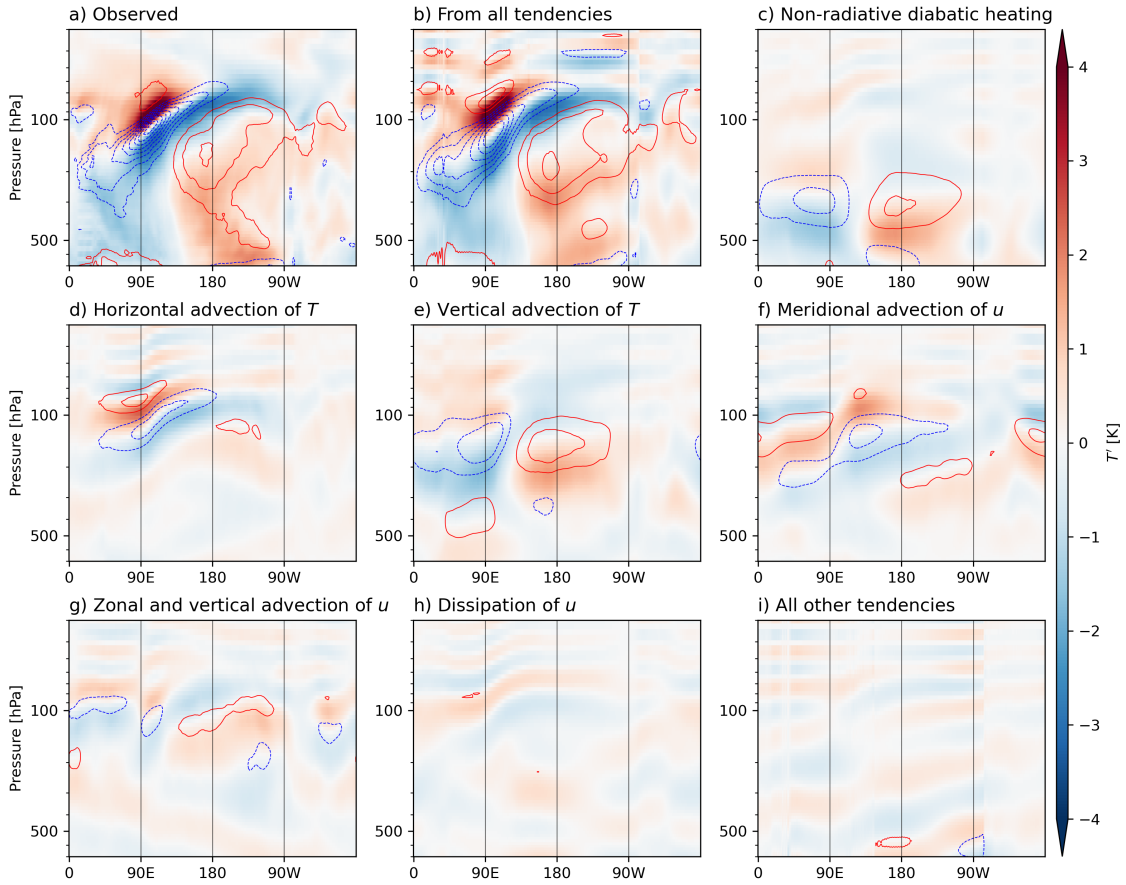

Figure B.2: Zonal wind (contours with a spacing of 2 m s^{-1}) and temperature (shading) of stationary Kelvin waves in January 2018 due to the process indicated in the sub-figure, computed according to Eq. (B.5). A truncation of the vertical modes is applied at $m = 40$.

While non-radiative diabatic heating sustains a KW circulation pattern whose wind directions match with those of the total stationary KWs, it is the advection of temperature from which the main part of the stationary KWs results (Fig. B.2d and B.2e). The winds resulting from vertical advection of temperature have the same direction as in the response to non-radiative diabatic heating, and they are located at higher levels (Fig. B.2e). This circulation results from positive temperature tendencies above the non-radiative diabatic heating, which appear due to upward advection of warm air. Note that the discussed temperature advection does not include cooling due to adiabatic expansion, which is contained in the conversion term and the linear terms in the thermodynamic equation (Eq. B.1c).

Advection of zonal momentum has a smaller contribution to the stationary KWs (Fig. B.2f and B.2g). Compared to the zonal and vertical advection, the meridional advection of zonal momentum has a greater influence. We will discuss later that this process induces easterly momentum tendencies over the Indian Ocean. Momentum tendencies due to parametrizations, including dissipation, induce an even smaller stationary KW response (Fig. B.2h). The stationary KWs resulting from the combination of all other tendencies have a similar magnitude (Fig. B.2i), with a large contribution of radiation.

In summary, temperature advection and diabatic temperature tendencies are the main contributors to the stationary KWs, while the responses to advection and dissipation of momentum are smaller. In July 2018, the relative contributions of these processes are similar (Fig. B.12). These results are consistent with the work of Stechmann and Ogrosky (2014), in that momentum advection and dissipation have a secondary influence on stationary KWs. In their model, the heat sources are derived from OLR; therefore, diabatic heating and temperature advection at different levels are not considered separately.

Most of the energy of the stationary KWs is contained in the zonal wavenumber $k = 1$. This is the case for the sum of all vertical modes, as well as for the most energetic vertical mode in January 2018, which is $m = 9$ (Fig. B.3). The power spectrum of the time-averaged non-radiative diabatic heating, projected on the KW with $m = 9$ as in Eq. (B.6), is flatter. There, similar power is found in $k = 1$ and $k = 2$ and only slightly less power in $k = 4$, presumably because the spatial distribution of the non-radiative diabatic heating is determined by the locations of the continents. The energy spectrum of the stationary KW has a steeper decay because the KW eigenfrequency, which increases with k, is in the denominator of Eq. (B.5). The energy spectrum of the part of the stationary KW determined from non-radiative diabatic heating resembles that of the total stationary KW (Fig. B.3), while deviations on synoptic and sub-synoptic scales are not further investigated here. A similar preference for low k is found for temperature advection (Fig. B.13).

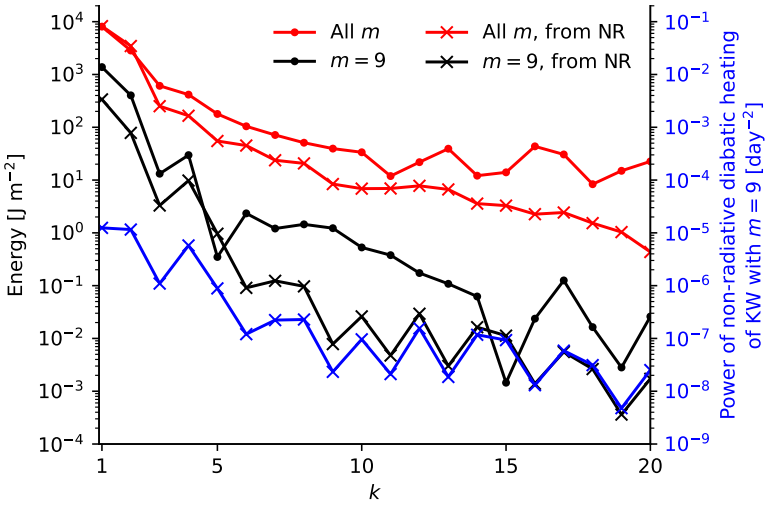

Figure B.3: Energy spectra of Kelvin waves as a function of zonal wavenumber for the vertical mode $m = 9$ and sum over all m, as determined from the normal-mode expansion of the data (dots), or from non-radiative diabatic heating (x). For comparison, the power spectrum of the KW tendency due to non-radiative diabatic heating is shown for $m = 9$.

B.4 Energy budget of stationary Kelvin waves

The stationary KWs described above have constant energy and therefore their energy tendency is zero. Nevertheless, different processes act as energy sources and sinks, which balance each other out. Figure B.4 shows the energy tendencies of the stationary KWs in

January 2018 due to different processes as thick bars. Their sum is the residual of the energy budget, which is smaller than most other terms (thick black bar in Fig. B.4). To put the energy tendencies into perspective, they are compared with the energy of the stationary KWs divided by a period of one day, i.e., 100% per day indicates that the KW energy would double in one day if other processes were absent. However, the absolute energy tendencies of the stationary KWs are smaller than 30 % per day.

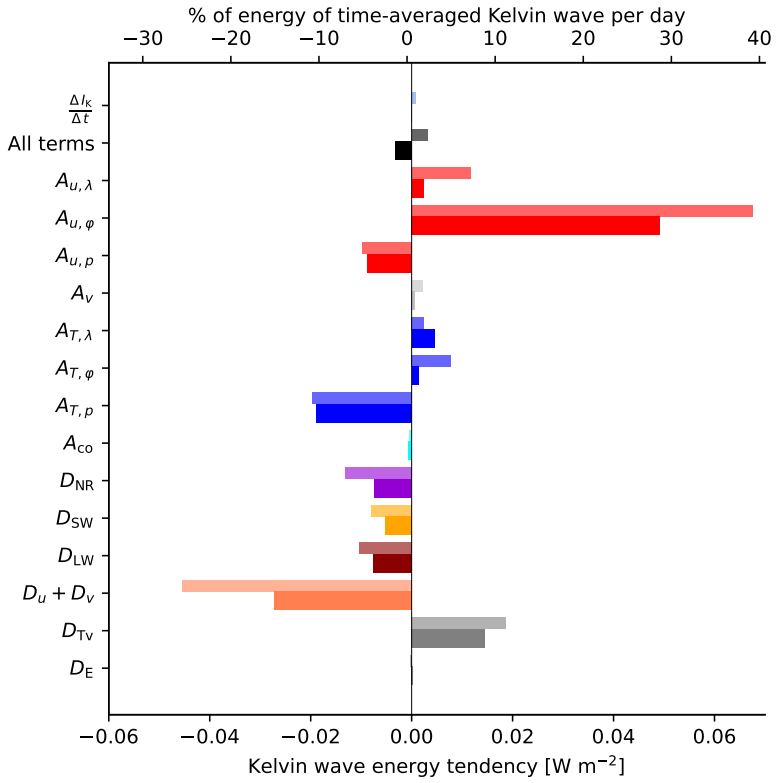

Figure B.4: Kelvin wave energy tendencies due to different processes as in Table B.1, for January 2018. Thick bars show energy tendencies for stationary Kelvin waves (first term in Eq. B.14), thin bars show the time-averaged energy tendencies of all Kelvin waves.

The largest energy source of the stationary KWs is due to meridional advection of zonal momentum, while their largest energy sink results from the momentum tendencies due to parametrizations (Fig. B.4). Temperature tendencies associated with vertical advection and diabatic processes induce smaller energy sinks of the stationary KWs. The processes associated with large energy tendencies of the stationary KWs (Fig. B.4) are thus not the same processes that have a strong stationary KW response (Fig. B.2), as explained in section B.2.2. In the following, the energy sources and sinks resulting from different processes are discussed. By omitting the integration over certain dimensions in their computation (Table B.1, section B.2.3.1), we obtain the contributions of individual longitudes or pressure levels to the integrated quantities, shown for selected terms in Fig. B.5.

Advection of zonal momentum is an energy source for the stationary KWs, while advection of meridional momentum results in negligible KW energy tendencies (Fig. B.4), because the meridional velocity of KWs is small. The contributions of each longitude and level to $\overline{A_{\overline{u}}}$ are shown in Fig. B.5a. The positive contributions to the KW energy source

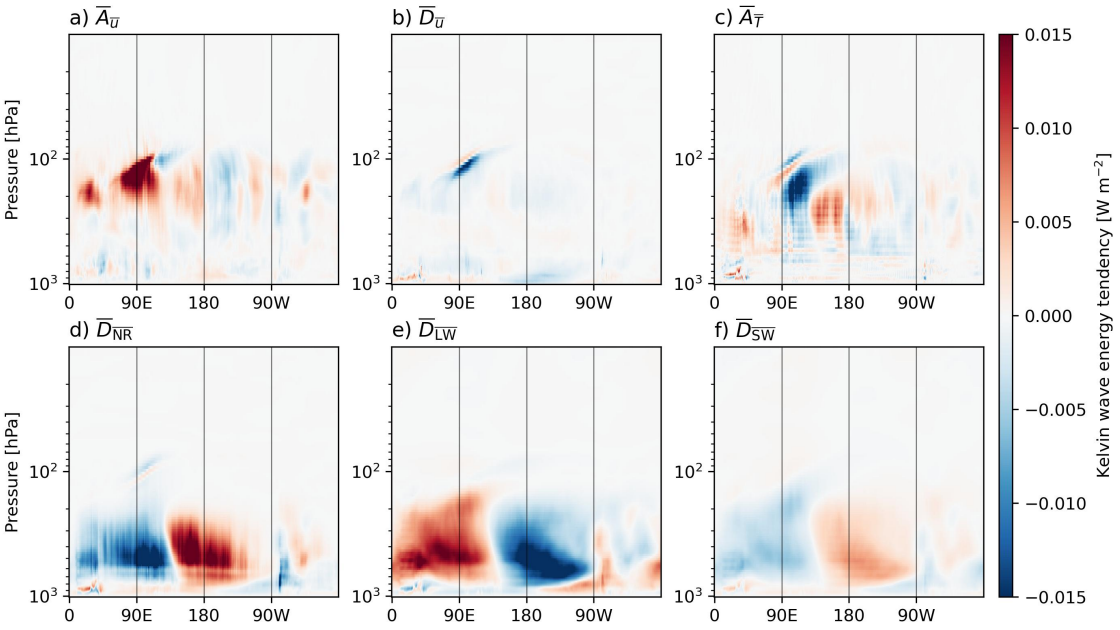

Figure B.5: Integrand of the energy tendencies of stationary Kelvin waves, e.g. $\overline{N}_u \overline{u}_\mathrm{K}$, for January 2018 as a function of longitude and pressure-level. To display the quantities in W m^{-2}, they are multiplied with $\Delta p/g$, where Δp is the pressure difference between two levels.

around 90° E imply that the KW easterlies in the eastern hemisphere are strengthened through momentum advection. Easterly momentum tendencies result from poleward-directed meridional wind, e.g., associated with upper-tropospheric divergence, superimposed on the latitudinal shear between the equatorial easterlies and the subtropical jet (Fig. B.6a). In the western hemisphere, $\overline{A}_{\overline{u}}$ is weaker and has alternating signs (Fig. B.5a). In July, both the KW easterlies and the energy source are located further west, around 60° E (Figs. B.12 and B.14).

The latitudinal position of the KW energy tendency due to meridional advection of u varies between January and July (Fig. B.6b). In January, shear in zonal wind is observed in the northern hemisphere subtropics (Fig. B.6a). The Hadley cell center is south of the equator, associated with southerly wind across the northern-hemispheric tropics. Therefore, the poleward advection of zonal momentum between 5° N and 25° N induces a KW energy source (Fig. B.6b). In July, the shear in zonal wind is stronger in the southern hemisphere, and therefore the KW energy source due to advection by the northerly wind is located between 0° and 30° S.

Momentum tendencies due to parametrizations result in an energy sink for stationary KWs, which is mainly located around 100° E (Fig. B.5b) in the upper troposphere. There, the easterlies of the stationary KW are strong, and the wind shear is strong as well (Fig. B.2a). The parametrized turbulent momentum fluxes (ECMWF, 2016b) thus reduce the strength of these easterlies, inducing a KW energy sink.

Advection of temperature also results in an energy sink for stationary KWs. The KW energy sink due to vertical advection of temperature has a greater effect than the small KW energy sources due to zonal and meridional advection (Fig. B.4). In the time average, positive $\overline{A}_{\overline{T}}$ is located around 300 hPa and 130°-180° E (Fig. B.5c). There, positive $\overline{T}_\mathrm{K}$ (Fig. B.2a) are enhanced by advection of warm air. The warm air advection

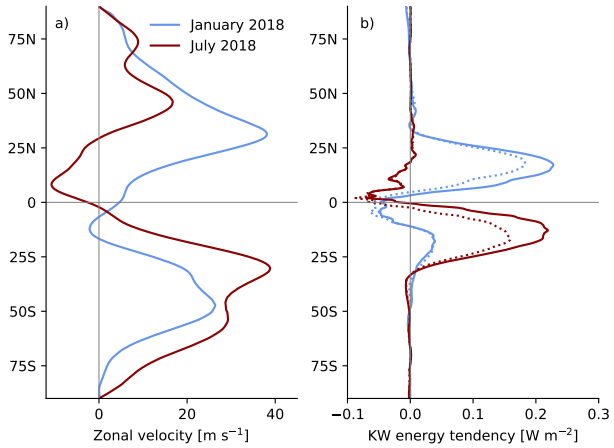

Figure B.6: a) Zonal mean zonal wind at 150 hPa, time-averaged over January and July 2018. b) Latitudinal distribution of Kelvin wave energy tendency $A_{u,\varphi}$ with time average (solid line), and energy tendency of stationary Kelvin waves (dashed line).

continues towards the west, into regions of negative $\overline{T}_\mathrm{K}$, and results in negative KW energy tendencies around 120° E and 200 hPa (Fig. B.5c). The narrow region of positive KW energy tendencies above can also be attributed to warm air advection, coinciding with positive $\overline{T}_\mathrm{K}$. The negative $\overline{A}_{\overline{T}}$ around 100 hPa and 100° E is due to the advection of colder surrounding air into the region with positive $\overline{T}_\mathrm{K}$. The conversion term also induces temperature tendencies, which however result in small KW energy tendencies (Fig. B.4).

Non-radiative diabatic heating acts as an energy sink for stationary KWs, reducing the magnitude of negative $\overline{T}_\mathrm{K}$ in the eastern hemisphere (Fig. B.5d and B.2a). This sink is partly compensated by the amplification of positive $\overline{T}_\mathrm{K}$ by the heating east of about 135° E. Below 600 hPa, the magnitude of $\overline{D}_{\overline{\mathrm{NR}}}$ is smaller, except for longitudes with large orography (Fig. B.5d). This sharp decrease might result from the truncation errors in the vertical expansion (section B.2.4). These errors affect both the KW temperature and the temperature tendencies due to parametrizations, because the latter are expanded in terms of vertical modes as part of the interpolation (section B.11).

The long-wave radiation mainly induces negative temperature tendencies, as the atmosphere emits heat into space. On average, the positive $\overline{T}_\mathrm{K}$ in the lower troposphere over the Pacific and at the tropopause over the Maritime Continent are reduced by the long-wave cooling (Fig. B.5e), which results in a KW energy sink (Fig. B.4). The heating due to short-wave radiation enhances the positive $\overline{T}_\mathrm{K}$ over the Pacific and leads to negative KW energy tendencies in regions of negative $\overline{T}_\mathrm{K}$ (Fig. B.5f).

The differences between temperature and virtual temperature result in an energy source for stationary KWs (Fig. B.4). If the geopotential used for the normal-mode expansion would be computed from virtual temperature, this term would not appear. However, in this case, the decomposition of the temperature tendencies would require a normal-mode framework incorporating moisture, which is currently not available.

Due to the extrapolation, further KW energy tendencies appear, which are small in January 2018 (Fig. B.4). In July and for the entire year, they differ from zero more substantially and have a similar magnitude as the KW energy tendencies due to virtual temperature (Figs. B.15 and B.16). The energy tendencies due to the extrapolation do

not have physical meaning, and they would not appear in terrain-following coordinates, where, however, variations in surface pressure would need to be considered.

B.5 Energy budget of all Kelvin waves and temporal variability

In the following, the energy tendencies of the combination of stationary and transient KWs are studied. For most processes, the time averages of these energy tendencies have larger magnitudes than the energy tendencies of the stationary KWs (Figs. B.4, B.15 and B.16), because the energy tendencies due to covariability are includes as well (Eq. B.14). Temporal variability of the KW energy tendencies is evident in the 12-month time-series shown in Fig. B.7. The variability of $\Delta I_K/\Delta t$ aligns with the sum of all source terms, as indicated by a Pearson correlation coefficient of 0.90 between the two time series.

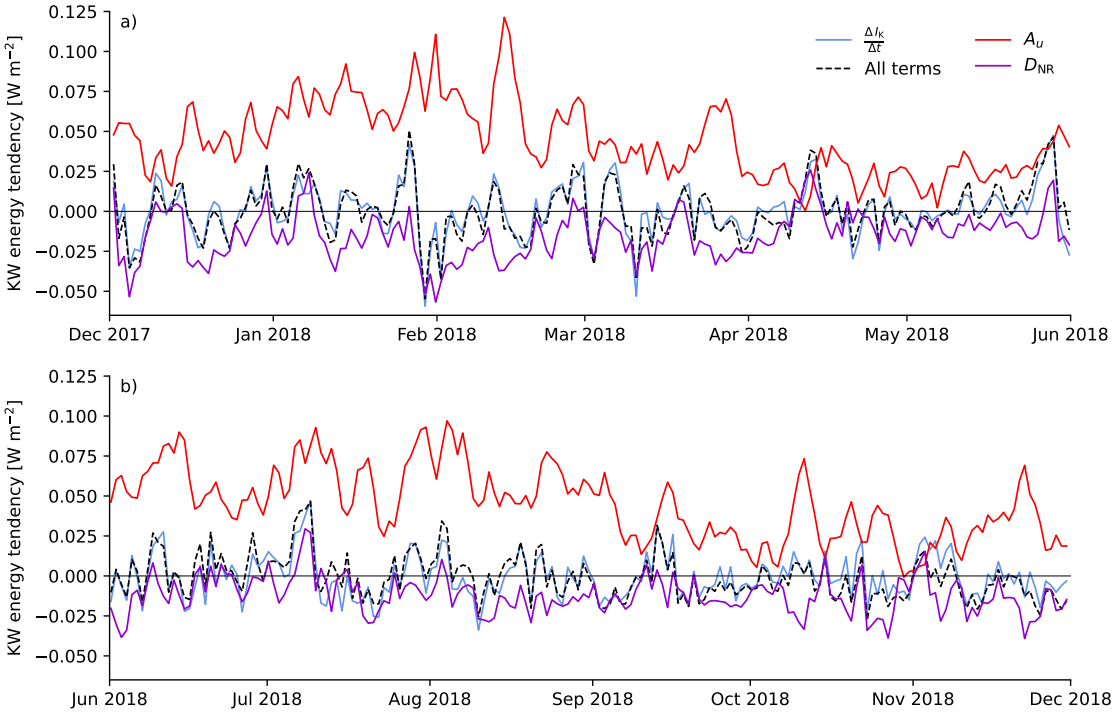

Figure B.7: Daily averages of Kelvin wave energy tendencies from 12-hourly data. a) 1 December 2017- 31 May 2018, b) 1 June 2018-30 November 2018. $\Delta I_K/\Delta t$: Eq. (B.19), All terms: Eq. (B.13).

The temporal variability of D_{NR} matches well with the variability of $\Delta I_K/\Delta t$ (Fig. B.7); their correlation coefficient is 0.61. The temporal variability of D_{NR} is related to both the temporal variability of T_K and that of the temperature tendencies. The temporal variability of T_K in January 2018 is shown in Fig. B.8a, where the stationary waves with cold T_K in the eastern hemisphere and warm T_K over the Pacific are still evident. The KW energy tendencies shows fluctuations in the KW energy source over the Pacific and the KW energy sink over the Indian Ocean (Fig. B.8b), which both show some correlation with convection variability, evident in OLR (Fig. B.8c). For instance, the peak in D_{NR} around 160° E between January 24 and 28 is due to high T_K coinciding with strong convection. On the other hand, the positive values of D_{NR} in the beginning of January 2018 (Fig. B.7a) are not associated with particularly strong convection; rather, they are

linked with weak negative D_{NR} due to small negative T_K at 60°-120° E. The KW energy sink due to non-radiative diabatic heating is mainly located in the mid-troposphere, while in the upper troposphere, positive $\overline{D}_{NR}$ is found (Fig. B.9a).

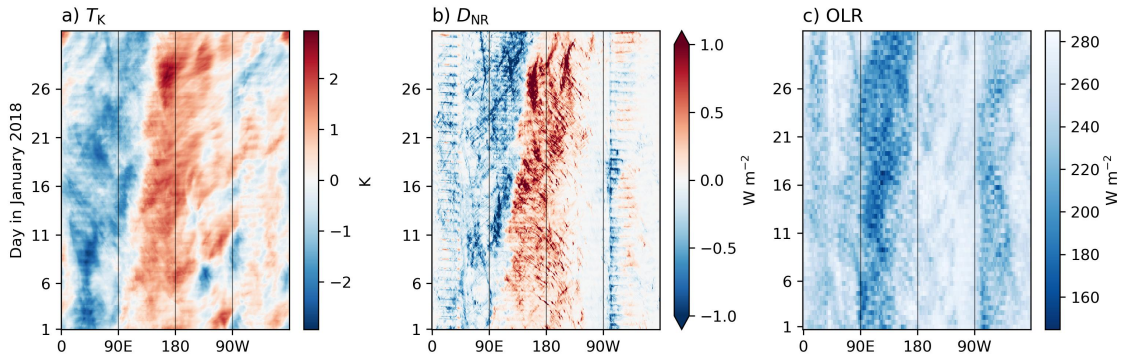

Figure B.8: Hovmoller diagrams of a) Kelvin wave temperature at 300 hPa, averaged over 15° S to 15° N, b) Longitudinal distribution of D_{NR}, c) outgoing long-wave radiation, averaged over 15° S to 15° N.

Advection of zonal momentum acts as an energy source throughout the year (Fig. B.7). This source is larger in the boreal winter and summer than in spring and fall. Like D_{NR}, A_u also varies on a time scale of several days, but it does not seem to co-vary with $\Delta I_K / \Delta t$, with the correlation coefficient being only 0.10. This correlation coefficient is relatively small, because A_u is balanced out by other processes, one of which is D_u (Fig. B.17). Because both A_u and D_u depend on u_K, the absolute values of these energy tendencies are connected. Therefore, the energy source A_u and energy sink D_u are anti-correlated with a correlation coefficient of -0.67.

As can be seen in Fig. B.5a for the stationary KWs, D_u is located in the upper and lower troposphere (Fig. B.9b), while A_u is mainly located in the upper troposphere (Fig. B.9c). There, the KW winds exhibit temporal variability superimposed on easterlies west of about 130° E and westerlies over the Pacific (Fig. B.10a). The main contribution to $A_{u,\varphi}$ is found around 90° E on January 15 and 28 (Fig. B.10b), coinciding with southerly wind averaged over 10°-20° N (Fig. B.10c). Weaker positive $A_{u,\varphi}$ is located around 160° E and 160° W in the second half of January (Fig. B.10b). At these longitudes, the westerly KW wind is strengthened by the advection of zonal momentum towards the equator by northerly winds (Fig. B.10c). In the western hemisphere, $A_{u,\varphi}$ is weak and has alternating signs at different longitudes. This is associated with larger variations in relatively weaker meridional velocities (Fig. B.10c), and the weaker shear of zonal wind (e.g. Simmons, 2022).

The vertical profile of $\overline{A}_u$ is similar to the remote eddy source determined by Tulich and Kiladis (2021) at each level from the co-spectra of eddy momentum flux forcing and zonal velocities, both projected on the Kelvin mode. The agreement of the vertical profiles is remarkable, despite several differences in the methodologies. While Tulich and Kiladis (2021) focus on eddy interactions poleward of 15°, A_u in this study contains the full advection terms, integrated over the 3D atmosphere. In addition, the majority of $\overline{A}_u$ is associated with the stationary waves (Fig. B.4). Furthermore, the vertical profile of $\overline{D}_{NR}$ (Fig. B.9a) agrees with the WFD-KW energy sources resulting from tropical heating simulated by Tulich and Kiladis (2021), featuring positive values in the upper troposphere and negative values below 400 hPa.

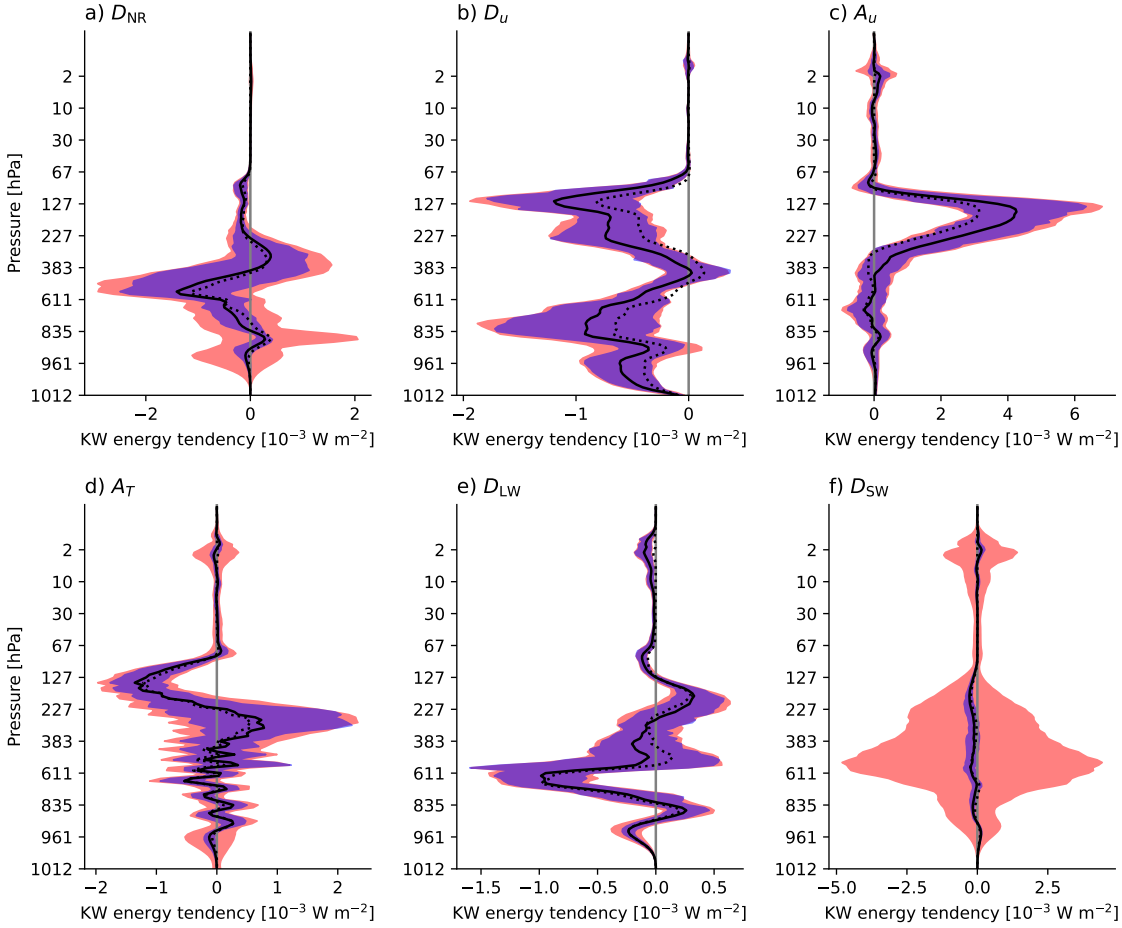

Figure B.9: Vertical distribution of Kelvin wave energy sources and sinks for January 2018. Solid line: Time-average. Dashed line: Energy tendency of stationary Kelvin wave. The shading shows the spread between the 10th and 90th percentile in time, for hourly (red) data and daily mean (blue) data. To display the quantities in W m^{-2}, they are multiplied with $\Delta p/g$, where Δp is the pressure difference between two levels.

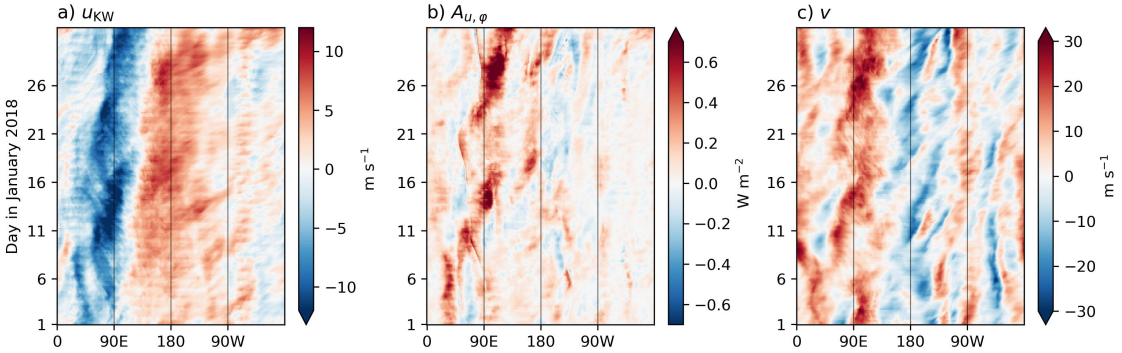

Figure B.10: Hovmoller diagrams of a) Kelvin wave zonal velocity at 150 hPa, averaged over 15° S to 15° N, b) Longitudinal distribution of $A_{u,\varphi}$, c) Meridional velocity at 150 hPa, averaged over 10°-20° N.

For the KW energy tendencies resulting from temperature tendencies, the time average is similar to the tendencies of the stationary waves. For A_T, the vertical profile features

strong vertical variations in the lower and mid-troposphere (Fig. B.9d). These might be a result of inaccuracies in computing temperature and its vertical derivatives due to the vertical truncation. The negative temperature tendencies due to long-wave radiation induce a KW energy sink at most levels, except for the slightly positive KW energy tendencies in the upper troposphere resulting from strengthening of the negative T_K (Fig. B.9e). While the temporal variability of the hourly and daily data is similar for most KW energy tendencies, a strong diurnal cycle is found for short-wave radiation (Fig. B.9f), which was already evident in Fig. B.1b. The KW energy tendencies resulting from short-wave radiation are partly located in the stratosphere (Fig. B.9f) where the short-wave radiation is absorbed by ozone. In the troposphere, the air density is higher so that the temperature increase due to absorbed short-wave radiation results in larger KW energy tendencies than in the stratosphere.

B.6 Discussion

Our results are consistent with the findings of Tulich and Kiladis (2021), Cheng et al. (2022) and Chien et al. (2025) in demonstrating that KWs obtain energy from nonlinear dynamical sources in the subtropical upper troposphere. We found that the meridional advection of momentum has a stronger effect than zonal and vertical advection. The ability of meridional winds to force KWs through vorticity advection has been demonstrated in idealized simulations (Barpanda et al., 2023). However, their study did not analyze which processes act as sources of KW energy.

The momentum tendencies that induce the KW energy source are located over the Indian Ocean (Fig. B.5a), where Chien et al. (2025) found a relatively small eddy kinetic energy growth rate compared to other regions. Furthermore, the sink of WFD-KW APE in the first baroclinic mode identified by Chien et al. (2025) is outweighed by the source of WFD-KW APE in the second baroclinic mode. For the sum of all vertical modes, however, we found that non-radiative diabatic heating acts as a KW energy sink. This difference could arise because Chien et al. (2025) consider only two vertical modes in tropospheric data, while we use multiple vertical modes that extend up to 1 Pa, along with further differences in the KW identification methods. Additionally, Chien et al. (2025) obtained the diabatic heating rate as the residual of the temperature equation, which is presumably less accurate than using the temperature tendencies due to parametrizations, as in our study.

The main KW energy sink results from momentum tendencies due to parametrizations, which have strong impacts in regions of vertical shear. The representation of the shear zones in the tropics is subject of significant uncertainties (Houchi et al., 2010). This becomes evident when assimilating the wind profile observations by the Aeolus satellite, and thereby enhancing the vertical shear in zonal mean wind and KWs (Žagar et al., 2025). As discussed in their paper, model biases that impact waves arise from the parametrized vertical diffusion, which is too strong in the lower stratosphere (Polichtchouk et al., 2021).

Part of the KW energy source is associated with covariability between KWs and momentum sources. While this is a prerequisite for resonance as described by, e.g., Hoskins and Yang (2000), Tulich and Kiladis (2021), and Cheng et al. (2022) and Holube et al. (2024), the wavenumbers and frequencies for which resonance occurs and the resulting KW energy tendencies have yet to be quantified.

Since our study covers a relatively short time period, the results might be influenced by the chosen time frame, although we suppose that the described physical mechanisms are independent of the time period. The results for January and July 2018 are not representative for the climatological summer and winter conditions. For instance, the KW zonal winds have similar magnitudes in January and July 2018 (Figs. B.2a and B.12), while in the climatology described by Žagar et al. (2022), the KW winds are stronger in boreal summer. The enhanced KWs in January 2018 might be related to the strong MJO event in this time-period (Barrett, 2019). Stronger KWs are found during the active phase of the MJO (Žagar and Franzke, 2015; Castanheira and Marques, 2021), and a climatological analysis of the energy tendencies of normal modes associated with the MJO, extending the work of Castanheira and Marques (2021), is subject of further studies. Additionally, the stationary KWs might depend on the phase of the El Niño Southern Oscillation. In the beginning of 2018, weak La Niña conditions are found, which change to weak El Niño during the course of the year (NOAA PSL, 2025a).

B.7 Conclusions and Outlook

We have analyzed how KWs are influenced by dynamical and diabatic processes by determining their contributions to the stationary KWs and to the KW energy tendencies following Tanaka (1985). Novel aspects of the method are the use of temperature and momentum tendencies due to parametrizations from ERA5 forecasts, while momentum and temperature advection were computed from the normal-mode expansion coefficients. We localized the energy tendencies due to advection and parametrized processes in physical space, and distinguished the effects of zonal, meridional and vertical momentum and temperature advection.

We have focused mostly on the stationary KWs because they account for more than 65% of the total KW energy. Stationary KWs represent part of the Walker Circulation. They are the response to heating over the Maritime Continent due to non-radiative diabatic processes, e.g. latent heat release, and due to temperature advection. The stationary KW circulation pattern is dominated by waves with low zonal wavenumbers, hence low eigenfrequencies. It should be noted that there is necessarily a phase shift of 90° between the tendencies shaping the stationary KW response and the stationary KW itself (cf. Eq. B.5). Because they are phase-shifted, non-radiative diabatic heating and temperature advection do not constitute KW energy sources. In fact, non-radiative heating is an energy sink in the time average because the release of latent heat balances out the negative T_K in the mid-troposphere in the eastern hemisphere. This is only partly compensated by the strengthening of positive T_K over the Pacific.

The main source of KW energy arises from meridional advection of zonal momentum in the upper troposphere in the eastern hemisphere, where the KW easterlies are strengthened. In boreal winter (summer), the meridional advection takes place in the northern hemisphere (southern hemisphere) subtropics. The largest KW energy sink results from momentum dissipation at low levels and shear zones in the upper troposphere.

With the KW energy budget, the temporal variability of the KW energy tendencies has been attributed to individual processes. While the diurnal cycle of KW energy is associated with short-wave radiation, the temporal variability of KW energy on a time scale of several days is governed by non-radiative diabatic heating. The KW energy

source due to advection of zonal momentum varies on a similar time scale, but this variability is partly counterbalanced by parametrized processes.

The meridional winds associated with the dynamical KW energy source may be induced by tropical processes or dry subtropical dynamics. Investigating these different mechanisms in future studies would contribute to the understanding of tropical-extratropical interactions. Additionally, the presented numerical framework that evaluates the nonlinear dynamical momentum and temperature tendencies from the expansion coefficients allows to study energy transfers between normal modes due to wave-wave and wave-mean flow interactions. Tanaka and Terasaki (2005) evaluated some of these interactions for the Arctic Oscillation using a spectral method. The pseudospectral numerical framework presented here enables a more efficient quantification. Recently, Mahó et al. (2024a), Mahó et al. (2024b) and Holube et al. (2024) identified the excitation of equatorial waves by wave-mean flow interactions with the help of shallow-water model simulations in the normal-mode framework. Quantifying wave-wave and wave-mean flow interactions would allow to clarify the role of these mechanisms in atmospheric data, which is subject of follow-on work.

B.8 Appendix A 3D normal-modes

Here, the 3D normal-modes in pressure coordinates are described following Tanaka (1985). A separation of variables is applied to Eqs. (B.1a), (B.1b) and (B.2), linearized around the state of rest with reference temperature T_0. This results in the vertical structure equation

$$\frac{d}{dp}\left(\frac{p^2 g}{R\gamma_0}\frac{dG}{dp}\right) + \frac{1}{D}G = 0 \tag{B.21}$$

with boundary conditions

$$p\frac{dG}{dp} + \frac{\gamma_0}{T_0}G = 0 \quad \text{at} \quad p = p_s\,, \quad \text{and} \quad \frac{p}{\gamma_0}\frac{dG}{dp} \to 0 \quad \text{as} \quad p \to 0 \tag{B.22}$$

(Staniforth et al., 1985), where the reference pressure $p_s = 1013.25$ hPa is the lower boundary of the pressure coordinate system. The solutions of Eq. (B.21) are the vertical structure functions G_m, which are orthonormal:

$$\frac{1}{p_s}\int_0^{p_s} G_m G_{m'} dp = \delta_{mm'}\,, \tag{B.23}$$

where $\delta_{mm'}$ is the Kronecker delta.

We compute vertical structure functions with finite differences as described by Kasahara and Puri (1981). To avoid using weights for the vertical integration, Kasahara and Puri (1981) introduced modified vertical structure functions Φ_m (their Eq. 4.10), a strategy that we do not follow here. Thus, G_m is identical to Ψ_m in the notation of Kasahara and Puri (1981), and the vertical integration of a function $F(p)$ is discretized as

$$\frac{1}{p_s}\int_0^{p_s} F G_m\, dp \approx \sum_i F(p_i) G_m(p_i)\frac{\Delta p_i}{p_s}\,, \tag{B.24}$$

where $\frac{\Delta p_i}{p_s}$ are the vertical integration weights.

Examples for vertical structure functions are shown in Fig. B.11. They were obtained with the static stability profile following from the reference temperature (Jablonowski and Williamson, 2006)

$$T_0 = T_{00}\left(\frac{p}{p_s}\right)^{\frac{R\Gamma_d}{g}} \quad \text{for } 1 \leq \frac{p}{p_s} \leq \eta_t\,, \tag{B.25a}$$

$$T_0 = T_{00}\left(\frac{p}{p_s}\right)^{\frac{R\Gamma_d}{g}} + \Delta T\left(\eta_t - \frac{p}{p_s}\right)^5 \quad \text{for } \eta_t > \frac{p}{p_s}\,, \tag{B.25b}$$

with lapse rate $\Gamma_d = 0.005\,\mathrm{K\,m^{-1}}$, temperature at the reference pressure $T_{00} = 288$ K, tropopause level $\eta_t = 0.2$ and empirical temperature difference $\Delta T = 4.8 \times 10^5$ K.

The expansion of the 3D linearized primitive equations in terms of G_m yields the set of linear rotating shallow-water equations

$$\frac{\partial}{\partial \tilde{t}}\,\mathbf{X}_m + \mathbf{L}_m\mathbf{X}_m = 0. \tag{B.26}$$

The components of $\mathbf{X}_m$ are nondimensional velocity and geopotential height perturbations associated with the vertical mode m:

$$\mathbf{X}_m = \begin{pmatrix} \tilde{u}_m \\ \tilde{v}_m \\ \tilde{h}_m \end{pmatrix} = \frac{1}{p_s}\int_0^{p_s} \begin{pmatrix} u\,\sqrt{gD_m}^{-1} \\ v\,\sqrt{gD_m}^{-1} \\ \Phi'(gD_m)^{-1} \end{pmatrix} G_m\,dp\,. \tag{B.27}$$

The linear operator

$$\mathbf{L}_m = \begin{pmatrix} 0 & -\sin\varphi & \frac{\gamma_m}{\cos\varphi}\frac{\partial}{\partial\lambda} \\ \sin\varphi & 0 & \gamma_m\frac{\partial}{\partial\varphi} \\ \frac{\gamma_m}{\cos\varphi}\frac{\partial}{\partial\lambda} & \frac{\gamma_m}{\cos\varphi}\frac{\partial}{\partial\varphi}(\cos\varphi()) & 0 \end{pmatrix} \tag{B.28}$$

contains the nondimensional parameter $\gamma_m = \frac{\sqrt{gD_m}}{2a\Omega}$. The equivalent depth D_m is the mean depth in the shallow-water equations, and the nondimensional time is $\tilde{t} = 2\Omega t$.

The 3D normal modes are $G_m(p)\mathbf{H}_r(\lambda,\varphi)$, where the Hough harmonics $\mathbf{H}_r$ are eigenfunctions of $\mathbf{L}_m$, i.e. they fulfill $\mathbf{L}\mathbf{H}_r = i\nu_r\mathbf{H}_r$ with eigenfrequency ν_r. The multi-index $r = (k, n, m)$ denotes a combination of zonal wavenumber k, meridional mode n and vertical mode m. The meridional structure of $\mathbf{H}_r(\lambda,\varphi) = \mathbf{\Theta}_r(\varphi)e^{ik\lambda}$ is given by the Hough functions $\mathbf{\Theta}_r = (U_r, -iV_r, Z_r)$, which are orthonormal:

$$\int_{-\pi/2}^{\pi/2} \mathbf{\Theta}_r \cdot \mathbf{\Theta}^*_{r'} \cos\varphi\,d\varphi = \delta_{rr'}\,, \tag{B.29}$$

where $*$ denotes the complex conjugate. For $k = 0$, the set of Hough harmonics is complemented by the K-modes (Kasahara, 1978). There are three types of Hough functions: Eastward-propagating inertia-gravity (IG) modes, westward-propagating IG modes and Rossby modes, and for each type, there is a range of meridional modes n. The Kelvin mode is the lowest meridional mode $(n = 0)$ of the eastward-propagating IG modes. We compute Hough functions and their eigenfrequencies with the algorithm of Swarztrauber and Kasahara (1985).

The horizontal velocity and geopotential height perturbations are expanded in terms of normal modes as

$$\begin{pmatrix} u \\ v \\ \Phi' \end{pmatrix} = \sum_{m=1}^{M} \sum_{n=0}^{R} \sum_{k=-K}^{K} \begin{pmatrix} \sqrt{gD_m} \\ \sqrt{gD_m} \\ gD_m \end{pmatrix} W_r \mathbf{H}_r G_m \,, \tag{B.30}$$

where K, M and R denote the number of positive zonal wavenumbers, vertical modes and meridional modes retained in the expansion. The expansion coefficients W_r are

$$W_r = \frac{1}{2\pi} \int_0^{2\pi} \int_{-\pi/2}^{\pi/2} \mathbf{X}_m \cdot \mathbf{\Theta}_r^* \, e^{-ik\lambda} \cos\varphi \, d\varphi \, d\lambda \,. \tag{B.31}$$

Since u, v and Φ' are real, the expansion coefficients for negative k are the complex conjugates of those for positive k. Therefore, the waves with $\pm k$ are combined in the following, making k non-negative.

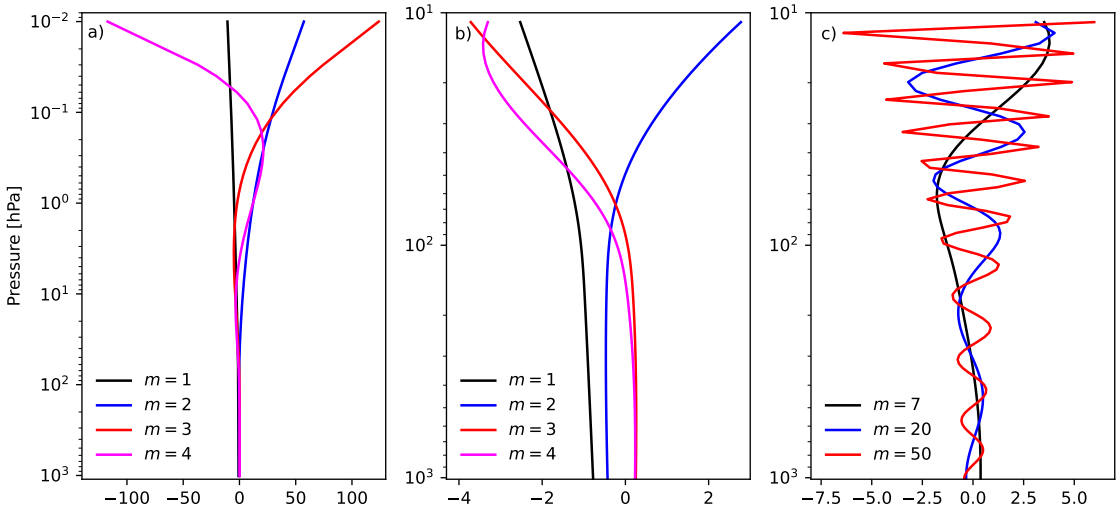

Figure B.11: Vertical structure functions for the static stability associated with the temperature profile in Eq. (B.25), a) and b) show the same vertical structure functions for different scaling of vertical axes.

B.9 Appendix B Temperature and energy tendencies at the reference pressure

The boundary conditions (Eq. B.22) lead to small temperature perturbations at the reference pressure, as outlined in section B.9.1. In section B.9.2, we discuss the boundary terms that appear in the energy tendencies resulting from temperature tendencies.

B.9.1 Temperature of normal modes

At the lowest pressure level, the temperature resulting from the normal-mode expansion deviates considerably from the observed temperature. This is due to the lower boundary condition (Eq. B.22), according to which the geopotential perturbations $\Phi' = \sum_r \Phi_r$ fulfill

$$p \frac{\partial \Phi'}{\partial p} + \frac{\gamma_0}{T_0} \Phi' = 0 \quad \text{at} \quad p = p_s \,. \tag{B.32}$$

Using the hydrostatic equation, the temperature perturbation at p_s depends on geopotential according to

$$T'(p_s) = \frac{\gamma_0(p_s)}{T_0(p_s)R}\Phi'(p_s)\,. \tag{B.33}$$

The resulting temperature variations around the globe amount to only a few Kelvin at p_s. Only at higher levels, the temperature perturbations assume physically meaningful values. Due to this problem and the vertical truncation (section B.2.4), the temperature advection computed from the Hough coefficients is subject to errors, which are largest in the lower troposphere and lead to errors in A_T. Especially $A_{T,p}$ is affected, as it contains the vertical derivative of temperature, which is distorted by the transition to the spuriously small values. Despite this disadvantage of computing N_T from the normal-mode expansion coefficients, the energy budget is well closed (section B.2.5).

B.9.2 Boundary terms in the integration by parts

In the derivation of Eq. (B.12), the following expression is integrated by parts:

$$\int_V \frac{\partial}{\partial p}\left(\frac{p}{\gamma_0}(N_T + S_T)\right) g h_K \, dV\,. \tag{B.34}$$

The resulting boundary terms

$$\frac{1}{4\pi}\int_0^{2\pi}\int_{-\pi/2}^{\pi/2} \frac{p_s}{\gamma_0(p_s)}\Phi_K(p_s)\,(N_T(p_s) + S_T(p_s))\,\cos\varphi\, d\varphi\, d\lambda\,, \tag{B.35}$$

are neglected. To approximate the neglected terms, the temperature tendencies $N_T(p_s) + S_T(p_s)$ are estimated as the difference between the total temperature tendencies and the temperature changes due to linear processes:

$$\begin{aligned} N_T(p_s) + S_T(p_s) \;&\approx\; \frac{T'(t_i + \Delta t) - T'(t_i)}{\Delta t} \\ &-\; \sum_r \mathrm{Re}\left[\frac{gD_m}{R}\left(p\frac{dG_m}{dp}\right)_{p_s} Z_r e^{ik\lambda} i\nu_r \frac{W_r(t_i + \Delta t) + W_r(t_i)}{2}\right], \end{aligned} \tag{B.36}$$

where T' is the temperature perturbation at the reference pressure resulting from the normal-mode expansion (Eq. B.33). The KW energy tendency resulting from Eqs. (B.35) and (B.36) is small compared to the other sources (Fig. B.1).

Tanaka and Kung (1988) also neglect the boundary terms under the assumption that the horizontal velocity at p_s is small. However, this assumption does not necessarily apply for atmospheric data interpolated to pressure levels (section B.11). At $p_s = 1013.25$ hPa, non-negligible velocities can occur in regions of high surface pressure, where $p = p_s$ is located several meters above the surface.

B.10 Appendix C Virtual temperature

In the IFS model, the temperature and velocity tendencies are the sum of dynamical sources and tendencies due to parametrizations. For the pressure gradient force, the

IFS model uses geopotential that is in hydrostatic balance with virtual temperature T_v (ECMWF, 2016a). By vertically integrating

$$T_v - T = T\left(\frac{R_v}{R} - 1\right) q\,, \tag{B.37}$$

in the hydrostatic equation, we obtain Φ_v, which is the difference between Φ in Eq. (B.1) and the geopotential in the IFS model. Specific humidity is denoted q, and R_v is the specific gas constant of water vapor.

Horizontal gradients in Φ_v cause the KW energy source D_{Tv} given in Table B.1, which is positive in the example in Fig. B.1. This term is calculated using specific humidity from hourly analysis data, interpolated to the horizontal grid by nearest-neighbor interpolation. For the conversion term, the IFS model also uses virtual temperature (ECMWF, 2016a). Quantifying modifications of A_{co} due to virtual temperature is beyond the scope of the current study.

B.11 Appendix D Vertical interpolation and extrapolation

In the following, the interpolation of ERA5 data, available on 137 hybrid model levels, to pressure coordinates is described. The velocities u and v, and the velocity tendencies due to parametrizations S_u and S_v are linearly interpolated to 137 pressure levels. The coordinate used for the interpolation is the logarithm of pressure as in Yessad (2016).

With the hydrostatic equation, we obtain geopotential on hybrid half-levels from the hybrid-level temperature. This geopotential is also linearly interpolated to pressure levels in the log-pressure coordinate. Perturbations of geopotential are obtained by subtracting the reference geopotential, which is in hydrostatic balance with the reference temperature in Eq. (B.25).

At certain horizontal grid points, the surface pressure is lower than the reference pressure p_s, for example in mountain regions and in low-pressure systems. At these locations, the values at levels below the surface are extrapolated. Velocity is extrapolated with zero, because this does not change the kinetic energy of the air column. The velocity tendencies S_u and S_v are also extrapolated with zero. Geopotential perturbations at each horizontal grid point are extrapolated with a constant, which is $\Phi'(\lambda, \varphi)$ at the lowest level with available data. The temperature perturbations in hydrostatic balance with these geopotential perturbations are zero, so that no source of potential energy is introduced by the extrapolation.

From the temperature tendencies due to parametrizations S_T, Q_{SW} and Q_{LW}, we obtain geopotential tendencies using the hydrostatic equation. These geopotential tendencies are also linearly interpolated in log-pressure to the pressure grid and extrapolated with zero. The geopotential tendencies at pressure levels are expanded in terms of vertical modes, in order to reconstruct the temperature tendencies as in Eq. (B.15).

The described extrapolation of geopotential introduces unphysical sources of energy due to horizontal gradients in geopotential below the surface:

$$D_{\mathrm{E}} = \frac{1}{4\pi g}\int_0^{2\pi}\int_{-\pi/2}^{\pi/2}\int_{p_{\mathrm{surf}}}^{p_s}\left(\frac{1}{a\cos\varphi}\frac{\partial\Phi}{\partial\lambda}u_{\mathrm{K}} + \frac{1}{a}\frac{\partial\Phi}{\partial\varphi}v_{\mathrm{K}}\right) dp\,\cos\varphi\,d\varphi\,d\lambda, \tag{B.38}$$

where p_{surf} is the surface pressure if its value is lower than p_s, else p_s. The horizontal gradients are computed on pressure levels with spherical harmonics. For the example

in Fig. B.1, D_E is an energy sink. For terrain-following coordinates, the energy source D_E would not appear, and the part of the atmosphere where pressure is higher than p_s would not be neglected.

B.12 Appendix E Tendencies of kinetic and available potential energy

In the prognostic equations for kinetic and available potential energy of the total atmosphere, sources of momentum influence kinetic energy, while heat sources influence APE. In contrast, for an individual normal-mode r, K_r and P_r can not be modified independently. A single coefficient W_r determines the values of u_r, v_r and T_r. Thereby, the ratio of K_r and P_r for each mode is fixed (Tanaka, 1985). Although the individual source terms in Table B.1 arise from momentum or heat sources, for a single mode they can not be categorized into those that influence only K_r and those affecting only P_r.

For example, the energy tendency of a Kelvin mode with a certain k and m due to nonlinear dynamical zonal momentum sources can be expressed as

$$A_{u,k,m} = p_s D_m \mathrm{Re}\left(f_{k,\mathrm{K},m}(N_u) W^*_{k,\mathrm{K},m}\right) , \tag{B.39}$$

where $f_{k,\mathrm{K},m}(N_u)$ is the scalar product of N_u with the Kelvin mode:

$$f_{k,\mathrm{K},m}(N_u) = \frac{1}{2\pi p_s} \int_0^{2\pi} \int_{-\pi/2}^{\pi/2} \int_0^{p_s} \frac{N_u}{\sqrt{gD_m}} U_{k,\mathrm{K},m} e^{-ik\lambda} G_m \, dp \, \cos\varphi \, d\varphi \, d\lambda \, . \tag{B.40}$$

This complex quantity determines the amplitude and phase of momentum and temperature tendencies associated with the Kelvin mode, which are

$$\frac{\partial}{\partial t} \begin{pmatrix} u_{k,\mathrm{K},m} \\ v_{k,\mathrm{K},m} \\ T_{k,\mathrm{K},m} \end{pmatrix} (N_u) = \begin{pmatrix} \sqrt{gD_m} G_m \\ \sqrt{gD_m} G_m \\ -D_m p \frac{dG_m}{dp} \frac{g}{R} \end{pmatrix} \left(\mathbf{H}_{k,\mathrm{K},m} f_{k,\mathrm{K},m}(N_u) + \mathbf{H}^*_{k,\mathrm{K},m} f^*_{k,\mathrm{K},m}(N_u)\right) \, . \tag{B.41}$$

In terms of these momentum and temperature tendencies, the energy tendency can be rewritten as

$$\begin{aligned} A_u = \int \Bigg(& \frac{\partial}{\partial t}\left(u_{k,\mathrm{K},m}(N_u)\right) u_{k,\mathrm{K},m} + \frac{\partial}{\partial t}\left(v_{k,\mathrm{K},m}(N_u)\right) v_{k,\mathrm{K},m} \\ & + \frac{\partial}{\partial p}\left(\frac{p}{\gamma_0} \frac{\partial}{\partial t}\left(T_{k,\mathrm{K},m}(N_u)\right)\right) g h_{k,\mathrm{K},m} \Bigg) \, dV \end{aligned} \tag{B.42}$$

Equation (B.42) illustrates that the energy of the Kelvin mode is affected by temperature and momentum tendencies, which were derived from N_u. Accordingly, both $K_{k,\mathrm{K},m}$ and $P_{k,\mathrm{K},m}$ are modified. For the sum of several Kelvin modes, N_u also affects both kinetic and potential energy, because the momentum or temperature tendencies resulting from N_u are a linear combination of the tendencies for different k and m, which are orthogonal. However, for the sum of all k, n and m, the source of APE due to N_u is zero, so that in total, N_u changes only the kinetic energy.

Open Research Section

ERA5 data (Hersbach et al., 2020) are distributed by the German Climate Computing Center (DKRZ). OLR data (NOAA PSL, 2025b) are available at https://psl.noaa.gov/data/gridded/data.olrcdr.interp.html. The default version of the MODES software for the normal-mode decomposition is available via https://modes.cen.uni-hamburg.de. The data and Python scripts used to produce the figures can be acquired from Holube et al. (2025a).

Acknowledgments

This study is funded by the German Research Foundation DFG, Grant No. 461186383. KMH acknowledges the graduate school of the Collaborative Research Center TRR 181, Grant No. 274762653. KMH would like to thank Sam Stechmann for insightful discussions. We are grateful to three anonymous reviewers for their constructive comments.

B.13 Supporting Figures

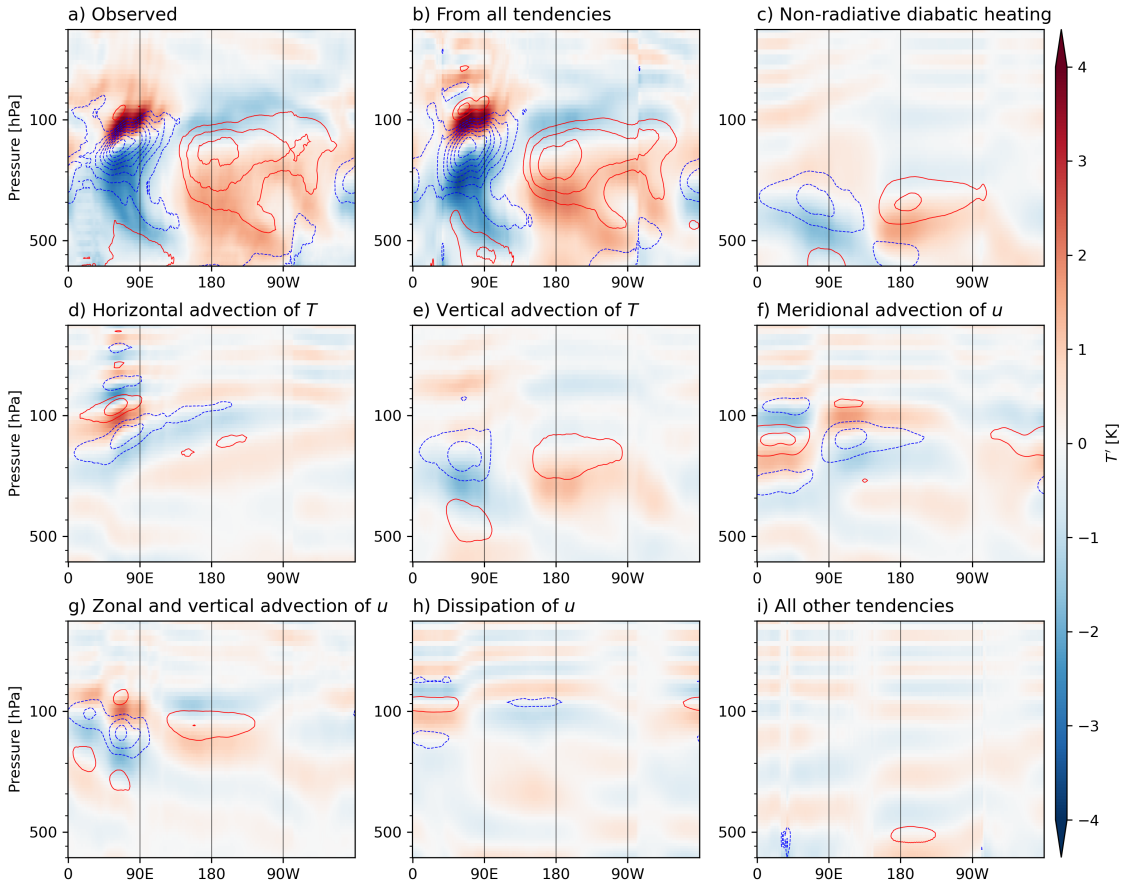

Figure B.12: Zonal wind (contours with a spacing of 2 m s^{-1}) and temperature (shading) of stationary Kelvin waves in July 2018 due to different processes. A truncation of the vertical modes is applied at $m = 40$.

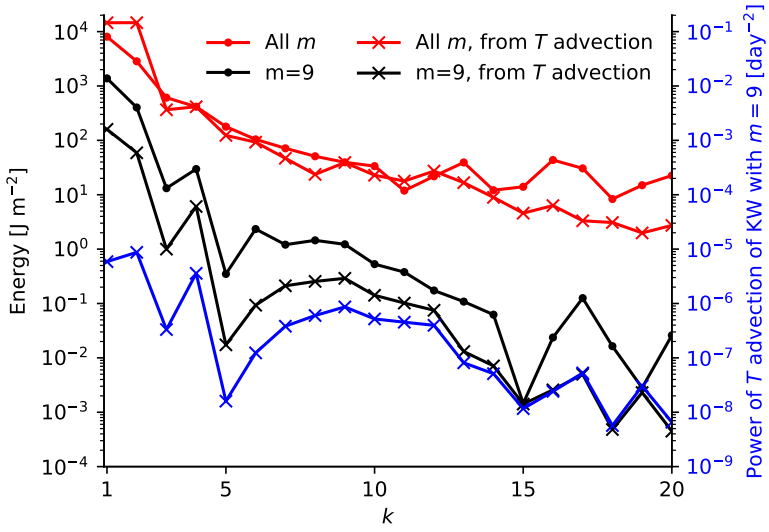

Figure B.13: Energy spectra of Kelvin waves as a function of zonal wavenumber for the vertical mode $m = 9$ and sum over all m, as determined from the normal-mode expansion of the data (dots), or from the temperature tendencies due to advection (x). For comparison, the power spectrum of the KW tendency due to temperature advection is shown for $m = 9$.

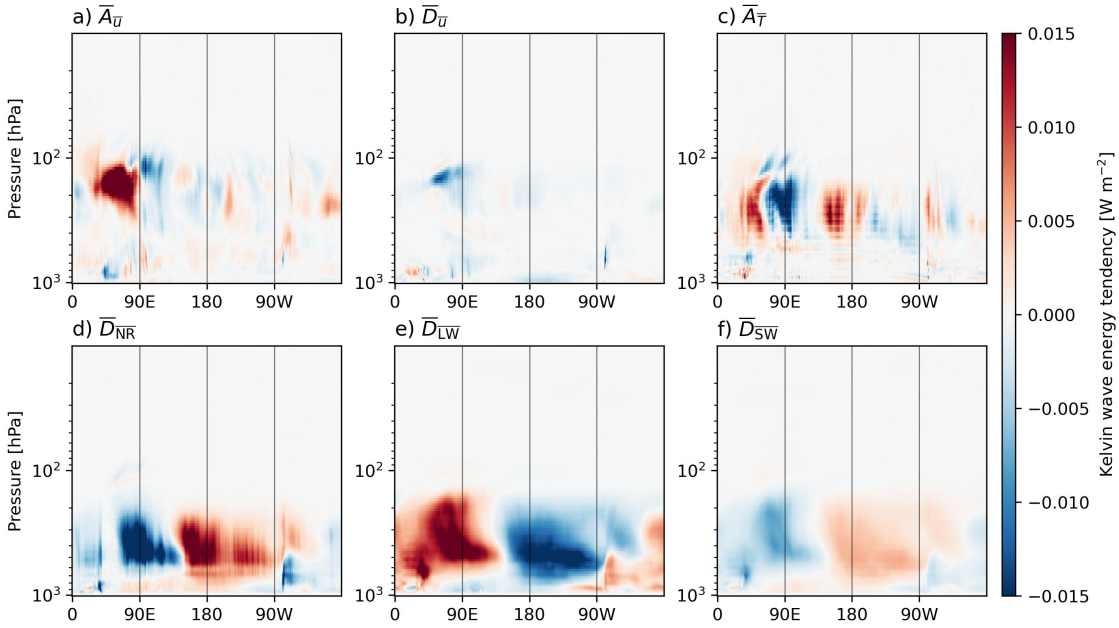

Figure B.14: Integrand of the energy tendencies of stationary Kelvin waves, e.g. $\overline{N}_u \overline{u}_{\mathrm{K}}$, for July 2018 as a function of longitude and pressure-level. To display the integrand in W m^{-2}, it is multiplied with $\Delta p/g$, where Δp is the pressure difference between two levels.

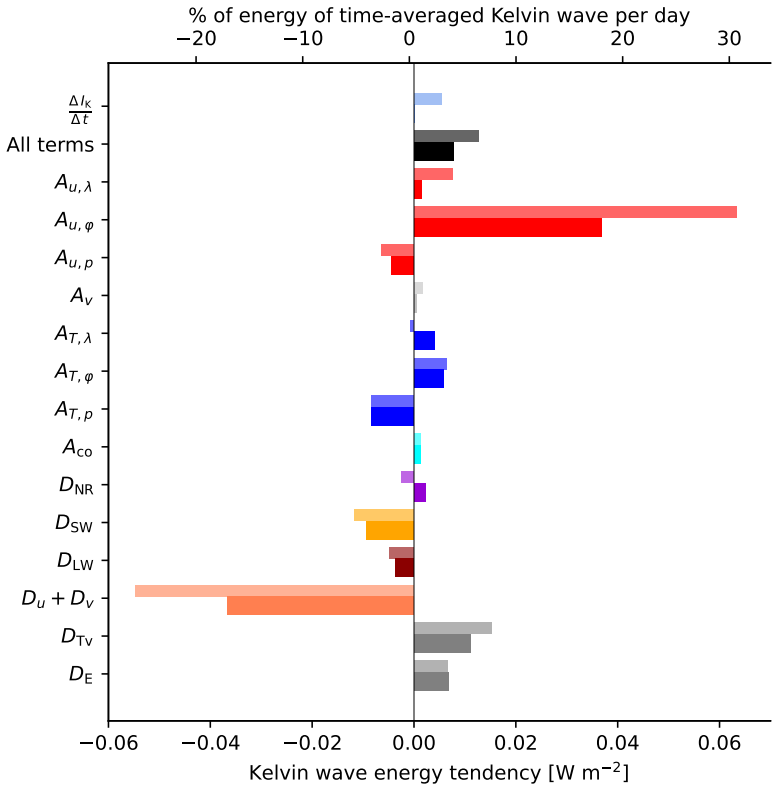

Figure B.15: Kelvin wave energy tendencies due to different processes as in Table 1, for July 2018. Thick bars show tendencies for stationary Kelvin waves (first term in Eq. B.14), thin bars show the time-averaged energy tendencies of all Kelvin waves.

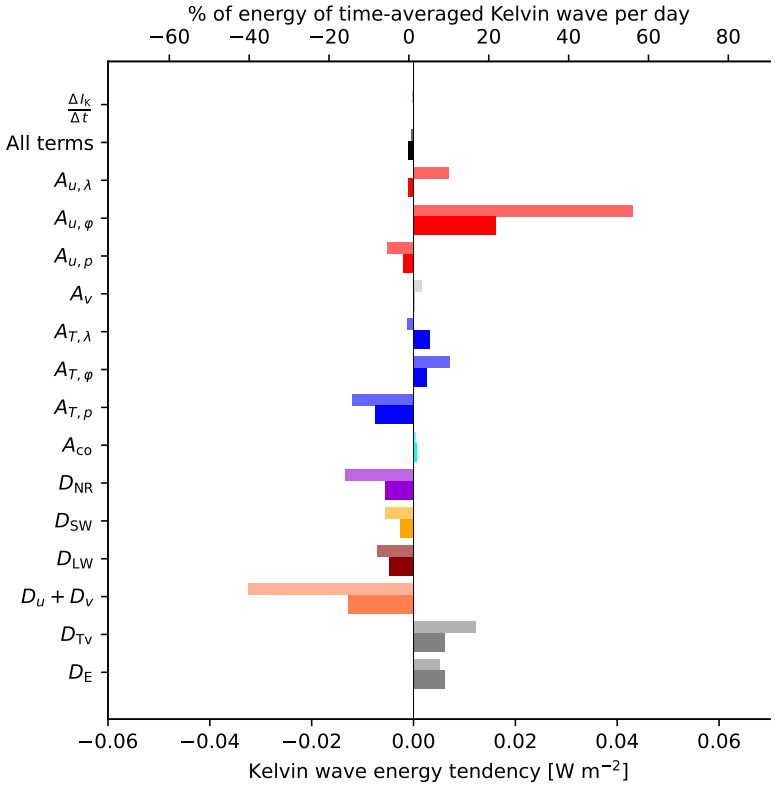

Figure B.16: Kelvin wave energy tendencies due to different processes as in Table 1, for December 2017-November 2018. Thick bars show tendencies for stationary Kelvin waves (first term in Eq. B.14), thin bars show the time-averaged energy tendencies of all Kelvin waves.

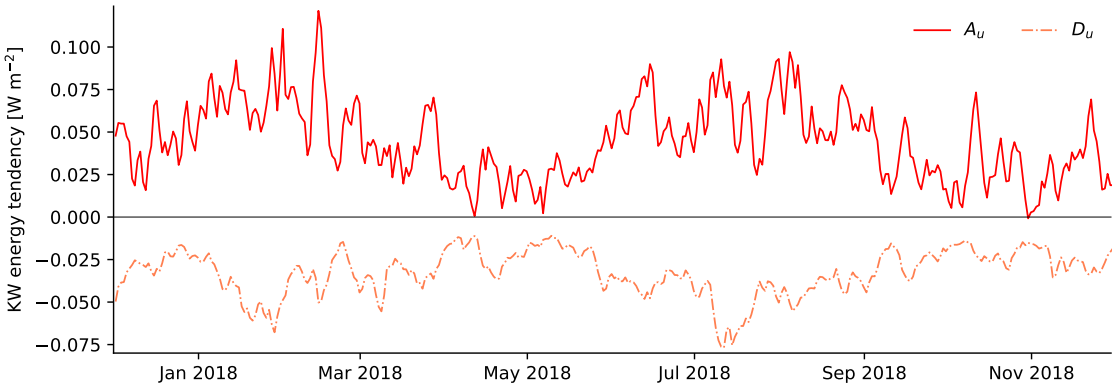

Figure B.17: Daily averages of Kelvin wave energy tendencies from 12-hourly data, due to momentum advection and momentum tendencies due to parametrizations.

C

ENERGY TRANSFER FROM THE ZONAL MEAN FLOW AND N=1 ROSSBY WAVES TO KELVIN WAVES THROUGH NORMAL-MODE INTERACTIONS

The work in this appendix is prepared for submission to the *Journal of Geophysical Research: Atmospheres* as:

Holube, K. M., Lunkeit, F., Vasylkevych, S., and Žagar, N. Energy transfer from the zonal mean flow and $n = 1$ Rossby waves to Kelvin waves through normal-mode interactions.

Authors' Contributions[1]

- Holube, K. M.: Conceptualization, Data curation, Formal analysis, Investigation, Methodology, Software, Visualization, Writing the original draft, Writing - Review and Editing.
- Lunkeit, F.: Conceptualization, Supervision, Writing - Review and Editing.
- Vasylkevych, S.: Conceptualization, Methodology, Validation, Writing - Review and Editing.
- Žagar, N.: Conceptualization, Funding Acquisition, Project Administration, Supervision, Writing - Review and Editing.

1 using the Contributor Role Taxonomy (CRediT) https://credit.niso.org/

Energy transfer from the zonal mean flow and $n = 1$ Rossby waves to Kelvin waves through normal-mode interactions

Katharina M. Holube,[1] Frank Lunkeit,[1] Sergiy Vasylkevych,[1] and Nedjeljka Žagar[1]

[1] Meteorological Institute, Center for Earth System Research and Sustainability, University of Hamburg, Hamburg, Germany

Key Points:

- Kelvin and $n = 1$ Rossby waves receive energy from the zonal mean flow through interactions with the respective other mode.
- Energy is transferred from $n = 1$ Rossby waves to Kelvin waves through zonal advection of momentum and temperature.
- The energy transfers are enabled by the Kelvin and $n = 1$ Rossby waves being phase-shifted relative to each other in the time average.

Abstract

Dynamical processes are an energy source for Kelvin waves (KWs) in the tropical atmosphere, as shown by previous studies. However, it is not clear how energy is transferred to KWs from other wave modes and from the zonal mean flow. This question is investigated by decomposing the dynamical KW energy source in ERA5 data into wave-mean flow and wave-wave interactions using 3D normal modes. In the time average, the main KW energy source results from interactions of equatorial ($n = 1$) Rossby waves (R1) with the balanced zonal mean flow. This is mainly associated with the stationary waves and low-frequency covariability between KWs and their tendencies. The stationary R1 is located further east than the stationary KW. This configuration leads to a KW energy source due to meridional advection of zonal mean zonal momentum by R1. Additionally, KW and R1 gain energy through vertical advection of the zonal mean temperature by the respective other mode. By these processes, energy is transferred from the zonal mean flow to the waves. In addition, KWs receive energy from R1 due to zonal advection of R1 momentum and temperature. Wave-wave interactions of R1 are a smaller KW energy source, while interactions of gravity waves with the mean flow result in a KW energy sink. The mode interactions and energy transfers illustrate how the linear KW and R1 modes are coupled with each other in the presence of a zonal mean flow.

C.1 Introduction

The Kelvin wave (KW) is the slowest eastward-propagating mode among the equatorial wave solutions derived from the shallow-water equations linearized around the state of rest (Matsuno, 1966; Longuet-Higgins, 1968). On the sphere, these solutions define the horizontal structure of the 3D normal modes, which are basis functions for the atmospheric circulation (Kasahara and Puri, 1981; Tanaka, 1985). Expanding atmospheric

data in terms of these basis functions allows to identify KWs based on their spatial structure (Žagar et al., 2015; Žagar et al., 2022). In contrast to other wave identification methods (Knippertz et al., 2022, and references therein), no assumptions about the wave propagation are made in the normal-mode decomposition. Therefore, the resulting KWs include phenomena with various time scales, including stationary waves (Žagar et al., 2022). The contribution of KWs to the time-averaged tropical circulation is evident in the easterlies over the eastern hemisphere and westerlies over the Pacific Ocean (Fig. C.1).

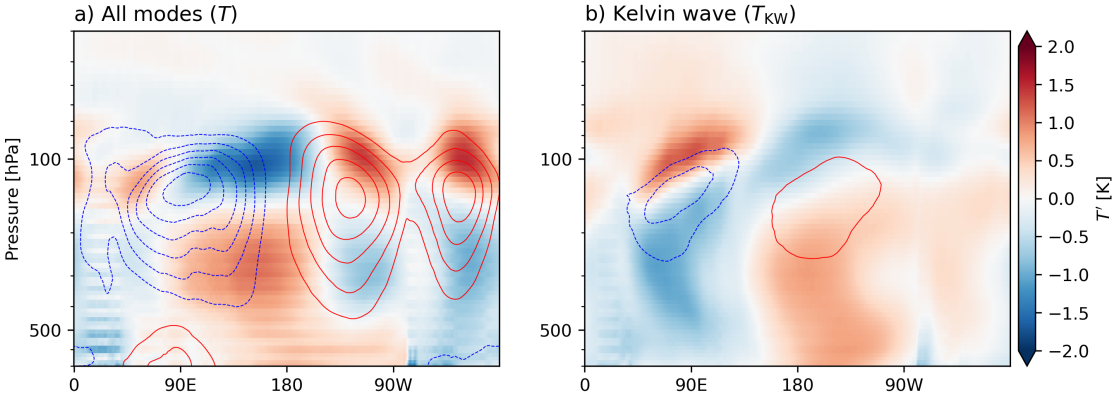

Figure C.1: Vertical cross-sections of temperature perturbations and zonal velocity with a spacing of 2 m s^{-1}, averaged over 15° N to 15° S and over 2016-2019 of a) All modes, excluding the zonal mean flow, b) Kelvin waves.

Since the normal-mode decomposition is multivariate, the energy of the normal modes consists of kinetic and available potential energy. The energy balance equation contains dynamical and diabatic processes as sources and sinks (Tanaka, 1985). For KWs, dynamical processes, comprising advection of momentum and temperature, result in an energy source (Tanaka, 1985; Castanheira and Marques, 2021), which is mainly due to meridional advection of zonal momentum (Holube et al., 2025b). In the normal-mode decomposition, the atmospheric circulation is interpreted as a superposition of 3D normal modes, which exchange energy through dynamical processes (Tanaka, 1985). This study addresses the question which modes transfer energy to KWs.

In general, three modes are involved in dynamical energy transfers, because the nonlinearity consists of quadratic terms. For example, momentum of one mode can be advected by another mode, and these momentum tendencies result in energy tendencies of a third mode. These three modes form a triad, which can contain modes of different types, e.g. both Rossby and gravity waves (Ripa, 1983b; Eden et al., 2019). Energy exchanges can only take place when the sum or difference of the zonal wavenumbers of two modes in the triad is equal to the zonal wavenumber of the third mode (Ripa, 1983b; Tanaka and Terasaki, 2005). A special type of triad is the resonant triad. Such triads are constituted of modes whose eigenfrequencies fulfill an additional condition. A variety of resonant triads in the tropical circulation has been determined theoretically for the shallow-water equations (Ripa, 1983b,c), including self-interactions of Kelvin waves (Ripa, 1982). In the primitive equations on the equatorial β-plane, the zonal mean flow does not gain or lose energy in resonant triads (Raupp et al., 2008). In triads that contain three different modes, the direct energy transfer from one mode to another can in general not be quantified, only the energy tendency of each mode resulting from the interaction

of the respective two other modes (see section C.2.2). Therefore, it might ultimately not be possible to conclude which modes transfer energy to KWs. However, the analysis in this paper allows to partially narrow down the possibilities for energy exchanges.

In systems with many modes, it is not practical to analyze each individual triad. Instead, energy fluxes can be regarded as the net effect of many triads (Eden et al., 2019). Accordingly, the energy tendencies due to dynamical processes consist of the interactions of various modes. The energy tendencies resulting from an arbitrary selection of triads can be computed with the numerical scheme described by Holube et al. (2025b), where the momentum and temperature tendencies due to advection are computed from the normal-mode expansion coefficients. By comparing with the energy tendencies due to diabatic processes, Holube et al. (2025b) validated the scheme and discussed the underlying processes for the KW. The current study is the first to take advantage of this scheme by decomposing the advection terms into interactions of different modes.

The mode interactions consist of wave-mean flow interactions and wave-wave interactions. The interactions of $n = 1$ Rossby waves with the zonal mean flow lead to the development of Kelvin waves (Namazi and Khouider, 2013). In idealized shallow-water model simulations, wave-mean flow interactions play a greater role than wave-wave interactions for the generation of KWs (Holube et al., 2024) and mixed Rossby-gravity (MRG) waves (Mahó et al., 2024a,b). The KW development due to meridional advection of vorticity by subtropical Rossby waves, demonstrated in the shallow-water framework by Barpanda et al. (2023), also hints at the importance of wave-mean flow interactions. In this study, the KW energy tendencies resulting from wave-mean flow and wave-wave interactions are quantified in reanalysis data. Such interactions have been computed in the context of the Arctic Oscillation (Tanaka and Terasaki, 2005), but not yet for equatorial waves.

The interactions and energy transfers involving KWs and $n = 1$ Rossby waves are of particular interest, because these modes are part of the spatial structure of the Madden-Julian Oscillation (MJO) (Hendon and Salby, 1994; Žagar and Franzke, 2015). Coherence spectra show a potential for nonlinear interactions of these modes (Kitsios et al., 2019). Using data-driven methods, Raphaldini et al. (2021) and Teruya et al. (2024) found that KWs transfer energy to $n = 1$ Rossby waves, this involves moist processes. In contrast, Castanheira and Marques (2021) evaluated the energy tendencies due to dynamical processes only. Their results show that KWs gain energy from the atmospheric circulation, and $n = 1$ Rossby waves transfer energy to the circulation. In this study, these energy tendencies are investigated in more detail by decomposing them into mode interactions and quantifying energy transfers from $n = 1$ Rossby waves to KWs that result from specific interactions.

The importance of Rossby wave dynamics as an energy source for KWs has been demonstrated in previous studies. When Rossby waves break at a critical line, KWs can be enhanced by eddy momentum flux convergence (Tulich and Kiladis, 2021; Cheng et al., 2022). This process induces a KW energy source across all seasons in the first and second baroclinic modes in the troposphere (Chien et al., 2025). The vertical structure of this KW energy source (Tulich and Kiladis, 2021) is similar to the KW energy tendencies due to advection of momentum discussed by Holube et al. (2025b). However, Tulich and Kiladis (2021), Cheng et al. (2022) and Chien et al. (2025) identified KWs associated with the variability of convection in the wavenumber-frequency spectrum, and their results might not be transferable to Kelvin waves identified using 3D normal-mode decomposition.

This article has the following structure. In section C.2, we summarize how energy tendencies of normal modes due to wave-mean flow and wave-wave interactions are evaluated. We present these energy tendencies for the KW, and provide details on the energy transfer processes constituting the main KW energy source (section C.3). We discuss our results in section C.4 and draw conclusions in section C.5.

C.2 Method

We use the normal-mode energetics scheme developed by Tanaka (1985), which is summarized in subsection C.2.1. The numerical implementation, including the computation of advection terms from normal-mode expansion coefficients, is described by Holube et al. (2025b). As explained in subsection C.2.2, this method allows to evaluate the energy transfer between normal modes resulting from wave-mean flow and wave-wave interactions. We also perform a spectral analysis in time of the expansion coefficients and their tendencies (subsection C.2.3). Subsection C.2.4 describes the reanalysis data used in this study.

C.2.1 Prognostic equation for energy of 3D normal modes

The 3D normal modes are eigensolutions of the hydrostatic primitive equations, linearized around the state of rest. They represent Rossby, Kelvin, inertia-gravity and mixed Rossby-gravity modes with different zonal wavenumbers k, meridional modes n and vertical modes m as multivariate functions containing horizontal velocity $\mathbf{V} = (u, v)^T$ and geopotential Φ (Tanaka, 1985). The horizontal structures of the modes are given by the Hough harmonics $\mathbf{H}_r$ (Longuet-Higgins, 1968; Swarztrauber and Kasahara, 1985), where $r = (k, n, m)$ is a multi-index. Combining $\mathbf{H}_r$ with the vertical structure functions G_m yields the 3D normal modes (Kasahara and Puri, 1981), the vertical structure functions for selected vertical modes are shown in Fig. C.16.

Using spectral expansion in terms of 3D normal modes, the prognostic equation for the complex expansion coefficient W_r is obtained:

$$\frac{dW_r}{dt} = -2\Omega i \nu_r W_r + f_r \tag{C.1}$$

(Tanaka, 1985). The first term on the right-hand side of Eq. (C.1), which includes the nondimensional eigenfrequency ν_r, represents the linear terms, which are retained when the equations are linearized with respect to the state of rest. The projection of the nonlinear terms and diabatic sources on the mode r is

$$f_r = \frac{1}{2\pi p_s} \int_0^{2\pi} \int_{-\pi/2}^{\pi/2} \int_0^{p_s} \begin{pmatrix} (B_u + S_u)\sqrt{gD_m}^{-1} \\ (B_v + S_v)\sqrt{gD_m}^{-1} \\ \frac{\partial}{\partial p}\left(\frac{p}{\gamma_0}\left(B_T + \frac{\omega R T'}{p c_p} + S_T\right)\right) \end{pmatrix} G_m \cdot \mathbf{H}_r^* \, dp \, \cos\varphi \, d\varphi \, d\lambda \,. \tag{C.2}$$

Momentum and temperature tendencies due to advection and metric terms are denoted $\mathbf{B} = (B_u, B_v, B_T)^T$. The nonlinear dynamical tendencies

$$\mathbf{N} = \mathbf{B} + \begin{pmatrix} 0 \\ 0 \\ \frac{\omega R T'}{p c_p} \end{pmatrix} \tag{C.3}$$

also include the nonlinear part of the potential energy source due to adiabatic expansion, which represents the conversion between kinetic and potential energy and which is in the following referred to as the conversion term. Diabatic momentum and temperature sources and sinks, such as radiative forcing or turbulent diffusion, are denoted $\mathbf{S} = (S_u, S_v, S_T)^T$. Temperature $T = T_0(p) + T'$ is split into the reference temperature $T_0(p)$, for which we use the analytical profile from Jablonowski and Williamson (2006), and perturbations. The pressure vertical velocity is denoted ω, the coordinates are pressure p, longitude λ and latitude φ, and t is time. Each vertical mode is associated with an equivalent depth D_m. Further parameters are Earth's gravity g and rotation rate Ω, the specific heat capacity c_p at constant pressure for dry air, the gas constant R, the reference pressure p_s, and the static stability $\gamma_0 = \frac{RT_0}{c_p} - p\frac{dT_0}{dp}$.

The expansion coefficients of real quantities for negative k are the complex conjugates of the coefficients for positive k. The waves with $\pm k$ are combined in the following, so that only non-negative k are discussed. Following Tanaka (1985), the energy of the mode r

$$I_r = (2 - \delta_{0k}) \frac{p_s}{4} D_m W_r W_r^* \,, \tag{C.4}$$

where δ_{0k} is the Kronecker delta, consists of kinetic and available potential energy. The prognostic equation for energy (with energy fluxes through the surface neglected) is

$$\frac{dI_r}{dt} = (2 - \delta_{0k}) \frac{p_s}{2} D_m \mathrm{Re}\left(f_r W_r^*\right) = \int_V (\mathbf{N} + \mathbf{S}) \cdot \begin{pmatrix} u_r \\ v_r \\ \frac{R}{\gamma_0} T_r \end{pmatrix} dV \,, \tag{C.5}$$

where the horizontal velocity $\mathbf{V}_r = (u_r, v_r)^T$ and temperature T_r of the mode r are reconstructed from the expansion coefficients, and the 3D integral over the atmosphere is abbreviated as

$$\int_V dV = \frac{1}{4\pi g} \int_0^{2\pi} \int_{-\pi/2}^{\pi/2} \int_0^{p_s} dp \, \cos\varphi \, d\varphi \, d\lambda \,. \tag{C.6}$$

Omitting the integration over a certain dimension in Eq. (C.5) yields the contributions of each longitude, latitude or pressure-level to the total energy tendencies, as discussed by Holube et al. (2025b).

We decompose the dynamical energy tendencies into different processes as:

$$\begin{aligned} \int_V \mathbf{N} \cdot \begin{pmatrix} u_r \\ v_r \\ \frac{R}{\gamma_0} T_r \end{pmatrix} dV = {} & A_{u,\lambda} + A_{u,\varphi} + A_{u,p} + A_{v,\lambda} + A_{v,\varphi} + A_{v,p} + A_{\text{metric}} \\ & + A_{T,\lambda} + A_{T,\varphi} + A_{T,p} + A_{\text{co}} \,. \end{aligned} \tag{C.7}$$

The energy tendency resulting from advection of velocity or temperature (x) in y-direction is denoted $A_{x,y}$. Further energy tendencies stem from the metric terms (A_{metric}) and the conversion term (A_{co}). The definition of each term is given in the Supporting Information.

C.2.2 Energy tendencies due to mode interactions

The nonlinear dynamical momentum and temperature tendencies $\mathbf{N}$ can be represented as interactions of normal modes by computing each variable from the expansion coefficients

as described by Holube et al. (2025b) and references therein. The total interactions are the sum over the interactions of all combinations of modes a and b, excluding permutations:

$$\mathbf{N} = \sum_{a,b} \mathbf{N}(a,b)\,. \tag{C.8}$$

We refer to the interactions as wave-mean flow interactions if one of the interacting modes has $k = 0$, and else as wave-wave interactions. Interactions of two modes a and b include the advection of momentum and temperature of the mode a by the mode b and vice versa. Specifically, the momentum and temperature tendencies resulting from these interactions are

$$\begin{aligned}\mathbf{N}(a,b) = &\begin{pmatrix} -\frac{1}{\cos\varphi}\mathbf{V}_a \cdot \nabla(u_b \cos\varphi) - \frac{1}{\cos\varphi}\mathbf{V}_b \cdot \nabla(u_a \cos\varphi) - \omega_a \frac{\partial u_b}{\partial p} - \omega_b \frac{\partial u_a}{\partial p} \\ -\frac{1}{\cos\varphi}\left(\mathbf{V}_a \cdot \nabla(v_b \cos\varphi) + \mathbf{V}_b \cdot \nabla(v_a \cos\varphi)\right) - \omega_a \frac{\partial v_b}{\partial p} - \omega_b \frac{\partial v_a}{\partial p} - 2(u_a u_b + v_a v_b)\frac{\tan\varphi}{a} \\ -\mathbf{V}_a \cdot \nabla T_b - \mathbf{V}_b \cdot \nabla T_a - \omega_a \frac{\partial T_b}{\partial p} - \omega_b \frac{\partial T_a}{\partial p} \end{pmatrix} \\ &+ \begin{pmatrix} 0 \\ 0 \\ \frac{\omega_a R T_b}{p c_p} + \frac{\omega_b R T_a}{p c_p} \end{pmatrix}, \end{aligned} \tag{C.9}$$

while the self-interactions of the mode a are

$$\mathbf{N}(a,a) = \begin{pmatrix} -\frac{1}{\cos\varphi}\mathbf{V}_a \cdot \nabla(u_a \cos\varphi) - \omega_a \frac{\partial u_a}{\partial p} \\ -\frac{1}{\cos\varphi}\mathbf{V}_a \cdot \nabla(v_a \cos\varphi) - \omega_a \frac{\partial v_a}{\partial p} - (u_a^2 + v_a^2)\frac{\tan\varphi}{a} \\ -\mathbf{V}_a \cdot \nabla T_a - \omega_a \frac{\partial T_a}{\partial p} \end{pmatrix} + \begin{pmatrix} 0 \\ 0 \\ \frac{\omega_a R T_a}{p c_p} \end{pmatrix}. \tag{C.10}$$

The first summands in Eqs. (C.9) and (C.10) are $\mathbf{B}(a,b)$ and $\mathbf{B}(a,a)$, respectively. A similar split of the quadratic nonlinearity into mode interactions has also been performed for single-layer models (e.g., Chouksey et al., 2023; Mahó et al., 2024a; Holube et al., 2024).

The dynamical energy tendency of the mode r is composed of mode interactions as

$$\int_V \mathbf{N} \cdot \begin{pmatrix} u_r \\ v_r \\ \frac{R}{\gamma_0} T_r \end{pmatrix} dV = \sum_{a,b} \int_V \mathbf{N}(a,b) \cdot \begin{pmatrix} u_r \\ v_r \\ \frac{R}{\gamma_0} T_r \end{pmatrix} dV\,. \tag{C.11}$$

Alternatively, the energy tendency of the mode r due to (a,b) interactions can be expressed using the spectral expansion coefficients of the modes a, b and r, and an interaction coefficient representing interactions of these modes in the spectral primitive equations (Tanaka and Kung, 1989). One difference is that Eq. (C.11) neglects boundary terms resulting from integration by parts (see Holube et al., 2025b), whereas these terms are retained in the interaction coefficients (Tanaka and Terasaki, 2005).

The energy tendency of the mode r due to (a,b) interactions is connected to an energy tendency of the mode a due to (b,r) interactions and an energy tendency of the mode b due to (a,r) interactions:

$$\int_V \left[\mathbf{B}(b,r) \cdot \begin{pmatrix} u_a \\ v_a \\ \frac{R}{\gamma_0} T_a \end{pmatrix} + \mathbf{B}(a,r) \cdot \begin{pmatrix} u_b \\ v_b \\ \frac{R}{\gamma_0} T_b \end{pmatrix} + \mathbf{B}(a,b) \cdot \begin{pmatrix} u_r \\ v_r \\ \frac{R}{\gamma_0} T_r \end{pmatrix} \right] dV = E_{abr} + F_{abr}\,. \tag{C.12}$$

The flux of kinetic energy through the surface is denoted E_{abr}, while F_{abr} contains the flux of available potential energy through the surface and terms resulting from vertical variations of γ_0. The Supporting Information provides more detail on E_{abr} and F_{abr}.

Equation (C.12) does not include the conversion term, because the energy tendencies of different modes resulting from this term do not balance out each other. If the conversion term is neglected and the right-hand side of Eq. (C.12) is assumed to be zero, energy is conserved in the triad consisting of the modes a, b and r. In the spectral framework, energy conservation in the triad can be represented by the condition that the sum of the interaction coefficients of these three modes equals zero (Ripa, 1983b; Raupp et al., 2008). Previous studies considering energy tendencies due to mode interactions neglected the conversion term and energy fluxes through the surface as well as vertical variations of γ_0, to obtain energy conservation (e.g. Tanaka, 1985; Tanaka and Kung, 1988; Marques et al., 2020). In this study, the surface is located at the reference pressure $p_s = 1013.25$ hPa, where the velocity and therefore the fluxes of kinetic and available potential energy are not necessarily small, if the surface pressure is higher than p_s. Therefore, we do not make a priori assumptions about the magnitudes of E_{abc}, F_{abc} and the conversion term. Instead, we evaluate the conversion term explicitly, and the right-hand side of Eq. (C.12) as part of the residual.

When Tanaka (1985) calculated the energy tendencies of each mode as in Eq. (C.5), he analyzed the contributions from the momentum and temperature tendency terms separately. Similarly, Eq. (C.12) consists of energy tendencies resulting from momentum tendencies,

$$\int_V \left[B_u(b,r)u_a + B_v(b,r)v_a + B_u(a,r)u_b + B_v(a,r)v_b + B_u(a,b)u_r + B_v(a,b)v_r\right] dV = E_{abr}\,, \tag{C.13}$$

and from temperature advection

$$\int_V \frac{R}{\gamma_0}\left[B_T(b,r)T_a + B_T(a,r)T_b + B_T(a,b)T_r\right] dV = F_{abr}\,. \tag{C.14}$$

In this study, we analyze mode interactions by combining multiple triads. For this, the atmospheric circulation is divided into 7 groups of modes, which do not intersect:

- Kelvin waves (KW)
- $n = 1$ Rossby waves (R1)
- $n > 1$ Rossby waves (R)
- Mixed Rossby-gravity waves (MRG)
- Inertia-gravity waves (G)
- the balanced zonal mean flow (R0), i.e. K-modes (Kasahara, 1978)
- the un-balanced zonal mean flow (G0)

The Rossby mode with $n = 1$ is considered separately from the other Rossby waves because it is closest to the equator and therefore presumably has a special influence on Kelvin waves. The wave modes in the first five groups are defined for $k \geq 1$, while the

zonal mean flow ($k = 0$) is split into R0 and G0, which each contain several meridional modes.

We apply the described diagnostics to the groups of modes, which is possible because the modes are L^2-orthogonal. For each group of modes, three-dimensional fields of horizontal velocity and temperature, their derivatives, and vertical velocity are evaluated from the normal-mode expansion coefficients. Using these fields, the interactions are evaluated with Equations (C.9) and (C.10), from which the energy tendencies of a group of modes are computed with Eq. (C.11). These energy tendencies represent the net effect of several triads. For example, the KW energy tendencies due to (R1, R0) interactions are the sum over the KW energy tendencies in the triads in which one mode is a KW with arbitrary k and m, one mode is a $n = 1$ Rossby wave with arbitrary k and m, and the third mode is a mode of the balanced zonal mean flow with arbitrary n and m.

C.2.3 Co-spectral analysis

According to Eq. (C.5), the energy of the mode r increases when its expansion coefficient is in phase with the tendency. To identify the relevant time scales on which this occurs, we expand W_r and f_r into Fourier series in time:

$$W_r(t) = \overline{W}_r + \sum_j \hat{W}_r(\omega_j) e^{i\omega_j t} \qquad \text{and} \qquad f_r(t) = \overline{f}_r + \sum_j \hat{f}_r(\omega_j) e^{i\omega_j t}\,, \tag{C.15}$$

where $\overline{W}_r$ is the time-averaged expansion coefficient, which is in the following referred to as the stationary wave, and $\overline{f}_r$ is the time-averaged nonlinear tendency. The time-averaged energy tendency consists of the contribution of the stationary wave and the co-spectrum:

$$\overline{\frac{dI_r}{dt}} = (2 - \delta_{0k}) \frac{p_s}{2} D_m \mathrm{Re} \left(\overline{f}_r \overline{W}_r^* + \sum_j \hat{f}_r(\omega_j) \hat{W}_r^*(\omega_j) \right) . \tag{C.16}$$

The co-spectrum shows at which frequencies the mode and its nonlinear tendency have favorable covariance for energy transfer.

C.2.4 Data

In this study, 6-hourly ERA5 reanalyses (Hersbach et al., 2020) are used for the four years 2016-2019. Velocity and geopotential fields are interpolated and expanded in terms of normal modes as described by Holube et al. (2025b). Specifically, the data is interpolated to 137 pressure-levels derived from the 137 hybrid model-levels. This is necessary to apply the described diagnostics, which is based on the decomposition of ω as in Žagar et al. (2023). The data is also interpolated onto a regular Gaussian grid with 400x800 points ($\approx 0.45°$ resolution) using the ECMWF libraries. A triangular truncation is applied with $k + n < 120$, and the vertical modes are retained up to $m = 94$.

For the spectral analysis in time, we split the timeseries into four windows of one year each, and apply tapering. The displayed spectra are the average over the four windows.

C.3 Results

We first split the dynamical KW energy source into wave-mean flow and wave-wave interactions and present the energy transfers associated with (R1, R0) interactions, which

are the primary contributor (subsection C.3.1). Subsequently, the interactions are decomposed into momentum and temperature advection in different spatial directions, and the energy transfer is conceptually illustrated using the stationary waves (subsection C.3.2).

C.3.1 Decomposition of Kelvin wave energy tendencies

The time-averaged KW energy tendencies resulting from wave-mean flow and wave-wave interactions with the largest absolute values are shown in Fig. C.2a. Interactions of $n = 1$ Rossby waves with the balanced zonal mean flow are the main contributor to this KW energy source. A KW energy sink results from interactions of gravity waves with the balanced zonal mean flow. Wave-wave interactions of $n = 1$ Rossby waves, as well as (KW, R0) interactions and (MRG, R0) interactions, induce smaller KW energy sources.

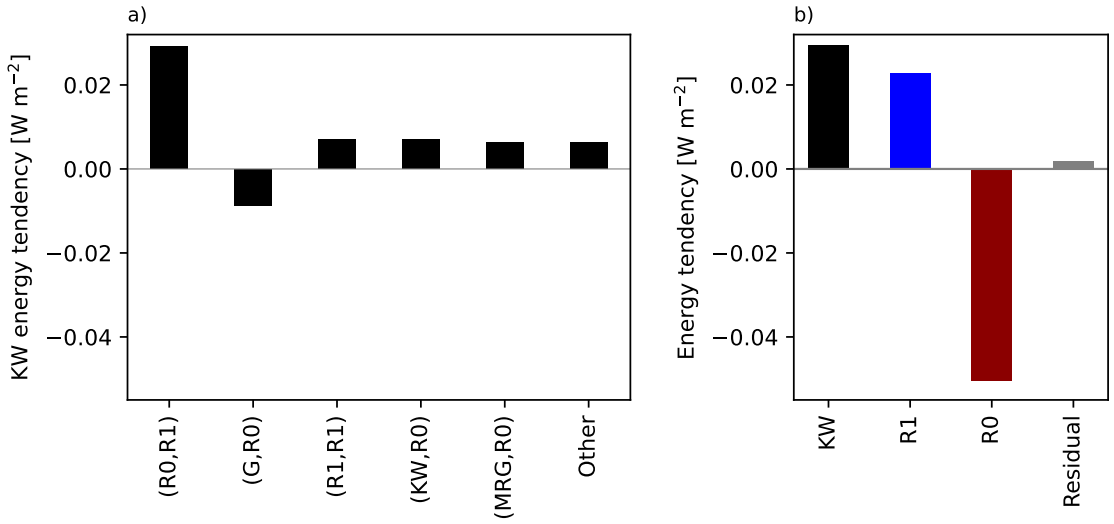

Figure C.2: Time-averaged energy tendencies in 2016-2019. a) Decomposition of dynamical KW energy tendencies into wave-mean flow and wave-wave interactions. b) KW energy tendency due to (R1, R0) interactions, R1 energy tendency due to (KW, R0) interactions and R0 energy tendency due to (KW, R1) interactions; the residual is the sum of these three energy tendencies.

The KW energy tendencies due to (R1, R0) interactions are associated with energy tendencies of R1 and R0, as in Eq. (C.12). The $n = 1$ Rossby waves receive energy due to (KW, R0) interactions, while R0 loses energy due to (KW, R1) interactions (Fig. C.2b). The residual displayed in Fig. C.2b, which contains the right-hand side of Eq. (C.12) and numerical errors, is small, and we will illustrate in section C.3.2 that the conversion term is also comparatively small. This indicates the approximate conservation of energy in the set of triads composed of one KW, one R1 and one R0 mode. A more detailed picture of the energy transfers becomes apparent when the advection of momentum and temperature are analyzed separately in section C.3.2.

The energy that KWs receive through (R1, R1) interactions is supplied by R1. In the set of triads in which one mode is a KW and the other two are R1 modes, the time-averaged residual is about 6% of the KW energy tendency, indicating that energy is approximately conserved here as well. This study does not provide further detail on the

(R1, R1) interactions and other interactions resulting in smaller KW energy tendencies (Fig. C.2a), but focuses on the larger KW energy tendencies.

Now we examine for which zonal wavenumbers and vertical modes the KW energy tendencies due to (R1, R0) interactions are strongest. Due to the triad interaction conditions, KWs with a certain k exchange energy only with R1 of the same k in wave-mean flow interactions. For the lowest k, the energy tendencies of KW, R1 and R0 are shown in Fig. C.3. The KW energy source is strongest for $k = 1$ and decreases for larger k. This is consistent with the fact that most of the KW energy is contained in low k (Fig. C.17). We also note that the magnitude of the R1 energy tendencies is comparable to that of the KW energy tendencies (Fig. C.2b and C.3), but it is not clear whether this similarity is coincidental or has a physical cause.

As with the zonal wavenumbers, the largest KW energy tendencies due to (R1, R0) interactions are found for the most energetic vertical modes (Fig. C.18). These vertical modes are baroclinic in the troposphere (Fig. C.16). In contrast to the zonal wavenumbers, there is no general condition to constrain the set of vertical modes that exchange energy with KWs of a certain vertical mode.

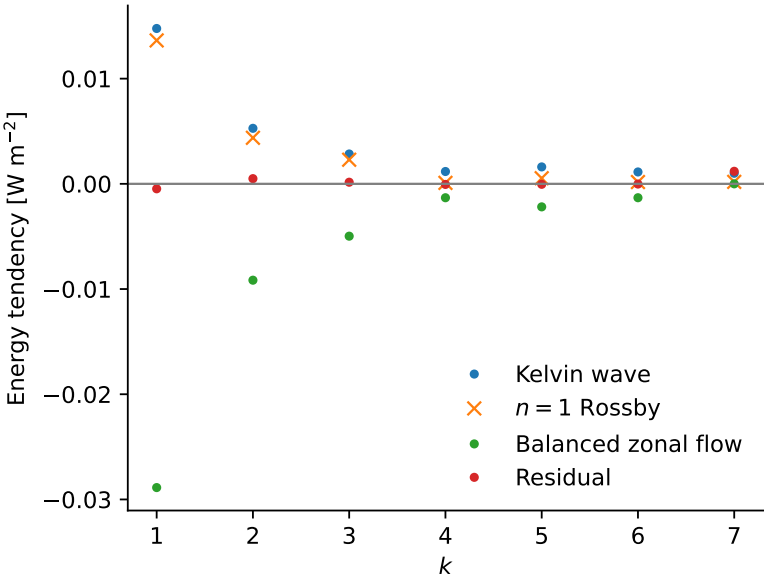

Figure C.3: As in Fig. C.2b, but for different zonal wavenumbers.

The KW energy tendencies due to (R1, R0) interactions are largely associated with the stationary KWs, accounting for 51% for the sum over all k, and 79% for $k = 1$. The remainder is related to temporal variability (Eq. C.16), mainly on seasonal time scales as evident in the co-spectrum (Fig. C.4a). This is consistent with the seasonal variability of KWs discussed by Blaauw and Žagar (2018) and Žagar et al. (2022), and with the power spectra of the KWs and their tendencies being red (Fig. C.19). The secondary peaks in the co-spectrum for eastward propagation on the subseasonal time scale (Fig. C.4a) indicate that the (R1, R0) interactions may play a role for the MJO. For larger positive k, positive KW energy tendencies are found for shorter periods (Figure C.4b), consistent with the dispersion relation of KWs.

In summary, the dynamical KW energy source primarily results from wave-mean flow interactions, mainly (R1, R0) interactions, while wave-wave interactions play a secondary

role. The KW energy tendencies due to (R1, R0) interactions are largest for the most energetic KWs, which have small zonal wavenumbers. The majority of the KW energy tendency due to (R1, R0) interactions is associated with the stationary KWs, and seasonal variability also has a considerable contribution. Therefore, the following analysis of individual advection terms is partly simplified by studying stationary KWs with $k = 1$ for the total time series and for individual seasons.

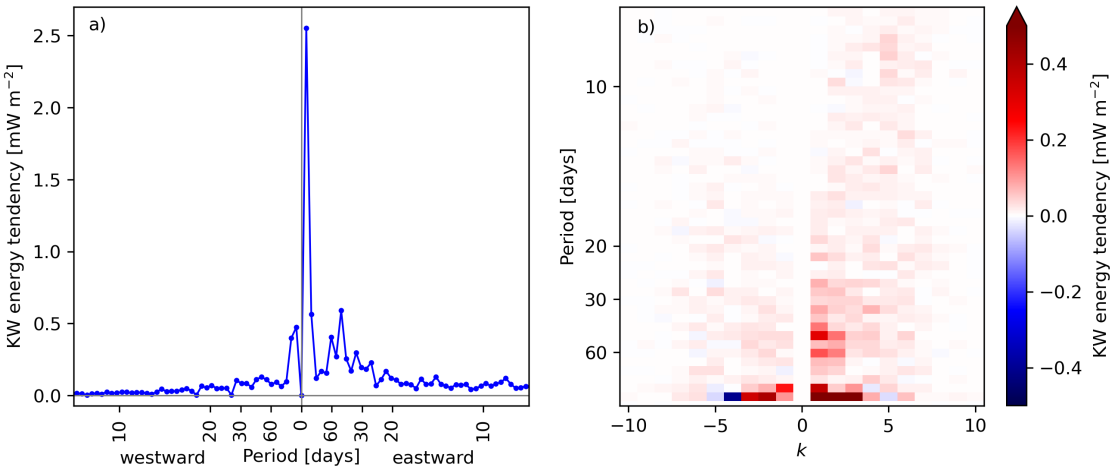

Figure C.4: Co-spectra of KWs and their tendencies due to (R1, R0) interactions, a) sum over all k and m and b) Sum over all m for selected k.

C.3.2 Energy tendencies due to momentum and temperature advection

Now we turn to the various dynamical processes through which energy is transferred between KW, R1 and R0. Figure C.5 shows the time-averaged energy tendencies of these waves decomposed into advection of momentum and temperature, as well as the conversion term, which is small. The KW energy source due to (R1, R0) interactions results from both momentum and temperature advection (Fig. C.5a). In the (G, R0) interactions, the KW energy sink due to vertical temperature advection outweighs the KW energy source due to meridional advection of momentum (Fig. C.5d), so that overall the (G, R0) interactions function as a KW energy sink (Fig. C.2a).

Figure C.6 shows the vertical distribution of the main terms that make up the KW energy tendencies due to (R1, R0) interactions. The KW energy tendencies due to advection of zonal momentum are located in the upper troposphere (Fig. C.6a, b), where the winds are strong (Fig. C.1, Fig. C.7a, c). The small contribution of the stratosphere to the energy tendencies is connected to the low air density. The KW energy tendencies resulting from temperature advection are located slightly below the momentum advection, around 300 hPa (Fig. C.6c, d), because high absolute T_{KW} are found below the strongest wind (Fig. C.1b). The small-scale vertical variations in $A_{T,p}$ are likely numerical, because errors resulting from vertical truncation are magnified in vertical derivatives.

In the following, we examine the mechanisms responsible for the sources and sinks of KW, R1 and R0 energy resulting from interactions of the respective other two modes. To provide simplified explanations of the main processes, we compute momentum and temperature tendencies from 3D fields averaged over the four-year timeseries, i.e., the

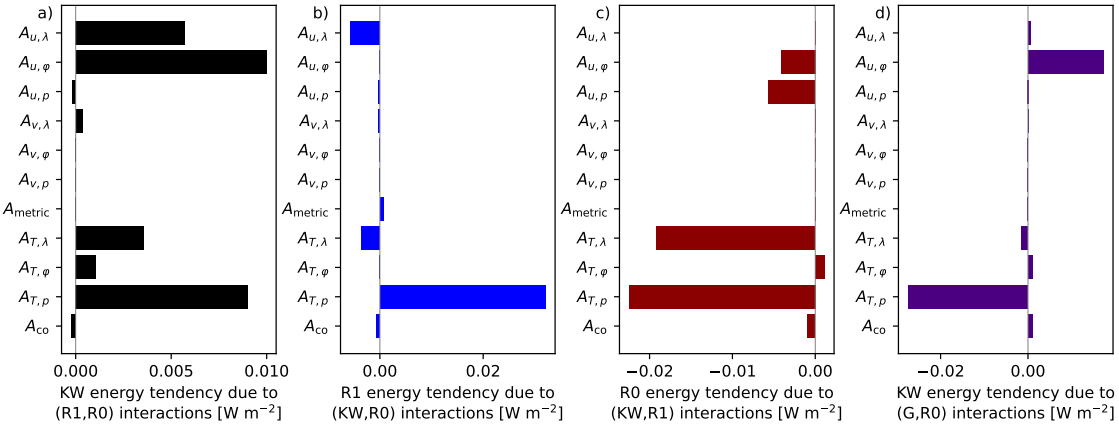

Figure C.5: Dynamical energy tendencies of a), d) KW, b) R1 and c) R0, decomposed into different advection terms, the metric terms and the conversion term as in Eq. (C.7).

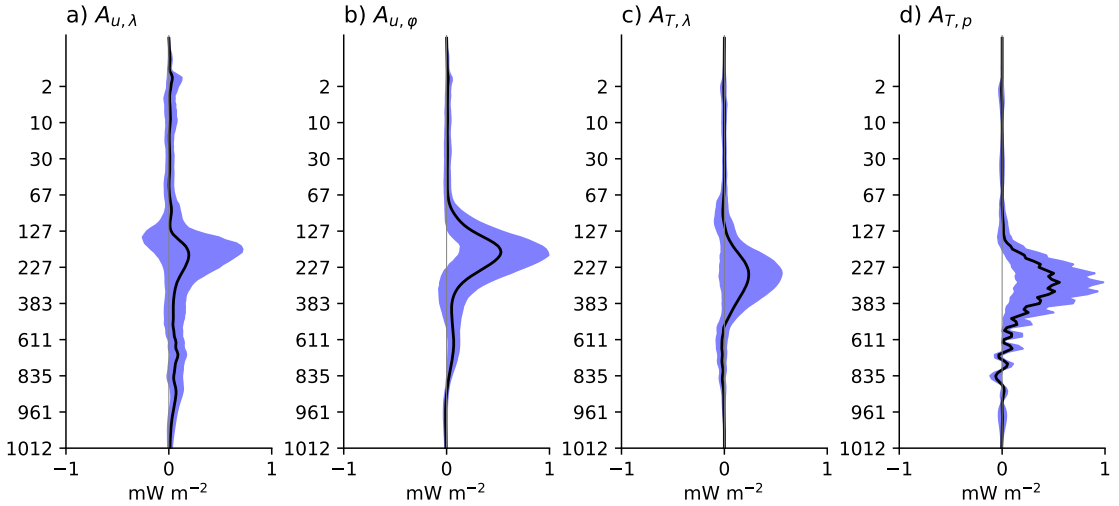

Figure C.6: Vertical distribution of KW energy tendencies due to (R1, R0) interactions resulting from a) zonal advection of zonal momentum, b) meridional advection of zonal momentum, c) zonal advection of temperature and d) vertical advection of temperature, see Eq. (C.7). Black line: time-average, shading: spread between the 10th and 90th percentiles. To display the quantities in W m^{-2}, they are multiplied with $\Delta p/g$, where Δp is the pressure difference between two levels.

stationary waves. The resulting energy tendencies only provide a qualitative overview because they are not equal to those associated with the time-averaged tendencies (first term in Eq. C.7). In addition, seasonal differences illustrate part of the covariability. For some processes, we will streamline the discussion by considering $k = 1$ only, which contributes most to the KW energy tendencies (Fig. C.3).

C.3.2.1 KW energy source due to meridional advection of momentum

The KW energy source due to meridional advection of zonal momentum results from both (R1, R0) and (G, R0) interactions (Fig. C.5a and d). In the following, we discuss $A_{u,\varphi}$ for the (R1, R0) interactions, which is located in the upper troposphere (Fig C.6b). There,

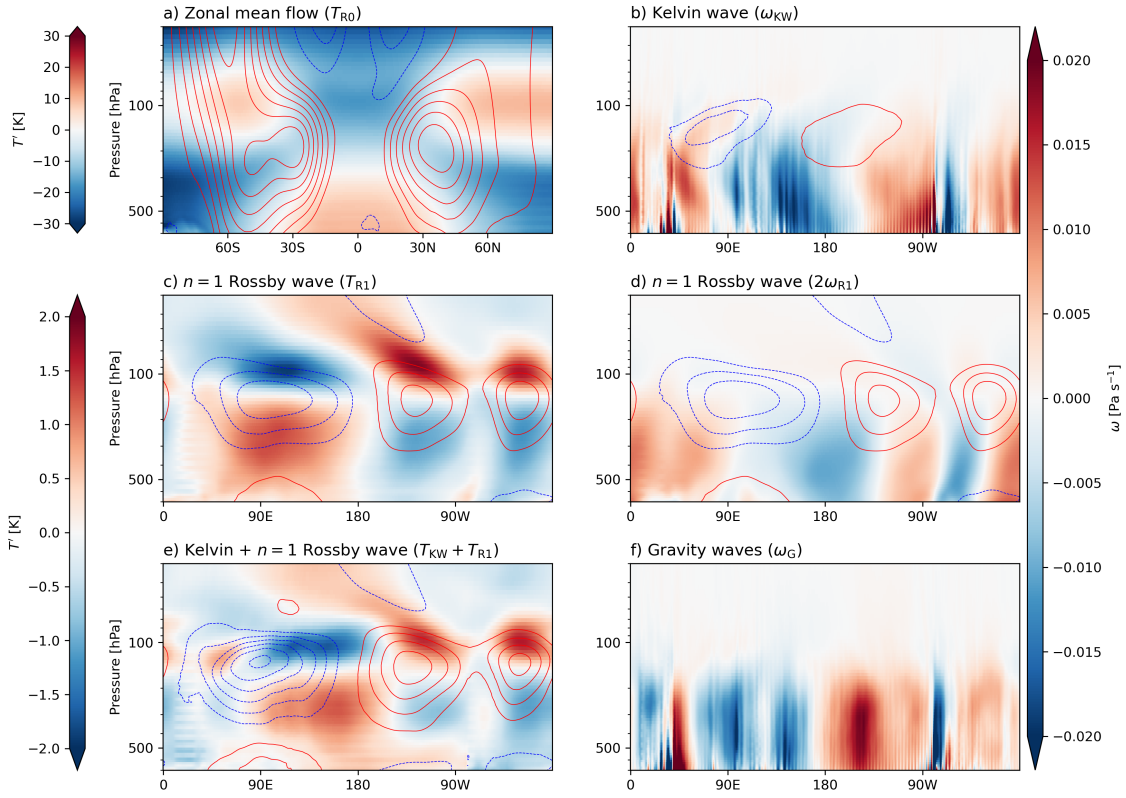

Figure C.7: Vertical cross-sections of velocity and temperature perturbations, averaged over 2016-2019. a) Zonal average, b)-f) average over 15° N to 15° S. Contours show westerly (red) and easterly (blue) winds, with a spacing of a) 4 m s^{-1}, and b)-e) 2 m s^{-1}. The shaded quantity is indicated in brackets.

the stationary KWs feature easterly winds over the Indian Ocean and Maritime Continent, and westerly winds over the Pacific (Fig. C.8a). The KW easterlies over the Indian Ocean are strengthened by advection of u_{R0} away from the equator by v_{R1} (Fig. C.8c, e). Over the Pacific, the KW westerlies are enhanced by advection of u_{R0} towards the equator. Since v_{R1} and the shear of u_{R0} maximize off the equator (Fig. C.9a), the meridional advection of zonal momentum is strongest at the flanks of the meridional structure of the KW (Fig. C.8e).

As described, the KW energy source is collocated with v_{R1}, which is located west of the maximum of u_{KW} (Fig. C.8a, c, e). The configuration of the modes that results in the KW energy source becomes clearer when considering $k = 1$ only (Fig. C.8b, d, f). At 150 hPa on the equator, u_{R1} is shifted eastward relative to u_{KW} by 43°. Therefore, the meridional flow towards (away from) the equator in R1 overlaps with positive (negative) u_{KW}, which are strengthened by the meridional advection (Fig. C.8f). The shift between KW and R1 is also important for the other advection terms, which will be discussed in sections C.3.2.2, C.3.2.3 and C.3.2.4.

The latitudinal location of $A_{u,\varphi}$ depends on the shear of u_{R0}, which is strongest in the northern (southern) hemisphere in DJF (JJA) (Fig. C.9a). Accordingly, the location of the KW energy tendencies varies with the seasons (Fig. C.9b). In the average over all seasons, the contributions of both hemispheres to $A_{u,\varphi}$ are of similar magnitude. The location of

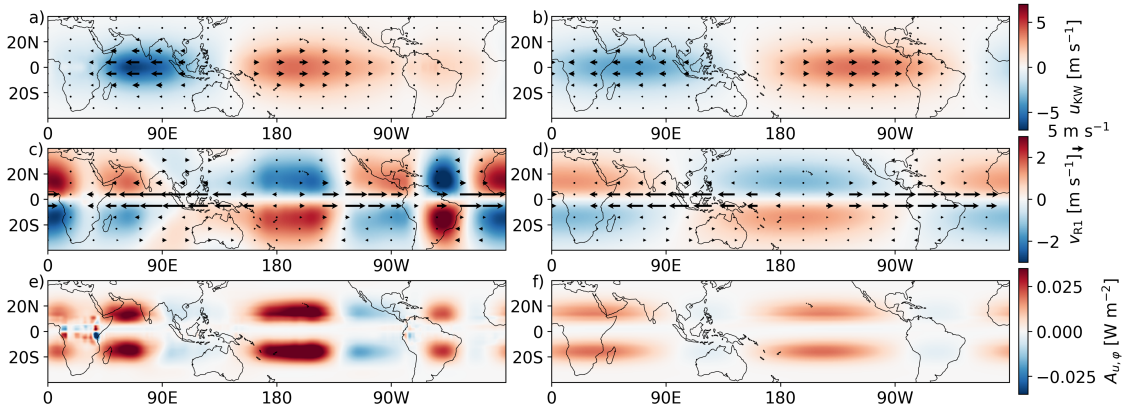

Figure C.8: Horizontal circulation of stationary a), b) Kelvin waves and c), d) $n = 1$ Rossby waves at 150 hPa, and e), f) horizontal distribution of KW energy tendencies due to meridional advection of u_{R0} by v_{R1}, computed from stationary waves. a), c) and e) show all zonal wavenumbers, b), d) and f) only $k = 1$.

$A_{u,\varphi}$ due to (R1, R0) interactions in the winter hemisphere is in line with the findings of Holube et al. (2025b) for the combined interactions of all modes.

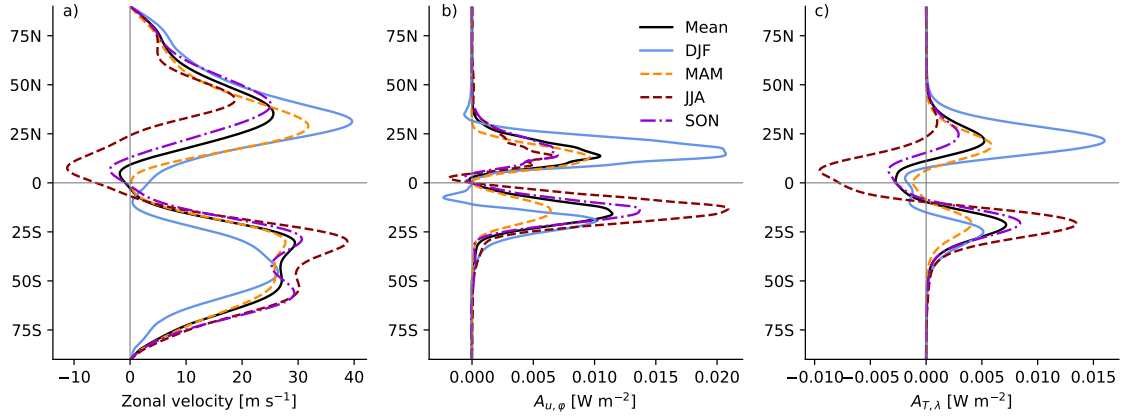

Figure C.9: Latitudinal profiles of a) time-averaged balanced zonal mean flow at 150 hPa, and b), c) KW energy tendencies, computed from stationary waves, due to b) meridional advection of u_{R0} by v_{R1}, and c) zonal advection of T_{R1} by u_{R0}.

C.3.2.2 Energy transfer from R1 to KW by zonal advection

KWs gain energy through zonal advection of both u_{R1} and T_{R1} by u_{R0} ($A_{u,\lambda}$ and $A_{T,\lambda}$ in Fig. C.5a). This KW energy source is associated with a R1 energy sink with the same magnitude, and therefore, energy is transferred from R1 to KW. These two energy tendencies are related as follows, due to the periodic boundary conditions in zonal direction:

$$\begin{aligned} 0 &= \int_V \frac{\partial}{\partial \lambda}\left(\frac{1}{a\cos\varphi} u_{R0} x_{KW} x_{R1}\right) dV \\ &= \int_V \frac{1}{a\cos\varphi} u_{R0} x_{KW} \frac{\partial x_{R1}}{\partial \lambda}\, dV + \int_V \frac{1}{a\cos\varphi} u_{R0} x_{R1} \frac{\partial x_{KW}}{\partial \lambda}\, dV\,. \end{aligned} \tag{C.17}$$

The first (second) summand on the right-hand side of Eq. (C.17) is the KW (R1) energy tendency due to zonal advection of x_{R1} (x_{KW}), where x can be u or T. In the case of T, the pressure-dependent factor R/γ_0 is included in both terms.

We first consider the KW energy tendency due to zonal advection of u_{R1}, which takes place in the upper troposphere (Fig. C.6a) around the equator (Fig. C.10a). There, positive (negative) $\partial u_{R1}/\partial\lambda$ is collocated with westerly (easterly) u_{KW} (Fig. C.8a-d). Advection by the zonal mean winds, which are easterlies in the time average (Fig. C.9a), therefore strengthens the KW wind, resulting in an energy source (Fig. C.10a). Conversely, zonal advection of u_{KW} by u_{R0} results in a R1 energy sink, as positive (negative) $\partial u_{KW}/\partial\lambda$ coincides with easterly (westerly) u_{R1}. For $k = 1$, this sink is located over the Maritime Continent and South America (Fig. C.10b). The energy sources and sinks in Fig. C.10a and b, which are computed from the stationary waves for the total time series, mainly show the effect of the equatorial easterlies in JJA (Fig. C.9a).

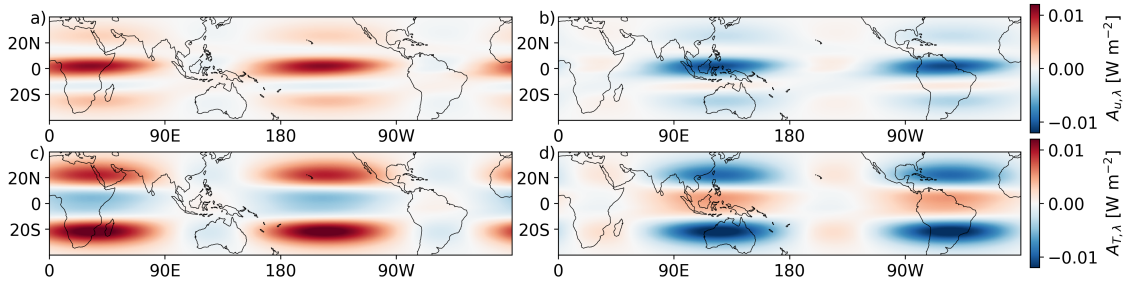

Figure C.10: Horizontal distribution of KW and R1 energy tendencies due to zonal advection by u_{R0}, computed from stationary waves with $k = 1$. a), c) KW energy tendencies due to advection of a) u_{R1}, c) T_{R1}; b), d) R1 energy tendencies due to advection of b) u_{KW}, d) T_{KW}.

Turning to the energy tendencies due to advection of temperature, we first note that the KW temperatures have the same sign as the KW zonal winds above, while the R1 temperatures have opposite signs as the R1 zonal winds above (Fig. C.1b and C.7c). At the longitudes where u_{R1} and u_{KW} coincide, the temperatures thus partly balance out each other (Fig. C.7e). This is consistent with Žagar and Franzke (2015), who found opposite signs of geopotential perturbations in the Rossby and inertia-gravity waves associated with the MJO. Around the date line, both KW and R1 contribute to the positive and negative temperature perturbations observed in the upper troposphere and lower stratosphere (Fig. C.1a).

The energy tendencies due to advection of temperature are governed by u_{R0} around 300 hPa, shown in Fig. C.20, which is however similar to u_{R0} at 150 hPa. The equatorial easterlies advect positive T_{R1} towards the longitudes of negative T_{KW}, and vice versa, resulting in a KW energy sink (Fig. C.10c). This sink is outweighed by the advection of T_{R1} into the other direction by the westerly u_{R0} at higher latitudes (Fig. C.10c), so that in total, $A_{T,\lambda}$ is a KW energy source. The R1 energy sink arises from zonal advection of T_{KW} by westerlies in the subtropics (Fig. C.10d).

In all seasons, zonal advection of temperature leads to a KW energy sink on the equator and sources off the equator, but their location and magnitude have an annual cycle (Fig. C.9c). The subtropical KW energy source due to advection of T_{R1} is located in the winter hemisphere, where the westerlies are stronger and closer to the equator (Fig. C.9a). In JJA, the KW energy sink resulting from the strong equatorial easterlies has

a similar magnitude as the KW energy source at higher latitudes, so that in total, $A_{T,\lambda}$ is small. The highest values of $A_{T,\lambda}$ are found in DJF (Fig. C.9c), when the equatorial easterlies are weaker (Fig. C.20).

The longitudinal phase shift between KW and R1 is essential for the energy transfer between them through zonal advection by R0. In particular, the maxima of u_{R1} are located east of those of u_{KW}, and positive T_{R1} is located west of T_{KW}. While the zonal advection of zonal momentum is associated with equatorial easterlies, temperature advection is dominated by the westerlies in the subtropics, because the decrease of T_{R1} away from the equator is less steep than that of u_{R1}. Therefore, zonal advection of both momentum and temperature by R0 result in a KW energy source and R1 energy sink. This sink is however outweighed by a R1 energy source due to vertical advection of T_{R0} by ω_{KW} (Fig. C.2), which will be explained in the following subsection.

C.3.2.3 KW and R1 energy tendencies due to vertical advection of temperature

Both KW and R1 gain energy through vertical advection of T_{R0} by the respective other mode ($A_{T,p}$ in Fig. C.5a and b). This process is located at similar vertical levels as the energy tendency resulting from zonal advection of temperature (Fig. C.6c, d). Because T_{R0} decreases with height (Fig. C.7a), upward (downward) advection of T_{R0} by negative (positive) ω leads to warming (cooling). Note that the cooling due to adiabatic expansion associated with ascending motion is not discussed here, because the linear part of this process is considered via the static stability in the linear terms, which do not result in energy tendencies, while the nonlinear part is the conversion term, which is small (Fig. C.5).

A KW energy source (Fig. C.11a) results from downward advection of T_{R0} by ω_{R1} around 70° E (Fig. C.7d), which intensifies the negative T_{KW} (Fig. C.1b), and also from positive T_{KW} being enhanced through upward advection of T_{R0} by ω_{R1} around the date line. Similarly, a R1 energy source (Fig. C.11b) arises from strengthened T_{R1} due to upward advection of T_{R0} by negative ω_{KW} between 90° E and 180°, and through downward advection of T_{R0} by positive ω_{KW} in the western hemisphere (Fig. C.7b, c).

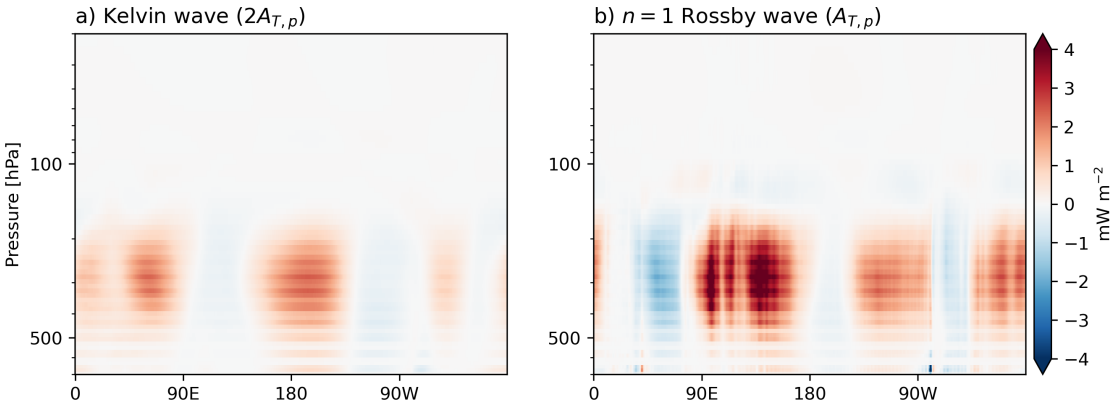

Figure C.11: Vertical cross-sections of a) KW energy tendencies due to vertical advection of T_{R0} by ω_{R1}, b) R1 energy tendencies due to vertical advection of T_{R0} by ω_{KW}, computed from stationary waves. To display the quantities in W m^{-2}, they are multiplied with $\Delta p/g$, where Δp is the pressure difference between two levels.

In contrast, $A_{T,p}$ resulting from (G, R0) interactions is a KW energy sink (Fig. C.5d). This can be explained by the opposite signs of ω_G and ω_{R1} at longitudes with large absolute T_{KW}. Specifically, upward advection of T_{R0} by ω_G around 90° E (Fig. C.7f) reduces the magnitude of the negative T_{KW}. East of the date line, downward ω_G coinciding with positive T_{KW} also contributes to the KW energy sink.

Returning to the (R1, R0) interactions, we now discuss the seasonal variations of the KW energy tendencies due to vertical advection of T_{R0} by ω_{R1}. In DJF, the largest upward ω_{R1} is located over the central Pacific (Fig. C.12a). This strengthens the positive T_{KW} at these longitudes by advecting warm T_{R0} upward (Fig. C.12c). A smaller KW energy source is located around 90° E, where ω_{R1} is downward. In the western hemisphere, ω_{R1} has larger absolute values, but the KW temperature is small (Fig. C.1b), so that the contribution to the KW energy tendencies is small there (Fig. C.12c). In JJA, strong downward ω_{R1} is found around 60° E (Fig. C.12b), which strengthens the negative T_{KW} and results in large values of $A_{T,p}$. This KW energy source is partly counteracted as the negative T_{KW} around 90° E are weakened through upward advection of T_{R0} by ω_{R1} (Fig. C.12b, c). In the transitional seasons and in the time average, the main contributions to the KW energy source are located at longitudes between the maxima in JJA and DJF.

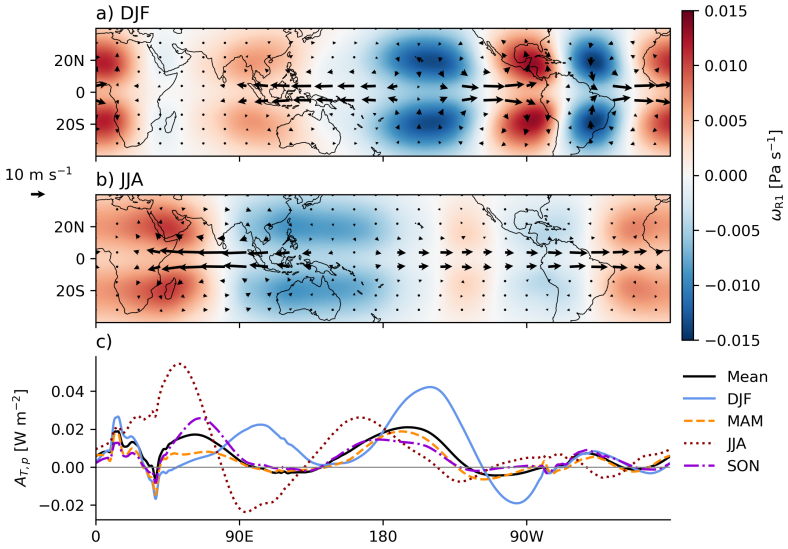

Figure C.12: Vertical velocity at 300 hPa (shading) and horizontal velocity at 150 hPa (arrows) of R1 in a) DJF, and b) JJA. c) KW energy tendency due to vertical advection of T_{R0} by ω_{R1}, computed from stationary waves.

In summary, vertical advection of T_{R0} by R1 and KW transfers energy to the respective other wave. As with zonal and meridional advection of momentum (section C.3.2.1 and C.3.2.2), this process takes place because of the phase shift between KW and R1.

C.3.2.4 R0 energy sink due to (KW, R1) interactions

This section discusses the R0 energy sink due to (R1, KW) interactions, which is connected to the KW energy source due to (R1, R0) interactions and the R1 energy source due to (KW, R0) interactions. These energy tendencies consist of several advection terms, some of which are small (Fig. C.5). For some terms, this results from v_{KW} being small and

$v_{R0} = \omega_{R0} = 0$, while for other terms, for example the KW energy tendencies due to vertical advection of momentum, no such explanation is provided here.

The largest of the energy tendency terms associated with momentum advection are

$$
\begin{aligned}
&- \int_V \frac{v_{R1}}{a\cos\varphi} \frac{\partial (u_{R0}\cos\varphi)}{\partial \varphi} u_{KW}\, dV - \int_V \left(\omega_{R1} \frac{\partial u_{KW}}{\partial p} + \omega_{KW} \frac{\partial u_{R1}}{\partial p} \right) u_{R0}\, dV \\
&\quad - \int_V \frac{1}{a\cos\varphi} \left(v_{R1} \frac{\partial (u_{KW}\cos\varphi)}{\partial \varphi} + v_{KW} \frac{\partial (u_{R1}\cos\varphi)}{\partial \varphi} \right) u_{R0}\, dV \approx 0\,,
\end{aligned}
\tag{C.18}
$$

which approximately balance out to zero because the corresponding other terms in Eq. (C.13) are small. Accordingly, the KW energy source due to meridional advection of zonal momentum (first integral in Eq. C.18) is associated with the R0 energy sink due to vertical advection of zonal momentum (second integral in Eq. C.18) and the R0 energy sink due to meridional advection of zonal momentum (third integral in Eq. C.18). This indicates an energy transfer from R0 to KW.

Similarly, the largest KW, R1 and R0 energy tendencies due to temperature advection, i.e. the largest terms in Eq. (C.14), are

$$
\begin{aligned}
&- \int_V \frac{R}{\gamma_0} \omega_{R1} \frac{\partial T_{R0}}{\partial p} T_{KW}\, dV - \int_V \frac{R}{\gamma_0} \omega_{KW} \frac{\partial T_{R0}}{\partial p} T_{R1}\, dV \\
&\quad - \int_V \frac{R}{\gamma_0} \frac{1}{a\cos\varphi} \left(u_{R1} \frac{\partial T_{KW}}{\partial \lambda} + u_{KW} \frac{\partial T_{R1}}{\partial \lambda} \right) T_{R0}\, dV \\
&\quad - \int_V \frac{R}{\gamma_0} \left(\omega_{R1} \frac{\partial T_{KW}}{\partial p} + \omega_{KW} \frac{\partial T_{R1}}{\partial p} \right) T_{R0}\, dV \approx 0\,.
\end{aligned}
\tag{C.19}
$$

The KW energy source due to vertical advection of temperature (first integral in Eq. C.19) is therefore connected to the R1 energy source due to vertical advection of temperature (second integral in Eq. C.19), as well as the R0 energy sinks due to zonal and vertical advection of temperature (third and fourth integral in Eq. C.19, respectively).

In the following, we will illustrate the processes underlying the R0 energy sink due to (R1, KW) interactions using the stationary waves for $k = 1$. The meridional advection of u_{KW} by v_{R1} results in easterly momentum tendencies, as v_{R1} advects easterly u_{KW} towards the subtropics in the eastern hemisphere, and westerly u_{KW} towards the equator over the Pacific (Fig. C.8b, d). These easterly momentum tendencies weaken the westerly u_{R0} off the equator, this is a R0 energy sink (Fig. C.13a). In JJA, the easterlies at the equator and in the northern-hemisphere subtropics are enhanced by the easterly tendencies, which partly balances the mentioned R0 energy sink, so that $A_{u,\varphi}$ is a smaller sink than in the other seasons. Overall, the R0 energy sink due to meridional advection is located in the winter hemisphere (Fig. C.13a).

The R0 energy sink due to vertical advection of u in the (KW, R1) interactions consists of two processes: Advection of u_{KW} by ω_{R1} and advection of u_{R1} by ω_{KW} (second integral in Eq. C.18). We first discuss the latter, which leads to greater energy tendencies because ω_{KW} and u_{R1} are stronger than ω_{R1} and u_{KW}, respectively. In the eastern hemisphere, upward ω_{KW} is collocated with u_{R1} that decreases with height (Fig. C.14a, b). This results in westerly momentum tendencies in the mid-troposphere. In the western hemisphere, westerly momentum tendencies are found as well, because the signs of both ω_{KW} and u_{R1} are flipped. This weakens the easterly u_{R0} on the equator and thus decreases the energy of R0 (Fig. C.14c). Seasonal variations of this process appear due to the annual

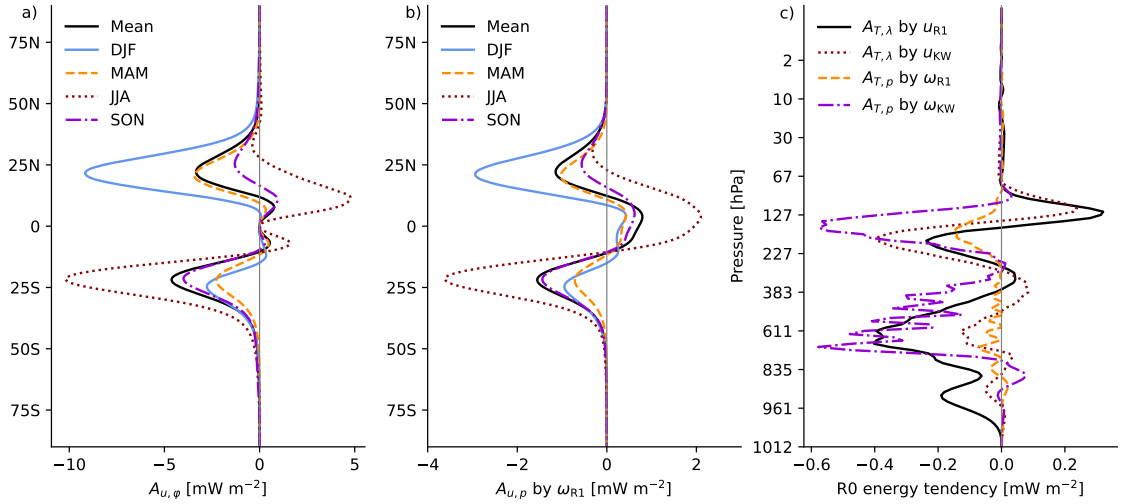

Figure C.13: R0 energy tendencies, computed from stationary waves with $k = 1$, due to a) meridional advection of u_{KW} by v_{R1}, b) vertical advection of u_{KW} by ω_{R1}, c) zonal and vertical temperature advection by KW and R1. To display the energy tendencies in c) in W m^{-2}, they are multiplied with $\Delta p/g$, where Δp is the pressure difference between two levels.

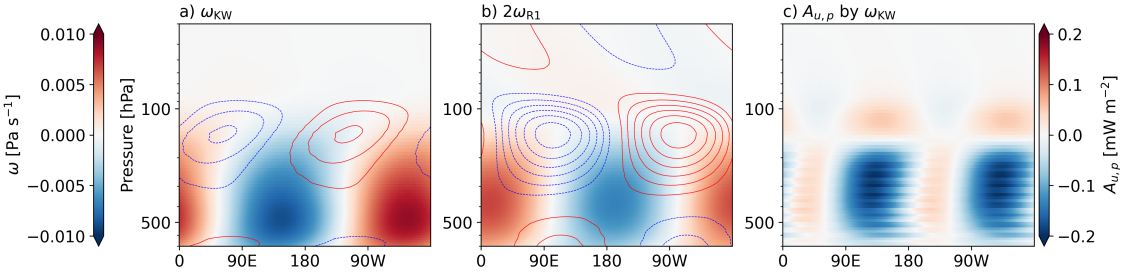

Figure C.14: Pressure vertical velocity ω of a) $n = 1$ Rossby waves and b) Kelvin waves with $k = 1$, averaged over 2016-2019 and over 15° N to 15° S. Contours show westerly (red) and easterly (blue) zonal winds, with a spacing of 1 m s^{-1}. c) R0 energy tendency due to vertical advection of u_{R1} by ω_{KW}, computed from stationary waves with $k = 1$. To display the energy tendency in W m^{-2}, it is multiplied with $\Delta p/g$, where Δp is the pressure difference between two levels.

cycle of KW and R1 energy and the weaker equatorial easterlies in DJF, for brevity we do not provide more detail here.

The R0 energy sink due to advection of u_{KW} by ω_{R1} (Fig. C.13b) has a similar latitudinal profile as the R0 energy sink due to meridional advection (Fig. C.13a). In the mid-troposphere, upward (downward) ω_{R1} is collocated with u_{KW} that increases (decreases) with height (Fig. C.14a, b). This results in easterly tendencies of u_{R0}, so that the westerlies in the winter hemisphere are weakened and the equatorial easterlies in JJA are strengthened (Fig. C.13b).

The R0 energy tendencies resulting from zonal and vertical temperature advection consist of two terms each (Eq. C.19), affecting different pressure-levels (Fig. C.13c). The positive T_{R0} in the lower tropical troposphere is weakened because upward (downward) ω_{KW} is located at the longitudes where T_{R1} increases (decreases) with height at lower levels ($A_{T,p}$ by ω_{KW} in Fig. C.13c). In the lower and mid-troposphere, westerly (easterly)

u_{R1} are collocated with eastward increasing (decreasing) T_{KW}, which also results in negative temperature tendencies, i.e. a R0 energy sink ($A_{T,\lambda}$ by u_{R1} in Fig. C.13c). Above 250 hPa, the two aforementioned processes also decrease the negative T_{R0} because u_{R1} and the zonal gradients of T_{R1} have a baroclinic structure. On higher levels, around 150 hPa, the R0 energy tendency due to zonal advection of T_{KW} by u_{R1} is positive (Fig. C.13c) due to the sign change of T_{KW} (Fig. C.1b). Such a sign change also appears in T_{R1}, so that its zonal advection also results in a R0 energy source around 150 hPa. Finally, the vertical advection of T_{KW} by ω_{R1} results in a smaller R0 energy sink.

In summary, the (KW, R1) interactions decrease the R0 energy by weakening the subtropical westerlies and equatorial easterlies of u_{R0}, as well as T_{R0} in the tropical upper and lower troposphere. However, the (KW, R1) interactions are associated with only 3.3% of the R0 energy sink due to all mode interactions.

C.4 Discussion

We demonstrated that the dynamical KW energy source mainly results from (R1, R0) interactions, which however do not involve resonant triads. The eigenfrequencies from linear theory of KW and R1 do not fulfill the resonance condition together with R0, which has an eigenfrequency of zero. Therefore, R0 does not necessarily act as a catalyst mode, in contrast to the resonant triads discussed by Raupp et al. (2008). In fact, we find that R0 loses energy. However, the energy exchange between R1 and KW due to their interactions with R0, i.e., the energy tendencies resulting from zonal advection of momentum and temperature, occurs independently of the R0 energy tendencies.

Wave-mean flow interactions result in greater KW energy tendencies than wave-wave interactions (section C.3.1), this is also found in shallow-water model simulations (Holube et al., 2024). In addition, we identified meridional advection of the zonal background flow as the primary process underlying the KW energy source in reanalysis data, which is composed of (R1, R0) and (G, R0) interactions. Similarly, meridional advection of vorticity amplifies KWs in shallow-water model simulations (Barpanda et al., 2023). However, our results do not provide conclusive evidence for the resonant KW excitation by subtropical Rossby waves as simulated by Holube et al. (2024). On the one hand, the positive KW energy tendencies for eastward-propagating waves (Fig. C.4b) support the possibility for resonance effects, and this spectrum qualitatively resembles the results of Cheng et al. (2022) for the KW excitation through eddy momentum flux convergence in the subtropics. On the other hand, the role of higher-latitude influences in our study remains unclear, because the R1 waves could be forced by tropical convection, they are not necessarily linked to wave trains advected by the subtropical jet. The equatorward propagation of such wave trains could be evident as an energy transfer from higher to lower meridional Rossby modes, this is subject of further studies.

We have described energy transfers from R1 to KW, both through zonal advection of momentum and temperature by R0 (section C.3.2.2) and through (R1, R1) interactions (Fig. C.2a). This direction of energy transfer is opposite to that found by Raphaldini et al. (2021) and Teruya et al. (2024) using data-driven methods. However, their results should be interpreted with caution because they were obtained from the time series of wave amplitudes or energy, which do not contain information about the wave phases. Further reasons for the differences could be that the previous studies also considered moist processes, while we evaluated the energy transfers due to dry dynamical processes

only. In addition, the energy exchange between KW and R1 in triads involving KW, R1 and a third mode except for R0 and R1 has not been evaluated here.

The large contribution of wave-mean flow interactions to the dynamical KW energy source suggests that the mean flow can be an important influencing factor for KWs. In a shear flow, KWs acquire meridional velocities, as demonstrated for the primitive equations, truncated to a few vertical modes (Ferguson et al., 2009; Namazi and Khouider, 2013), also when convection is accounted for (Han and Khouider, 2010). These meridional velocities deviate from the KW structure that follows from the linear shallow-water equations, so that the KWs in the mentioned previous studies would be represented as a combination of normal modes in the framework applied here. While a flow-dependent definition of KWs might reflect the atmospheric conditions more accurately, it would complicate the energy diagnostics. In contrast, the KW as one of the eigenmodes of the linearized equations around the state of rest is an unambiguous definition, which has the advantage that these eigenmodes are orthogonal.

C.5 Conclusions and Outlook

To investigate which modes transfer energy to KWs through dynamical processes, we have split the KW energy tendencies into the contributions of wave-wave and wave-mean flow interactions. The interactions of R1 waves with the balanced zonal mean flow are the largest contributor to the dynamical KW energy source, mainly through advection of R0 zonal momentum by the R1 meridional velocity. The KW energy source due to meridional advection of zonal momentum is to a larger extent due to gravity wave-mean flow interactions than (R1, R0) interactions. However, in total, the (G, R0) interactions result in a KW energy sink, because the upward advection of positive temperature perturbations by gravity waves weakens the negative KW temperature over the Maritime Continent. In contrast, vertical advection of temperature by R1 induces negative temperature tendencies over the Indian Ocean, which result in a KW energy source. Another KW energy source consists of (R1, R1) interactions, which transfer energy from R1 to KWs.

The energy gained by KWs through (R1, R0) interactions is supplied by R1 and R0 in different portions (Fig. C.15). Zonal advection of momentum and temperature by the mean flow transfers energy from R1 to KW. The associated energy loss of R1 is outweighed by a R1 energy source due to vertical advection of R0 temperature by the Kelvin waves.

The KW energy source due to vertical advection of R0 temperature by R1 is associated with an energy loss of R0 due to zonal and vertical advection of temperature (Fig. C.15). The relative contribution of these two processes to the KW energy source is not clear because the energy tendencies due to advection of temperature (Eq. C.19) are also connected to a R1 energy source.

Finally, energy is transferred from R0 to KW by meridional advection of u_{R0} by v_{R1} in the upper troposphere. Located on the flanks of the KW meridional structure, this strengthens the KW zonal winds, and weakens the subtropical westerlies of R0 in the winter hemisphere.

Most of the KW energy source due to (R1, R0) interactions is found in the zonal wavenumbers and vertical modes for which the KW energy is high, i.e. small k and troposphere-baroclinic vertical modes. For these modes, a considerable part of the energy

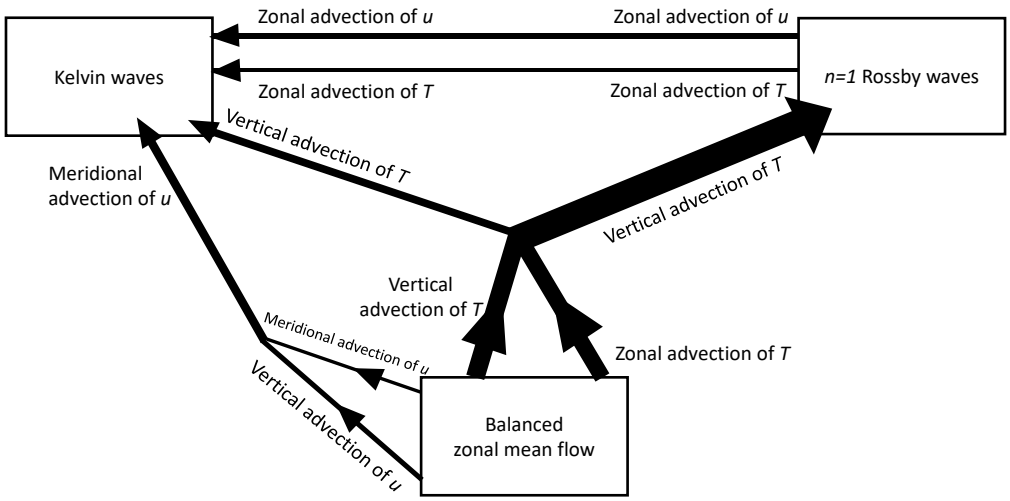

Figure C.15: Schematic illustration of the main energy tendency terms, i.e. those in Equations (C.17), (C.18) and (C.19), where the thickness of the arrows is proportional to the energy tendencies, also shown in Fig. C.5a-c.

source is associated with the stationary waves, and a smaller fraction comes from seasonal variability. In addition, (R1, R0) interactions are found to be an energy source for higher zonal wavenumbers and frequencies, which could hint at resonance effects with propagating waves that have a period of several days.

The described momentum and temperature tendencies result in a KW energy source because the stationary KW is shifted relative to R1, this shift amounts to 43° for $k = 1$ in the time-averaged upper-troposphere zonal velocity. The stationary circulation response to heating with a specific zonal wavenumber, discussed by Matsuno (1966), also shows a shift between KW and R1, which depends on the dissipation rate. However, using strong dissipation for modeling stationary waves might not be realistic (Stechmann and Ogrosky, 2014, and references therein). The configuration of KW and R1 could also depend on the background flow, which can impact the response to a heat source as evident in idealized simulations (e.g., Monteiro et al., 2014). The reasons for the described shift of the stationary waves in the atmosphere remain to be investigated in further studies.

Future work should address the question whether part of the energy source results from waves originating at higher latitudes, because this is a possible avenue for extratropical impacts on the tropics. In addition, the described dry dynamical processes could be complemented by considering effects of moisture. Finally, quantifying wave-mean flow and wave-wave interactions might provide a better understanding of the coupling between KW and R1 in the dynamical structure of the MJO.

C.6 Supporting Information

C.6.1 Introduction

This Supporting Information contains:

- Equations for energy tendencies resulting from different dynamical processes (Text S1).
- Equations for energy fluxes through the surface and additional terms resulting from the vertical variation of the reference stability (Text S2).
- A figure of vertical structure functions for selected vertical modes (Fig. C.16).
- The spectrum of Kelvin wave energy as a function of zonal wavenumber (Fig. C.17).
- Spectra of energy and energy tendencies of Kelvin waves as a function of vertical mode (Fig. C.18).
- Power spectra of Kelvin waves and their energy tendencies due to (R1, R0) interactions (Fig. C.19).
- A figure showing the balanced zonal mean flow, averaged over different seasons and the entire year (Fig. C.20).

C.6.2 Text S1.

Energy tendencies of a 3D normal mode are obtained by integrating the product of velocity (temperature) of this mode and the velocity (temperature) tendency over the atmosphere. The nonlinear momentum and temperature tendencies result from advection in different spatial directions, metric terms and the conversion term. In the following, the individual energy tendencies of the mode r are listed:

$$A_{u,\lambda} = -\int_V \frac{u}{a\cos\varphi}\frac{\partial u}{\partial \lambda}u_r\,dV\,, \tag{C.20}$$

$$A_{u,\varphi} = -\int_V \frac{v}{a\cos\varphi}\frac{\partial (u\cos\varphi)}{\partial \varphi}u_r\,dV\,, \tag{C.21}$$

$$A_{u,p} = -\int_V \omega\frac{\partial u}{\partial p}u_r\,dV\,, \tag{C.22}$$

$$A_{v,\lambda} = -\int_V \frac{u}{a\cos\varphi}\frac{\partial v}{\partial \lambda}v_r\,dV\,, \tag{C.23}$$

$$A_{v,\varphi} = -\int_V \frac{v}{a\cos\varphi}\frac{\partial (v\cos\varphi)}{\partial \varphi}v_r\,dV\,, \tag{C.24}$$

$$A_{v,p} = -\int_V \omega\frac{\partial v}{\partial p}v_r\,dV\,, \tag{C.25}$$

$$A_{\text{metric}} = -\int_V \frac{\tan\varphi}{a}(u^2+v^2)v_r\,dV\,, \tag{C.26}$$

$$A_{T,\lambda} = -\int_V \frac{R}{\gamma_0}\frac{u}{a\cos\varphi}\frac{\partial T}{\partial \lambda}T_r\,dV\,, \tag{C.27}$$

$$A_{T,\varphi} = -\int_V \frac{R}{\gamma_0}\frac{v}{a}\frac{\partial T}{\partial \varphi}T_r\,dV\,, \tag{C.28}$$

$$A_{T,p} = -\int_V \frac{R}{\gamma_0}\omega\frac{\partial T}{\partial p}T_r\,dV\,, \tag{C.29}$$

$$A_{\text{co}} = \int_V \frac{\omega R T'}{\gamma_0 c_p}T_r\,dV\,. \tag{C.30}$$

Substituting the velocity and temperature tendencies with the respective terms of the wave-mean flow or wave-wave interactions yields the energy tendencies of the mode r due to these interactions. For example, the energy tendency resulting from meridional advection of u_{R0} by R1 is

$$A_{u,\varphi}(\text{R1},\text{R0}) = -\int_V \frac{v_{\text{R1}}}{a\cos\varphi}\frac{\partial (u_{\text{R0}}\cos\varphi)}{\partial \varphi}u_r\,dV\,. \tag{C.31}$$

c.6.3 Text S2.

In a triad consisting of the modes a, b and r, the energy tendencies of a due to (b,r) interactions are connected to energy tendencies of b due to (a,r) interactions and energy tendencies of r due to (a,b) interactions according to

$$\int_V \left[\mathbf{B}(b,r) \cdot \begin{pmatrix} u_a \\ v_a \\ \frac{R}{\gamma_0} T_a \end{pmatrix} + \mathbf{B}(a,r) \cdot \begin{pmatrix} u_b \\ v_b \\ \frac{R}{\gamma_0} T_b \end{pmatrix} + \mathbf{B}(a,b) \cdot \begin{pmatrix} u_r \\ v_r \\ \frac{R}{\gamma_0} T_r \end{pmatrix} \right] dV = E_{abr} + F_{abr} \,. \quad \text{(C.32)}$$

The right-hand side of Eq. (C.32) represents the flux of kinetic energy through the surface

$$E_{abr} = -\int_S \left[\omega_a (u_b u_r + v_b v_r) + \omega_b (u_a u_r + v_a v_r) + \omega_r (u_a u_b + v_a v_b) \right] dS \quad \text{(C.33)}$$

and

$$\begin{aligned} F_{abr} = \; & - \frac{R}{\gamma_0(p_s)} \int_S [\omega_a(p_s) T_b(p_s) T_r(p_s) + \omega_b(p_s) T_a(p_s) T_r(p_s) \\ & + \omega_r(p_s) T_a(p_s) T_b(p_s)] dS \\ & - \int_V \left[R T_b T_r \omega_a \frac{\partial}{\partial p} \left(\frac{1}{\gamma_0} \right) - R T_r T_a \omega_b \frac{\partial}{\partial p} \left(\frac{1}{\gamma_0} \right) - R T_a T_b \omega_r \frac{\partial}{\partial p} \left(\frac{1}{\gamma_0} \right) \right] dV \,, \end{aligned} \quad \text{(C.34)}$$

which combines the flux of available potential energy through the surface and terms resulting from vertical variations of the reference stability.

c.6.4 Supporting Figures

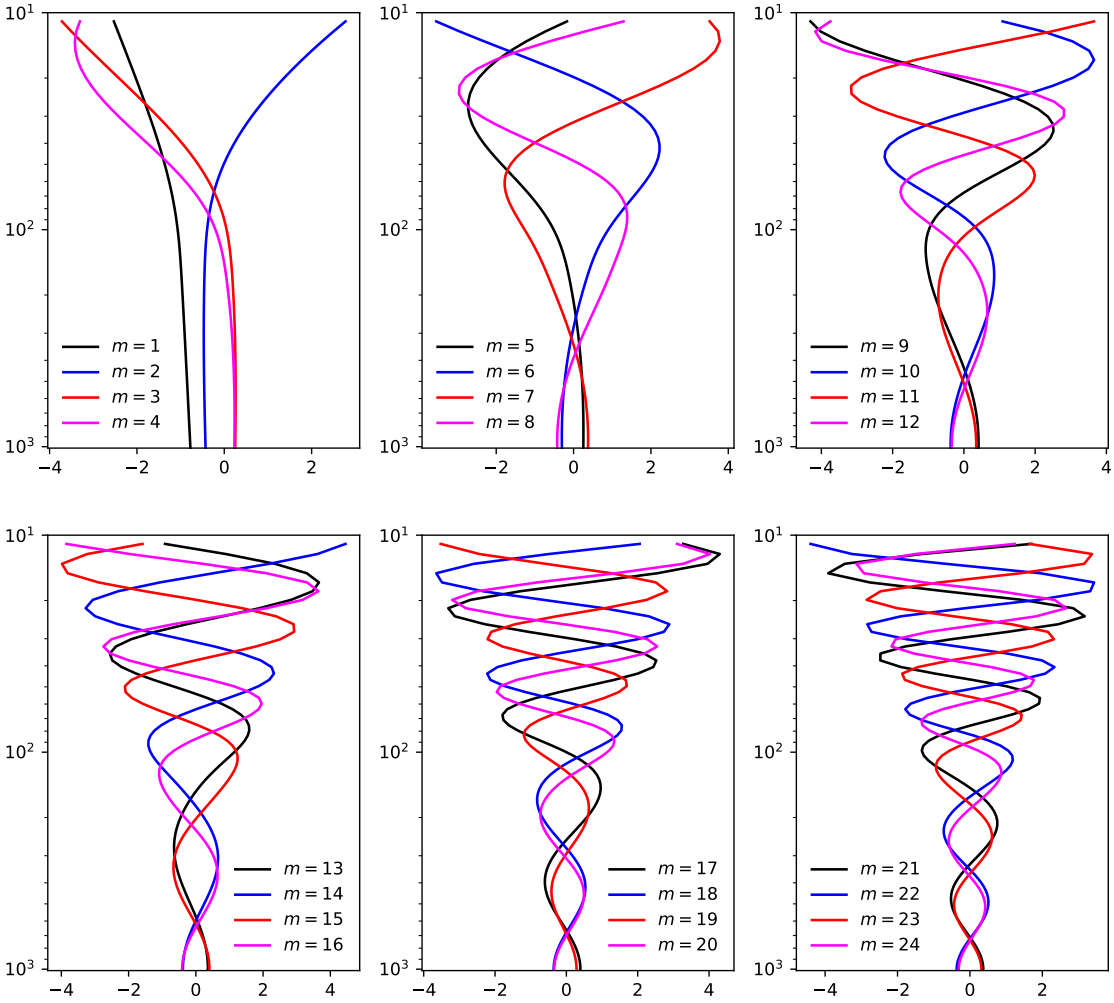

Figure C.16: Vertical structure functions for selected modes used for the vertical expansion of the data. For clarity, they are only shown up to 10 hPa, but they extend further up to 1 Pa.

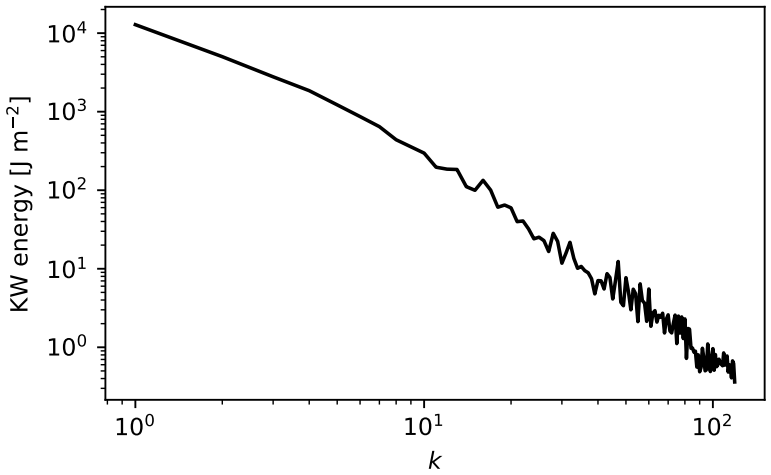

Figure C.17: Energy of Kelvin waves as a function of zonal wavenumber k, averaged over 2016-2019.

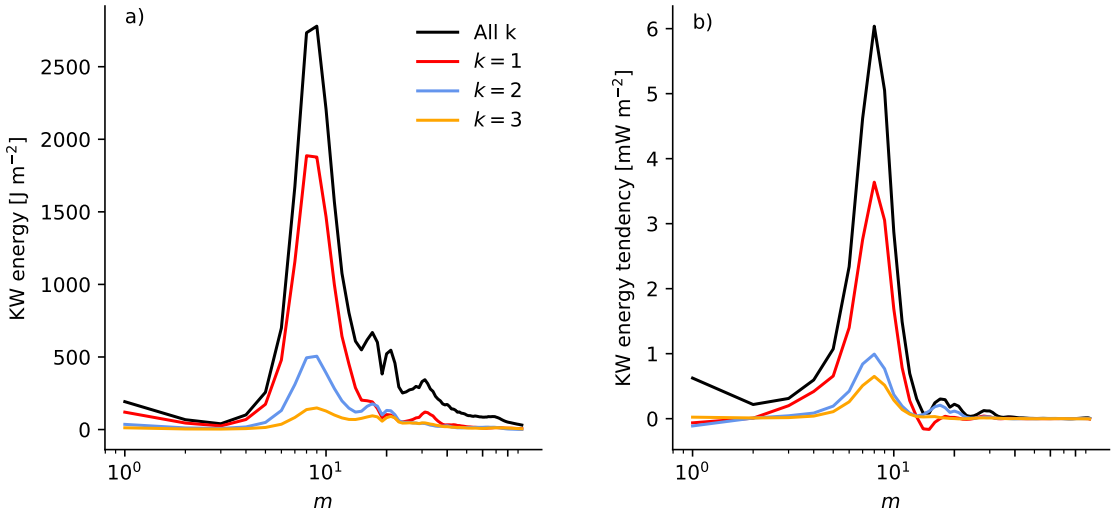

Figure C.18: a) Kelvin wave energy and b) Kelvin wave energy tendency due to (R1, R0) interactions as a function of vertical mode m, for different zonal wavenumbers k, averaged over 2016-2019.

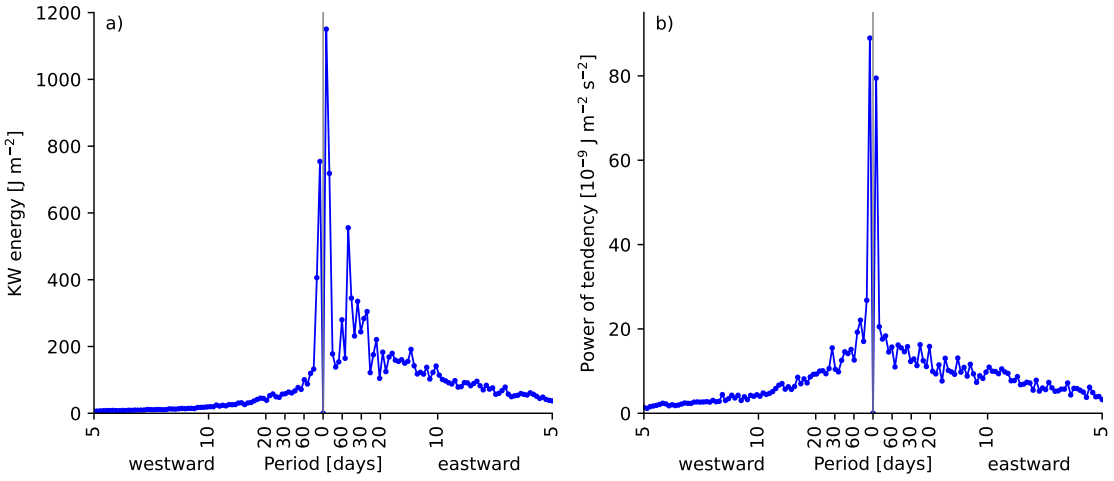

Figure C.19: Power spectra of a) Kelvin waves and b) their tendencies due to (R1, R0) interactions, for the sum over all k and m, averaged over four windows of one year each (2016-2019). The longest period shown is 365 days.

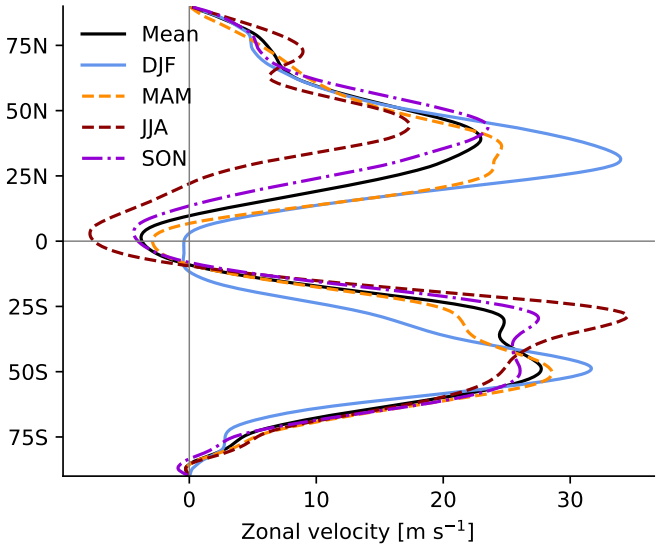

Figure C.20: Balanced zonal mean flow u_{R0} at 300 hPa, averaged over 2016-2019.

BIBLIOGRAPHY

Adames, Á. F. and J. M. Wallace (2014). Three-Dimensional Structure and Evolution of the MJO and Its Relation to the Mean Flow. *Journal of the Atmospheric Sciences* 71.6, 2007–2026. DOI: 10.1175/JAS-D-13-0254.1.

Augier, P. and E. Lindborg (2013). A New Formulation of the Spectral Energy Budget of the Atmosphere, with Application to Two High-Resolution General Circulation Models. *Journal of the Atmospheric Sciences* 70.7, 2293–2308. DOI: 10.1175/JAS-D-12-0281.1.

Bao, J., V. Dixit, and S. C. Sherwood (2022). Zonal Temperature Gradients in the Tropical Free Troposphere. *Journal of Climate* 35.24, 7937–7948. DOI: 10.1175/JCLI-D-22-0145.1.

Barpanda, P., S. N. Tulich, J. Dias, and G. N. Kiladis (2023). The Role of Subtropical Rossby Waves in Amplifying the Divergent Circulation of the Madden–Julian Oscillation. *Journal of the Atmospheric Sciences* 80.10, 2377 –2398. DOI: 10.1175/JAS-D-22-0259.1.

Barrett, B. S. (2019). Connections between the Madden–Julian Oscillation and surface temperatures in winter 2018 over eastern North America. *Atmospheric Science Letters* 20.1, e869. DOI: https://doi.org/10.1002/asl.869.

Bartana, H., C. I. Garfinkel, O. Shamir, and J. Rao (2023). Projected Future Changes in Equatorial Wave Spectrum in CMIP6. *Climate Dynamics* 60.11, 3277–3289. DOI: 10.1007/s00382-022-06510-y.

Bergman, J. W. and M. L. Salby (1994). Equatorial Wave Activity Derived from Fluctuations in Observed Convection. *Journal of the Atmospheric Sciences* 51.24, 3791–3806. DOI: 10.1175/1520-0469(1994)051<3791:EWADFF>2.0.CO;2.

Blaauw, M. and N. Žagar (2018). Multivariate Analysis of Kelvin Wave Seasonal Variability in ECMWF L91 Analyses. *Atmospheric Chemistry and Physics* 18.11, 8313–8330. DOI: 10.5194/acp-18-8313-2018.

Boyd, J. P. (2018). *Dynamics of the Equatorial Ocean*. Springer.

Boyd, J. P. (1978). The Effects of Latitudinal Shear on Equatorial Waves. Part II: Applications to the Atmosphere. *Journal of the Atmospheric Sciences* 35.12, 2259–2267. DOI: 10.1175/1520-0469(1978)035<2259:TEOLSO>2.0.CO;2.

Boyd, J. P. and C. Zhou (2008a). Kelvin Waves in the Nonlinear Shallow Water Equations on the Sphere: Nonlinear Travelling Waves and the Corner Wave Bifurcation. *Journal of Fluid Mechanics* 617, 187–205. DOI: 10.1017/S0022112008003959.

– (2008b). Uniform Asymptotics for the Linear Kelvin Wave in Spherical Geometry. *Journal of the Atmospheric Sciences* 65.2, 655–660. DOI: 10.1175/2007JAS2356.1.

Castanheira, J. M. and C. A. F. Marques (2015). Convectively Coupled Equatorial-Wave Diagnosis Using Three-Dimensional Normal Modes. *Quarterly Journal of the Royal Meteorological Society* 141.692, 2776–2792. DOI: 10.1002/qj.2563.

– (2019). The Energy Cascade Associated with Daily Variability of the North Atlantic Oscillation. *Quarterly Journal of the Royal Meteorological Society* 145.718, 197–210. DOI: 10.1002/qj.3422.

– (2021). The Equatorial Wave Skeleton of the Madden–Julian Oscillation. *Quarterly Journal of the Royal Meteorological Society* 147.740, 3778–3788. DOI: 10.1002/qj.4156.

Charney, J. G. (1969). A Further Note on Large-Scale Motions in the Tropics. *Journal of the Atmospheric Sciences* 26.1, 182–185. DOI: 10.1175/1520-0469(1969)026<0182:AFNOLS>2.0.CO;2.

Cheng, Y.-M., S. Tulich, G. N. Kiladis, and J. Dias (2022). Two Extratropical Pathways to Forcing Tropical Convective Disturbances. *Journal of Climate* 35.20, 2987–3009. DOI: 10.1175/JCLI-D-22-0171.1.

Chien, M.-T. and D. Kim (2023). Representation of the Convectively Coupled Kelvin Waves in Modern Reanalysis Products. *Journal of the Atmospheric Sciences* 80.2, 397–418. DOI: 10.1175/JAS-D-22-0067.1.

– (2024). Response of Convectively Coupled Kelvin Waves to Surface Temperature Forcing in Aquaplanet Simulations. *Journal of Advances in Modeling Earth Systems* 16.10, e2024MS004378. DOI: 10.1029/2024MS004378.

Chien, M.-T., D. Kim, and P. Haertel (2025). Maintenance of Convectively Coupled Kelvin Waves: Relative Importance of Internal Thermodynamic Feedback and External Momentum Forcing. *Geophysical Research Letters* 52.17, e2024GL113602. DOI: 10.1029/2024GL113602.

Cho, J. Y.-K. and L. M. Polvani (1996). The Emergence of Jets and Vortices in Freely Evolving, Shallow-water Turbulence on a Sphere. *Physics of Fluids* 8.6, 1531–1552. DOI: 10.1063/1.868929.

Chouksey, M., C. Eden, G. T. Masur, and M. Oliver (2023). A Comparison of Methods to Balance Geophysical Flows. *Journal of Fluid Mechanics* 971, A2. DOI: 10.1017/jfm.2023.602.

Craik, A. D. D. (1985). *Wave interactions and fluid flows*. Cambridge University Press.

Davey, M. K. and A. E. Gill (1987). Experiments On Tropical Circulation With A Simple Moist Model. *Quarterly Journal of the Royal Meteorological Society* 113.478, 1237–1269. DOI: 10.1002/qj.49711347809.

Dias, J., M. Gehne, G. N. Kiladis, and L. Magnusson (2023). The Role of Convectively Coupled Equatorial Waves in Sub-Seasonal Predictions. *Geophysical Research Letters* 50.21, e2023GL106198. DOI: 10.1029/2023GL106198.

Dias, J., M. Gehne, G. N. Kiladis, N. Sakaeda, P. Bechtold, and T. Haiden (2018). Equatorial Waves and the Skill of NCEP and ECMWF Numerical Weather Prediction Systems. *Monthly Weather Review* 146.6, 1763–1784. DOI: 10.1175/MWR-D-17-0362.1.

Dickinson, R. E. and D. L. Williamson (1972). Free Oscillations of a Discrete Stratified Fluid with Application to Numerical Weather Prediction. *Journal of the Atmospheric Sciences* 29.4, 623–640. DOI: 10.1175/1520-0469(1972)029<0623:FOOADS>2.0.CO;2.

Dolaptchiev, S. I. and R. Klein (2013). A Multiscale Model for the Planetary and Synoptic Motions in the Atmosphere. *Journal of the Atmospheric Sciences* 70.9, 2963–2981. DOI: 10.1175/JAS-D-12-0272.1.

ECMWF (2016a). IFS Documentation CY41R2 - Part III: Dynamics and Numerical Procedures. 3. DOI: 10.21957/83wouv80.

– (2016b). IFS Documentation CY41R2 - Part IV: Physical Processes. 4. DOI: 10.21957/tr5rv27xu.

Eden, C., M. Chouksey, and D. Olbers (2019). Mixed Rossby–Gravity Wave–Wave Interactions. *Journal of Physical Oceanography* 49.1, 291–308. DOI: 10.1175/JPO-D-18-0074.1.

Ferguson, J., B. Khouider, and M. Namazi (2009). Two-Way Interactions between Equatorially-Trapped Waves and the Barotropic Flow. *Chinese Annals of Mathematics, Series B* 30.5, 539–568. DOI: 10.1007/s11401-009-0102-9.

Ferrett, S., G.-Y. Yang, S. J. Woolnough, J. Methven, K. Hodges, and C. E. Holloway (2020). Linking Extreme Precipitation in Southeast Asia to Equatorial Waves. *Quarterly Journal of the Royal Meteorological Society* 146.727, 665–684. DOI: 10.1002/qj.3699.

Flannaghan, T. J. and S. Fueglistaler (2013). The Importance of the Tropical Tropopause Layer for Equatorial Kelvin Wave Propagation. *Journal of Geophysical Research: Atmospheres* 118.11, 5160–5175. DOI: 10.1002/jgrd.50418.

Garcia, R. R. and J. H. Richter (2019). On the Momentum Budget of the Quasi-Biennial Oscillation in the Whole Atmosphere Community Climate Model. *Journal of the Atmospheric Sciences* 76.1, 69–87. DOI: 10.1175/JAS-D-18-0088.1.

Garfinkel, C. I., O. Shamir, I. Fouxon, and N. Paldor (2021). Tropical Background and Wave Spectra: Contribution of Wave–Wave Interactions in a Moderately Nonlinear Turbulent Flow. *Journal of the Atmospheric Sciences* 78.6, 1773–1789. DOI: 10.1175/JAS-D-20-0284.1.

Gelb, A. and J. P. Gleeson (2001). Spectral Viscosity for Shallow Water Equations in Spherical Geometry. *Monthly Weather Review* 129.9, 2346–2360. DOI: 10.1175/1520-0493(2001)129<2346:SVFSWE>2.0.CO;2.

Gill, A. E. (1980). Some Simple Solutions for Heat-Induced Tropical Circulation. *Quarterly Journal of the Royal Meteorological Society* 106.449, 447–462. DOI: 10.1002/qj.49710644905.

Gill, A. E. and P. J. Phlips (1986). Nonlinear Effects on Heat-Induced Circulation of the Tropical Atmosphere. *Quarterly Journal of the Royal Meteorological Society* 112.471, 69–91. DOI: 10.1002/qj.49711247105.

Haertel, P. T. and G. N. Kiladis (2004). Dynamics of 2-Day Equatorial Waves. *Journal of the Atmospheric Sciences* 61.22, 2707–2721. DOI: 10.1175/JAS3352.1.

Haltiner, G. J. and R. T. Williams (1980). *Numerical prediction and dynamic meteorology*. 2nd ed. Wiley.

Hamilton, K. (1984). Evidence for a Normal Mode Kelvin Wave in the Atmosphere. *Journal of the Meteorological Society of Japan. Ser. II* 62.2, 308–311. DOI: 10.2151/jmsj1965.62.2_308.

Han, Y. and B. Khouider (2010). Convectively Coupled Waves in a Sheared Environment. *Journal of the Atmospheric Sciences* 67.9, 2913–2942. DOI: 10.1175/2010JAS3335.1.

Hayashi, Y. and D. G. Golder (1978). The Generation of Equatorial Transient Planetary Waves: Control Experiments with a GFDL General Circulation Model. *Journal of the Atmospheric Sciences* 35.11, 2068–2082. DOI: 10.1175/1520-0469(1978)035<2068:TGOETP>2.0.CO;2.

Hayashi, Y. (1970). A Theory of Large-Scale Equatorial Waves Generated by Condensation Heat and Accelerating. *Journal of the Meteorological Society of Japan. Ser. II* 48.2, 140–160. DOI: 10.2151/jmsj1965.48.2_140.

– (1971). A Generalized Method of Resolving Disturbances into Progressive and Retrogressive Waves by Space Fourier and Time Cross-Spectral Analyses. *Journal of the Meteorological Society of Japan. Ser. II* 49.2, 125–128. DOI: 10.2151/jmsj1965.49.2_125.

– (1982). Space-Time Spectral Analysis and Its Applications to Atmospheric Waves. *Journal of the Meteorological Society of Japan. Ser. II* 60.1, 156–171. DOI: 10.2151/jmsj1965.60.1_156.

Held, I. M. (1985). Pseudomomentum and the Orthogonality of Modes in Shear Flows. *Journal of the Atmospheric Sciences* 42.21, 2280–2288. DOI: 10.1175/1520-0469(1985)042<2280:PATOOM>2.0.CO;2.

Hendon, H. H. (1986). Streamfunction and Velocity Potential Representation of Equatorially Trapped Waves. *Journal of the Atmospheric Sciences* 43.23, 3038–3042. DOI: 10.1175/1520-0469(1986)043<3038:SAVPRO>2.0.CO;2.

Hendon, H. H. and M. L. Salby (1994). The Life Cycle of the Madden–Julian Oscillation. *Journal of the Atmospheric Sciences* 51.15, 2225–2237. DOI: 10.1175/1520-0469(1994)051<2225:TLCOTM>2.0.CO;2.

Hersbach, H. et al. (2020). The ERA5 Global Reanalysis. *Quarterly Journal of the Royal Meteorological Society* 146.730, 1999–2049. DOI: 10.1002/qj.3803.

Holt, L. A. et al. (2022). An Evaluation of Tropical Waves and Wave Forcing of the QBO in the QBOi Models. *Quarterly Journal of the Royal Meteorological Society* 148.744, 1541–1567. DOI: 10.1002/qj.3827.

Holton, J. R. (1972). Waves in the Equatorial Stratosphere Generated by Tropospheric Heat Sources. *Journal of the Atmospheric Sciences* 29.2, 368–375. DOI: 10.1175/1520-0469(1972)029<0368:WITESG>2.0.CO;2.

– (1992). *An Introduction to Dynamic Meteorology*. 3rd ed. International Geophysics Series v. 48. San Diego: Academic Press.

Holube, K. M., F. Lunkeit, S. Vasylkevych, and N. Žagar (2024). Resonant Excitation of Kelvin Waves by Interactions of Subtropical Rossby Waves and the Zonal Mean Flow. *Journal of the Atmospheric Sciences* 81.11, 1833–1848. DOI: 10.1175/JAS-D-24-0033.1.

– (2025a). *Energetics of the equatorial Kelvin wave*. [Data set]. DOI: 10.5281/zenodo.15351646.

– (2025b). Energy budget of the equatorial Kelvin wave: Comparing dynamical and diabatic sources. *submitted to the Journal of Advances in Modeling Earth Systems*. DOI: 10.22541/essoar.174776017.78570412/v1.

Hoskins, B. J. and G.-Y. Yang (2000). The Equatorial Response to Higher-Latitude Forcing. *Journal of the Atmospheric Sciences* 57.9, 1197–1213. DOI: 10.1175/1520-0469(2000)057<1197:TERTHL>2.0.CO;2.

Houchi, K., A. Stoffelen, G. J. Marseille, and J. De Kloe (2010). Comparison of Wind and Wind Shear Climatologies Derived from High-Resolution Radiosondes and the ECMWF Model. *Journal of Geophysical Research: Atmospheres* 115.D22. DOI: 10.1029/2009JD013196.

Jablonowski, C. and D. L. Williamson (2006). A Baroclinic Instability Test Case for Atmospheric Model Dynamical Cores. *Quarterly Journal of the Royal Meteorological Society* 132.621C, 2943–2975. DOI: 10.1256/qj.06.12.

Jiang, X., Á. F. Adames, D. Kim, E. D. Maloney, H. Lin, H. Kim, C. Zhang, C. A. DeMott, and N. P. Klingaman (2020). Fifty Years of Research on the Madden-Julian Oscillation: Recent Progress, Challenges, and Perspectives. *Journal of Geophysical Research: Atmospheres* 125.17, e2019JD030911. DOI: 10.1029/2019JD030911.

Kacimi, A. and B. Khouider (2018). The Transient Response to an Equatorial Heat Source and Its Convergence to Steady State: Implications for MJO Theory. *Climate Dynamics* 50.9, 3315–3330. DOI: 10.1007/s00382-017-3807-6.

Kasahara, A. (2020). 3D Normal Mode Functions (NMFs) of a Global Baroclinic Atmospheric Model. *Modal View Of Atmospheric Variability: Applications Of Normal-Mode Function Decomposition in Weather and Climate Research*. Ed. by N. Žagar and J. Tribbia. Springer, pp. 1–62.

Kasahara, A. (1976). Normal Modes of Ultralong Waves in the Atmosphere. *Monthly Weather Review* 104.6, 669–690. DOI: 10.1175/1520-0493(1976)104<0669:NMOUWI>2.0.CO;2.

– (1978). Further Studies on a Spectral Model of the Global Barotropic Primitive Equations with Hough Harmonic Expansions. *Journal of the Atmospheric Sciences* 35.11, 2043–2051. DOI: 10.1175/1520-0469(1978)035<2043:FSOASM>2.0.CO;2.

– (1980). Effect of Zonal Flows on the Free Oscillations of a Barotropic Atmosphere. *Journal of the Atmospheric Sciences* 37.5, 917–929. DOI: 10.1175/1520-0469(1980)037<0917:EOZFOT>2.0.CO;2.

– (1981). Corrigendum. *J. Atmos. Sci.* 38, 2284 –2285. DOI: 10.1175/1520-0469(1981)038<2284:>2.0.CO;2.

– (1984). The Linear Response of a Stratified Global Atmosphere to Tropical Thermal Forcing. *Journal of the Atmospheric Sciences* 41.14, 2217–2237. DOI: 10.1175/1520-0469(1984)041<2217:TLROAS>2.0.CO;2.

Kasahara, A. and K. Puri (1981). Spectral Representation of Three-Dimensional Global Data by Expansion in Normal Mode Functions. *Monthly Weather Review* 109.1, 37–51. DOI: 10.1175/1520-0493(1981)109<0037:SROTDG>2.0.CO;2.

Khouider, B. and A. J. Majda (2006). A Simple Multicloud Parameterization for Convectively Coupled Tropical Waves. Part I: Linear Analysis. *Journal of the Atmospheric Sciences* 63.4, 1308–1323. DOI: 10.1175/JAS3677.1.

Khouider, B., A. J. Majda, and S. N. Stechmann (2012). Climate Science in the Tropics: Waves, Vortices and PDEs. *Nonlinearity* 26.1, R1. DOI: 10.1088/0951-7715/26/1/R1.

Kiladis, G. N., M. C. Wheeler, P. T. Haertel, K. H. Straub, and P. E. Roundy (2009). Convectively Coupled Equatorial Waves. *Reviews of Geophysics* 47.2. DOI: 10.1029/2008RG000266.

Kitamura, Y. and Y. Matsuda (2010). Energy Cascade Processes in Rotating Stratified Turbulence with Application to the Atmospheric Mesoscale. *Journal of Geophysical Research: Atmospheres* 115.D11. DOI: 10.1029/2009JD012368.

Kitamura, Y. and K. Ishioka (2007). Equatorial Jets in Decaying Shallow-Water Turbulence on a Rotating Sphere. *Journal of the Atmospheric Sciences* 64.9, 3340–3353. DOI: 10.1175/JAS4015.1.

Kitsios, V., T. J. O'Kane, and N. Žagar (2019). A Reduced-Order Representation of the Madden–Julian Oscillation Based on Reanalyzed Normal Mode Coherences. *Journal of the Atmospheric Sciences* 76.8, 2463–2480. DOI: 10.1175/JAS-D-18-0197.1.

Knippertz, P. et al. (2022). The Intricacies of Identifying Equatorial Waves. *Quarterly Journal of the Royal Meteorological Society* 148.747, 2814–2852. DOI: 10.1002/qj.4338.

Kosovelj, K., F. Kucharski, F. Molteni, and N. Zagar (2019). Modal Decomposition of the Global Response to Tropical Heating Perturbations Resembling MJO. *Journal of the Atmospheric Sciences* 76.5, 1457–1469. DOI: 10.1175/JAS-D-18-0203.1.

Kraucunas, I. and D. L. Hartmann (2007). Tropical Stationary Waves in a Nonlinear Shallow-Water Model with Realistic Basic States. *Journal of the Atmospheric Sciences* 64.7, 2540–2557. DOI: 10.1175/JAS3920.1.

Lawton, Q. A. and S. J. Majumdar (2023). Convectively Coupled Kelvin Waves and Tropical Cyclogenesis: Connections through Convection and Moisture. *Monthly Weather Review* 151.7, 1647–1666. DOI: 10.1175/MWR-D-23-0005.1.

Li, Z., J. Peng, and L. Zhang (2023). Spectral Budget of Rotational and Divergent Kinetic Energy in Global Analyses. *Journal of the Atmospheric Sciences* 80.3, 813–831. DOI: 10.1175/JAS-D-21-0332.1.

Lindzen, R. S. and J. R. Holton (1968). A Theory of the Quasi-Biennial Oscillation. *Journal of the Atmospheric Sciences* 25.6, 1095–1107. DOI: 10.1175/1520-0469(1968)025<1095:ATOTQB>2.0.CO;2.

Longuet-Higgins, M. S. (1968). The Eigenfunctions of Laplace's Tidal Equation over a Sphere. *Philosophical Transactions of the Royal Society of London. Series A, Mathematical and Physical Sciences* 262.1132, 511–607. DOI: 10.1098/rsta.1968.0003.

Mahó, S. I., S. Vasylkevych, and N. Žagar (2024a). Excitation of mixed Rossby–gravity waves by wave–mean flow interactions on the sphere. *Quarterly Journal of the Royal Meteorological Society* 150.762, 2920–2936. DOI: 10.1002/qj.4742.

Mahó, S. I., N. Žagar, F. Lunkeit, and S. Vasylkevych (2024b). The Mechanism of Scale Selection for Mixed Rossby-Gravity Waves in the Upper Troposphere and the Upper Stratosphere. *Geophysical Research Letters* 51.23, e2024GL110811. DOI: 10.1029/2024GL110811.

Mahó, S. I. (2024). Explaining mixed Rossby-gravity wave generation in the tropical atmosphere. Available at https://ediss.sub.uni-hamburg.de/handle/ediss/11486. PhD thesis. University of Hamburg.

Majda, A. J. and J. A. Biello (2003). The Nonlinear Interaction of Barotropic and Equatorial Baroclinic Rossby Waves. *Journal of the Atmospheric Sciences* 60.15, 1809–1821. DOI: 10.1175/1520-0469(2003)060<1809:TNIOBA>2.0.CO;2.

Majda, A. J. and R. Klein (2003). Systematic Multiscale Models for the Tropics. *Journal of the Atmospheric Sciences* 60.2, 393–408. DOI: 10.1175/1520-0469(2003)060<0393:SMMFTT>2.0.CO;2.

Malardel, S. and N. P. Wedi (2016). How Does Subgrid-Scale Parametrization Influence Nonlinear Spectral Energy Fluxes in Global NWP Models? *Journal of Geophysical Research: Atmospheres* 121.10, 5395–5410. DOI: 10.1002/2015JD023970.

Mapes, B. E. (2000). Convective Inhibition, Subgrid-Scale Triggering Energy, and Stratiform Instability in a Toy Tropical Wave Model. *Journal of the Atmospheric Sciences* 57.10, 1515–1535. DOI: 10.1175/1520-0469(2000)057<1515:CISSTE>2.0.CO;2.

Marques, C. A. F., J. M. Castanheira, and A. Rocha (2014). Changes in the Normal Mode Energetics of the General Atmospheric Circulation in a Warmer Climate. *Climate Dynamics* 42.7, 1887–1903. DOI: 10.1007/s00382-013-1750-8.

Marques, C. a. F. and J. M. Castanheira (2012). A Detailed Normal-Mode Energetics of the General Circulation of the Atmosphere. *Journal of the Atmospheric Sciences* 69.9, 2718–2732. DOI: 10.1175/JAS-D-11-0324.1.

– (2017). Barotropic Decelerations of the Southern Stratospheric Polar Vortex. *Quarterly Journal of the Royal Meteorological Society* 143.703, 744–755. DOI: 10.1002/qj.2961.

Marques, C. A. F., M. Marta-Almeida, and J. M. Castanheira (2020). Three-Dimensional Normal Mode Functions: Open-Access Tools for Their Computation in Isobaric Coordinates (p-3DNMF.V1). *Geoscientific Model Development* 13.6, 2763–2781. DOI: 10.5194/gmd-13-2763-2020.

Matsuno, T. (1966). Quasi-Geostrophic Motions in the Equatorial Area. *Journal of the Meteorological Society of Japan. Ser. II* 44.1, 25–43. DOI: 10.2151/jmsj1965.44.1_25.

Matthews, A. J. (2021). Dynamical Propagation and Growth Mechanisms for Convectively Coupled Equatorial Kelvin Waves over the Indian Ocean. *Quarterly Journal of the Royal Meteorological Society* 147.741, 4310–4336. DOI: 10.1002/qj.4179.

Matthews, A. J. and R. A. Madden (2000). Observed Propagation and Structure of the 33-h Atmospheric Kelvin Wave. *Journal of the Atmospheric Sciences* 57.21, 3488–3497. DOI: 10.1175/1520-0469(2000)057<3488:OPASOT>2.0.CO;2.

Mitchell, K. A. (2013). Rossby Wave Propagation in the Tropics and Midlatitudes. Available at https://summit.sfu.ca/item/13748. PhD thesis. Simon Fraser University.

Monteiro, J. M., Á. F. Adames, J. M. Wallace, and J. S. Sukhatme (2014). Interpreting the Upper Level Structure of the Madden-Julian Oscillation. *Geophysical Research Letters* 41.24, 9158–9165. DOI: 10.1002/2014GL062518.

Morfa, Y. A. and C. C. Stephan (2025). Mesoscale Spectral Energy Transfers in Global Storm-resolving Simulations. *Journal of the Atmospheric Sciences* 82.10, 2121 –2139. DOI: 10.1175/JAS-D-24-0102.1.

Murakami, M. (1974). Influence of Mid-Latitudinal Planetary Waves on the Tropics under the Existence of Critical Latitude. *Journal of the Meteorological Society of Japan. Ser. II* 52.3, 261–271. DOI: 10.2151/jmsj1965.52.3_261.

NOAA PSL (2025a). *Multivariate ENSO Index Version 2 (MEI.v2)*. URL: https://www.psl.noaa.gov/enso/mei/.

– (2025b). *NOAA Interpolated Outgoing Longwave Radiation (OLR) data provided by the NOAA PSL, Boulder, Colorado, USA [Dataset]*. Accessed: 15 February 2025.

Nakamura, Y. and Y. N. Takayabu (2022). Convective Couplings with Equatorial Rossby Waves and Equatorial Kelvin Waves. Part I: Coupled Wave Structures. *Journal of the Atmospheric Sciences* 79.1, 247–262. DOI: 10.1175/JAS-D-21-0080.1.

Namazi, M. and B. Khouider (2013). The Interaction of Equatorial Waves with a Barotropic Shear: A Potential Test Case for Climate Model Dynamical Cores. *Theoretical and Computational Fluid Dynamics* 27.1, 149–176. DOI: 10.1007/s00162-012-0257-y.

Ortland, D. A. (2005). Generalized Hough Modes: The Structure of Damped Global-Scale Waves Propagating on a Mean Flow with Horizontal and Vertical Shear. *Journal of the Atmospheric Sciences* 62.8, 2674–2683. DOI: 10.1175/JAS3500.1.

Polichtchouk, I. and J. Y.-K. Cho (2016). Equatorial Superrotation in Held and Suarez like Flows with Weak Equator-to-Pole Surface Temperature Gradient. *Quarterly Journal of the Royal Meteorological Society* 142.696, 1528–1540. DOI: 10.1002/qj.2755.

Polichtchouk, I. et al. (2021). *Stratospheric modelling and assimilation*. ECMWF Technical Memoranda. DOI: 10.21957/25hegfoq.

Raphaldini, B., A. S. W. Teruya, C. F. M. Raupp, P. L. Silva-Dias, and D. Y. Takahashi (2021). Information Flow between MJO-related Waves: A Network Approach on the Wave Space. *The European Physical Journal Special Topics* 230.14, 3009–3017. DOI: 10.1140/epjs/s11734-021-00170-5.

Raupp, C. F. M. and P. L. Silva Dias (2005). Excitation Mechanism of Mixed Rossby–Gravity Waves in the Equatorial Atmosphere: Role of the Nonlinear Interactions among Equatorial Waves. *Journal of the Atmospheric Sciences* 62.5, 1446–1462. DOI: 10.1175/JAS3412.1.

Raupp, C. F. M., P. L. Silva Dias, E. G. Tabak, and P. Milewski (2008). Resonant Wave Interactions in the Equatorial Waveguide. *Journal of the Atmospheric Sciences* 65.11, 3398–3418. DOI: 10.1175/2008JAS2387.1.

Ripa, P. (1982). Nonlinear Wave–Wave Interactions in a One-Layer Reduced-Gravity Model on the Equatorial β Plane. *Journal of Physical Oceanography* 12.1, 97–111. DOI: 10.1175/1520-0485(1982)012<0097:NWIIAO>2.0.CO;2.

– (1983a). General Stability Conditions for Zonal Flows in a One-Layer Model on the β-Plane or the Sphere. *Journal of Fluid Mechanics* 126, 463–489. DOI: 10.1017/S0022112083000270.

– (1983b). Weak Interactions of Equatorial Waves in a One-Layer Model. Part I: General Properties. *Journal of Physical Oceanography* 13.7, 1208–1226. DOI: 10.1175/1520-0485(1983)013<1208:WIOEWI>2.0.CO;2.

– (1983c). Weak Interactions of Equatorial Waves in a One-Layer Model. Part II: Applications. *Journal of Physical Oceanography* 13.7, 1227–1240. DOI: 10.1175/1520-0485(1983)013<1227:WIOEWI>2.0.CO;2.

Sakazaki, T. and K. Hamilton (2020). An Array of Ringing Global Free Modes Discovered in Tropical Surface Pressure Data. *Journal of the Atmospheric Sciences* 77.7, 2519–2539. DOI: 10.1175/JAS-D-20-0053.1.

Sakazaki, T. and M. Schindelegger (2025). Global Atmospheric Normal Modes Identified in Surface Barometric Observations. *Journal of the Meteorological Society of Japan. Ser. II* 103.3, 371–388. DOI: 10.2151/jmsj.2025-019.

Salby, M. L. and R. R. Garcia (1987). Transient Response to Localized Episodic Heating in the Tropics. Part I: Excitation and Short-Time Near-Field Behavior. *Journal of the Atmospheric Sciences* 44.2, 458–498. DOI: 10.1175/1520-0469(1987)044<0458:TRTLEH>2.0.CO;2.

Shigehisa, Y. (1983). Normal Modes of the Shallow Water Equations for Zonal Wavenumber Zero. *Journal of the Meteorological Society of Japan. Ser. II* 61.4, 479–494. DOI: 10.2151/jmsj1965.61.4_479.

Simmons, A. J. and D. M. Burridge (1981). An Energy and Angular-Momentum Conserving Vertical Finite-Difference Scheme and Hybrid Vertical Coordinates. *Monthly Weather Review* 109.4, 758–766. DOI: 10.1175/1520-0493(1981)109<0758:AEAAMC>2.0.CO;2.

Simmons, A. J. (2022). Trends in the Tropospheric General Circulation from 1979 to 2022. *Weather and Climate Dynamics* 3.3, 777–809. DOI: 10.5194/wcd-3-777-2022.

Staniforth, A., M. Béland, and J. Côté (1985). An Analysis of the Vertical Structure Equation in Sigma Coordinates. *Atmosphere-Ocean* 23.4, 323–358. DOI: 10.1080/07055900.1985.9649232.

Stechmann, S. N. and H. R. Ogrosky (2014). The Walker Circulation, Diabatic Heating, and Outgoing Longwave Radiation. *Geophysical Research Letters* 41.24, 9097–9105. DOI: 10.1002/2014GL062257.

Stephan, C. C., N. Žagar, and T. G. Shepherd (2021). Waves and Coherent Flows in the Tropical Atmosphere: New Opportunities, Old Challenges. *Quarterly Journal of the Royal Meteorological Society* 147.738, 2597–2624. DOI: 10.1002/qj.4109.

Straub, K. H. and G. N. Kiladis (2003). Extratropical Forcing of Convectively Coupled Kelvin Waves during Austral Winter. *Journal of the Atmospheric Sciences* 60.3, 526–543. DOI: 10.1175/1520-0469(2003)060<0526:EFOCCK>2.0.CO;2.

Suzuki, J., N. Nishi, M. Fujiwara, and K. Yoneyama (2025). Changes in Equatorial Kelvin Wave Activity in the Upper Troposphere and Lower Stratosphere Associated with Interannual Variability of the Upper-Tropospheric Equatorial Zonal Wind. *Journal of Climate* 38.3, 749–759. DOI: 10.1175/JCLI-D-23-0192.1.

Swarztrauber, P. N. and A. Kasahara (1985). The Vector Harmonic Analysis of Laplace's Tidal Equations. *SIAM Journal on Scientific and Statistical Computing* 6.2, 464–491. DOI: 10.1137/0906033.

Takayabu, Y. N. (1994). Large-Scale Cloud Disturbances Associated with Equatorial Waves. *Journal of the Meteorological Society of Japan. Ser. II* 72.3, 433–449. DOI: 10.2151/jmsj1965.72.3_433.

Tanaka, H. L. (1991). A Numerical Simulation of Amplification of Low-Frequency Planetary Waves and Blocking Formations by the Upscale Energy Cascade. *Monthly Weather Review* 119.12, 2919–2935. DOI: 10.1175/1520-0493(1991)119<2919:ANSOAO>2.0.CO;2.

Tanaka, H. L. and E. C. Kung (1988). Normal Mode Energetics of the General Circulation during the FGGE Year. *Journal of the Atmospheric Sciences* 45.23, 3723–3737. DOI: 10.1175/1520-0469(1988)045<3723:NMEOTG>2.0.CO;2.

– (1989). A Study of Low-Frequency Unstable Planetary Waves in Realistic Zonal and Zonally Varying Basic States. *Tellus A: Dynamic Meteorology and Oceanography* 41.3, 179–199. DOI: 10.3402/tellusa.v41i3.11833.

Tanaka, H. L. and K. Terasaki (2005). Energy Spectrum and Energy Flow of the Arctic Oscillation in the Phase Speed Domain. *Sola* 1, 65–68. DOI: 10.2151/sola.2005-018.

Tanaka, H. (1985). Global Energetics Analysis by Expansion into Three-Dimensional Normal Mode Functions during the FGGE Winter. *Journal of the Meteorological Society of Japan. Ser. II* 63.2, 180–200. DOI: 10.2151/jmsj1965.63.2_180.

Teruya, A. S. W., B. Raphaldini, C. F. M. Raupp, P. S. Peixoto, V. C. Mayta, and P. L. Silva-Dias (2024). Data-Driven Modeling of Equatorial Atmospheric Waves: The Role of Moisture and Nonlinearity on Global-Scale Instabilities and Propagation Speeds. *Chaos: An Interdisciplinary Journal of Nonlinear Science* 34.6, 063137. DOI: 10.1063/5.0201716.

Tulich, S. N. and G. N. Kiladis (2021). On the Regionality of Moist Kelvin Waves and the MJO: The Critical Role of the Background Zonal Flow. *Journal of Advances in Modeling Earth Systems* 13.9, e2021MS002528. DOI: 10.1029/2021MS002528.

Valdes, P. J. and B. J. Hoskins (1989). Linear Stationary Wave Simulations of the Time-Mean Climatological Flow. *Journal of the Atmospheric Sciences* 46.16, 2509–2527. DOI: 10.1175/1520-0469(1989)046<2509:LSWSOT>2.0.CO;2.

Vallis, G. K. (2017). *Atmospheric and Oceanic Fluid Dynamics: Fundamentals and Large-Scale Circulation*. 2nd ed. Cambridge: Cambridge University Press. DOI: 10.1017/9781107588417.

Vasylkevych, S. and N. Žagar (2021). A High-Accuracy Global Prognostic Model for the Simulation of Rossby and Gravity Wave Dynamics. *Quarterly Journal of the Royal Meteorological Society* 147.736, 1989–2007. DOI: 10.1002/qj.4006.

Ventrice, M. J., C. D. Thorncroft, and M. A. Janiga (2012). Atlantic Tropical Cyclogenesis: A Three-Way Interaction between an African Easterly Wave, Diurnally Varying Convection, and a Convectively Coupled Atmospheric Kelvin Wave. *Monthly Weather Review* 140.4, 1108–1124. DOI: 10.1175/MWR-D-11-00122.1.

Wallace, J. M., D. S. Battisti, D. W. J. Thompson, and D. L. Hartmann (2023). *The Atmospheric General Circulation*. Cambridge University Press. DOI: 10.1017/9781108563857.

Wallace, J. M. and V. E. Kousky (1968). Observational Evidence of Kelvin Waves in the Tropical Stratosphere. *Journal of the Atmospheric Sciences* 25.5, 900–907. DOI: 10.1175/1520-0469(1968)025<0900:OEOKWI>2.0.CO;2.

Wang, B. and X. Xie (1996). Low-Frequency Equatorial Waves in Vertically Sheared Zonal Flow. Part I: Stable Waves. *Journal of the Atmospheric Sciences* 53.3, 449–467. DOI: 10.1175/1520-0469(1996)053<0449:LFEWIV>2.0.CO;2.

Wang, P. and J. L. Mitchell (2014). Planetary Ageostrophic Instability Leads to Superrotation. *Geophysical Research Letters* 41.12, 4118–4126. DOI: 10.1002/2014GL060345.

Webster, P. J. and J. R. Holton (1982). Cross-Equatorial Response to Middle-Latitude Forcing in a Zonally Varying Basic State. *Journal of the Atmospheric Sciences* 39.4, 722–733. DOI: 10.1175/1520-0469(1982)039<0722:CERTML>2.0.CO;2.

Wedi, N. P. and P. K. Smolarkiewicz (2010). A Nonlinear Perspective on the Dynamics of the MJO: Idealized Large-Eddy Simulations. *Journal of the Atmospheric Sciences* 67.4, 1202–1217. DOI: 10.1175/2009JAS3160.1.

Wheeler, M. and G. N. Kiladis (1999). Convectively Coupled Equatorial Waves: Analysis of Clouds and Temperature in the Wavenumber–Frequency Domain. *Journal of the Atmospheric Sciences* 56.3, 374–399. DOI: 10.1175/1520-0469(1999)056<0374:CCEWAO>2.0.CO;2.

Yanai, M., S. Esbensen, and J.-H. Chu (1973). Determination of Bulk Properties of Tropical Cloud Clusters from Large-Scale Heat and Moisture Budgets. *Journal of the Atmospheric Sciences* 30.4, 611–627. DOI: 10.1175/1520-0469(1973)030<0611:DOBPOT>2.0.CO;2.

Yang, G.-Y., B. Hoskins, and J. Slingo (2003). Convectively Coupled Equatorial Waves: A New Methodology for Identifying Wave Structures in Observational Data. *Journal of the Atmospheric Sciences* 60.14, 1637–1654. DOI: 10.1175/1520-0469(2003)060<1637:CCEWAN>2.0.CO;2.

– (2007). Convectively Coupled Equatorial Waves. Part III: Synthesis Structures and Their Forcing and Evolution. *Journal of the Atmospheric Sciences* 64.10, 3438–3451. DOI: 10.1175/JAS4019.1.

Yano, J.-I. and J. J. Tribbia (2017). Tropical Atmospheric Madden–Julian Oscillation: A Strongly Nonlinear Free Solitary Rossby Wave? *Journal of the Atmospheric Sciences* 74.10, 3473–3489. DOI: 10.1175/JAS-D-16-0319.1.

Yessad, K. (2016). *FULL-POS in the cycle 43 of ARPEGE/IFS, Météo-France, CNRM, GMAP, Algo*. Available at https://www.umr-cnrm.fr/gmapdoc/IMG/pdf/ykfpos43.pdf.

Žagar, N., L. Isaksen, D. Tan, and J. Tribbia (2013). Balance Properties of the Short-Range Forecast Errors in the ECMWF 4D-Var Ensemble. *Quarterly Journal of the Royal Meteorological Society* 139.674, 1229–1238. DOI: 10.1002/qj.2033.

Žagar, N., A. Kasahara, K. Terasaki, J. Tribbia, and H. Tanaka (2015). Normal-Mode Function Representation of Global 3-D Data Sets: Open-Access Software for the Atmospheric Research Community. *Geoscientific Model Development* 8.4, 1169–1195. DOI: 10.5194/gmd-8-1169-2015.

Žagar, N., R. Pilch Kedzierski, G. De Chiara, S. Healy, M. Rennie, and F. Sielmann (2025). ESA's Aeolus Mission Reveals Uncertainties in Tropical Wind and Wave-Driven Circulations. *Geophysical Research Letters* 52.8, e2025GL114832. DOI: 10.1029/2025GL114832.

Žagar, N., J. Tribbia, J. L. Anderson, and K. Raeder (2009). Uncertainties of Estimates of Inertia–Gravity Energy in the Atmosphere. Part I: Intercomparison of Four Analysis Systems. *Monthly Weather Review* 137.11, 3837–3857. DOI: 10.1175/2009MWR2815.1.

Žagar, N., E. Andersson, and M. Fisher (2005). Balanced Tropical Data Assimilation Based on a Study of Equatorial Waves in ECMWF Short-Range Forecast Errors. *Quarterly Journal of the Royal Meteorological Society* 131.607, 987–1011. DOI: 10.1256/qj.04.54.

Žagar, N. and C. L. E. Franzke (2015). Systematic Decomposition of the Madden-Julian Oscillation into Balanced and Inertio-Gravity Components. *Geophysical Research Letters* 42.16, 6829–6835. DOI: 10.1002/2015GL065130.

Žagar, N., K. Kosovelj, E. Manzini, M. Horvat, and J. Castanheira (2020). An Assessment of Scale-Dependent Variability and Bias in Global Prediction Models. *Climate Dynamics* 54.1, 287–306. DOI: 10.1007/s00382-019-05001-x.

Žagar, N., F. Lunkeit, F. Sielmann, and W. Xiao (2022). Three-Dimensional Structure of the Equatorial Kelvin Wave: Vertical Structure Functions, Equivalent Depths, and Frequency and Wavenumber Spectra. *Journal of Climate* 35.7, 2209 –2230. DOI: 10.1175/JCLI-D-21-0342.1.

Žagar, N., V. Neduhal, S. Vasylkevych, Ž. Zaplotnik, and H. L. Tanaka (2023). Decomposition of Vertical Velocity and Its Zonal Wavenumber Kinetic Energy Spectra in the Hydrostatic Atmosphere. *Journal of the Atmospheric Sciences* 80.11. DOI: 10.1175/JAS-D-23-0090.1.

Zhang, C., A. F. Adames, B. Khouider, B. Wang, and D. Yang (2020). Four Theories of the Madden-Julian Oscillation. *Reviews of Geophysics* 58.3, e2019RG000685. DOI: 10.1029/2019RG000685.

Zhang, C. (1993). Laterally Forced Equatorial Perturbations in a Linear Model. Part II: Mobile Forcing. *Journal of the Atmospheric Sciences* 50.6, 807–821. DOI: 10.1175/1520-0469(1993)050<0807:LFEPIA>2.0.CO;2.

Zhang, C. and P. J. Webster (1989). Effects of Zonal Flows on Equatorially Trapped Waves. *Journal of the Atmospheric Sciences* 46.24, 3632–3652. DOI: 10.1175/1520-0469(1989)046<3632:EOZFOE>2.0.CO;2.

– (1992). Laterally Forced Equatorial Perturbations in a Linear Model. Part I: Stationary Transient Forcing. *Journal of the Atmospheric Sciences* 49.7, 585–607. DOI: 10.1175/1520-0469(1992)049<0585:LFEPIA>2.0.CO;2.